Light Matter Interfaces with Single-Atom Arrays and Rydberg Ensembles

by

Huy N. Nguyen

A dissertation submitted in partial fulfillment
of the requirements for the degree of
Doctor of Philosophy
(Physics)
in the University of Michigan
2022

Doctoral Committee:

Professor Alexander Kuzmich, Chair
Professor Emeritus Paul Berman
Professor Vanessa Sih
Professor Herbert Winful
Professor Liuyan Zhao

Huy N. Nguyen
huynnguy@umich.edu
ORCID iD: 0000-0002-2393-2236

DEDICATION

Resilience in the face of hardships is an important life lesson that has been instilled in me since I was a child. Struggling to make ends meet amidst a war-torn country, my parents uprooted their lives in Vietnam to move to America. As immigrants, we faced a multitude of cultural, linguistic, and financial adversities. Despite taking on several jobs to support my three siblings and me, the only housing that my family was able to afford was in a low-income community afflicted with drug and gang violence. In spite of the negative external influences surrounding my siblings and me, we remained steadfast on our pursuit of knowledge. This was because my parents cultivated a home environment around the value of education and how it will pave the way for further opportunities to enrich our future. Working aside my father after he started his landscaping business was initially a means for me to reduce the financial burden of college on my family. I later came to realize an important life lesson on perseverance and adaptability: individuals, like cacti, can blossom in the harshest of conditions by making the best out of all of the opportunities provided to them. Without their immense sacrifice and consistent encouragement, I would not be where I am today. For that, I dedicate this thesis to them.

ACKNOWLEDGMENTS

In the realm of academia, it has been an immense honor to have been directly mentored by two luminaries in the field of atomic physics and quantum optics, Professor Alexander Kuzmich and Professor Paul Berman. Under their guidance, I have gained a broad suite of experimental and theoretical skills that have shaped me into a well-rounded physicist.

From my first interactions with Prof. Kuzmich in the lab, I was awestruck by his sharp intellect and intensity for research. Coupled with his impressive intuition for atomic physics, he has a keen ability for formulating questions that efficiently lead to solutions within the lab. Alex has always been incredibly generous with both his time and resources. I'll always cherish fondly the hands-on teaching moments of aligning optics and locking lasers that he shared with me in my early stages of my PhD. During that time, he taught me the importance of having a quantitative grasp of all of the experimental parameters. Without his guidance, I wouldn't have been able to accomplish any of the things that I did in his lab, so I want to extend my sincerest gratitude for making my PhD a fantastic experience.

Prof. Berman has been a continuous and abundant source of knowledge. It is immediately evident from his unique method of explaining concepts that he has a deep interest in sharing his skills and expertise with others. He has a distinctive proficiency in breaking difficult theories down to its core ideas. He always made sure that my understanding of a given topic was his top priority. His extraordinary genius combined with his humble demeanor and laid back personality made it easy to approach him with any questions that I had. All of those qualities have made him an excellent role model for me, and I hope that I can be even half the physicist that he is in the future.

Having come from a single-atom and quantum simulation group in Japan, Dr. Hikaru Tamura was a blessing to have in the lab. With his guidance, we were able to build up the single-atom array experiment from scratch. His work in Japan including the development of a suite of Labview programs, homebuilt SLM software, and electronics are the foundation for which our experiment was developed. He generously shared his expertise in atomic physics, electronics, alignment of optical elements, and digital holography. His intense work ethic was contagious, and he always pushed me to be the best that I could be. I sincerely hope him the best of luck in his future endeavors and I am excited to see all that he accomplishes.

Dr. Jacob Lampen was a tremendous labmate throughout his time in the lab. He ensured that the lab was a environment conducive for growth and learning. He taught me the fundamentals of Rydberg atoms along with the principles of state-insensitive trapping of Rydberg atoms.

I especially want to thank all of the current members of the lab for making the lab an enjoyable place to be, despite the pandemic. Andrea Londono, Carola Jansohn, Carlos Owens, Brian Yang, Yin Li and Dr. Yefeng Mei all have grown to become like a family to me. I wish them the very best of luck in the future, and I'm confident that they will be able to take their experiments to new heights.

I would like to thank the remainder of the committee: Professor Vanessa Sih, Professor Liuyan Zhao, and Professor Herbert Winful for their time and effort in reviewing and providing edits to this thesis.

TABLE OF CONTENTS

LIST OF FIGURES

FIGURE

LIST OF TABLES

TABLE

ABSTRACT

A principal goal of distributed quantum processing is the ability to generate, manipulate, and transfer quantum states between distant nodes of a quantum network. These protocols generally require connecting photonic and material carriers of quantum information. In this thesis, I present investigations of two experimental realizations of light-matter interfaces that allow for engineered atom-photon interactions in free-space settings.

First, we utilize reconfigurable arrays of trapped single atoms to study light scattering in low-dimensional systems. We observe noncollinear phase-matching geometries that have suppressed sensitivity to particle localization. We show that the scattered radiation can be controllably enhanced or diminished as a result of Bragg interference. Such scattering can be used for mapping collective states within an array of neutral atoms onto propagating light fields and for establishing quantum links between separated arrays.

Second, we utilize ensembles of trapped Rydberg atoms to study collective many-body phenomena that arise due to strong dipole-dipole interactions. To do so, we employ a magic-wavelength optical lattice that allows for the simultaneous trapping of both ground and Rydberg levels. Using the enhanced coherence times enabled by this trapping scheme, we measure the so-called magic lattice detunings and use them to extract the $|6P_{3/2}\rangle - |nS_{1/2}\rangle$ reduced electric dipole matrix elements. Furthermore, we perform precision measurements of differential nuclear-spin dependent light shifts in the Paschen-Back regime in order to determine the hyperfine splitting of Rydberg levels.

We create a quasi-two-level system in a regime of Rydberg excitation blockade for a mesoscopic ensemble of several hundred atoms. Using this system, we study Hanbury Brown-Twiss interference between the field radiated by the atoms and an input probe field with a controllable relative phase. Finally, we demonstrate coherent driving and Ramsey interference measurements of light shifts, with timescales on the order of $\simeq 10\ \mu s$. Whereas the coupling producing the Rabi oscillations is enhanced by a factor of $\sqrt{N}$, there is no corresponding enhancement for the light shifts. These results may prove useful in applying collective qubits with Rydberg interactions to scalable quantum networking architectures.

CHAPTER 1

Introduction

The continued increase of computational power has been one of the main driving forces for a plethora of technological and economic developments in the past few decades. Behind the exponential growth of processing power described by Moore's Law, is the ever-shrinking size of electrical components in the integrated circuits. However, transistors are rapidly approaching length scales in which quantum effects will severely limit their performance. If this exponential growth is to continue, it is critical that we develop new paradigms of information processing.

Quantum information processing is one of these paradigms. Rather than being limited by quantum effects, it leverages quantum mechanical superposition and entanglement to achieve exponentially faster performance of several classes of computational algorithms. Utilizing such quantum algorithms, a host of difficult problems that are not tractable using classical computation schemes may be tackled. Realizing an experimental platform capable of leveraging these unique resources to achieve a quantum advantage in practical applications has been an ongoing pursuit for the past few decades.

The term "Noisy Intermediate Scale Quantum" (NISQ), accurately summarizes current state-of-the-art quantum devices. "Noisy" refers to the fact that the quantum state manipulations necessary for logical operations are susceptible to errors, while quantum error correction (QEC) has only been experimentally implemented at a limited capacity. "Intermediate scale" means that these devices are comprised of up to a few hundred qubits, which is still far from the 10,000-1,000,000 qubits estimated to demonstrate a quantum advantage in algorithms such as unstructured database searches and integer factorization.

Despite this fact, NISQ-era algorithms implemented on existing quantum devices have taken results out of the realm of pure scientific interest into the domain for practical use in the industrial setting. For example, extending beyond Google's quantum supremacy claim related to random number generation on their superconducting processor, Quantinuum is now generating quantum cryptographic keys on their trapped-ion device and distributing them through their QuantumOrigin product. Furthermore, generation of entangled Greenberger-Horne-Zeilinger states, quantum

phase estimation, and quantum approximate optimization algorithms (QAOA) has been demonstrated on the ColdQuanta neutral atom processor and have applications in optimization and quantum chemistry. While superconducting, trapped-ions, and neutral atoms are some of the more established technologies for quantum information processing, there are whole host of unique platforms that are being actively investigated in industry and academic settings. Figure 1.1 shows an overview of some of the predominant experimental platforms and the institutions at which they are being developed.

In addition to the technical and engineering complications that need to be overcome to move beyond the NISQ era, these platforms must also contend with two requirements imposed by the laws of quantum physics. These requirements seem to be in stark opposition with one another, and substantiate the difficulty of developing such an experimental platform.

First, preservation of sensitive quantum coherences requires that the qubits interact weakly with its surroundings, as radiative processes and interactions with its environment can destroy the fragile quantum coherence. A pristine environment often implies the use of ultra-high vacuum, cryogenics, and electromagnetic shielding technology. Even more important is a proper choice of an intrinsically stable quantum-mechanical system to be used as a qubit. The coherence properties of the qubit are often characterized by the T_1, T_2' and T_2^* coherence times, corresponding to the longitudinal relaxation, polarization decay, and inhomogenous dephasing rates respectively. Second, for high fidelity control, the qubit must interact strongly with its control mechanisms, whether they be laser pulses, microwaves, or even other qubits. The rate at which at which quantum state manipulations can be performed must be much faster than the rate at which decoherence results in loss of quantum information.

Figure 1.1: Overview of the various experimental platforms being investigated for quantum control of qubits in the NISQ era. The inner circle indicates the physical quantum system used for the qubit, and the outer circle shows the institutions developing the technology.

For these reasons, strong and controllable interactions are a crucial ingredient for qubits in an high-fidelity quantum processor. This fact is what makes the neutral atom an attractive quantum-mechanical platform to realize a qubit. Due to charge neutrality, they interact weakly with stray electric fields and other atoms in their ground state. As a result, they possess excellent coherence properties, elucidated by the fact that they have been the industry standard for optical clocks, and underpinning the definition of the second for several decades. When strong interactions are required for logical operations, a neutral atom can be excited to highly excited Rydberg states. As a result of the strong van der Waals interaction, atom pairs can experience interactions with a strength 12 orders of magnitude larger than ground state atoms. Utilizing these attributes, high-fidelity quantum gates have been demonstrated, making them competitive with other leading platforms.

Another benefit to neutral atoms is their innate ability to scale. Neutral atoms can be prepared in a magneto optical trap, where millions of atoms are gathered into a dense atomic sample before being transferred into arrays of 100s – 1000s of individually addressable optical tweezers. There has been consistent progress on scaling the number of qubits in the local quantum devices by

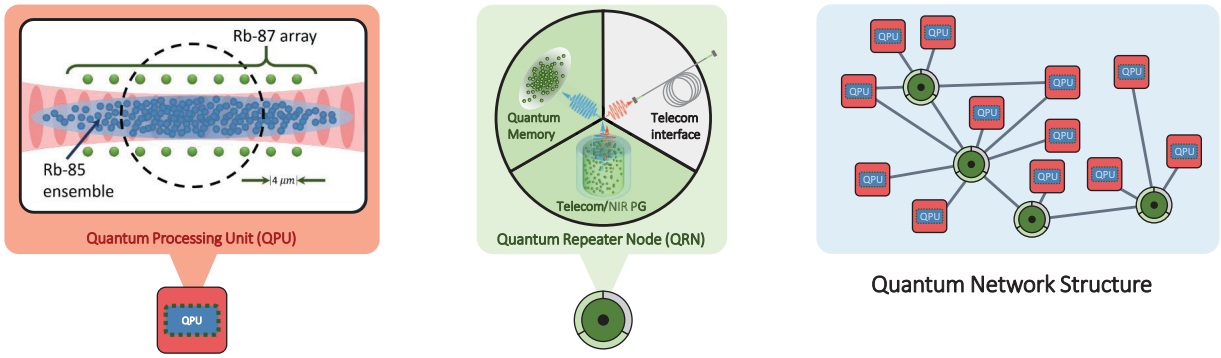

Figure 1.2: A network architecture with (left) hybrid atomic array/ensemble quantum processor nodes, (middle) quantum repeater node consisting of a quantum memory, telecom/ near infrared (NIR) pair generators (PG) and telecom interfaces. (Right) Entanglement between qubits in remote nodes can be achieved by processing of photonic modes with subsequent joint measurements of photons emitted at these nodes.

confining atoms in optical lattices, as well as optical tweezer arrays generated by acousto-optic deflectors, and spatial light modulators.

Beyond fault-tolerant scalable quantum processors, neutral atoms show promise as foundational ingredients for a large-scale quantum information network. In this model, the existing system of telecommunication fibers will connect distant quantum processors in this quantum network, and photons will transmit information between nodes as in classical distributed computing. This will relax the technical requirements for an individual processor, and the continued addition of nodes to the network will enable long-term scaling. To utilize the distributed information processing capabilities of a quantum network, long distance entanglement between quantum processing nodes is required. One limitation is that attenuation within telecommunication optical fibers results in an exponential loss of entanglement fidelity. To overcome this restraint, the distance between two nodes is divided into lengths smaller than the attenuation length and connected by quantum repeaters. Entangled pairs of photons are sent to adjacent repeater stations and through multiple iterations of entanglement swapping, will extend entanglement the entire internodal distance.

Due to requirements imposed by the finite propagation speed of light and entanglement-swapping protocols, quantum repeater nodes must have the following capabilities: storage of quantum information in excess of one second, efficient generation of entangled photons in the telecom wavelength, interfacing between matter and photonic qubits, and high fidelity local quantum state manipulations. Our lab, amongst others in the world, have realized long-lived quantum memories, atom-photon entanglement, and telecommunication conversion capabilities using ultra-cold neutral atoms and their highly excited Rydberg states. Figure 1.2 shows a high-level overview for how

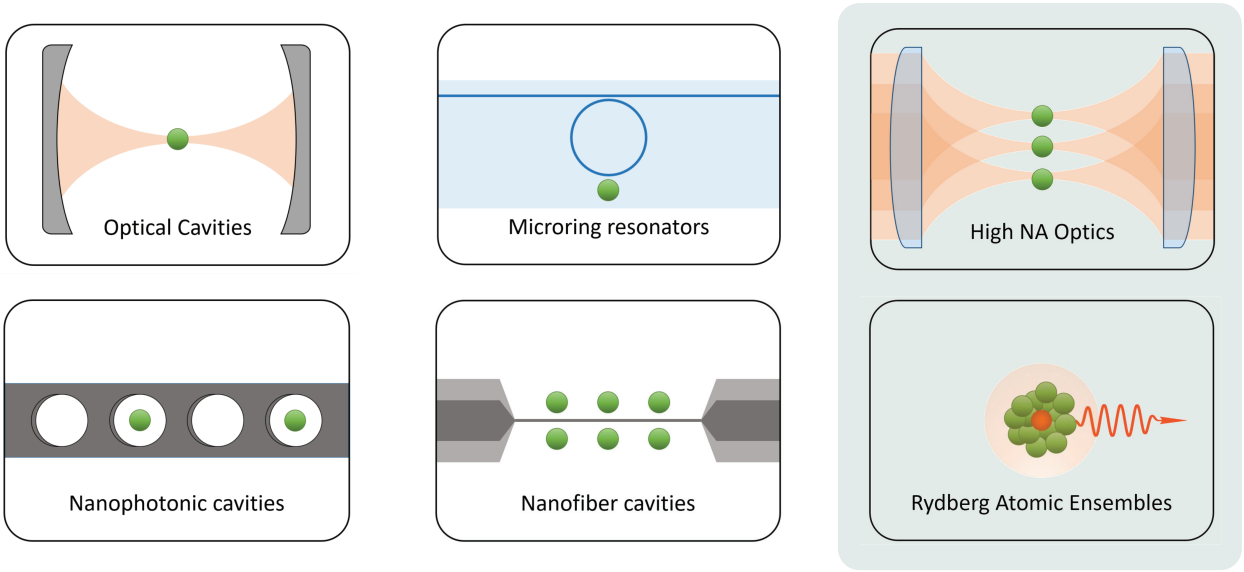

Figure 1.3: Several different methods for engineeering the photonic density of states. A common approach is to utilize artificial dielectric structures such as optical cavities, nanophotonics, and microring resonators such that there is just a single electromagnetic mode interacting with the qubit. In this thesis, we will explore how the light-matter interaction can be enhanced utilizing interference properties of light as well as strong Rydberg interactions.

a quantum network based on neutral atom components may be realized.

For many of the aforementioned capabilities to be realized with high efficiency, strong interaction between the material and photonic carriers of quantum information is required. Many research groups around the world are pursuing different techniques to engineer this light-atom interaction, some of which are displayed in Figure 1.3. A common approach is by utilizing fabricated dielectric structures, which allow for the local photonic density of states surrounding the qubit to be manipulated. In the ideal setting, a single electromagnetic mode is dominant, thereby increasing the atom-light interaction with the qubit. Examples of such platforms include optical cavities, microring resonators, nanophotonic and nanofiber cavities. For these applications, precise positioning of optical traps within these dielectric structures is necessary, and dealing with the deleterious effects that can result from the interactions between the Rydberg atom with the dielectric surfaces is essential. In the Kuzmich lab, we investigate light matter interfaces in the free-space setting using two approaches. The first is by employing the inference properties of light in single-atom arrays and utilizing high numerical aperature (NA) optics. The second is by implementing state-insensitive optical lattices to confine ensembles of Rydberg atoms and utilizing collective-many body effects to achieve an enhancement of the atom-light interaction strength.

CHAPTER 2

Overview

This thesis will present investigations of the fundamental components of these light-matter interfaces. In these investigations, I was involved in various experimental design, fabrication, and data acquisition processes. I also was heavily engaged in the implementation of theoretical models to process, understand, and extract useful information from the experimental data. This thesis is divided into three parts, each of which are comprised of multiple chapters.

Part 1 will lay the foundation for the relevant physics discussed in the subsequent sections of the thesis. Here I will discuss a simple description of the light-matter interaction, and the fundamentals of optical dipole traps. These notions will be extended to describe how a state-insensitive trap can be used to equalize the trapping potentials for ground and Rydberg states of Rubidium. I will provide the theoretical background for understanding Rydberg atoms, their scaling properties, and explain how collective states of hundreds of atoms can be manipulated and described theoretically utilizing a Dicke state formalism.

Part 2 will be an overview of the experimental apparatus for generating reconfigurable arrays of trapped single-atoms. There I will explain how a spatial light modulator can be utilized to generate arrays of optical tweezers capable of confining single atoms. I will explain methods for improving the uniformity of traps via wavefront correction and iterative feedback protocols utilizing trap intensity, atomic fluorescence, and light-shift measurements. I will describe the process of characterizing the performance of high numerical aperature objective lenses. Finally I will describe the optical layouts and laser systems as well as provide an introduction to laser stabilization.

Part 3 will be a compilation of published works during the time of my PhD career:

- **"Long-lived coherence between ground and Rydberg levels in a magic wavelength lattice,"** J. Lampen, H. Nguyen, L. Li, P. R. Berman, and A. Kuzmich, Physical Review A 98, 033411 (2018).

  By confining atoms in a state-insensitive optical lattice, the lifetime of the ground-state–Rydberg coherence is increased to $\geq 20\ \mu s$, an order of magnitude improvement over previous experiments using freely diffusing atoms. Using these enhanced lifetimes, we measure

the so-called magic lattice wavelengths for Rb and use them to extract the $6P_{3/2} - nS_{1/2}$ reduced electric dipole matrix elements. Good agreement is found with values obtained using an effective one-electron potential for principal quantum numbers n between $n = 30$ and $n = 70$. We develop a theoretical model based on quantized motion to map out the ground-state–Rydberg coherence as a function of time that is in good agreement with the experimental results. The availability of long coherence times may present new opportunities for high-resolution spectroscopy and quantum information science.

- **"Theory of coherent optical transients with quantized atomic motion,"** P. R. Berman, H. Nguyen, and A. Kuzmich, Physical Review A 99, 013427 (2019).

  A theory of coherent transients is developed in which a sequence of optical pulses is incident on a sample of trapped atoms and gives rise to phase-matched emission from the sample. The trapping potential for the atoms can be state dependent, necessitating a quantum treatment of the center-of-mass motion. A source-field approach is followed, modified to account for the quantized motion of the atoms. The theory is illustrated with two examples, one involving the creation of ground-Rydberg level coherence in an optical lattice and the second Raman coherence between two ground-state sublevels of atoms in a dipole trap. For state-independent potentials, a comparison is made with a theory in which the center-of-mass motion is treated classically.

- **"Differential nuclear-spin-dependent light shifts and state mixing of Rydberg atoms,"** H. Nguyen, J. Lampen, P. R. Berman, and A. Kuzmich, Physical Review A 100, 033412 (2019).

  In this paper we present a detailed analysis of the nuclear-spin manifolds associated with the ns Rydberg levels of ^{87}Rb atoms that interact with both magnetic and optical lattice fields. Eigenvalues and eigenkets for the Rydberg manifold are obtained and used to study the dynamics of phase-matched emission following illumination of an ensemble of cold atoms with excitation and readout laser pulses. By comparing the measured emission signal to predictions of a model that accounts for the quantized motion of atoms in a one-dimensional optical lattice potential, we are able to extract the Rydberg hyperfine and light shift contributions to the observed modulation frequencies. In this way the hyperfine splitting of Rydberg nS levels is measured for n in the range of 30 to 65. Our results should be relevant for realizations of high-fidelity Rydberg qubits confined in optical potentials.

- **"Hanbury Brown–Twiss Correlations for a Driven Superatom,"** J. Lampen, A. Duspayev, H. Nguyen, H. Tamura, P. R. Berman, and A. Kuzmich, Physical Review Letters 123, 203603 (2019).

Hanbury Brown–Twiss interference and stimulated emission, two fundamental processes in atomic physics, have been studied in a wide range of applications in science and technology. We study interference effects that occur when a weak probe is sent through a gas of two-level atoms that are prepared in a singly excited collective (Dicke or "superatom") state and for atoms prepared in a factorized state. We measure the time-integrated second-order correlation function $g^{(2)}$ of the output field as a function of the delay τ between the input probe field and radiation emitted by the atoms and find that, for the Dicke state, $g^{(2)}$ is twice as large for $\tau = 0$ as it is for $\gamma_e \tau \gg 1$ (γ_2 is an excited state decay rate), while for the product state, this ratio is equal to 3 / 2 . The results agree with those of a theoretical model in which any effects related to stimulated emission are totally neglected—the coincidence counts measured in our experiment arise from Hanbury Brown–Twiss interference between the input field and the field radiated by the atoms.

- **"Phase Matching in Lower Dimensions,"** H. Tamura, H. Nguyen, P. R. Berman, and A. Kuzmich, Physical Review Letters 125, 163601 (2020).

  Phase matching refers to a process in which atom-field interactions lead to the creation of an output field that propagates coherently through the interaction volume. By studying light scattering from arrays of cold atoms, we show that conditions for phase matching change as the dimensionality of the system decreases. In particular, for a single atomic chain, there is phase-matched reflective scattering in a cone about the symmetry axis of the array that scales as the square of the number of atoms in the chain. For two chains of atoms, the phase-matched reflective scattering can be enhanced or diminished as a result of Bragg scattering. Such scattering can be used for mapping collective states within an array of neutral atoms onto propagating light fields and for establishing quantum links between separated arrays.

- **"Trapped Alkali-Metal Rydberg Qubit,"** Y. Mei, Y. Li, H. Nguyen, P.R. Berman, and A. Kuzmich, Physical Review Letters. 128, 123601 (2022).

  Rydberg interactions of trapped alkali-metal atoms are used widely to facilitate quantum gate operations in quantum processors and repeaters. In most laboratory realizations using this protocol, the Rydberg states are repelled by the trapping laser fields, requiring that the fields be turned off during gate operations. Here we create a quasi-two-level system in a regime of Rydberg excitation blockade for a mesoscopic Rb ensemble of several hundred atoms confined in a magic-wavelength optical lattice. We observe many-body Rabi oscillations between the ground and collective Rydberg state. In addition we use Ramsey interference techniques to obtain the light shifts of both the lower and upper states of the collective qubit. Whereas the coupling producing the Rabi oscillations is enhanced by a factor of $\sqrt{N}$

, there is no corresponding enhancement for the light shifts. We derive an effective two-level model which is in good agreement with our observations. Trapped Rydberg qubits and an effective two-level description are expected to have broad applicability for studies of quantum simulation and networking using collective encoding in ensembles of neutral atoms.

- **"Theory of the Rydberg blockade with multiple intermediate-state excitations,"** P. R. Berman, H. Nguyen, and A. G. Rojo Phys. Rev. A 105, 043715 (2022).

  We present a detailed theory of the Rydberg blockade, including contributions from multiple intermediate-state excitations. Two fields drive transitions between ground and Rydberg levels via an off-resonance intermediate state. Assuming a perfect blockade, we calculate the probability to excite fully symmetric collective states having either zero or one Rydberg excitation, but an arbitrary number of intermediate-state excitations. Both "bare" state and "dressed" state approaches are used for (1) constant amplitude driving fields and (2) adiabatic pulse driving fields. It is shown that a dressed state approach offers distinct advantages when multiple intermediate-state excitations occur. In the case of fixed amplitude fields, the multiple intermediate excitations can result in comblike modulated populations of individual states having one Rydberg excitation and $n \ll N$ intermediate-state excitations. However, when summed over all such state populations, most of the modulation disappears and the system is described to a good approximation by an effective two-level model. In the case of adiabatic, pulsed fields, there is no such modulation and an effective two-level model (in the dressed basis), corrected for light shifts, can be used to model the system. In addition to solving this problem using conventional methods, we show that similar results could be obtained using a form of the Holstein-Primakoff transformation.

CHAPTER 3

Light-Matter Interaction

Laser cooling and trapping techniques have served as an enabling technology for the cold-atom laboratory since their development in the 1980s. These techniques make it possible for efficient preparation of dense collections of atoms, allowing for atomic transitions to be interrogated without the effect of broadening. As such, laser cooled atoms are an ideal platform to study emergent many-body collective dynamics in degenerate states of matter as well as fundamental quantum optical phenomena.

In this section, I give a brief overview of the subject in the viewpoint of an experimental physicist. First I will describe the relevant physics associated with the light-matter interaction which is a cornerstone for all of atomic, molecular, and optical physics. I will then introduce a simple model to understand optical molasses and it's role in the formation of magneto optical traps. I will then describe the notion of Bloch-Siegert shifts (lightshifts) and how they are utilized to form optical trapping potentials.

3.1 The two-level atom

To understand how lasers can be used to affect atomic motion, we first look at the simplest example of the interaction between light and matter. First we consider a stationary atom with an incident monochromatic laser field of frequency ω. While an atom's energy structure can consist of many states, the "resonance" or "two-level" approximation can dramatically simplify the situation when the frequency of the laser field coincides with the natural frequency of an atomic transition.

For a given pair of states $|1\rangle$ and $|2\rangle$ with energies E_1 and E_2 respectively, we can define a transition frequency ω_0 such that $\omega_0 = \frac{E_2 - E_1}{\hbar}$. The laser detuning, defined as $\Delta = \omega - \omega_0$, is the difference between the laser frequency and the transition frequency. When the laser detuning is much less than the frequency of the transition, that is $|\Delta| \ll \omega_0$, we say that the laser is in resonance with the

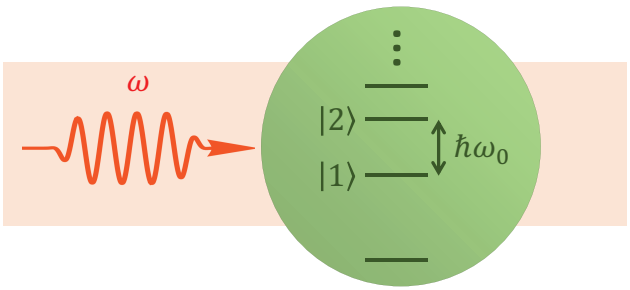

Figure 3.1: Depiction of the two-level approximation of an atom. When the laser frequency coincides with an atomic transition, the effect of other atomic transitions can be neglected.

transition. The effect of other atomic transitions on the dynamics of the atom can be neglected if the laser is sufficiently detuned from other transitions. As a result, the atomic wavefunction can be written as $|\psi(t)\rangle = c_1(t)|1\rangle + c_2(t)|2\rangle$. To find the time-dependent solutions for coefficients $c_1(t)$ and $c_2(t)$, we must solve the time-dependent Schrödinger equation,

$$\hat{H}|\psi(t)\rangle = i\hbar\frac{\partial|\psi(t)\rangle}{\partial t}.$$

The Hamiltonian can be written as a sum of two terms, $\hat{H}_0(r)$ is the time-independent part associated with the atomic energy structure, and $\hat{V}(t)$ is a perturbative term attributed to the light-matter interaction. The total Hamiltonian is given by

$$\hat{H} = \hat{H}_0(r) + \hat{V}(t).$$

The Schrödinger equation can be solved to find the dynamics of the relevant states in the system, where the resulting equations of motion are

$$\dot{c_1}(t) = -\frac{i}{\hbar}\left(c_1(t)V_{11} + c_2(t)V_{12}e^{-i\omega_0 t}\right),$$
$$\dot{c_2}(t) = -\frac{i}{\hbar}\left(c_1(t)V_{21}e^{i\omega_0 t} + c_2(t)V_{22}\right).$$

Where $V_{ij}(t) = \langle i|\hat{V}|j\rangle = \int \psi_i^* \hat{V}(t)\psi_j d^3r$ are matrix elements of the perturbation and $|\alpha\rangle$ are eigenkets of the unperturbed Hamiltonian. If we consider a classical electric field $\vec{\mathcal{E}}(t)$ associated with the incident laser, the interaction of the atomic dipole in the electric field is given by $\hat{V}(t) = e\vec{r}\cdot\vec{\mathcal{E}}(t)$. If we arbitrarily choose the polarization of the electric field to be in the $\hat{x}$ direction, we have that the matrix elements are given by

$$V_{ij}(t) = -\frac{\mathcal{E}_0}{2}\left(e^{i\omega t} + e^{-i\omega t}\right)\mu_{ij},$$

where μ_{ij} are dipole matrix elements defined as

$$\mu_{ij} = -e \int \psi_i^* \hat{x} \psi_j d^3\boldsymbol{r} = -e\langle i|\hat{x}|j\rangle.$$

An important thing to note is that due to the parity of the position operator, the diagonal elements of the interaction vanish, that is $V_{11} = V_{22} = 0$. As a result, we can write the equations of motion for the state amplitudes as

$$\begin{aligned} \dot{c}_1(t) &= \frac{i}{2}\Omega \left(e^{i(\omega-\omega_0)t} + e^{-i(\omega+\omega_0)t}\right) c_2(t), \\ \dot{c}_2(t) &= \frac{i}{2}\Omega \left(e^{-i(\omega-\omega_0)t} + e^{i(\omega+\omega_0)t}\right) c_1(t), \end{aligned} \tag{3.1}$$

where Ω is the Rabi frequency, which quantifies the strength of the atom-light interaction and is defined as

$$\Omega = |\mu_{12}\mathcal{E}_0/\hbar|.$$

Contained within this seemingly simple set of differential equations, a whole host of physical phenomena from the Einstein B coefficients in the weak-field limit and Rabi flopping and AC stark shifts in the strong-field limits respectively can be understood.

3.2 Inclusion of spontaneous decay - The Lindblad Master Equation

Not included in the previous formulation was the fact that atoms in the excited state can spontaneously decay back to the ground state. In order to describe the state of the full quantum system in the presence of decay, it is necessary to utilize the notion of the density operator. For a two level system, the density matrix is given by

$$\rho = \begin{pmatrix} \rho_{11} & \rho_{12} \\ \rho_{21} & \rho_{22} \end{pmatrix}.$$

For a pure quantum state, this can be written in terms of state amplitude coefficients,

$$\rho = \begin{pmatrix} c_1 c_1^* & c_1 c_2^* \\ c_2 c_1^* & c_2 c_2^* \end{pmatrix}.$$

For unitary dynamics, like those described in the previous section, the time dependence of the density matrix is determined by the Hamiltonian, and can be described by the Liouville-Von Neumann

equation or quantum master equation

$$\frac{\partial \rho}{\partial t} = -\frac{i}{\hbar}[\hat{H}, \rho],$$

which is equivalent to the Schrödinger formulation for the time evolution of the wavefunction. This evolution equation for the density matrix can be modified to incorporate spontaneous emission from the excited state by introducing a relaxation superoperator $\mathcal{L}_{\text{relax}}(\rho)$, with

$$\mathcal{L}_{\text{relax}}(\rho) = -\frac{1}{2}\sum_m (C_m^\dagger C_m \rho + \rho C_m^\dagger C_m) + \sum_m C_m \rho C_m^\dagger.$$

Where C_m are collapse operators associated with different dissipation channels. For the two-level system with spontaneous emission from the excited state, the collapse operator is given as

$$C_1 = \sqrt{\Gamma}|1\rangle\langle 2|,$$

where Γ is the spontaneous decay rate of the excited state. As a result, the total differential equation governing the evolution of the density matrix is given by the so-called Lindblad Master equation,

$$\frac{\partial \rho}{\partial t} = -\frac{i}{\hbar}[\hat{H}, \rho] + \mathcal{L}_{relax}(\rho).$$

The effective Hamiltonian in the rotating wave approximation (RWA) for the single atom interacting with the laser field with a real-valued Rabi frequency Ω and detuning Δ is

$$H = \frac{\hbar\Omega}{2}\left(|1\rangle\langle 2| + |2\rangle\langle 1|\right) - \hbar\Delta|2\rangle\langle 2| = \hbar\begin{pmatrix} 0 & \frac{\Omega}{2} \\ \frac{\Omega}{2} & -\Delta \end{pmatrix}.$$

When we include the relaxation operators into the equation, the resulting set of differential equations often called the optical Bloch equations (OBE)

$$\begin{aligned}
\dot{\rho_{11}}(t) &= +\Gamma\rho_{22} + \frac{i\Omega}{2}\left(\rho_{21} - \rho_{12}\right) \\
\dot{\rho_{12}}(t) &= -\left(\frac{\Gamma}{2} + i\Delta\right)\rho_{12} + \frac{i\Omega}{2}(\rho_{11} - \rho_{22}) \\
\dot{\rho_{21}}(t) &= -\left(\frac{\Gamma}{2} - i\Delta\right)\rho_{21} + \frac{i\Omega}{2}\left(\rho_{11} - \rho_{22}\right) \\
\dot{\rho_{22}}(t) &= -\Gamma\rho_{22} + \frac{i\Omega}{2}\left(\rho_{12} - \rho_{21}\right).
\end{aligned}$$

By solving these equations in steady state, that is by setting the time derivatives equal to zero, we find equations that relate to the topics of power broadening and saturation. One commonly used quantity in atomic physics experiments is the scattering rate, which is related to the steady state

density matrix $\rho_{22}(t \to \infty)$ by

$$R_{sc} = \Gamma \rho_{22}(t \to \infty).$$

After solving the density matrix equations outlined above, we arrive at the following expression for the steady state density matrix element as

$$\rho_{22}(t \to \infty) = \frac{(\Omega/\Gamma)^2}{1 + 4(\Delta/\Gamma)^2 + 2(\Omega/\Gamma)^2}.$$

It is often convenient to define an on-resonance saturation parameter which is defined as

$$s_0 = \frac{2|\Omega|^2}{\Gamma^2} = \frac{I}{I_s}$$

where I is the intensity of the incident field, and I_s is the saturation intensity given by

$$I_s = \frac{c\epsilon_0 \Gamma^2 \hbar^2}{4|\vec{\epsilon} \cdot \vec{d}|^2}.$$

As a result, the scattering rate can then be written as

$$R_{sc} = \left(\frac{\Gamma}{2}\right) \frac{s_0}{1 + s_0 + (2\Delta/\Gamma)^2}.$$

During the process of scattering a photon, momentum from the field is transferred to the atom. As a result, we can associate an effective force given by

$$F_{sp} = \hbar k R_{sc} = \left(\frac{\Gamma}{2}\right) \frac{s_0 \hbar k}{1 + s_0 + (2\Delta/\Gamma)^2}. \tag{3.2}$$

This force associated with radiation pressure is an underlying principle for laser cooling and trapping.

3.3 Magneto-Optical Traps

In many cold-atom laboratories, the magneto-optical trap (MOT) serves as a primary step in the sample preparation process. As the name suggests, the trap employs both optical and magnetic fields to compress and cool atoms into a dense cloud. A MOT typically is formed via three pairs of retroreflected beams, and a quadrupole magnetic field. However, in order to get an understanding of the dissipative mechanisms it is instructive to consider just a one-dimensional system.

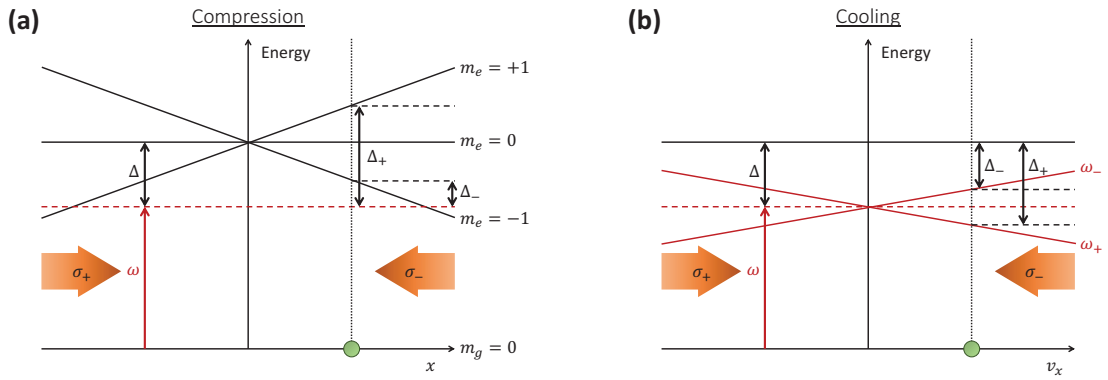

Figure 3.2: (a) Compression as a result of preferential absorption due to Zeeman interactions. (b) Cooling as a result of preferential absorption due to Doppler shifts.

In this simplified system, we consider two optical fields, denoted $\mathcal{E}_+$ and $\mathcal{E}_-$. The $\mathcal{E}_+$ ($\mathcal{E}_-$) field propagates in the positive (negative) x-direction with $\sigma_+(\sigma_-)$ polarized light. There is a magnetic field gradient in the x direction such that $B(x) = Ax$. Due to the magnetic field gradient, the Zeeman effect results in position-dependent level shifts as shown in Fig 3.2(a). In addition, the velocity of the atom results in a Doppler shift; the atom observes a different frequency for each of the fields depending on the direction of motion, as shown in Fig. 3.2(b). The detuning in Eq. 3.2 is modified to take into account these effects,

$$\Delta_\pm = \Delta \mp \underbrace{\vec{k}\cdot\vec{v}}_{\text{Doppler Shift}} \pm \underbrace{\mu' B/\hbar}_{\text{Zeeman Shift}} .$$

Where $\mu' = (g_e m_e - g_g m_g)\mu_B$, is an effective magnetic moment for the transition used, g_e (g_g) is the Lande g-factor, and m_e (m_g) is the magnetic quantum number associated with the excited (ground) level. As a result, the total force the atom experience is given by

$$F_{total} = F_+ + F_- = \left(\frac{\Gamma s_0 \hbar k}{2}\right)\left[\frac{1}{1+s_0+(2\Delta_+/\Gamma)^2} + \frac{1}{1+s_0+(2\Delta_-/\Gamma)^2}\right].$$

When the Doppler and Zeeman shifts are smaller than the detuning, the total force can be approximated as

$$F_x \approx -\beta v_x - \kappa x.$$

Looking at this equation of motion, one might notice that it resembles that of a damped harmonic oscillator, where β can be associated with a damping coefficient corresponding to the optical molasses portion of the trap, and κ as an spring constant due to the magnetic gradient, defined as

$$\beta = \frac{8\hbar k^2 \Delta s_0}{\Gamma(1+s_0+(2\Delta/\Gamma)^2)^2},$$

and

$$\kappa = \frac{\mu' A}{\hbar k}\beta.$$

The magnetic portion of the interaction results in compression of the atomic sample. For a red-detuned molasses beam, the $\Delta m = -1$ transition is shifted closer to resonance due to the Zeeman effect. As a result, the atom is more likely to scatter a photon from the σ_- beam, and the radiation pressure will push the atom in the $-x$ direction. Conversely, when the atom is to the left of the $B = 0$ position, the atom is more likely to scatter the σ_+ beam. Note that if the polarization of each beam is swapped, radiation pressure will cause the atoms to be repelled from the zero-field position, rather than be attracted.

The velocity-dependent interaction results in a cooling of the atomic sample. To elaborate, the positive velocity atoms see a larger frequency for the $\mathcal{E}_-$ field, which results in a smaller detuning and a higher probability to scatter a photon from the $\mathcal{E}_-$ beam. As a consequence, the radiation pressure opposing the direction of motion causes a decrease in velocity. Conversely, when the velocity is negative, the atom is more likely to scatter a photon from the $\mathcal{E}_+$ beam, again causing a decrease in the magnitude of the velocity.

3.4 Optical dipole traps

3.4.1 Theory of dipole polarizability

In the previous section, radiation pressure forces are the main mechanism for cooling and condensing in the MOT. Another type of force that can be exerted by light is the dipole force. For spatially inhomogenous light fields, e.g. optical tweezers, the dipole force can lead to precise localization of neutral atoms. In order to understand the origin of the trapping potential, we look at the atom-light interaction for an incident field that is far-detuned from an atomic transition. In this case, the chance for optical excitation is low, and therefore we can neglect radiation pressure forces. To begin, we can treat the atom as a classical dipole, and derive the interaction potential. We can then see how those equations are modified in the quantum mechanical picture of an atomic dipole. First, we can relate the complex amplitude of the dipole $\tilde{p}$ to the amplitude of the electric field $\tilde{\mathcal{E}}$.

$$\tilde{p} = \alpha\tilde{\mathcal{E}}$$

The induced dipole can then act again with the driving field to produce a time-averaged interaction potential given by

$$U_{dip}(\boldsymbol{r}) = -\frac{1}{2}\langle \boldsymbol{p}\mathcal{E}\rangle = -\frac{1}{2\epsilon_0 c}\mathrm{Re}(\alpha)I(\boldsymbol{r}). \tag{3.3}$$

From this expression, we see that the dipole potential is proportional to the real part of the polar-

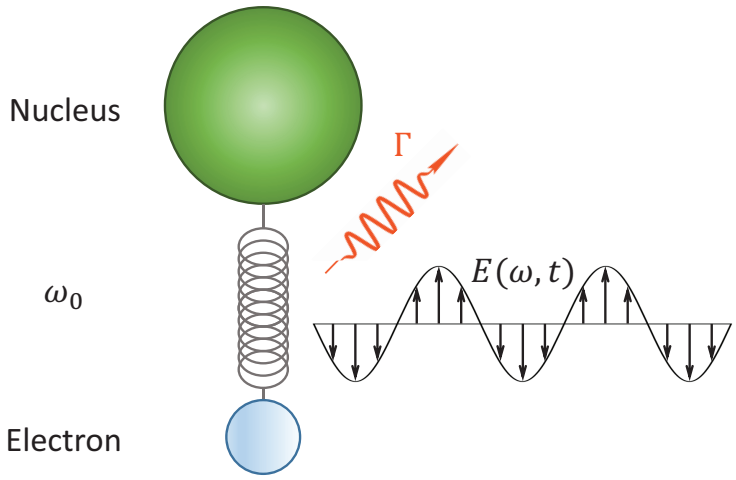

Figure 3.3: Lorentz model for the induced dipole of an atom driven by an electromagnetic field.

izability. Conversely, the imaginary component of the polarizability can be related to the absorbed power from the dipole.

$$P_{abs} = \frac{\omega}{\epsilon_0 c}\text{Im}(\alpha)I$$

We can ultimately relate this to the scattering rate, by taking the power and dividing by the average energy of each photon, $\hbar\omega$.

$$\Gamma_{sc}(\boldsymbol{r}) = \frac{1}{\hbar\epsilon_0 c}\text{Im}(\alpha)I(\boldsymbol{r}) \tag{3.4}$$

3.4.2 A classical model to derive the atomic polarizability

A simple model that does surprisingly well at describing the nature of light-matter interactions is the Lorentz oscillator model. In this phenomenological model, we treat the electron as bound to the nucleus with a spring-like force, and with a resonant frequency ω_0 corresponding to the frequency of the atomic transition. In addition, we can include a damping term Γ, which will describe dissipation of energy out of the system. Similar to damped mass on a spring, we can write a Newtonian equation of motion governing the motion of the electron,

$$\ddot{x} + \Gamma\dot{x} + \omega_0^2 x = -\frac{e\mathcal{E}(t)}{m_e},$$

where e is the fundamental electronic charge, $\mathcal{E}(t)$ is the time-dependent amplitude of the electric field with frequency ω, and m_e is the mass of the electron. Upon solving the differential equation for the position of the electron, x, we can find the classical dipole moment for this system is given

by

$$p(\omega) = -ex(\omega) = \frac{e^2}{m_e}\frac{\mathcal{E}}{[(\omega_0^2 - \omega^2) - i\omega\Gamma]}.$$

When we use the relation between the induced dipole moment and the polarizability, we can identify that the classical frequency-dependent polarizability is given by

$$\alpha(\omega) = \frac{p(\omega)}{\mathcal{E}} = \frac{e^2}{m_e}\frac{\mathcal{E}}{[(\omega_0^2 - \omega^2) - i\omega\Gamma]}$$

where the damping rate Γ, is given by Larmor formula for the power dissipated by a radiating dipole.

Now that we have derived an expression for the polarizability, we can use Eqs. 3.3 and 3.4 to obtain the dipole potential and scattering rate respectively.

$$U_{dip}(\boldsymbol{r}) = -\frac{3\pi c^2}{2\omega_0}\left(\frac{\Gamma}{\omega_0 - \omega} + \frac{\Gamma}{\omega_0 + \omega}\right) I(\boldsymbol{r})$$

$$\Gamma_{sc}(\boldsymbol{r}) = \frac{3\pi c^2}{2\hbar\omega_0^3}\left(\frac{\omega}{\omega_0}\right)^3\left(\frac{\Gamma}{\omega_0 - \omega} + \frac{\Gamma}{\omega_0 + \omega}\right)^2 I(\boldsymbol{r})$$

Even for so-called far off resonance traps, the detuning $\Delta = \omega - \omega_0$ is much less than the optical transition frequency, that is, $|\Delta| \ll \omega_o$. In this case, we can invoke the rotating-wave approximation (RWA) and we can neglect the second terms, and set $\frac{\omega}{\omega_0} \approx 1$. As a result, the expressions for the dipole potential and scattering rate reduces to

$$U_{dip}(\boldsymbol{r}) = \frac{3\pi c^2}{2\omega_0^3}\frac{\Gamma}{\Delta} I(\boldsymbol{r}),$$
$$\Gamma_{sc}(\boldsymbol{r}) = \frac{3\pi c^2}{2\hbar\omega_0^3}\left(\frac{\Gamma}{\Delta}\right)^2 I(\boldsymbol{r}).$$

From this expression, we can note a few important details that have practical application in the realm of optical dipole trapping. The first is that the trapping potential and scattering rate have different dependencies on the detuning. This means that it is advantageous to choose a trapping wavelength that is far-off resonance from the relevant optical transition. By reducing the photon scattering rate for a fixed trap depth, the effects of recoil heating can be reduced, therefore leading to longer lifetimes of the atom within the trap.

Also note that the trapping potential depends on the sign of the detuning. For a trapping field with a laser frequency smaller than the resonance frequency of the atom, the detuning is negative, often denoted as "red-detuned". In this case, the resulting dipole potential is negative, and therefore

the maximal potential depth occurs at the maximum of the intensity field. On the contrary, for "blue-detuned" trapping fields, the atoms will be attracted to the intensity minima. This can be advantageous as the rate of photon scattering can be further reduced. Utilizing this fact, many atomic physics groups are actively investigating and implementing clever geometries for single-atom trapping such as blue-detuned line-grid arrays and optical bottle beam traps.

3.4.3 Quantum mechanical model of polarizability

As we saw in the previous section, the classical model of the bound electron gives a simple framework to understand the origin of the induced dipole. It provides us with expressions that reveal important aspects of the origin of the dipole potential and polarizability. However in this model, we neglect two important truths about the atom. The first of which is that the atom at a fundamental level is a quantum mechanical object. The allowed energies of the electron are not continuous, rather they are discretized. Another important fact that we neglected is the fact that an atom consists of multiple levels. We now consider how the classical expressions of the polarizability need to be modified.

To derive the energy correction associated with the incident trapping field, we write the total atom-field Hamiltonian

$$H = H_0 + \mathcal{E}\hat{\mathcal{E}} \cdot \boldsymbol{d},$$

where H_0 is the atomic Hamiltonian, in the absence of the electric field. If we treat the electric field amplitude $|\mathcal{E}|$ as a perturbative parameter, we know from perturbation theory that the wavefunction and energy for an atomic state ν can be expressed as

$$|\psi_\nu\rangle = |\psi_\nu^{(0)}\rangle + \mathcal{E}|\psi_\nu{}^{(1)}\rangle + \mathcal{E}^2|\psi_\nu{}^{(2)}\rangle + ...$$
$$E_\nu = E_\nu^{(0)} + \mathcal{E}E_\nu^{(1)} + \mathcal{E}^2E_\nu^{(2)} + ...$$

For now we focus on the energy corrections due to the electric field perturbation. From time-independent perturbation theory, the first order correction to the energy is given by

$$E_\nu^{(1)} = \langle\psi_\nu^{(0)}|\mathcal{E}\hat{\mathcal{E}} \cdot \boldsymbol{d}|\psi_\nu^{(0)}\rangle,$$

$$E_\nu^{(1)} = -\boldsymbol{\mathcal{E}} \cdot \langle\boldsymbol{d}\rangle.$$

Since neutral atoms do not have a permanent dipole, this quantity vanishes. The second order

correction to the energy from perturbation theory is given by

$$E_\nu^{(2)} = \sum_{n \neq k} \frac{|\langle \psi_\nu^{(0)} | \boldsymbol{d} \cdot \boldsymbol{\mathcal{E}} | \psi_k^{(0)} \rangle|^2}{E_\nu^{(0)} - E_k^{(0)}}.$$

Since the energy shift is related to the static electric field by the polarizability by

$$\Delta E_\nu = -\frac{1}{2} \alpha_\nu |\mathcal{E}|^2,$$

we can identify the polarizability of the state as

$$\alpha_\nu = -2 \sum_{k \neq \nu} \frac{|\langle \psi_\nu^{(0)} | \boldsymbol{d} \cdot \boldsymbol{\mathcal{E}} | \psi_k^{(0)} \rangle|^2}{E_\nu^{(0)} - E_k^{(0)}}.$$

Here we can see the polarizability has contributions from all dipole-allowed transitions. In order to take into account an ac field with frequency ω, we simply modify the static polarizability with the same frequency factor that arose in the classical oscillator case,

$$\alpha_\nu(\omega) = -2 \sum_{k \neq \nu} |\langle \psi_\nu^{(0)} | \boldsymbol{d} \cdot \boldsymbol{\mathcal{E}} | \psi_k^{(0)} \rangle|^2 \left[\frac{1}{\delta E_{\nu,k} + \omega} + \frac{1}{\delta E_{\nu,k} - \omega} \right].$$

Where $\delta E_{\nu,k} = E_\nu^{(0)} - E_k^{(0)}$ is the difference in the unperturbed energies. Furthermore, the polarizability depends on the angular momentum j and m_j of the atomic state, and therefore we can further modify the expression as

$$\alpha_\nu(\omega) = \alpha_\nu^{(0)}(\omega) + \mathcal{A} cos\theta_k \frac{m_j}{j} \alpha_\nu^{(1)}(\omega) + \left\{ \frac{3cos^2\theta_p - 1}{2} \right\} \frac{3m_j^2 - j(j+1)}{j(2j-1)} \alpha_\nu^{(2)}(\omega).$$

The factors $\mathcal{A}$ defines the degree of polarization. $\mathcal{A} = -1, 0, 1$ for left-handed, linear, and right-handed polarization respectively. Here θ_k represents the angle between the wave vector and the z-axis. θ_p is the angle between the polarization of the electric field with respect to the z-axis. Here $\alpha_\nu^{(0)}(\omega)$,$\alpha_\nu^{(1)}(\omega)$, and $\alpha_\nu^{(2)}(\omega)$ represent the scalar, vector, and tensor polarizabilities respectively

[2], and are defined as

$$\alpha_\nu^{(0)}(\omega) = \frac{1}{3(2j_\nu+1)} \sum_{j_k} |\langle \psi_\nu^{(0)} || D || \psi_k^{(0)} \rangle|^2 \left[\frac{1}{\delta E_{\nu,k} + \omega} + \frac{1}{\delta E_{\nu,k} - \omega} \right]$$

$$\alpha_\nu^{(1)}(\omega) = -\sqrt{\frac{6j_\nu}{(j_\nu+1)(2j_\nu+1)}} \sum_{j_k} \begin{Bmatrix} j_\nu & 1 & j_\nu \\ 1 & j_k & 1 \end{Bmatrix} (-1)^{j_\nu + j_k + 1} |\langle \psi_\nu^{(0)} || D || \psi_k^{(0)} \rangle|^2 \left[\frac{1}{\delta E_{v,k} + \omega} - \frac{1}{\delta E_{\nu,k} - \omega} \right]$$

$$\alpha_\nu^{(2)}(\omega) = -2\sqrt{\frac{5j_\nu(2j_\nu-1)}{6(j_\nu-1)(2j_\nu+1)(2j_\nu+3)}} \sum_{j_k} \begin{Bmatrix} j_\nu & 2 & j_\nu \\ 1 & j_k & 1 \end{Bmatrix} (-1)^{j_\nu + j_k + 1} |\langle \psi_\nu^{(0)} || D || \psi_k^{(0)} \rangle|^2 \left[\frac{1}{\delta E_{\nu,k} + \omega} - \frac{1}{\delta E_{\nu,k} - \omega} \right]$$

Where $|\langle \psi_\nu^{(0)} || D || \psi_k^{(0)} \rangle|$ are reduced dipole matrix elements. These expressions for the polarizability show that they can change dramatically near the frequency of an atomic transition. Utilizing this fact, we can employ near-resonant trapping wavelengths in order to match the polarizabilities of two atomic levels of interest. The wavelength at which the polarizabilities of two levels are equal is a so-called "magic wavelength". In this thesis, we employ a magic wavelength near a $|6P_{3/2}\rangle \leftrightarrow |nS_{1/2}\rangle$ transition to achieve state-insensitive trapping for the ground-Rydberg transition. In doing so, we minimize the undesirable effect of differential lightshifts and extend lifetimes of the ground-Rydberg coherence an order of magnitude over those achieved in traditional far-off-resonance traps (FORTs).

3.4.4 Specific application: Lightshift calculation for the line of Rb for a trapping wavelength of 1064 nm

For Rubidium, a common wavelength used for FORTs is 1064 nm. This is because the wavelength is sufficiently far from any atomic transitions and can be generated with high power via Neodymium doped Yttrium-Aluminum-Garnet (Nd:YAG) lasers. In this section, I describe the process of calculating differential lightshifts for the D_2 line of Rubidium for 1064 nm light. The Mathematica notebook, "1_LightshiftCalculator", used for these calculations is available online. This notebook allows experimentally measured trapping beam powers and waists to be converted into theoretical predictions of trap depths (light shift of the ground state), and state-dependent light shifts of the D_2 line.

Polarizability	Value in atomic units
$\alpha^{(0)}_{5S_{1/2}}$	687.3
$\alpha^{(0)}_{5P_{1/2}}$	-1226
$\alpha^{(0)}_{5P_{3/2}}$	-1114
$\alpha^{(2)}_{5P_{3/2}}$	551

Table 3.1: Scalar and tensor polarizabilities for 1064nm light used in calculating differential light-shifts for the D_2 transition in Rubidium taken from Ref [1].

The light shifts for the state γ with quantum numbers F and m_F are calculated using

$$\Delta E_{\gamma,F,m_F} = -\frac{1}{4}\alpha_{\gamma,F,m_F}\mathcal{E}^2$$

where the state-dependent polarizability is defined as

$$\alpha_{\gamma,F,m_F} = \alpha^{(0)}_{\gamma} + \alpha^{(2)}_{\gamma,F}\frac{3m_F^2 - F(F+1)}{F(2F+1)},$$

where

$$\alpha^{(2)}_{\gamma,F} = \alpha^{(2)}_{\gamma}\frac{3X(X-1) - 4F(F+1)J(J+1)}{(2F+3)(2F+2)J(2J-1)},$$

with

$$X = F(F+1) + J(J+1) - I(I+1).$$

To perform these calculations, I utilize tabulated values of the scalar ($\alpha^{(0)}_{\gamma}$) and tensor ($\alpha^{(2)}_{\gamma}$) polarizabilities listed in Ref [1] for 1064 nm, the values of which are detailed in Table 3.1.

A common convention is to utilize Hartree atomic units when calculating quantities for theoretical atomic physics. In this system of units, fundamental constants i.e., the reduced Planck constant $\hbar$, the elementary charge e, the Bohr radius a_0, and the electron mass m_e are set to unity making the calculations more convenient. To convert the values of polarizability from atomic units to SI units , we utilize a conversion factor Λ such that

$$\alpha[\text{au}] \times \Lambda = \alpha[\text{SI}],$$

with

$$\Lambda = 4\pi\epsilon_0 a_0^3 \approx 1.648 \times 10^{-41}.$$

Energy shifts when calculated are in SI units (Joules), however, it is common to express them in

	$\|m_F\| = 3$	$\|m_F\| = 2$	$\|m_F\| = 1$	$\|m_F\| = 0$
$F = 3$	17.07	33.77	43.80	47.14
$F = 2$		33.77	33.77	33.77
$F = 1$			40.45	33.77

Table 3.2: Level shifts in units of MHz, of the D_2 line for a 1064 nm trapping wavelength and 1 mK trap depth.

either temperature or frequency units.

$$\Delta E[\text{J}] = k_B \left(\Delta E[\text{K}]\right) = h \left(\Delta E[\text{Hz}]\right)$$

For example, a 1 mK trap depth corresponds to an energy shift of the ground state of

$$\Delta E = k_B(1 \times 10^{-3}\text{K}) = 1.38 \times 10^{-26}\text{J}$$

with a corresponding frequency shift of

$$\frac{k_B(1 \times 10^{-3}\text{K})}{h} \Rightarrow 20.84\text{MHz}.$$

The state-dependent differential light shifts are calculated for a 1 mK trap depth which can be achieved with a 1 μm beam waist and laser power of 10.16 mW or equivalently a trap intensity of $I \approx 6.47 \times 10^5$W/cm^2. The results are shown in Figure 3.4, and tabulated in Table 3.2. A few things to note are that there are no tensor shifts for the ground level, and therefore the trap depth is independent of quantum numbers F and m_F . Also, there are no tensor light shifts for the D_1 line, and therefore all levels are shifted equally with a sensitivity of 37.17 MHz/mK.

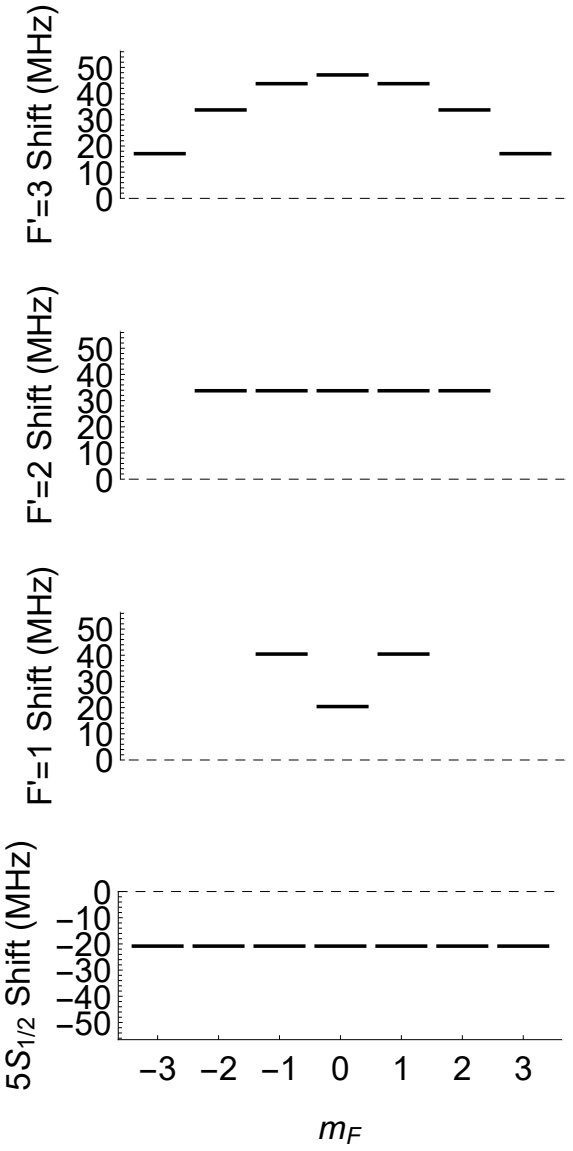

Figure 3.4: Magnetic sublevel differential lightshifts for the D_2 line and a trap depth of 1 mK. Individual values are tabulated in Table 3.2.

CHAPTER 4

Apparatus for Single-Atom Trapping

While being able to trap, detect, and coherently manipulate the state of a single atom is an achievement in and of itself, in order to study emergent many-body physical phenomena, it is necessary to increase the number of quantum constituents within the system. Technological development along this direction have enabled the generation of multi-dimensional structured arrays of optical tweezers and is an active area of research. Some of the predominant methods used to scale up the size of the quantum system include:

A) Acousto-optic deflectors (AODs)

One- and two- dimensional arrays of optical tweezers can be generated by utilizing AODs driven by multi-tone radiofrequency (RF) sources derived from software define radio (SDR) or arbitrary waveform generators (AWG). While this scheme allows for a relatively simple method for generating trap arrays, this method has several limitations. 1) Only rectangular geometries can be achieved, 2) the number of traps is limited by the total efficiency of all of the first order diffracted beams and the frequency spacing of RF tones within the bandwidth of the AOD, 3) nonlinearities within the AOD and RF amplifier can cause frequency intermodulation between the different frequency tones, which severely limits the achievable trap uniformity.

B) 2D Lattices - Superfluid to Mott insulator transition

A powerful method for realizing deterministic loading of single atoms into a sub-wavelength square array is by utilizing ultra-cold bosonic gases in two-dimensional optical lattices. A Bose-Einstein condensate (BEC) within the 2D lattice can undergo a quantum phase transition from the superfluid to mott-insulator phases via ramping of the lattice depth. As a result of this phase transition, single-atoms are prepared in each lattice site with a high probability. Some restrictions of this method is that the geometry of traps is limited, and the process of generating and manipulating a BEC is technically challenging and time consuming.

C) Holographic methods

By utilizing holographic methods, spatially varying phases can be imprinted on a trapping beam, resulting in nearly arbitrary patterns of light at the focus of a lens. Traditionally this is

performed via static phase masks which are comprised of transparent media with spatially varying refractive indices. With the development of spatial light modulators (SLMs) and digital micromirror devices (DMDs), on-demand reconfiguration of trapping geometries is possible. Due to the high power utilization factor and flexibility of the approach, this is the method that is used in the Kuzmich lab.

4.1 Scalar-diffraction theory: Huygens-Fresnel, Fresnel, and Fraunhofer diffraction

To understand how the phase hologram is computed for the desired intensity pattern, we first turn to scalar diffraction theory to describe propagation of electric fields between different planes of interest. This formalism allows us to understand the mathematical relation between the scalar electric field at two planes separated by a distance z. In this particular example, we are interested in the electric field at the SLM plane $E_{\text{SLM}}(x', y')$ and at the focal plane of the high NA objective lens, $E_{\text{Focal}}(x, y)$. Given that the electric field at the SLM plane is known, we can utilize the Huygens-Fresnel principle to calculate the electric field at the focal plane such that,

$$E_{\text{Focal}}(x, y) = \frac{z}{i\lambda} \int \int_{-\infty}^{+\infty} E_{\text{SLM}}(x', y') \frac{\exp(ikr)}{r^2} dx' dy', \tag{4.1}$$

where r is defined as the distance

$$r = \sqrt{z^2 + (x - x')^2 + (y - y')^2}.$$

One can interpret this integral as every point in the SLM plane as a source of outgoing spherical waves. In general, this integral can be difficult to evaluate. By invoking two approximations, the expression can be dramatically simplified. First we invoke the Fresnel or paraxial approximation. In this approximation, we have that the distance z between the planes is much larger than the transverse extent of the aperture in the SLM plane, that is

$$z \gg \sqrt{(x - x')^2 + (y - y')^2}.$$

When this condition is satisfied, we can expand the distance r via a binomial expansion,

$$r = z\sqrt{1 + \left(\frac{x-x'}{z}\right)^2 + \left(\frac{y-y'}{z}\right)^2},$$
$$r \approx z\left[1 + \frac{(x-x')^2}{2z^2} + \frac{(y-y')^2}{2z^2} + ...\right].$$

As a result, we can keep just the first term for the expansion of r in the denominator, however for values of r in the exponential, we keep the first three terms since variations in the phase on the order of unity can result in a large deviation of the resulting value. As a result, the diffraction integral simplifies to

$$E_{\text{Focal}}(x,y) = \frac{e^{ikz}}{i\lambda z}\int\int_{-\infty}^{+\infty} E_{\text{SLM}}(x',y')\text{exp}\left[i\frac{k}{2z}\left[(x-x')^2 + (y-y')^2\right]\right]dx'dy'.$$

For a further simplification, we can expand out the phase factor in the integral

$$\left[(x-x')^2 + (y-y')^2\right] = (x^2+y^2) + (x'^2+y'^2) - (2x'x + 2y'y)$$

At this point, we can apply the Fraunhofer approximation, under the condition that $z \gg \frac{k(x'^2+y'^2)}{2}$ is satisfied. Under this assumption, the phase factor $e^{ik(x'^2+y'^2)} \approx 1$, over the region of interest and the diffraction integral simplifies to

$$E_{\text{Focal}}(x,y) = \frac{e^{ikz}e^{i\frac{k}{2z}(x^2+y^2)}}{i\lambda z}\int\int_{-\infty}^{+\infty} E_{\text{SLM}}(x',y')\text{exp}\left[-i\left(\frac{kx}{z}x' + \frac{ky}{z}y'\right)\right]dx'dy'.$$

This can be identified as a 2D Fourier transform of the field in the reference plane, with spatial frequencies $f_x = \frac{x}{\lambda z}$ and $f_y = \frac{y}{\lambda z}$.

To summarize, if one knows the electric field in one plane, the electric field at a different plane in the far-field can be obtained via a 2D Fourier transform. This means that in principle, an arbitrary electric field profile $E_{\text{Focal}}(x,y)$ can be generated by manipulating the electric field at the SLM plane to be the inverse FT, $E_{\text{SLM}}(x',y') = \mathcal{F}^{-1}[E_{\text{Focal}}(x,y)]$.

4.2 Phase modulation using a spatial light modulator

4.2.1 Gerchberg-Saxton Algorithm

In reality, simultaneous control over the amplitude and phase of the electric field at the SLM plane is not feasible, and instead the amplitude is constrained to that of a Gaussian beam. While the

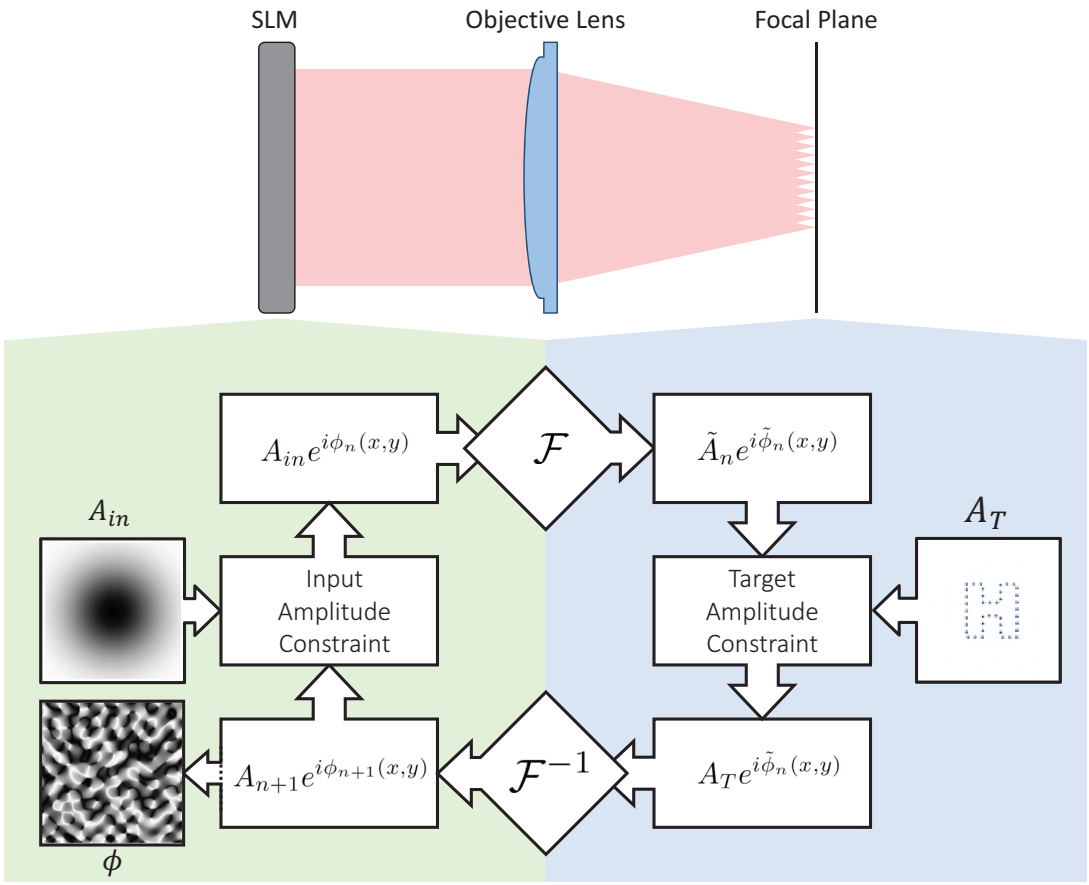

Figure 4.1: Flow diagram for the Gerchberg-Saxton algorithm.

exact intensity pattern at the focal plane cannot be achieved, an excellent approximation can be obtained by an appropriate choice of the phase modulation on the Gaussian beam at the surface of the SLM. With this amplitude constraint, the direct inverse transform can be no longer used to obtain the optimal phase hologram, rather a phase retrieval algorithm such as the Gerchberg-Saxton (GS) algorithm must be used. The GS algorithm is amongst a class of algorithms that utilize a sequence of forward and inverse discrete Fourier transforms (DFTs) along with amplitude constraints to obtain convergence on the optimal phase hologram. Figure 4.1 shows a basic flow diagram for the implementation of the GS algorithm.

Given an input electric field amplitude at the SLM plane ,A_{in}, and a target amplitude at the focal plane, A_T, we can obtain an optimized phase hologram ϕ_{opt} such that $\left|\mathcal{F}\left[A_{\text{in}}e^{i\phi_{\text{opt}}}\right]\right|^2 \approx |A_T|^2$ by performing the following iterative procedure:

1. Initialize each pixel in the discrete grid $\phi_n(x_i, y_j)$ to be a randomly distributed between 0 and 2π.

2. Using the amplitude of the electric field at the SLM plane, A_{in}, and the phase pattern at the SLM plane, ϕ_n, propagate the electric field to the focal plane by DFT, which results in the electric field amplitude $\tilde{A}_n$ and phase $\tilde{\phi}_n$.

3. Enforce an amplitude constraint in the focal plane, that is, substitute $\tilde{A}_n$ with $A_{T.}$

4. Propagate the resulting field backward to the SLM plane via inverse DFT to obtain the phase ϕ_{n+1}.

5. Check to see if the amplitude error, $\epsilon = \frac{\left|A_T - \left|\mathcal{F}[A_{\text{in}}e^{i\phi_{n+1}}]\right|\right|^2}{|A_T|^2}$, is within the desired tolerance level. If the error is sufficiently low, the algorithm concludes and ϕ_{n+1} is the optimized phase, ϕ_{opt}. If not, return to step 2.

The program "2_PhaseHologramGenerator", available via the online repository provides a minimal working example of such a procedure. The GS algorithm is implemented for 30 iterations to generate phase holograms corresponding to a ring geometry consisting of 1-7 traps at the focal plane. The final intensity profile at the focal plane is shown in the first row of Fig. 4.2, and the corresponding phase holograms are displayed in the second row. The phase holograms show patterns indicative of the dominant spatial frequencies present in the array geometry as well as the increasing degree of symmetry. To further emphasize the flexibility of this approach, the Mathematica notebook has the capabilities of generating phase holograms for input target amplitudes defined from an imported bitmap file. This feature is utilized to generate phase holograms for trap arrays spelling out the letters in "KUZMICH".

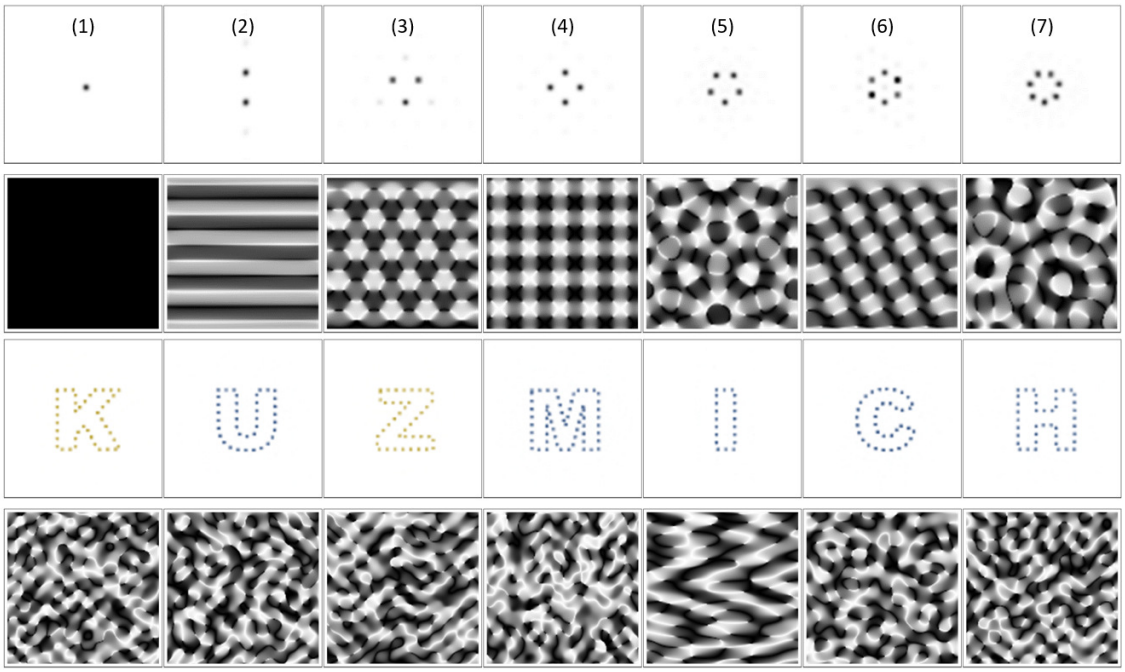

Figure 4.2: Gallery of traps: Calculated intensity pattern for increasing number of traps in a ring geometry and corresponding phase holograms in rows 1 and 2 respectively. Demonstration of arbitrary trap geometry formation by trap geometries spelling out "KUZMICH" and their respective phase holograms in row 3 and 4 respectively.

Precise positioning of the traps on the focal plane A useful application of digital holography is the precise positioning of the focal point of optical beams. Transverse displacements Δ_x and Δ_y in the focal plane can be achieved by introducing a linear phase ramp across the input beam. As the modulation phase is limited between 0 and 2π , a linear phase modulo 2π, becomes what is known as a "blazed" grating. The phase required for such a transverse displacement is given by

$$\phi_{\text{Blaze}}(\Delta_x, \Delta_y, x', y') = [K_x x' + K_y y'] \mod 2\pi,$$

where K_x and K_y are effective wavenumbers at the SLM plane defined as

$$K_x = k\left(\frac{\Delta_x}{f}\right),$$
$$K_y = k\left(\frac{\Delta_y}{f}\right).$$

Where $k = \frac{2\pi}{\lambda}$ is the wavenumber of the trapping beam, and f is the focal length of the objective lens. Note that the maximum possible displacement is limited by the size of each pixel (pixel pitch) of the SLM. An example of a blazed grating is shown in Fig. 4.3. In addition to precise alignment in the focal plane, a blazed grating allows for the spatial separation of the diffracted beam from the 0th order undiffracted beam, eliminating unwanted trapping potentials in the region of interest.

In addition to transverse displacements, it is possible to move the trap focal position an axial distance Δ_z. To achieve this, the divergence properties of the trapping beam is changed by imprinting a quadratic phase. This quadratic phase modulation is the underlying principle for metasurface and Fresnel lenses, and is identical to the accumulated phase as a beam propagates through a lens made of glass. The radial phase ramp can be written in terms of an effective wavenumber $K_z = k\left(\frac{\Delta_z}{f}\right)$,such that the Fresnel phase is,

$$\phi_{\text{Fresnel}}(\Delta_z, x', y') = \left[K_z \frac{(x'^2 + y'^2)}{2f}\right] \mod 2\pi.$$

In order to detect fluorescence emitted from the array of single-atoms, it is important to match the focal plane of the imaging system with the focal plane of the trapping beam. Rather than using a physical translation stage, digital holography allows for a precise control of the focal position via the Fresnel phase. An example of a Fresnel phase pattern is shown in Fig. 4.3.

In an ideal setup, the phase across the input Gaussian beam is uniform, and therefore the only phase modulation necessary is that obtained from the GS algorithm and the blazed grating. However, due to experimental limitations on the quality of the wavefront, there are additional holograms

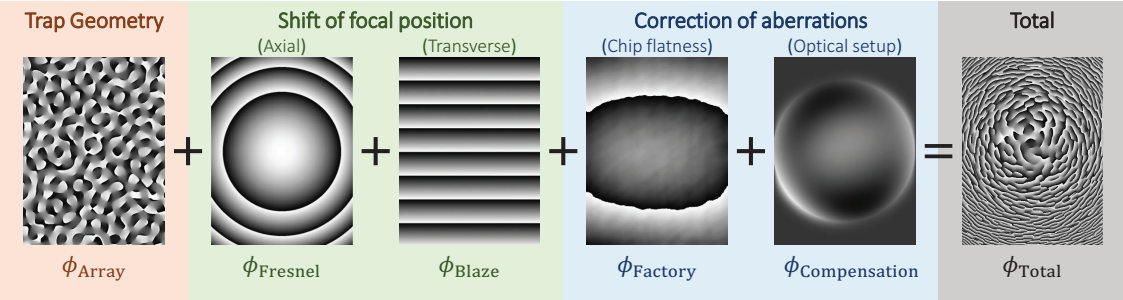

Figure 4.3: Composition of the hologram to generate an array of traps at the focus of an objective lens. Additional holograms are necessary for precise positioning of the traps in the focal plane, and to compensate for optical aberrations.

that need to be superimposed in order to compensate for such imperfections. In the subsequent sections, I will discuss where these limitations arise and how they are taken into account.

4.3 Wavefront correction

4.3.1 Introduction

For applications such as the imaging of distance light sources (astronomy), or microscopic objects (atomic physics) the quality of a wavefront as it passes through the optical system is of the utmost importance. In the optimal situation, the wavefronts coming from the light source are approximately those associated with a plane-wave. Distortions from a planar wavefront can be the result of variety of sources. In the case of astronomy, these deviations may arise from changes in the refractive index of the atmosphere due to temperature gradients or turbulent air.

In the optics laboratory setting, these aberrations can occur due imperfect alignment through an optical system, or due to the intrinsic construction of each optical element. In this section, I describe the process of utilizing a Shack-Hartmann wavefront sensor and Spatial Light Modulator as an adaptive optics platform capable of eliminating monochromatic aberrations that occur in our system. In order to understand that process, we first look at the origin of these aberrations in our system, and review the formalism of aberration theory in order to characterize and compensate such aberrations.

4.3.2 Aberration theory

Aberrations can come in the form of two types 1) chromatic and 2) monochromatic aberration. The former is the result of dispersion and wavelength dependent transmission through an optical

system. The latter is the result of rays originating from the same point in the image propagating through different optical paths on it's way to the imaging plane.

The deviations of the wavefront that result can be described via aberration theory. One method of quantifying the amount and nature of the aberrations in a wavefront is via an expansion of the wavefront into Zernike polynomials. Zernike polynomials comprise an orthogonal and complete basis on the unit disk, and therefore an arbitrary wavefront can be described by a unique set of Zernike coefficients. The Zernike polynomials can be expressed in polar coordinates in a factorized form using radial and angular components,

$$Z_n^m(\rho,\phi) = R_n^m(\rho)\cos(m\phi).$$

Where the radial polynomials are given by

$$R_n^m(\rho) = \sum_{k=0}^{\frac{n-m}{2}} \frac{(-1)^k(n-k)!}{k!\left(\frac{n+m}{2}-k\right)!\left(\frac{n-m}{2}-k\right)!}\rho^{n-2k}.$$

These radial functions obey the following orthogonality condition

$$\int_0^1 \sqrt{2n+2}R_n^m(\rho)\sqrt{2n'+2}R_{n'}^m(\rho)\rho d\rho = \delta_{n,n'}.$$

These polynomials can be tabulated utilizing a single index, of which there are several schemes. The Waveview software suite utilizes the Wyant index, and therefore is the indexing scheme used in our wavefront correction protocol. Fig. 4.4 shows the first 21 polynomials ordered vertically by radial degree n, and horizontal by azimuthal degree m.

The experimental wavefront $E_{\text{exp}}(\rho,\phi)$ can be expanded into a sum of such Zernike polynomials, in the form of

$$E_{\text{exp}}(\rho,\phi) = \sum_{m,n}[a_{mn}Z_n^m(\rho,\phi) + b_{mn}Z_n^{-m}(\rho,\phi)]$$

In order to determine the expansion coefficients, one follows the standard basis expansion recipe utilizing inner products. The inner product on the unit disk is defined as

$$\langle F,G\rangle = \int_0^{2\pi}\int_0^1 F(\rho,\phi)G(\rho,\phi)\rho d\rho d\phi.$$

The expansion coefficients of the experimental wavefront can be described in terms of the inner

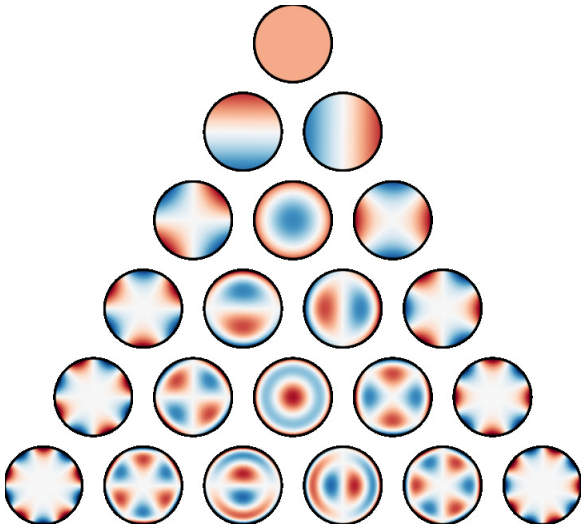

Figure 4.4: The first 21 Zernike polynomials plotted on the unit disk.

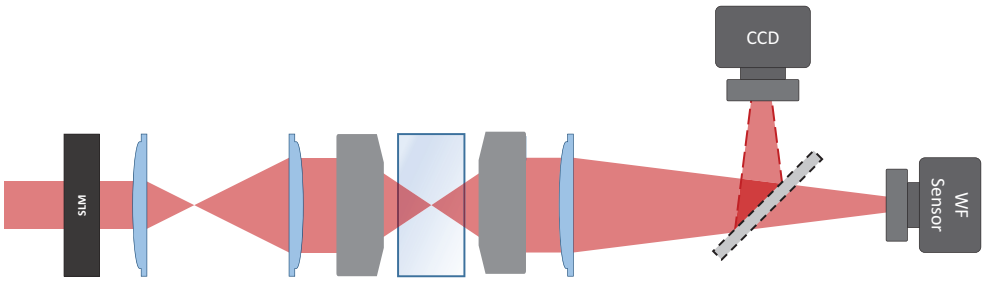

Figure 4.5: Simplified diagram for analyzing the phase (Shack-Hartmann wavefront sensor) and intensity of the trapping beam.

product as

$$a_{mn} = \frac{2n+2}{\epsilon_m \pi} \langle E_{\text{exp}}(\rho,\phi), Z_n^m(\rho,\phi) \rangle$$
$$b_{mn} = \frac{2n+2}{\epsilon_m \pi} \langle E_{\text{exp}}(\rho,\phi), Z_n^{-m}(\rho,\phi) \rangle$$

Compensating for imperfections in the surface of the SLM chip Even in the absence of an applied phase hologram on the SLM surface, there is a phase modulation across the Gaussian beam. This phase modulation arises from miniscule deviations of the SLM chip surface that occur during the manufacturing process. The manufacturing company of the SLM (Hamamatsu) provides us with a phase pattern that can be used to compensate for such deviation of the chip surface. This phase pattern, denoted as ϕ_{factory} is displayed in Fig. 4.3.

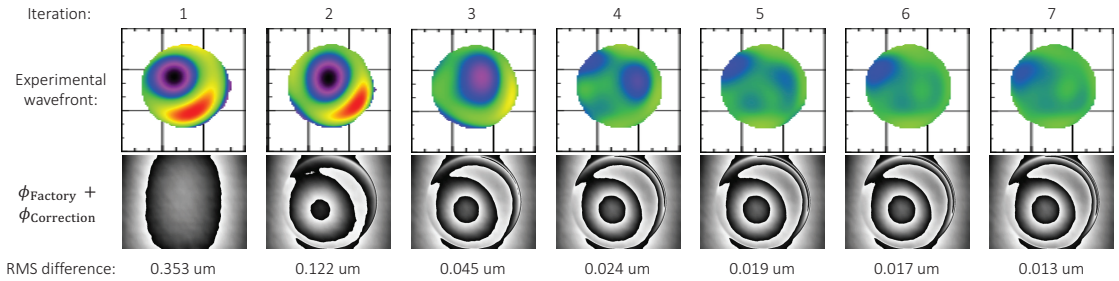

Figure 4.6: Measured wavefront and phase hologram as a function of the iteration number for feedback.

Detecting and correcting aberrations caused by optical elements in the beam path One method of measuring an optical wavefront is by using a Shack-Hartmann wavefront sensor. This sensor consists of a microlens array, with lenses of the same focal length, generating focused spots on a CCD sensor. For an optical beam that uniformly illuminates the microlens array with a perfect wavefront, all of the spots will be focused at the direct center of each of the microlenses. In the case where optical aberrations are present, the microlens arrays allows for discrete sampling of the wavefront at each position on the array. The deviation of the spot focal position is proportional to the discretized deviation of the wavefront.

For our correction protocol, we utilize a HASO4-FIRST wavefront sensor from ImagineOptic. The sensor features $\lambda/100$ absolute accuracy, $\lambda/200$ repeatability, a microlens array consisting of 32×40 lenses, a pupil size of 3.6×4.6 mm^2 and allows for wavefront detection between 400-1100 nm. After measuring the wavefront, we perform a Zonal reconstruction to extract the Zernike coefficients. Using the coefficients, we generate a phase hologram $\phi_{\text{Compensation}}$ that attempts to rectify the wavefront distortion. An example of such a phase hologram is shown in Fig. 4.3. Due to nonlinearity present in the optical system, multiple iterations of this correction procedure is required to obtain convergence of the wavefront. Figure 4.6 shows the experimentally reconstructed wavefront, phase hologram, and RMS difference after multiple iterations of the correction procedure. As a result of the iterative correction, the RMS deviation of the wavefront is reduced monotonically from 0.353 um to 0.013 um.

Now after taking into account the different mechanisms that lead to deviations of the wavefront, the total phase hologram displayed on the SLM is the sum of all phase holograms described in the previous sections, $\phi_{\text{total}} = \phi_{\text{Array}} + \phi_{\text{Fresnel}} + \phi_{\text{Blaze}} + \phi_{\text{Factory}} + \phi_{\text{Compensation}}$.

4.4 Objective lens

In order to produce tightly focused trapping beams that allow for the collisional blockade mechanism to be operative, we require the use of high-numerical aperture objective lenses. In this section, I will discuss how we can measure the point spread function (PSF) of an objective lens in order to experimentally quantify the focusing performance. The Airy disk radius of the PSF of an objective with a numerical aperture NA can be given as $R = \frac{0.61\lambda}{\text{NA}}$, where λ is the wavelength of the trapping field.

As the objective lens is placed on the outside of a vacuum cell, a long working distance is required. In the case of our specific application, we require a working distance of approximately 24 mm in order to have a pair of lenses in a confocal configuration surrounding the glass vacuum cell. The optical design of such objective lens, should properly take into account the 4 mm thick glass walls of the cell which may alter the focusing performance. Improper compensation of the glass thickness of the cell can result in spherical aberration, and severely limit the trapping performance.

Lastly, the focal position for the different wavelengths used in the experiment must coincide with one another, that is, by proper design of the optical elements that comprise the objective lens system, the effect of chromatic aberration must be minimized. The primary wavelengths that are utilized in our experiment are 780 nm, 795 nm, 1064 nm, 420 nm and 1012 nm light. This objective lens must have high transmission for these wavelengths.

Given the above list of specific requirements, the objective lens is a highly customized piece of optical equipment that needs to be specifically tailored to fit each experimental platform. In this section, I will discuss two common approaches; the first is to design a composite lens system constructed from stock components which can achieve a suitable performance. The second approach which can be more costly involves purchasing a commercially customized objective set.

4.4.1 Homebuilt objective lens housing

One cost efficient method to creating a custom objective lens is utilizing a combination of stock lenses and combining them into a composite optical system. We implemented an optical layout with a five lens system in order to achieve the following requirements for our system.

1) Numerical aperture: NA$>$0.35 for 780 nm and 1064 nm

2) Working distance: $>$32 mm

3) High transmission for wavelengths of 780 nm and 1064 nm.

By starting with the base design and the set of lenses, summarized in Table 4.1, we were able to optimize the design to fit our needs. In order to determine the optimal configuration, one can use the spot size of one of the beams, or a weighted average of spot sizes for different wavelengths, one can use the parameters such as the separation of lenses in order to perform optimization. Another

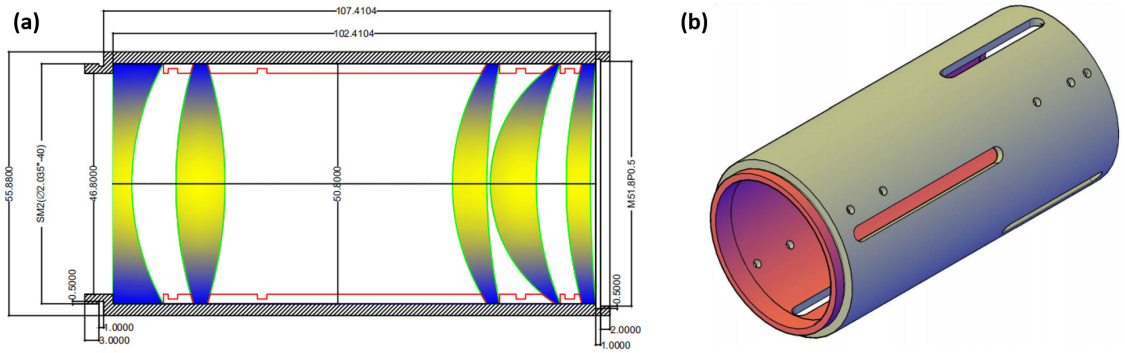

Figure 4.7: (a) Five lens objective system design. All measurements are in units of mm. (b) Three-dimensional drawing of the lens system housing. The material used in the design is Black Delrin.

feature allowed by OpticStudio from Zemax is the ability to optimize the geometric parameters of individual surfaces of lenses. Once the optimal focusing performance is achieved, one can perform "stock lens" matching in order to determine if there are stock lenses that can replace the custom lens while maintaining the desired performance.

Once the lens combination and separations are determined, we generated 3D models for the housing and spacers used to stabilize the lenses at the desired positions. Fig. 4.7 shows the objective lens layout and 3D housing design. To achieve high transmission properties for the two primary wavelengths in our experiment, we utilize Thorlabs 2 inch diameter lenses with a broadband B-coated AR coating suitable for wavelengths between 650-1050 nm. The housing and spacers were machined out of Black Delrin, which is tough machinable thermoplastic with a high modulus of elasticity, high strength, and good rigidity. An important thing to note is that the majority of the costs are attributed to the machining process, which can be dramatically reduced with in-house machining capabilities.

The performance of the design including the supporting optics was analyzed using OpticsStudio from Zemax. The results of the simulations are shown in Fig. 4.8. After quantifying the focusing performance by measuring the PSF, we determined that the measured resolution was in agreement with the Zemax simulations. However, when monitoring the long-term stability of the focusing performance, we noticed deviations that would have dramatic implications in the experimental longevity. We attribute these fluctuations to minute deviations of the spacing between lenses. A future improvement of the design should include cementing of the spacers after optimizing the PSF in order to "lock in" the results. It is also necessary to perform tolerance simulations that take into account thermal deviations of the spacers in order to determine a "chance of success" metric.

Special Optics Commercial Lens Our custom commercially designed objective lens from Special Optics / Navitar is designed for diffraction limited performance at 780 nm and 1064 nm with a

Item	Description	Price
Lens 1: LC1093-B	Plano-concave: $f = -100\ mm$	$44.65
Lens 2: KBX151AR.16	Bi-convex: $f = 88.3\ mm$	$95.00
Lens 3: LE1418-B	Positive Meniscus: $f = 150\ mm$	$54.90
Lens 4: LE1076-B	Positive Meniscus: $f = 100\ mm$	$53.79
Lens 5: LE1985-B	Positive Meniscus: $f = 300\ mm$	$50.75
Machine shop (Housing + Spacers)	Black Delrin Plastic	$1,341.25

Table 4.1: Overview of lenses used in the custom objective design.

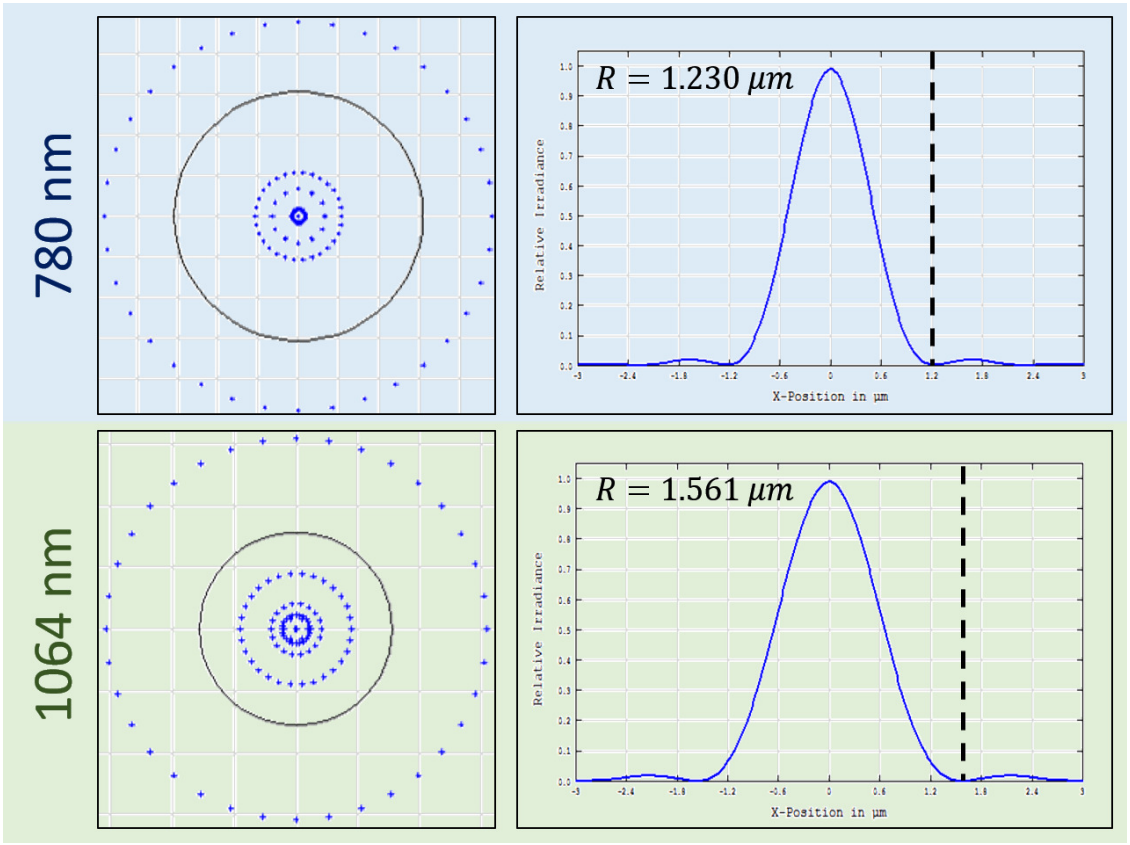

Figure 4.8: Zemax simulations for the performance of the homebuilt custom objective.

numerical aperature of NA=0.50 and working distance of 24 mm. The top panel of Fig. 4.9 shows the RMS wavefront error as a function of the paraxial image height, (the displacement from the center in the focal plane) from the optical axis for 780 nm light. The black line indicates diffraction limited performance (RMS=0.072 waves), and blue line shows RMS error for the simulated system. Note that the system can achieve diffraction limited performance for axial displacement in the focal plane of $\pm$180 um, implying a Full Field of View (FFOV) of ˜360 um for 780 nm. The middle panel of Fig. 4.9 shows the spot diagram, that is the end position of rays (blue crosses) traced through the optical system for a hexapolar distribution of rays at the entrance plane for central paraxial heights of 0 μm, 50 μm, 100 μm, and 150 μm. The bottom panel of Fig. 4.9 shows a cross-section of the Huygens Point Spread Function (PSF). A similar set of plots is shown in Fig. 4.10 for the wavelength of 1064 nm. The objective lens was designed to reduce the chromatic focal shifts between the different wavelengths used in the experiment as indicated by Fig.4.11.

4.5 Measuring the point spread function

In order to quantify the focusing performance of an optical element, it is necessary to measure the point spread function (PSF). The PSF is the response function of an imaging system to a point source. This is analogous to the Green's function formalism to calculate the electric field generated by sources and similar to the Huygens-Fresnel principle. Each point in the object plane is a source of light which is mapped to the PSF in the image plane. By summing over all points in the object, we can determine the image formed in the image plane.

In the ideal case, the PSF is a two-dimensional delta function and the light distribution in the object plane is mapped directly to the image plane with a factor of the magnification in the system. In practice, the PSF is an Airy function due to the diffraction properties of light. Therefore, in order to mathematically determine the image that is formed, one must perform a convolution of the object with the PSF. The main geometric parameter, the Airy disk radius, defined as the location of the first minima of the intensity is related to the effective numerical aperture of the system. For a diffraction limited optical system, the Airy disk radius R is given by

$$R = \frac{0.61\lambda}{\text{NA}}.$$

If we approximate the PSF with a Gaussian intensity profile, then the PSF can be approximated with a Gaussian waist σ of

$$\sigma \approx \frac{r}{2.9}.$$

If the PSF can be measured, we can determine directly the effective numerical aperture of the optical system. Another way to evaluate diffraction-limited performance is based on the root-

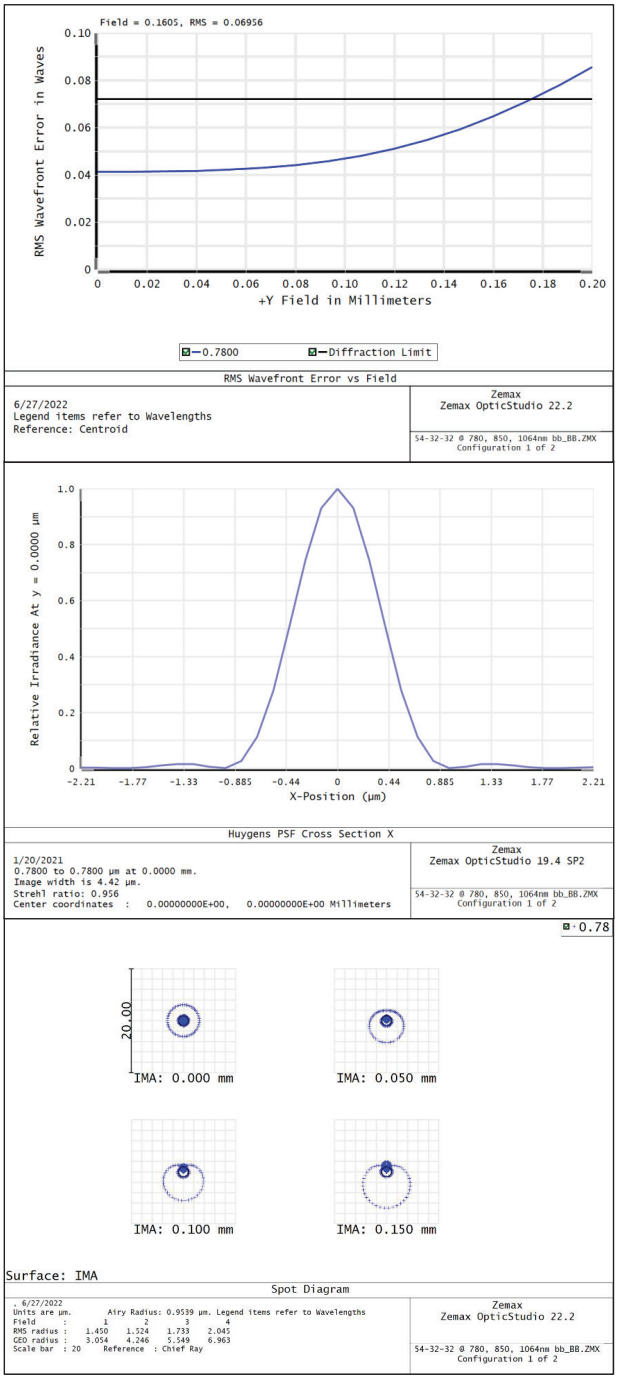

Figure 4.9: Zemax simulations for the focusing capabilities of the objective lens at 780 nm. Top: RMS Wavefront error as a function of the paraxial image height. We can achieve diffraction limited performance for a field of view of $\pm 180\ \mu m$ at the focal plane. Middle: Spot diagram for paraxial heights 0 μm, 50 μm, 100 μm, and 150 μm. The blue crosses indicate the position of traced rays at the focal plane. The black circle represents the Airy disk, that is a circle with radius of the Airy Radius 0.954 μm, performance limited only by diffraction. Bottom: Huygens Point Spread Function (PSF) cross section.

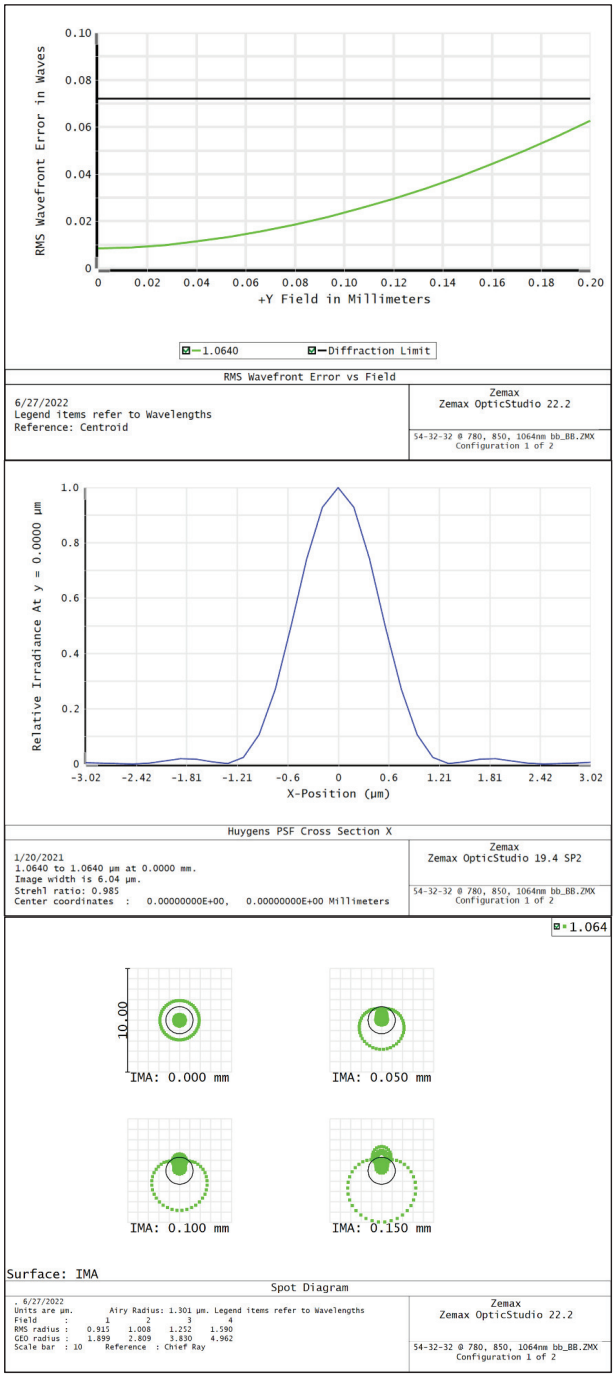

Figure 4.10: Zemax simulations for the focusing capabilities of the objective lens at 1064 nm. Top: RMS Wavefront error as a function of the paraxial image height. We can achieve diffraction limited performance for a field of view of $\pm 210\ \mu m$ at the focal plane. Middle: Spot diagram for paraxial heights 0 μm, 50 μm, 100 μm, and 150 μm. The green crosses indicate the position of traced rays at the focal plane. The black circle represents the Airy disk, that is a circle with radius of the Airy Radius 1.301 μm, performance limited only by diffraction. Bottom: Huygens Point Spread Function (PSF) cross section.

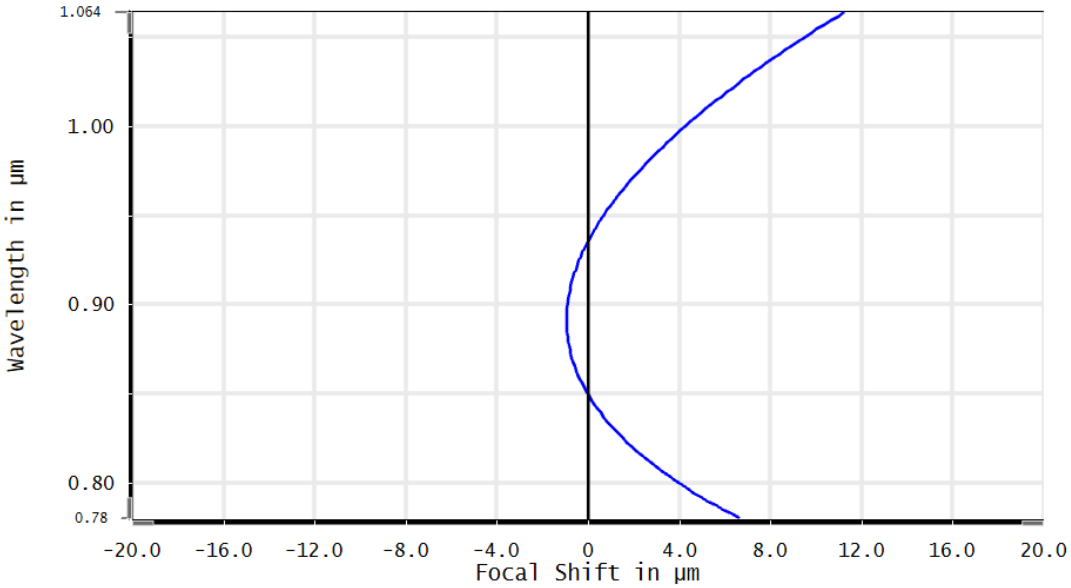

Chromatic Focal Shift	
1/20/2021 Maximum Focal Shift Range: 12.2052 µm Diffraction Limited Range: 3.420 µm Pupil Zone: 0.0000	Zemax Zemax OpticStudio 19.4 SP2 54-32-32 @ 780, 850, 1064nm bb_BB.ZMX Configuration 1 of 2

Figure 4.11: Chromatic focal shift (x-axis) as a function of the wavelength (y-axis). There is a focal shift of ˜4 μm between 780 nm and 1064 nm light. Since these two fields propagate through different optical paths, the focal positions can be matched by adjusting axial positions of various optical elements within each path.

mean-squared error (RMSE) of the wavefront. For an RMSE of less than 0.072 waves, the system is denoted as "diffraction-limited". This method however is more difficult as it requires a measurement of the wavefront, which is technically more challenging than measurement of intensity. To measure the PSF of the objective lens, we utilize an optical layout shown in Fig. 4.12. First, a collimated TEM_{00} beam is generated at the output of single mode optical fiber. This beam is directed towards a precision manufactured resolution target to generate quasi-point sources of light. The resolution target from Technologie Manufaktur contains 58 line patterns ranging from 7.5 mm to 3300 line pairs per mm. Also there are 5 pinholes ranging from diameters between 0.25-4.0 μm.

The resolution target is mounted onto a three-dimensional translation stage for precise positioning of the beam onto the target (x,y) and positioning the target with respect to the objective lens (z). After the target, the point source of light expands rapidly due to diffraction, and passes through a glass window, with thickness and materials chosen to match those used in the glass cell on the experimental table. The light is then collimated by the objective lens that is being tested. Finally, the light is focused onto the Andor sCMOS camera by a final field lens. In this optical system, the plane at the resolution target and the plane located at the CCD chip are conjugate planes, with a magnification factor given by the ratio of focal lengths of the telescope. That is, there is a magnification factor M

$$M = \frac{f_{\text{field}}}{f_{\text{obj}}}.$$

For a field lens focal length of $f_{\text{field}} = 750$ mm and $f_{\text{obj}} = 32$ mm, $M \approx 23.43$. For the camera used in our setup, with square pixels of length, 6.5 μm, the magnification means that each pixel will map to size at the target plane of 0.277 μm. Therefore an Airy disk radius of ˜1.5 μm corresponds to a spot with a diameter between 10 and 11 pixels. In order to calibrate the size of each pixel precisely, we can measure various line pair groups and correspond their linewidths to physical distances. The line pair per mm (lp/mm) can be converted to a linewidth of the line by using the following conversion.

$$\frac{1000}{\text{Resolution[lp/mm]}} = \text{Line width}[\mu\text{m}]$$

This means that for our resolution target, 7.5-3300 lp/mm translates to linewidths of 66.66 μm to 0.15 μm respectively. For the focal lengths of the lenses used in our system, linewidths less than 0.27 μm cannot be resolved due to the magnification factor and pixel size of the CCD camera. For additional camera resolution, an additional telescope can be placed after the field lens.

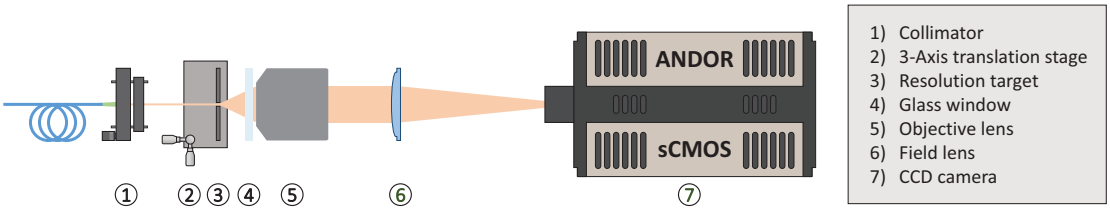

Figure 4.12: Simplified optical layout to measure the PSF of optical elements.

CHAPTER 5

Laser Systems and Optical Layouts

In this section, I describe the laser systems used in our experiment as well as provide an overview of optical layouts and details on the relevant elements. In summary, our system is comprised of eight optical subsystems (SS). Each of these subsystems are indicated and described in brief detail in Table 5.1.

Subsystem label	Brief description
SS0: EXP	Prep. of 1064 nm trapping beam, vacuum cell, and MOT formation.
SS1: 780 RP	Prep. of D_2 repumper. Locking to sat-spec and phase locking.
SS2: 780 AMP	Optical amplification of 780 nm light used for SS3.
SS3: MOT / IMG	Divert amplified light into different paths for the MOT and imaging.
SS4: OP / EXC	D_1 optical pumping frequency prep. and D_2 exc. prep.
SS5: 420 EXC	420 nm freq. prep for Rydberg excitation.
SS6: 1012 EXC	1012 nm freq. prep for Rydberg excitation.
SS7: CAVITY	Frequency locking via PDH and high-finesse optical cavity.

Table 5.1: Overview of optical subsystems.

The optical layouts presented in this section are approximately to scale with each square grid representing a square inch. To assist future students in developing optical layouts, a Powerpoint file can be found via the online repository which contains a library of optical element icons which can be used to track changes and aid in the the layout design process. Single mode fibers (SMFs) directing light to and from different optical subsystems are labeled with the direction of light propagation, as well as the subsystems corresponding to the input and output of the fiber. For example, a fiber labeled "[5/0] 420 EXC" corresponds to a fiber that carries 420 nm excitation light, with input port located in subsystem 5, and output port located in subsystem 0. Unless explicitly stated, all SMFs are polarization maintaining. For only the main experimental table layout, the

beam diameters are indicated via the width of the lines, where relative sizes are approximately to scale for a given optical path, but relative scales between different paths are not accurate.

5.1 Subsystem 0 (EXP): The experimental table

5.1.1 Overview of the 1064 nm optical path.

Our trapping laser is derived from a Neodymium-doped Yttrium-Aluminum-Garnet (Nd:YAG) fiber-based amplifier. The input seed laser of ˜5 mW is amplified to produce a coherent, single-mode output of up to 50 W. The power directly out of the laser head is determined by the pump current setpoint. Figure 5.1 shows the measured power scaling of the amplifier output as a function of the pump current setpoint. At the output of the laser, the beam diameter ($1/e^2$ intensity) is 3 mm. The first-order diffracted spot through a 200 MHz AOM is used to modulate the power of the trapping field, whereas the undiffracted beam is dumped. A portion of the light is picked off and directed toward a photodiode for intensity stabilization. In order to adapt the beam size to completely fill the active area (15.8 $\times$12 mm^2) of the spatial light modulator, the beam passes through two telescopes. The first is formed by a 300 mm and 400 mm lens pair, and the second telescope pair consists of 100 mm and 300 mm focal length lenses resulting in a total magnification factor of four. Afterwards the beam is directed to a breadboard above via periscope. The resulting beam diameter after magnification at the SLM plane is approximately 12 mm.

A spatially varying phase is imprinted on the trapping beam by the spatial light modulator. The computer generated hologram (CGH) is calculated using a weighted Gerchberg-Saxton algorithm (WGS), and is projected onto the SLM display via home-built software and communicated via DVI cable. After diffraction off the SLM, the beam is directed through an additional telescope consisting of 150 mm and 300 mm lenses. This final telescope is important for two reasons; the first is to expand the beam diameter to 24 mm before the objective lens. Secondly, the telescope configuration ensures that off-axis traps are not clipped by the time that they reach the objective lens. At the focus of the objective lens, the array of traps is formed.

The light is then recollimated by an identical microscope objective placed on the opposite end of the cell in a confocal configuration. To ensure that the two lenses are aligned parallel to each other, both objectives are mounted onto a 2-inch cage mount system, and cage rods extend across the glass cell. The glass cell is manufactured by Japan Cell, made with quartz glass, and is not anti-reflective coated. The cell thickness is 4 mm, with an inner cell length of 28 mm. The inside of the cell is pumped down to a vacuum pressure of 10^{-8} Torr. After being recollimated after the cell, the majority of the trapping light is dumped. A small fraction of the beam power is picked off via a glass window, directed toward two instruments for characterization. To monitor the intensity

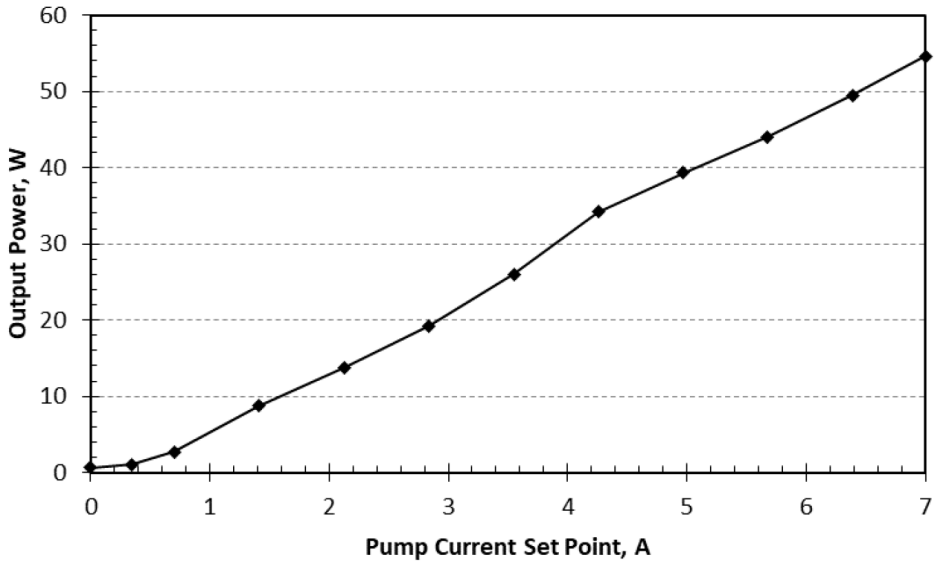

Figure 5.1: YAG output power scaling as a function of pump current set point.

profile of the trapping beam, we direct the light towards an Andor Zyla 4.2 sCMOS camera. The intensity images are used for verifying optimal alignment of the trapping beam through the optics, as well as used for an iterative trap feedback procedure. Alternatively, the light can be redirected towards a HASO4-FIRST wavefront sensor by a mirror mounted onto a flip mount. The wavefront sensor is used to quantify the amount of aberration present in our optical system and generate compensation holograms. Fig. 5.2 shows a detailed layout of the experimental table.

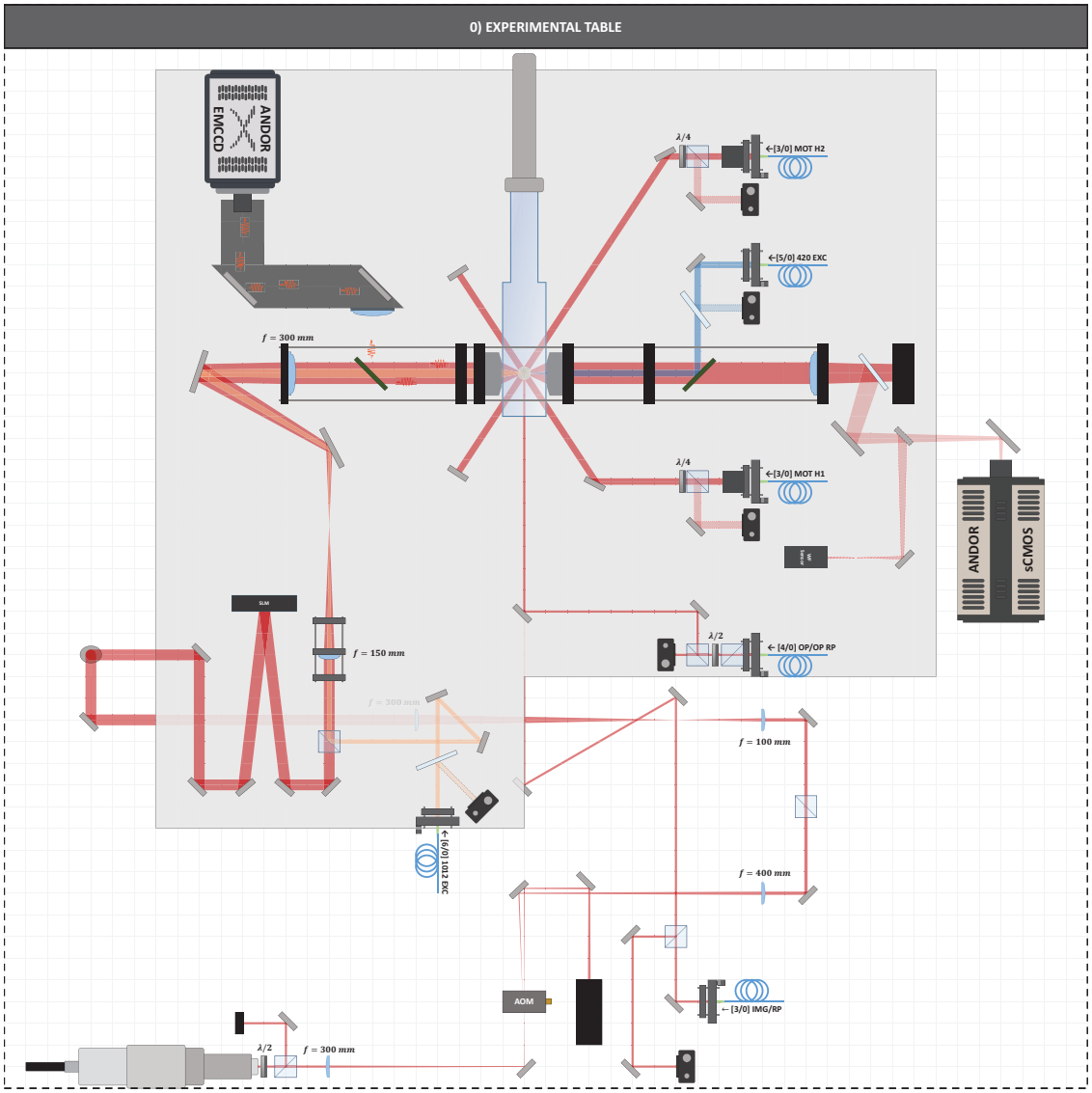

Figure 5.2: Main experimental table where trapping and manipulation of single-atoms takes place.

5.1.2 Magneto-optical trap

The magneto-optical trap is loaded from background vapor. The three beams for the magneto-optical trap are directed from SS3 and are output on the experimental table with a beam diameter of $\simeq 3$ mm. Each beam has powers $\simeq 3$ mW. Each beam is retroreflected using a mirror mounted with a $\lambda/4$ waveplate so that the retroflected beam has orthogonal polarization to the input beam. To reduce the effects of interference, each mirror mount utilizes piezoelectric transducers (PZTs) to vibrate the mirror mounts at different frequencies. During a typical experimental sequence, the MOT is loaded for 100 ms and the YAG trap array is on during the entirety of the MOT loading process.

5.1.3 List of additional specifications for equipment in SS0:

Nd:YAG Fiber Amplifier:
Model number: YLR-50-1064-LP-SF
Maximum power: 50 W
Center wavelength: 1064 nm
Output polarization: Linear
Intensity noise: $\Delta\nu > 100$ kHz : -110 dB/Hz, $\Delta\nu > 3MHz : -120$ dB/Hz
Beam quality:1.05-1.15 M^2

Spatial Light Modulator:
Model number: LCOS-SLM X10468-03
Wavelength: 1050$\pm$50 nm
Light utilization efficiency: 97% at 1064nm
Number of pixels: 792 $\times$ 600 pixels
Pixel pitch: 20 um
Fill factor: 98%
Effective area size: 15.8$\times$12 mm^2

Vapor cell:
Manufacturer: Japan Cell
Model number: JPC-4-0933
AR Coating: Without coating
Material: Quartz Glass
Dimensions: Cell thickness of 4 mm and inner cell width of 38 mm

Objective lens:
Manufacturer: Special Optics
Model Number: 54-32-32
Numerical Aperature: 0.5
Effective Focal Length: 32 mm
Design wavelength: 780 nm, 850 nm, and 1064 nm.

$$R_{780} = 951.6\ nm$$
$$R_{850} = 1037.0\ nm$$
$$R_{1064} = 1298.1\ nm$$

Transmission: >95% at each of the specified wavelengths

Andor EMCCD:
Model: Andor iXon Ultra 897
Sensor type: Back-illuminated 512x512 EMCCD
Pixel Size: 16 um
Readout rate: 17 MHz
Cooling: -80^oC Air Cooled
Quantum Efficiency: $>$90%

Andor sCMOS:
Model: Zyla 4.2 sCMOS
Quantum Efficiency: 82%
Number of pixels: 4.2 Megapixels
Read noise: $0.9e^-$
Linearity: 99.8%

Wavefront Sensor:
Model: HASO4First
Absolute Accuracy: $\lambda/100$ RMS
Acquisition Rate: 100 Hz
Aperture Dimension: 3.6$\times$4.5 mm
Number of microlenses: 32 $\times$40
Spatial sampling: 100 μm
Interface: USB 3

5.2 Subsystem 1 (780 RP): D_2 line (780 nm) repumper

The 780 nm light used to repump atoms from the F=1 hyperfine state to the F=2 hyperfine ground state of Rb is derived from a Moglabs ECDL. The light is directed to a saturation spectroscopy cell which is used to generate an error signal and locked to the F=1 $\leftrightarrow$ F'=0-1 crossover transition. The beam is then frequency shifted by 105x2 MHz via a doublepass AOM configuration in order to be near resonance with the F=1$\leftrightarrow F' = 2$ freespace transition. A portion of the beam (before frequency shifting) is directed to a heterodyne module in order to be used as the master laser for offset phase locking. Fig. 5.3 shows a detailed optical path.

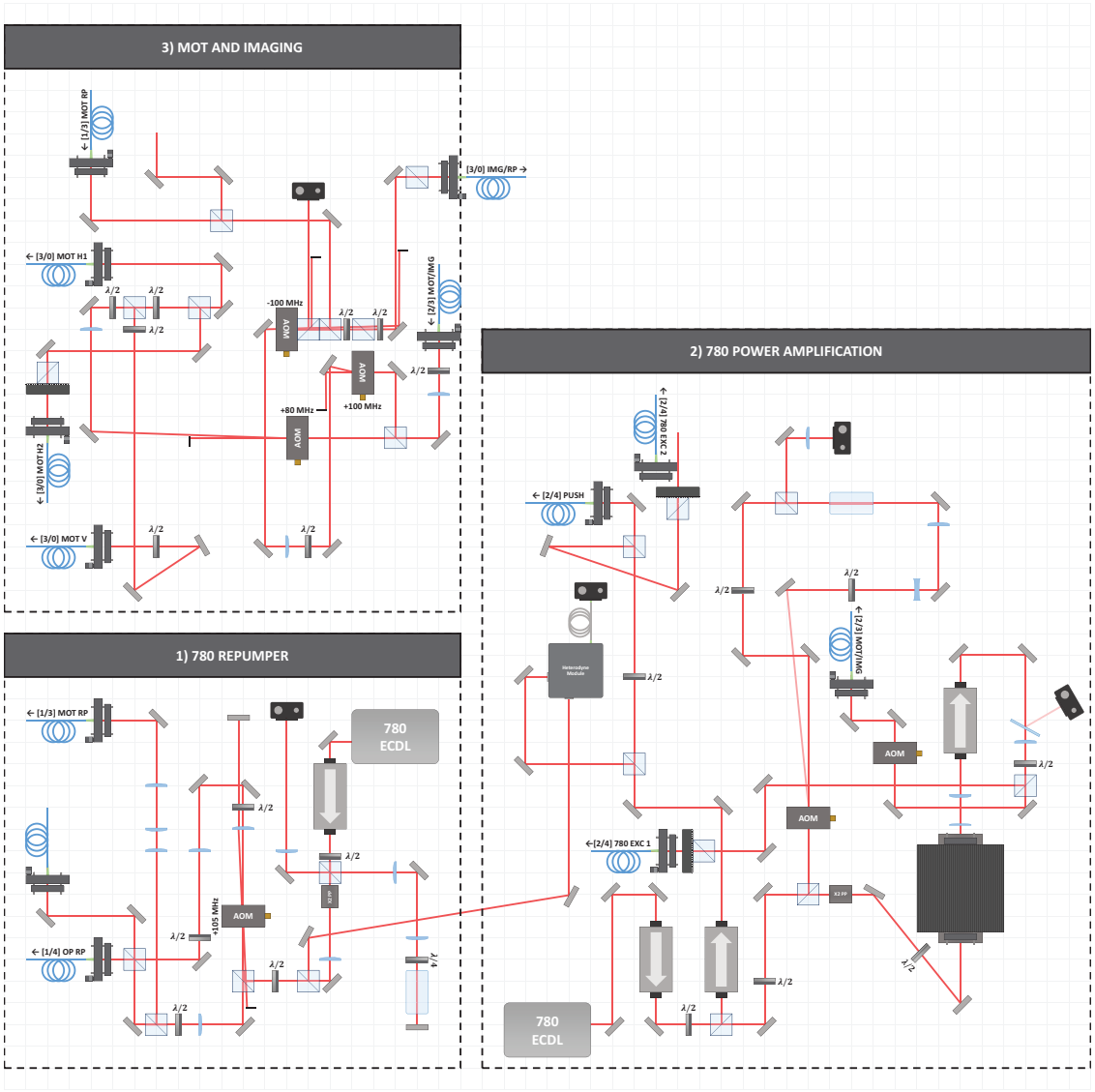

Figure 5.3: Optical subsystems 1-3. 780 nm laser preparation for MOT, imaging, and repumper.

5.3 Subsystem 2 (780 AMP): 780 nm optical amplification

A second ECDL with a central wavelength of 780 nm is used for a variety of purposes:

1. Optical molasses beams for the magneto-optical trap,
2. In-trap fluorescence imaging,
3. State-sensitive radiation pressure pushout beam,
4. Polarization gradient cooling.

In order to have sufficient power for these purposes, we employ optical amplification via a tapered amplifier (TA) in a Master Oscillator Power Amplifier (MOPA) configuration. The TA chip, TA-0785-2000, from Coherent/DILAS semiconductor is housed in a home-built opto-mechanical mount in order to achieve high seed mode matching with the TA chip. The mount consists of two aspheric lenses mounted to XYZ translations stages in order reduce the sensitivity to thermal fluctuations of the alignment.

The TA chip is fabricated with a c-mount heatsink, which is secured to a copper block in thermal contact with the thermoelectric cooler (TEC) for active stabilization of the temperature. To channel heat away from the chip, large fins are attached to the top of the MOPA, and a fan ensures that there is significant airflow through the fins in order to efficiently dissipate the heat.

A Newport Laser Diode Controller Model 6000 is used to implement the temperature stabilization and provide electrical power to the TA. Under typical conditions, we use an operating current of 2.5 A, which results in an amplification of the 15 mW seed light to roughly 500 mW at the output of the MOPA. The current setting was chosen as the maximal current that is allowed without feedback. Therefore, even if the seed beam is blocked unintentionally, there will not be any damage to the TA. Due to the geometry of the TA waveguide and tapered gain region within the chip, the output mode is rectangular and highly astigmatic. To compensate for the astigmatism, we use the position of the output lens to collimate the beam in the vertical direction, and an additional cylindrical lens to collimate the beam in the horizontal direction. To reduce the effect of direct back-reflections into the MOPA, which can damage the TA, we use AR coated lenses, optical isolators, and slightly skew the angle of the lens directly after the MOPA. The amplified light is then directed to SS3 and SS4 via polarization maintaining single mode fibers. A detailed optical layout is shown in Fig. 5.3.

5.3.1 MOPA Alignment procedure:

For the initial alignment of the MOPA, we follow the procedure described below.

1. Set the current of the MOPA to a value much lower than the maximal current without feedback, for our TA chip, this is ˜100-300 mA.

2. Observe a backward propagating beam due to the amplified spontaneous emission (ASE) at the input of the MOPA.

3. Spatially overlap the seed laser with this backward propagating beam over an extended distance.

4. While monitoring the output power of the MOPA, block and unblock the seed light. If there is amplification when the seed light is unblocked, this means that the seed light is roughly coupled with the TA chip.

5. Maximize the output power of the MOPA using the alignment of the seed beam. Also, the amplification is polarization dependent, so rotate the polarization using a $\lambda/2$ waveplate before the MOPA.

6. Once the output power is maximized for a given operating current, increase the current in steps, making sure to see if the alignment is still optimal.

7. Measure the output power using a high-power powermeter (e.g. a thermopile) to see if the power scaling tracks with the test report.

5.4 Subsystem 3 (MOT/IMG): Optical fields for the magneto-optical trap and resonant fluorescence imaging

After amplification of 780 nm light in SS2, the light is directed to SS3. The light is split between two paths to be used for resonant fluorescence imaging and the MOT. The +1st order diffracted beam of an AOM is split into two horizontal beams and a vertical MOT beam, all of which directed to the experimental table via separate SMFs. For the imaging path, a portion of light is picked off via a beam splitter, and used for intensity stabilization. Before being coupled to a SMF, repumper light from SS1 is spatially overlapped with the imaging beam via a PBS. A detailed optical layout is shown in Fig. 5.3.

5.5 Subsystem 4 (OP/EXC): D_1 Line optical pumping and D_2 line excitation

For state preparation into a desired ground hyperfine magnetic sublevel, we utilize optical pumping (OP) on the D_1 line. The 795 nm laser used to address this transition is derived from a Moglabs ECDL and is locked via sat. spec. to the 2-2' transition. The light passes through multiple AOMs in double pass configuration in order for the final frequency at the experimental table to be +80 MHz from the free-space transition, and near resonance with the 2-2' transition in the presence of lightshifts. To make alignment of the OP beam on the experimental table easier, we combine a

designated D_2 repumper beam into the same optical fiber via a bandpass filter. A detailed optical layout is shown in Fig. 5.4.

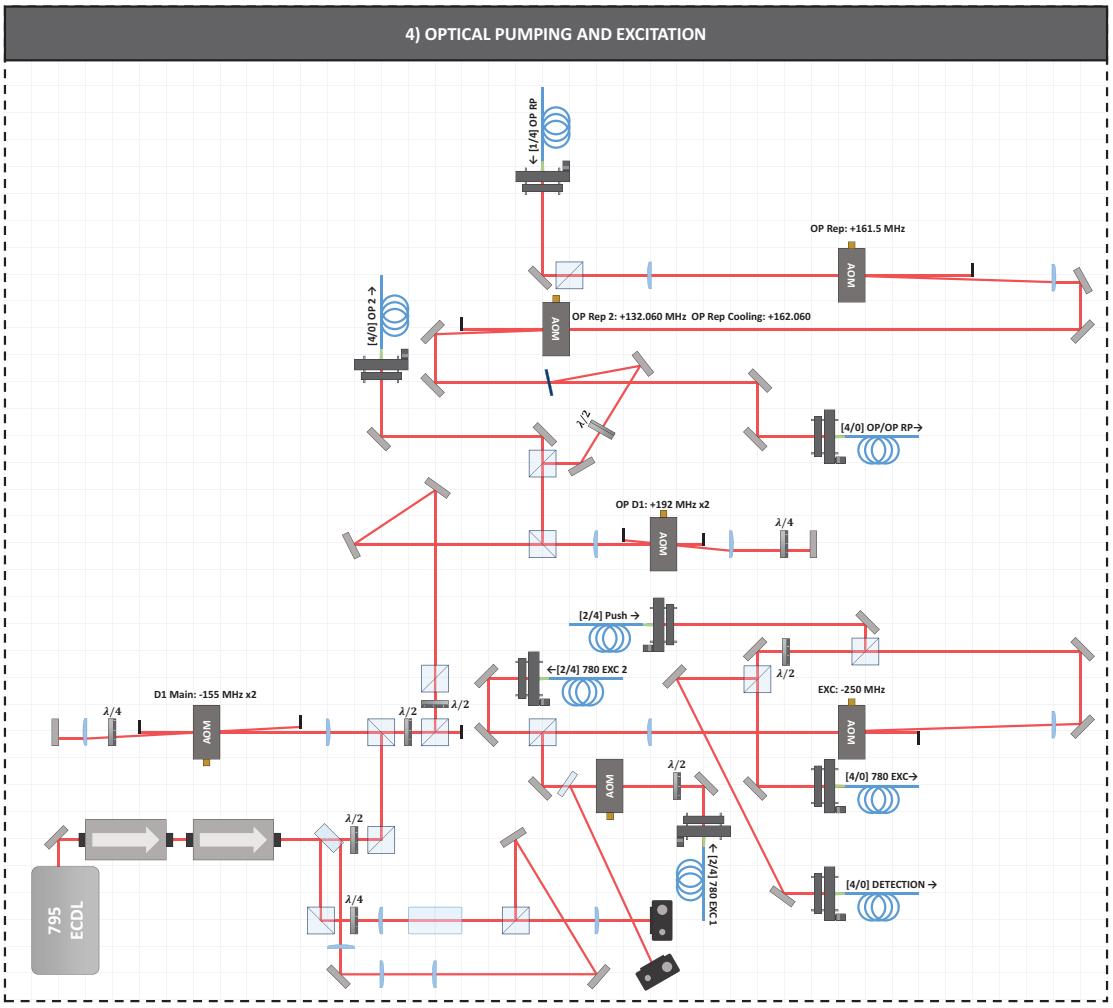

Figure 5.4: Optical subsystem 4.

5.6 Subsystem 5 (420 EXC): 420 nm Rydberg excitation laser

Due to the small frequency separations between neighboring Rydberg transitions, we employ PDH locking with high-finesse optical cavities to achieve narrow linewidth lasers used for excitation. The 420 nm light used to excite atoms on the $|5S_{1/2}\rangle \leftrightarrow |6P_{3/2}\rangle$ transition, is derived from a Moglabs ECDL. The light is sent to SS7 where a PD measures the cavity reflection spectrum to be used for generation of the error signal. The photodiode signal is sent to a Toptica PDD110 Pound-Drever-Hall module for error signal generation. The local oscillator signal is derived from

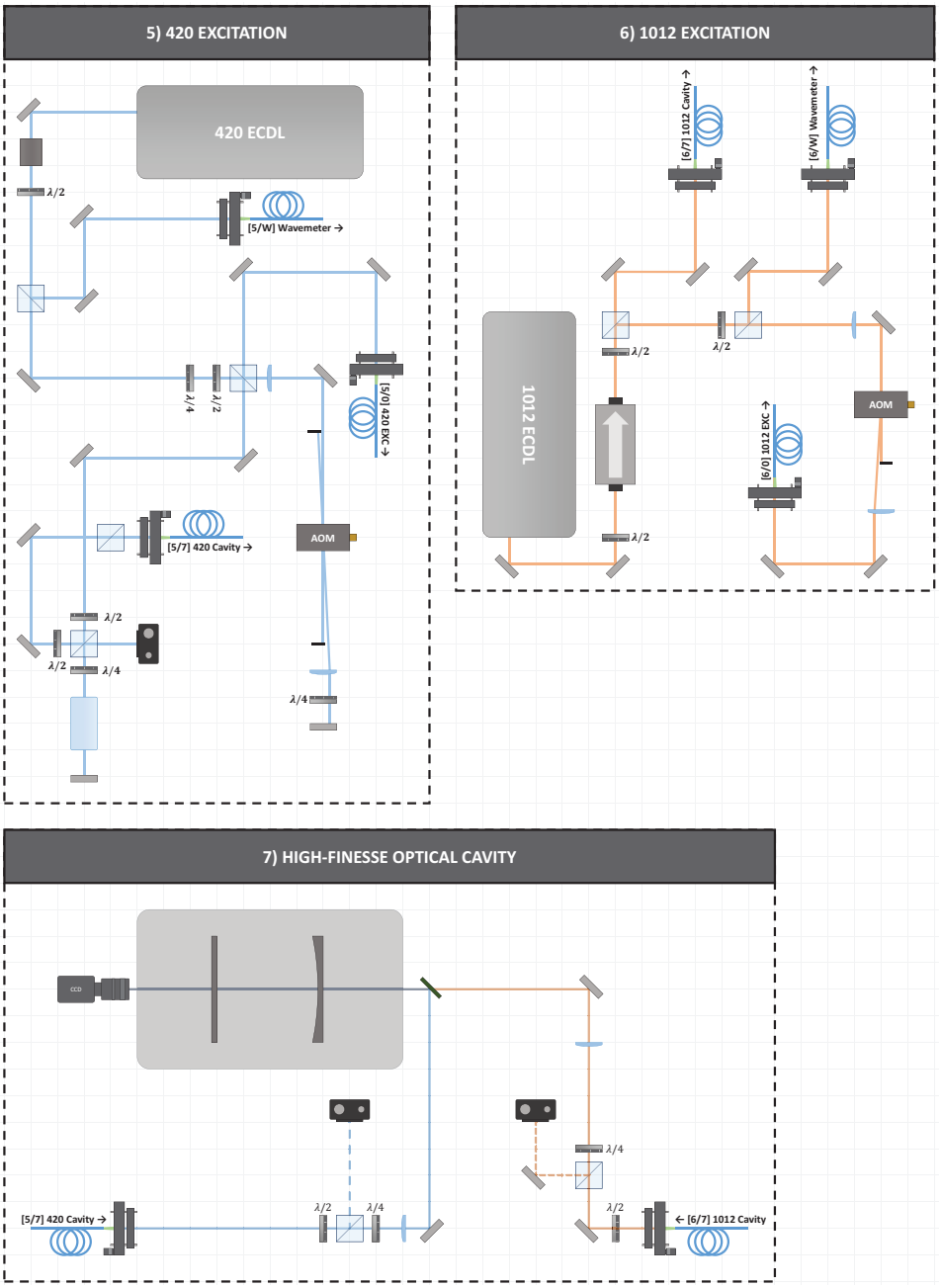

Figure 5.5: Optical subsystems 5-7.

Parameter	Specification
Cavity design	Half-symmetric planar concave resonator
Cavity length	100 mm
Free spectral range	1.5 GHz
Concave mirror ROC	50 cm

Table 5.2: Parameters of the high-finesse optical cavity

the PDH module and used to directly modulate the Moglabs laser. The error signal is then sent to a Toptica Falc110 Fast Analog Linewidth Control module for additional signal conditioning. The final filtered signal is sent into the back of the Moglabs Laser Diode Controller, where it is split for the two feedback channels, current modulation for fast feedback, and PZT modulation for slow feedback. A detailed optical layout is shown in Fig. 5.5.

5.7 Subsystem 6 (1012 EXC): 1012 nm Rydberg excitation laser

The second Rydberg excitation laser is used to complete the two-photon transition to Rydberg. Similar to the 420 nm laser, the 1012 nm light is derived from a Moglabs ECDL, and locked to the same high-finesse optical cavity. Due to the fact that this laser addresses the $|6P_{3/2}\rangle \leftrightarrow |nS_{1/2}\rangle$ transition, it is necessary to have a large tuning range so that one can swap to different principal quantum numbers more easily. To achieve this, the laser light is modulated using an electro-optic modulator (EOM) rather than direct modulation of the laser current. The PM-0S5-10-PFA-PFA-1012 EOM from EOspace features a 10 GHz Lithium Niobate Phase modulator with a central wavelength of 1012 nm. A similar electronics setup is used for the PDH error signal processing and feedback implementation.

5.8 Subsystem 7 (CAVITY): High-finesse optical cavity

For narrow linewidth lasers, we utilize the reflectance spectrum of a high-finesse optical cavity to generate a Pound-Drever-Hall locking signal. In order to have multiple fields locked simultaneously to the same cavity, we use bandpass filters to spatially overlap fields of different wavelengths. To ensure that the TEM_{00} mode is being transmitted through the cavity, the spatial mode of the transmitted light is analyzed using a CCD camera. Mode matching optics are placed along each optical path to optimally match the output of the SMF to the resonant cavity mode. The parameters of the cavity are listed in Table 5.2.

CHAPTER 6

Laser Stabilization

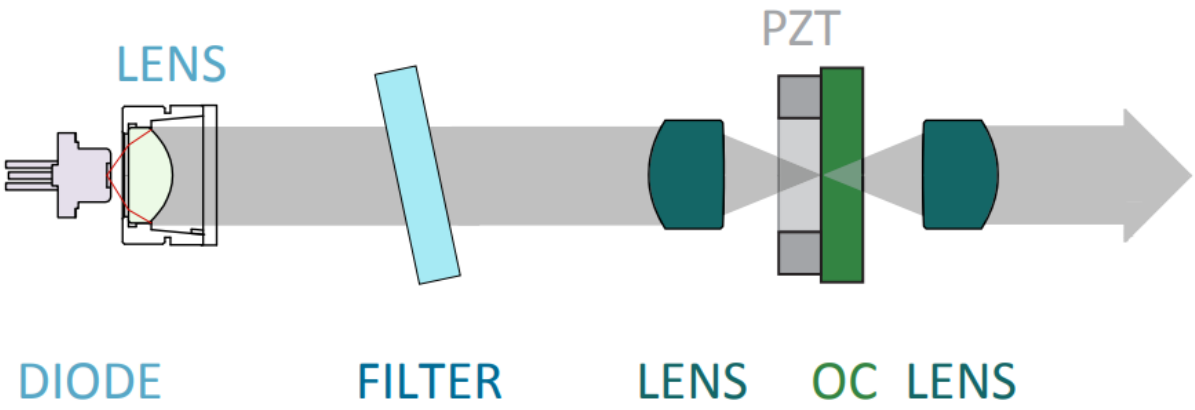

Figure 6.1: Schematic of MOGlabs ECDL.

In the field of atomic physics, the laser is the laboratory workhorse. Laser fields are often used for trapping, cooling, and coherent state manipulation of atoms. For the D_1 and D_2 line transitions, the energy splittings between hyperfine states are on the order of 100s of MHz to several GHz. In order to properly address individual levels, it is crucial to have lasers that have frequency bandwidths less than this separation. Additionally, laser noise can cause dephasing of quantum coherences. To combat the frequency instability of the laser, active frequency stabilization protocols can be used.

Frequency stabilization is often performed utilizing some form of a feedback loop. In general, a feedback loop consists of a few important ingredients. The first requirement is a method of regulating the target variable to be stabilized, whether that be the frequency or intensity of the laser. The second requirement is a method for measuring the variable of interest at the output of the control loop. The final requirement is a stable reference in which the laser will be locked to. From this reference, we can derive a control signal that can be fed back into the laser. In the upcoming sections for frequency stabilization, I'll first describe the basic operating principles of a

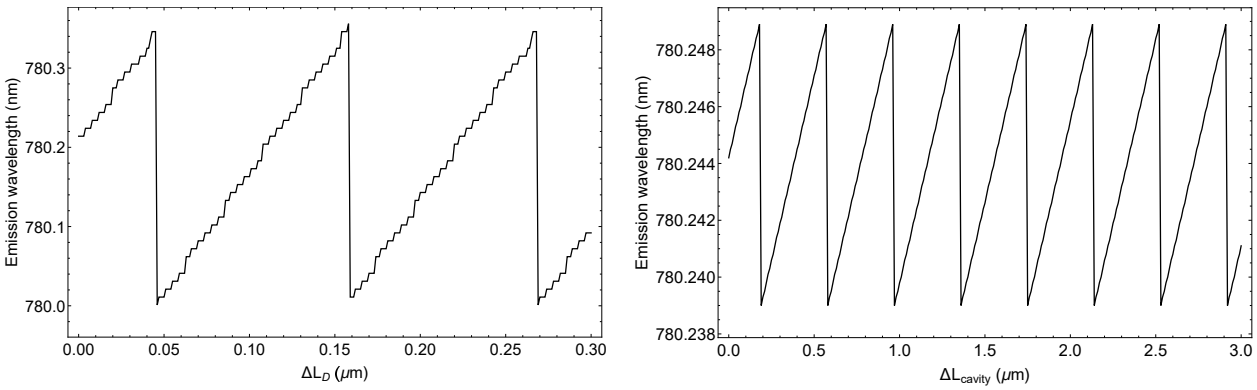

Figure 6.2: Left: Emission wavelength as a function of the deviation of the diode cavity length. The tunable range is roughly 0.345 nm which corresponds to 169.925 GHz. Right: Emission wavelength as a function of the deviation of the external cavity length. The tunable range of 0.01 nm corresponds to 4.92 GHz.

main type of laser used in our lab, the external cavity diode laser, and describe the PDH locking scheme.

6.1 Frequency selection in ECDLs

Here I'll explain the basic principles of the external cavity diode laser (ECDL), what factors effect the output wavelength, and with this knowledge, describe how the laser frequency can be modulated and eventually stabilized. The output frequency ν of an ECDL laser depends on the frequency dependence of the gain and loss factors. For the case of the ECDL, cavities formed by different reflective surfaces largely determine the structure of the gain factors. The first cavity that we need to consider is the one formed by the front and rear facets of the laser diode itself. This cavity results in a transmission function given by

$$T_D = \frac{1}{1 + F\sin^2(\delta(\nu))}, \tag{6.1}$$

where $F = 4r_1r_2/(1 - r_1r_2)^2$ is the finesse of the cavity diode with $r_{1,2}$ being the amplitude reflection coefficients of the rear and front faces of the diode. Here $\delta(\nu) = 2\pi n L_D \nu/c$ is an acquired phase-shift after one round trip within the cavity where L_D is the length of the diode cavity, n is the refractive index of the semiconductor and ν is the oscillation frequency of the laser. The second cavity that we need to consider is the one that is formed by the rear facet of the diode, and in our case, the cateye reflector. We have a similar transmission function T_{cavity} where now the length of the cavity L_{cavity} and the refractive index n is that of free space.

Finally, most ECDLs feature a wavelength selection element. Sometimes this can come in the form of a diffraction grating, as for Littman-Metcalf and Littrow type configurations. In the majority of the lasers that we utilize in the lab, a bandpass filter is placed between the reflecting surfaces of the external cavity with a transmission function T_{filter}. The central wavelength of the bandpass filter can be tuned based on the angle of incidence with the filter given by

$$\lambda_c(\theta) = \lambda_0 \sqrt{1 - \left(\frac{sin(\theta)}{n_{\text{eff}}}\right)^2}. \tag{6.2}$$

Where λ_0 is the wavelength at normal incidence, θ is the incident angle, and $n_{\text{eff}} \approx 2.13$ is an effective refractive index. For the purposes of simulating mode selection within the ECDL, we treat the transmission function of the bandpass as a generalized Gaussian of the form

$$T_{\text{filter}}(\theta, \lambda) = \exp\left[-2\left(\frac{(\lambda - \lambda_c(\theta)}{\sigma_\nu}\right)^{2m}\right] \tag{6.3}$$

where the typical bandpass filter bandwidth is roughly $\sigma_\lambda = 3$ nm. Even though the bandpass filter has a bandwidth of roughly 3 nm, we will see that utilizing the edges of the bandpass gain profile, it's possible to realize single-mode operation from the laser. The final factor is the gain profile of the semiconductor G_D, which for our specific application can be approximated as a Gaussian with FWHM of 10 nm.

$$G_D = \exp\left[-2\frac{(\lambda - \lambda_D)^2}{\sigma_\lambda^2}\right] \tag{6.4}$$

here $\sigma_\lambda \approx 8.49$ nm. Since this bandwidth is much larger than the other bandwidths in consideration, it's nearly linear within the range we are considering. The total gain profiles of the laser is therefore given by

$$T_{\text{total}} = T_{\text{D}} T_{\text{cavity}} T_{\text{filter}} G_{\text{D}}. \tag{6.5}$$

The dominant lasing mode can be tuned by changing the various parameters associated with the system. By tuning the angle of incidence for the bandpass filter, the emission wavelength can be tuned on the order of a few nanometers. This angle however has to be adjusted by hand and therefore is only used for coarse tuning of the wavelength to the desired value. Next, the laser diode cavity length can be adjusted, which can be done by varying either the temperature of the diode, or via the injection current. This will process gives a tuning range of up to a few hundred GHz. While this process can be controlled through the diode laser controller, the thermal response is slow and therefore can't be effectively used to modulate the frequency of the laser on the timescale needed for feedback. Finally, the external cavity length can be varied.

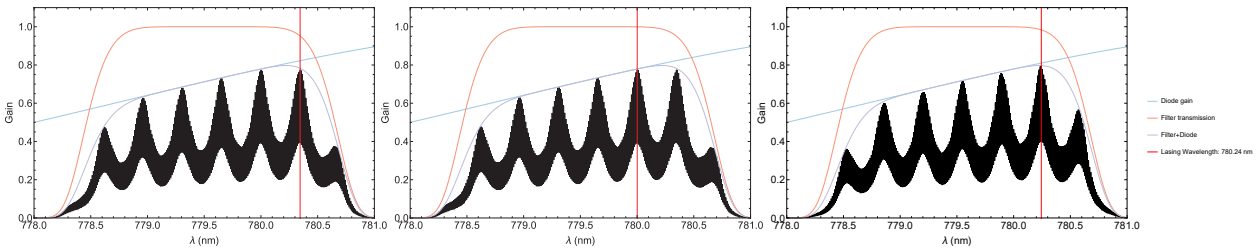

Figure 6.3: Total wavelength dependent gain profiles. Left: Operating near the modehop wavelength: $\Delta L_D = 0.045\ \mu m$, $\lambda_{\text{emission}} = 780.35$ nm, Middle: Operating near the modehop wavelength: $\Delta L_D = 0.046\ \mu$m, $\lambda_{\text{emission}} = 780.00$ nm.Right: Tuned to D2 line in Rb. $\Delta L_D = 0.012\ \mu m$, $\lambda_{\text{emission}} = 780.24$ nm

For the MOGLABs CEL laser, this is varied by changing the the voltage across a multilayer piezoelectric stack mounted to the output coupler. The cavity length variation is roughly 20 nm per volt. For the maximal piezo voltage of 150 V, this corresponds to a external cavity length displacement of 3 μm. This can result in a tuning range between 5-20 GHz which can be modulated at a rate of 25 kHz.

In figure 6.2, I plot the emission wavelength, defined as the wavelength that produces that maximal total gain, as a function of either the diode cavity length or external cavity length. Instead of a linear response with wavelength as a function of these cavity lengths, there is a periodic sawtooth graph. The discontinuity in the emission wavelength can be attributed to modehops, which occur where nearby frequency modes have comparable gain. To demonstrate this, in figure 6.3, I plot the total wavelength dependent gain factors for the parameters described in [3] for 3 different values of the cavity length. First, we can see that even though there are many cavity modes within the spectral bandwidth defined by the bandpass filter, the laser can operate at a single frequency, defined by the mode with maximal gain. The first panel shows the lasing condition to the left of the modehop, that is $\Delta L_D = 0.045\ \mu m$. The emission wavelength in this case is $\lambda_{\text{emission}} = 780.35$ nm. There is a frequency mode with comparable gain at $\lambda =$780.00nm. By varying the cavity length to $\Delta L_D = 0.046\ \mu m$, the emission frequency "hops" to $\lambda_{\text{emission}} = 780.0$ nm. From this, we can see that the frequency stability on the output relies critically on the wavelength selection mechanism.

First, the diode gain, shown in light blue, is a gaussian with a bandwidth of roughly 10 nm, with a central wavelength of 783 nm results in an approximately linear gain curve in the desired tuning range around the D_2 transition wavelength of 780.24 nm. This means that within our region of interest, the higher wavelength frequency modes will have a larger gain. On the contrary, the transmission profile of the bandpass filter, shown in pink, makes it such that higher wavelength modes are diminished. These two mechanisms combined are what allow for the wavelength selectivity and single-mode frequency operation of the CEL laser. Finally, in the right panel of Fig.6.3, I plot

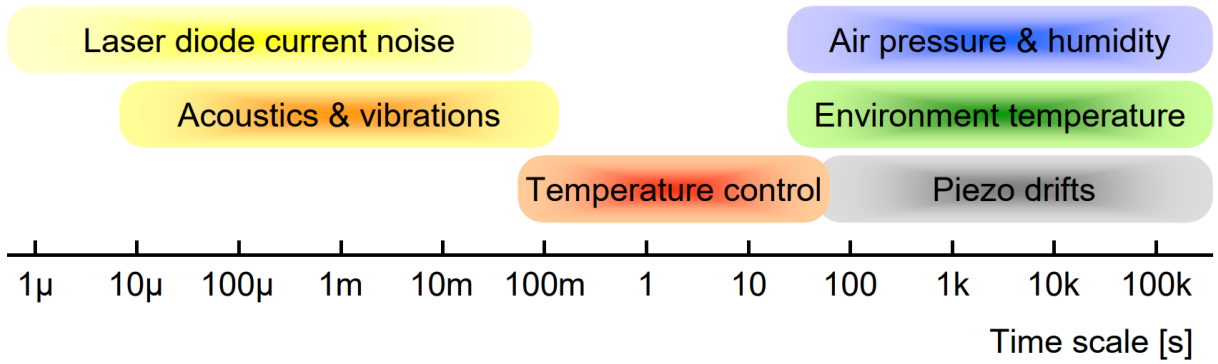

Figure 6.4: Sources of laser frequency fluctuation, with associated timescales. From toptica Appl-1012 notes.

Laser	Locking Mechanism
780 nm Repumper	Saturated Absorption Spectroscopy
795 nm Optical Pumping	Saturated Absorption Spectroscopy
420 nm Rydberg Excitation	Cavity Locking - Direct Current Modulation
1012 nm Rydberg Excitation	Cavity Locking - EOM Phase Modulation
780 nm Cooling, Imaging, Excitation, Pushout	Offset Phase Locking
1012 nm Ti-Sapphire Trapping Laser	Wavemeter Locking

Table 6.1: Summary of different locking mechanisms used in the experiment

the gain profile for $\Delta L_D = 0.012\ \mu m$, where the emission wavelength is $\lambda_{\text{emission}} = 780.24$ nm , the transition wavelength of the D_2 line in ^{87}Rb .

6.2 Frequency Stabilization

Without active stabilization of frequency and intensity, lasers exhibit a variety of noise all of which may have detrimental effects on the experiment. Figure 6.4 shows the main sources of laser frequency fluctuation, and their relevant timescales. In this section, we describe the underlying principles and techniques for employing active feedback to our lasers.

In our lab, we utilize several mechanisms for stabilizing the frequency of the laser, some of which are listed in table 6.1. While the reference source is different in each of the mechanisms, the underlying principle of applying the derived control signal is similar in each of the approaches. As such I will describe in detail the principle of PDH locking using the resonance spectrum of a cavity as an illustrative example.

6.3 Pound-Drever Hall Technique

6.3.1 Theoretical background

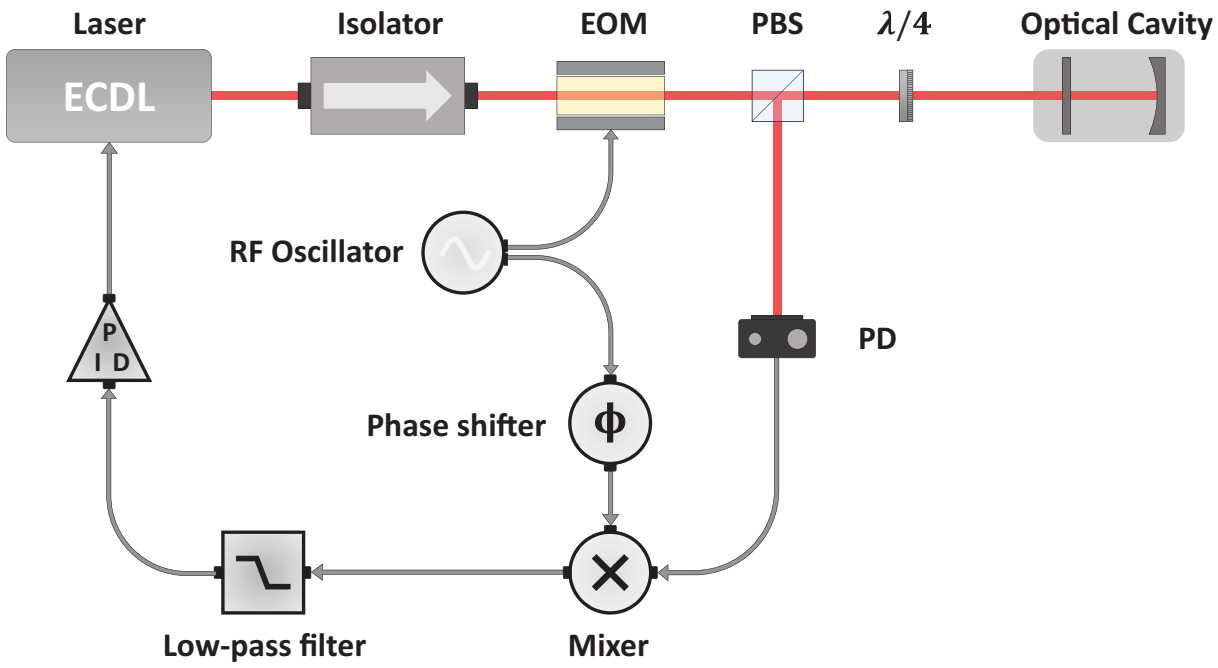

Figure 6.5: Simplified diagram for PDH locking.

Now that we understand one mechanism for modulating the frequency of the laser, we will turn our attention to the most general strategy for stabilizing the laser. The next ingredient to implement the feedback is to be able to have a error signal whose amplitude is proportional to the frequency difference between the laser and the frequency reference. To do this, we will use the example of a high-finesse optical cavity to derive our error signal. To understand why an optical cavity can act as a frequency reference, we need to look at the transmission function of the optical cavity. As one might recall, the optical cavity is simply a pair of mirrors in which light can bounce back and forth within the cavity. As a result of the boundary conditions, light can only pass through the cavity if the round-trip path length is equal to an integer number of wavelengths. An important parameter the defines an optical cavity is the free spectral range $\Delta\nu_{\text{fsr}} = c/2L$,where L is the length of the cavity, and c is the speed of light. If the frequency of the light is an integer multiple of the free-spectral range, then the light is said to be tuned to resonance with the cavity. With this fact, we can use a measurement of either the reflected or transmitted light in order to get a measurement of the frequency of the laser light. In Fig. 6.6I plot cavity transmissions for a finesse $\mathcal{F} = 1$ (red), which is the order of those for laser diode cavities, $\mathcal{F} = 100$ (blue) and a high finesse $\mathcal{F} = 10,000$.

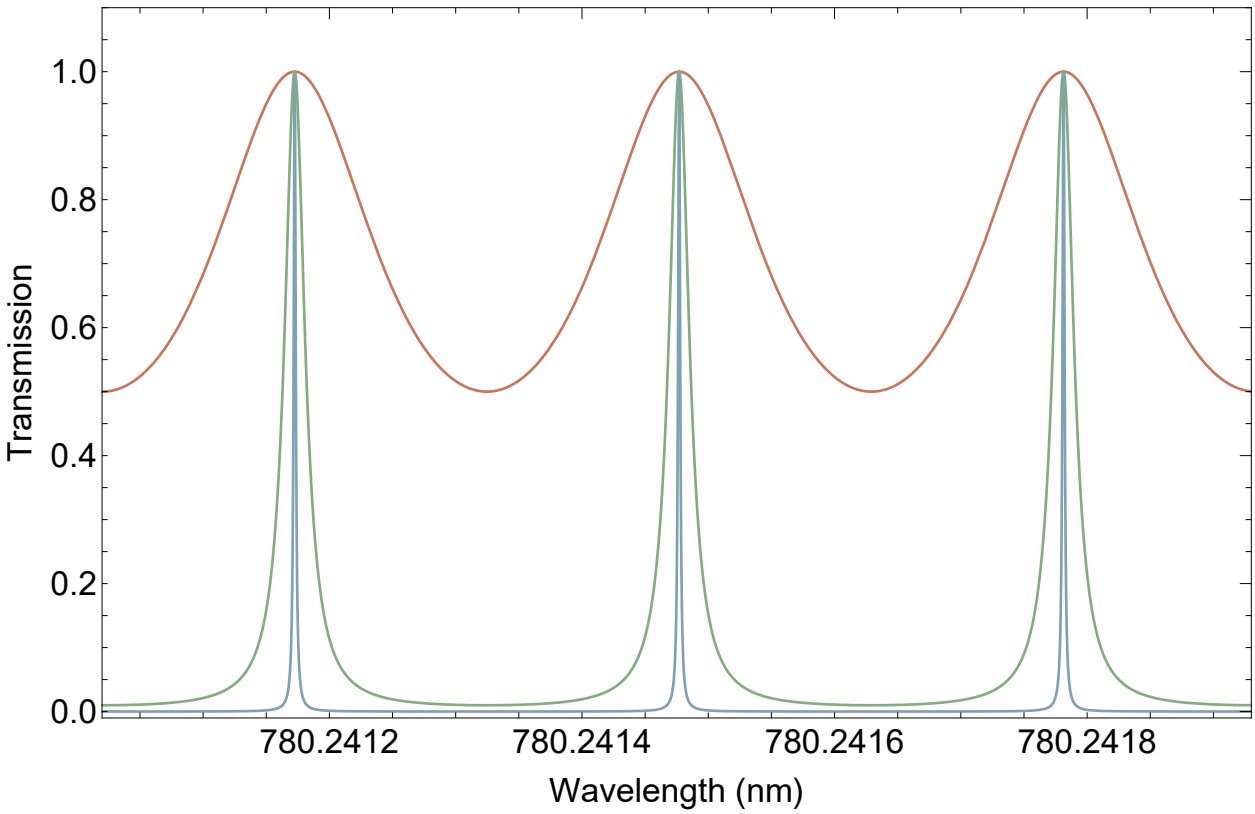

Figure 6.6: Simulation of cavity transmission for $\mathcal{F} = 1$ in red, $\mathcal{F} = 100$ green, and $\mathcal{F} = 10,000$ in blue.

One method of stabilizing the laser frequency is to tune the frequency of the laser to the slope of the transmission function. In this region, as we scan the laser, we can detect the change in the transmitted light in the cavity. If the transmitted intensity increases as we increase the wavelength of the laser field, that indicates that we are to the left of the peak. If the transmitted light decreases as a function of the tuning wavelength, then we are to the right of the peak. With this knowledge, we can generate an error signal that is proportional to the measured power and the desired power. This control signal can then be fed back into the laser to stabilize the power, and as a result the frequency of the incident laser field. This method of frequency locking was used for quite a long time, however an inherent disadvantage to this technique is that it is not possible to distinguish fluctuations of the transmitted power due to frequency shifts of the laser, and inherent amplitude noise present in the laser itself.

One method of decoupling the laser power and frequency fluctuations is to lock the frequency to the resonance position of the cavity. In order to do that, we require a control signal that is an asymmetric function around the resonance. The Pound-Drever-Hall (PDH) locking technique generates such a control signal utilizing phase modulation, measuring the reflected light from the cavity, and demodulation.

The incident electric field before phase modulation is given by

$$E_{\text{inc}} = E_0 e^{i\omega t}$$

The electric field of the reflected beam is given by

$$E_{\text{ref}} = E_1 e^{i\omega t}$$

The reflection coefficient is which is ratio of these amplitudes is given by

$$R(\omega) = \frac{E_{\text{ref}}}{E_{\text{inc}}} = \frac{r\left(\exp\left(i\frac{\omega}{\Delta\nu_{\text{fsr}}}\right) - 1\right)}{1 - r^2\exp\left(i\frac{\omega}{\Delta\nu_{\text{fsr}}}\right)}$$

Now we can incorporate a time-dependent modulation of the phase with a modulation depth β and modulation frequency Ω. As a result the phase-modulated field is written as

$$E_{\text{inc}} = E_0 e^{i(\omega t + \beta\sin\Omega t)}$$

We can expand this expression using Bessel functions by utilizing the Jacobi-Anger expansion that states

$$e^{iz\sin\theta} = \sum_{n=-\infty}^{\infty} J_n(z)e^{in\theta}$$

For the modulation depths that we consider, the electric field can be approximated by just the carrier frequency ($n = 0$) and the two frequency sidebands ($n = -1$,and $n = 1$)

$$E_{\text{inc}} \approx E_0[J_0(\beta)e^{i\omega t} + J_1(\beta)e^{i(\omega+\Omega)t} - J_1(\beta)e^{i(\omega-\Omega)t}]$$

The resulting reflected electric field is given by multiplying the incident electric field by the reflection coefficient. Each of the terms can be treated independently due to the fact that the optical cavity is a linear time-invariant system.

$$E_{\text{ref}} = E_0\left[R(\omega)J_0(\beta)e^{i\omega t} + R(\omega+\Omega)J_1(\beta)e^{i(\omega+\Omega)t} - R(\omega-\Omega)J_1(\beta)e^{i(\omega-\Omega)t}\right]$$

As a result, the reflected power is given by

$$\begin{aligned} P_{\text{ref}} = |E_{\text{ref}}|^2 &= P_c|R(\omega)|^2 + P_s\{|R(\omega+\Omega)|^2 + |R(\omega-\Omega)|^2\} \\ &+ 2\sqrt{P_cP_s}\{\text{Re}[\Theta(\omega)]\cos\Omega t + \text{Im}[\Theta(\omega)]\sin\Omega t\} + (2\Omega \text{ terms}) \end{aligned}$$

where Θ is defined as

$$\Theta = R(\omega)R^*(\omega+\Omega) - R^*(\omega)R(\omega-\Omega)$$

The time-averaged power is shown in Figure 6.7 for a modulation frequency $\Omega = 50$ MHz, reflectivity $r = 0.99$, cavity length $L = 100$ cm and modulation depths $\beta = 0$, 0.5 and 1.08. As the modulation depth is increased, the amount of power in the red ($n = -1$) and blue ($n = 1$) frequency sidebands is increased.

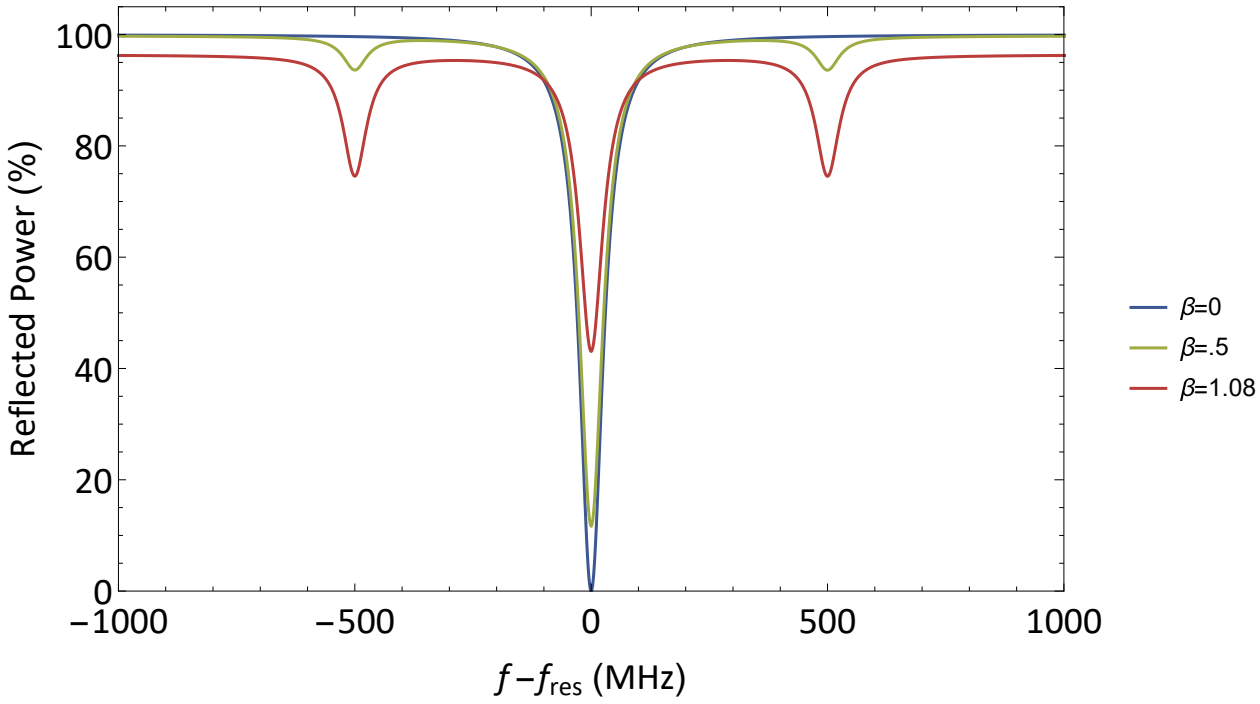

Figure 6.7: Reflected power for $r = 0.99$, $\Omega = 50$ MHz, modulation depths of $\beta = 0, 0.5$,and 1.08 in blue, green, and red, respectively.

The quantity of interest that will be used for the control signal is Θ, which is an asymmetric function about the cavity resonance. In order to extract this signal from the reflected power, we employ frequency mixing. To do this, we note that the real and imaginary components of the Θ function oscillates with cosine and sine of the modulation frequency, respectively. We can consider two regimes, defined by the modulation frequency. For large modulation frequencies, $(\Omega \gg \Delta\nu_{\text{fsr}}/\mathcal{F})$, Θ is purely imaginary and therefore P_{ref} oscillates at with $\sin(\Omega t)$, whereas for small modulation frequencies, $(\Omega \ll \Delta\nu_{\text{fsr}}/\mathcal{F})$, Θ is purely real and therefore oscillates at $\cos(\Omega t)$. Lets just consider the high modulation frequency case, in order to measure the control signal Θ, we mix the photodiode signal V_{PD} with the a signal that oscillates at Ω' such that $V_{LO} = \cos(\Omega' t)$.

The output port of the mixer simply gives the product of the two inputs, that is

$$V_{\text{mix}} \propto V_{PD} V_{LO}$$
$$V_{\text{mix}} \propto \text{Im}[\Theta(\omega)]\sin(\Omega t)\cos(\Omega' t)$$

Utilizing the trignometric identity

$$\sin(\Omega t)\cos(\Omega' t) = \frac{1}{2}\left\{\sin[(\Omega - \Omega')t] - \sin[(\Omega + \Omega')t]\right\}$$

If we utilize a signal that oscillates at the same frequency as the modulation frequency, that is $\Omega' = \Omega$, then there will have

$$V_{\text{mix}} \propto \frac{\text{Im}[\Theta(\omega)]}{2}\left[\sin(2\Omega t)\right]$$

As one can notice, the signal oscillates at twice the modulation frequency, which is not particularly useful when trying to implement as a feedback signal. Instead, if we consider that mixing signal is $\pi/2$ out of phase with the modulation source, or is a sin function, then we have

$$V_{mix} \propto \text{Im}[\Theta(\omega)]\sin(\Omega t)\sin(\Omega' t)$$

utilizing the trigonometric identity,

$$\sin(\Omega t)\sin(\Omega' t) = \frac{1}{2}\left\{\cos[(\Omega - \Omega')t] - \cos[(\Omega + \Omega')t]\right\}$$

the resulting mixed signal at the output when ($\Omega' = \Omega$) is given by

$$V_{\text{mix}} \propto \frac{\text{Im}[\Theta(\omega)]}{2}\left[1 + \cos(2\Omega t)\right]$$

we can now note that there are two frequency components, one that is a DC signal (non-oscillatory) and one that oscillates at 2Ω. To isolate the DC signal to use for implementing the frequency feedback, we can filter the signal using a low-pass filter with a cutoff that is lower than 2Ω. The only difference between having a DC error signal and a vanishing one is a phase shift of $\pi/2$. In addition, there could be additional phase shifts that could be induced by unequal path lengths between the local oscillator and the modulation source. Therefore it is necessary to have a arbitrary phase-shifter of the local oscillator source.

$$V_{LO} = \cos(\Omega' t + \phi)$$

With the arbitrary phase-shift, the output of the mixer is given by

$$V_{\text{mix}} \propto \text{Re}[\Theta(\omega)]\cos(\phi) + \text{Im}[\Theta(\omega)]\sin(\phi)$$

The resulting measured error signal is shown in Figure 6.8 for varying values of the phase. The optimal phase occurs when $\phi = \pi/2$, as the slope used for feedback is the largest near resonance.

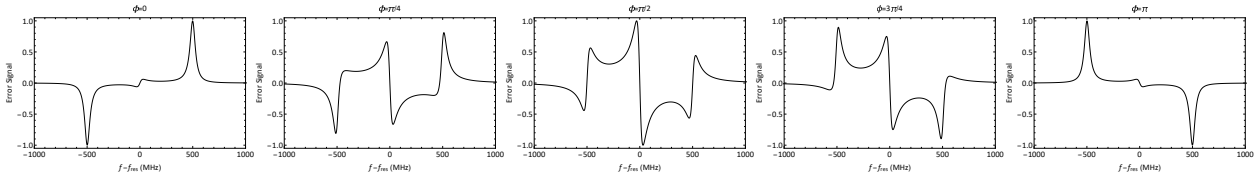

Figure 6.8: PDH error signal for various phase-shifts. The optimal error signal occurs at $\phi = \pi/2$. Due to signal delays that occur in the experimental implementation, the optimal phase needs to be empirically found to match the shape shown in the middle panel.

6.3.2 Matching the cavity mode to the output of a single-mode optical fiber

In order to ensure that that the reflection dip is maximized, we need to optimize the input mode into the optical cavity. That is, we need to match the principal mode of the optical cavity. Due to the boundary conditions imposed by the mirrors that form the cavity, the fundamental standing wave modes are given by Hermite-Gaussian Modes. Their electric field profile is given by

$$E_{nm}(x,y,z) = E_0 \frac{w_0}{w(z)} H_n\left(\sqrt{2}\frac{x}{w(z)}\right) \exp\left(-\frac{x^2}{w(z)^2}\right) H_m\left(\sqrt{2}\frac{y}{w(z)}\right) \exp\left(-\frac{y^2}{w(z)^2}\right)$$
$$\exp\left(-i\left[kz - (1+n+m)\text{arctan}\left(\frac{z}{z_R}\right) + \frac{k(x^2+y^2)}{2R(z)}\right]\right)$$

Where H_n is the Hermite polynomial. In Figure 6.9 I show the transverse intensity profiles of the first 9 Hermite-Gaussian modes at the focus, that is $z = 0$. One thing to note is that the lowest order mode, the TEM $_{00}$ mode is simply that of a Gaussian mode, the intrinsic mode that propagates through single-mode optical fibers. Using this fact, we only need to match the intrinsic beam waist and divergence of the cavity.

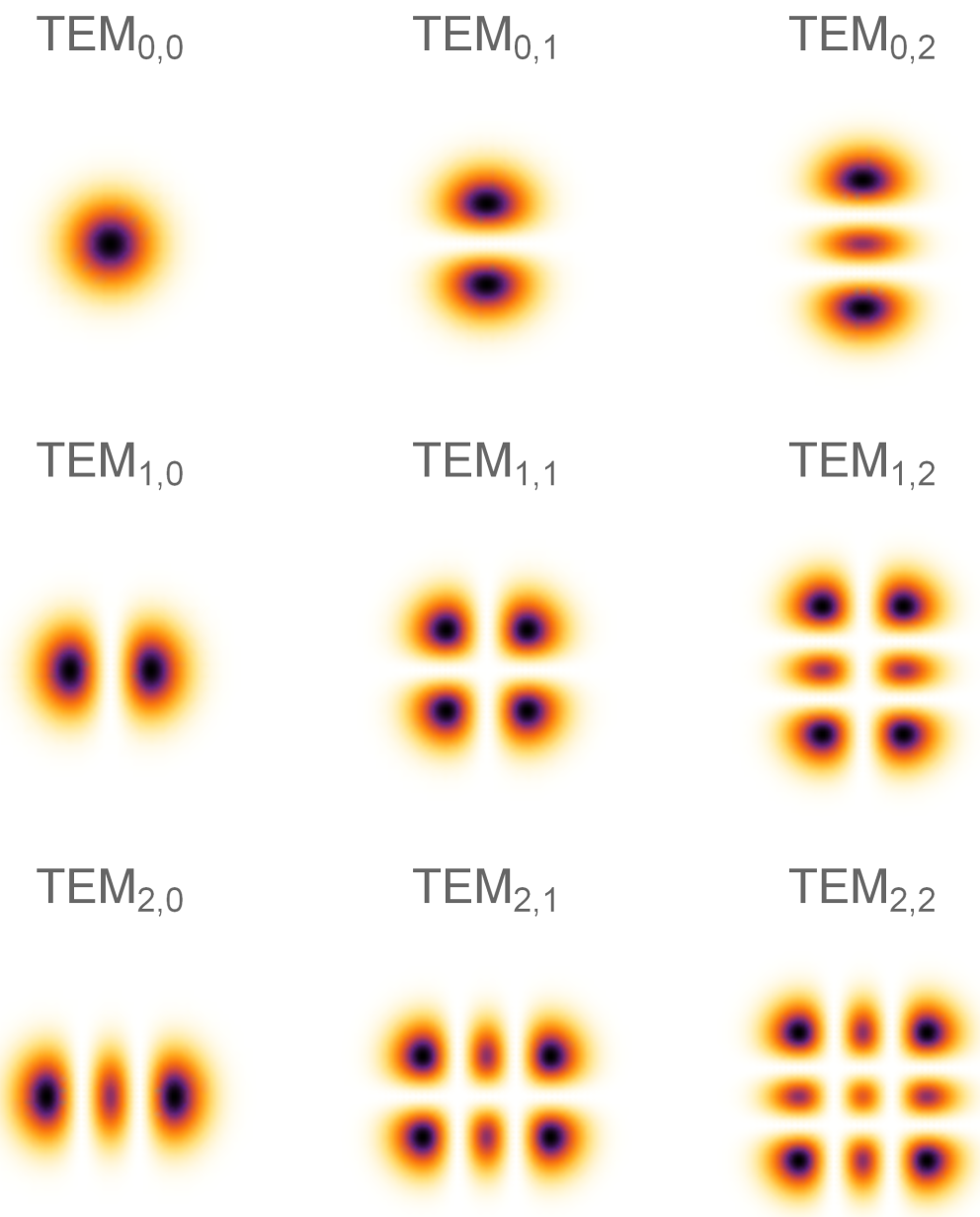

Figure 6.9: TEM modes of the optical cavity. The fundamental TEM_{00} matches the Gaussian output of a single-mode fiber, and will have the largest coupling efficiency.

To do so, it's important to note that our cavity is a half-symmetric planar concave cavity, and therefore have stable standing-wave modes with waist that are located at the planar mirror. To determine the waists w_1 and w_2 at the planar and curved mirror surfaces respectively, we utilize the following equations

$$w_1^2 = \frac{L\lambda}{\pi}\sqrt{\frac{g}{1-g}},$$
$$w_2^2 = \frac{L\lambda}{\pi}\sqrt{\frac{1}{g(1-g)}},$$

where L is the length of the cavity, λ is the wavelength of the light, and g is related to the geometry of the mirror and defined as

$$g = 1 - \frac{L}{R_2}$$

where R_2 is the radius of curvature of the mirror. For the parameters $L = 10$ cm , $R_2 = 50$ cm, and $\lambda = 420$ nm, we get

$$w_1 = 163.5\ \mu\text{m}$$
$$w_2 = 182.8\ \mu\text{m}$$

Now the beam divergence is given by

$$\theta = \frac{\lambda}{\pi n w_1} = 0.818 \text{ mrad.}$$

To match this divergence, we can choose the focal length of the lense before the cavity and the input beam size. Based on our optical setup, a 50cm lens was the most convenient, and therefore the the input beam waist can be given by

$$w_i = f_{\text{cavity}}\theta \approx 408.8\ \mu\text{m}$$

To achieve this beam waist at the position of the 50 cm lense, we can choose the appropriate fiber collimation lens by

$$f_{\text{coll}} = \frac{w_i}{\theta_{\text{fiber}}}$$

where θ_i is the angular divergence out of the fiber. For the majority of the fibers used in the lab, $\theta_{\text{fiber}} = 0.12$ rad. This gives us an optimal collimation lens of $f_{\text{coll}} \approx 3.4$ mm. The closest available match comes from a molded glass aspheric lens (N414TM-A) from Thorlabs with an effective focal length of 3.3 mm.

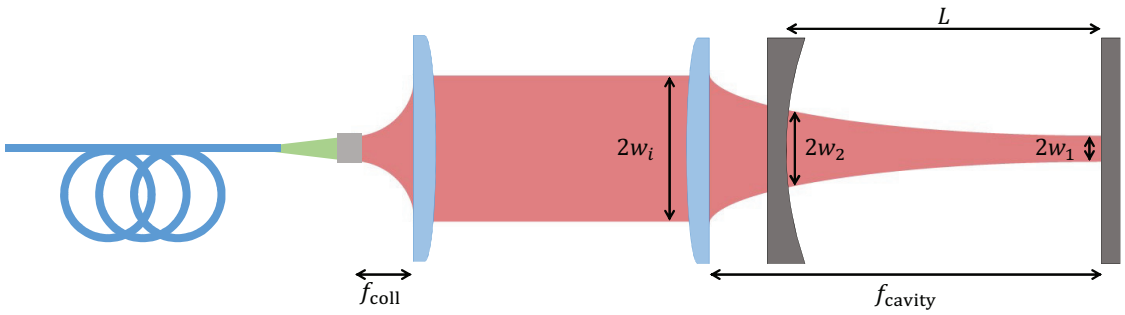

Figure 6.10: Simplified diagram of an optical setup to match the output mode of a single-mode fiber to the intrinsic TEM_{00} mode of the optical cavity.

6.3.3 Procedure for alignment

After choosing the proper choice of the mode-matching optics, the next step is to align the input beam into the optical cavity. To do this, perform the following steps:

1. Make sure that the reflected light is perfectly retroreflected and centered at the opening aperature of the cavity enclosure.

2. Monitor the reflectance spectrum via a photodiode and oscilliscope.

3. Set the frequency scan range of the laser to maximum.

4. Walk the two mirrors in the optical setup until a dip is observed in the cavity reflectance spectrum.

5. There may be multiple dips observed. Continue walking the mirrors to optimize the dip size. You may notice that there is a dip that is much larger than the rest. This may be the TEM_{00} mode.

6. To check if this in fact the TEM_{00} mode, position a CCD camera at the opposite end of the cavity to detect the spatial mode of the transmitted beam.

7. Reduce the frequency span of the laser such that the dip in question is at the center.

8. Check the spatial mode of the transmitted light. If the output mode is gaussian, then you have identified the TEM_{00} mode. If it is a higher order mode, return to step 5.

9. If it is the TEM_{00} mode, then continue optimizing the alignment as well as the output fiber coupler.

CHAPTER 7

Long-Lived Coherence Between Ground and Rydberg Levels in a Magic-Wavelength Lattice

7.1 Introduction

Ground-Rydberg state coherence in ensembles of ultra-cold atoms plays a critical role in many quantum information, quantum communication, and precision metrology protocols [4, 5, 6, 7, 8, 9, 10, 11]. Single-photon generation [12], photon anti-bunching [13], many-body Rabi oscillations [14], creation of entanglement of light and atomic excitations [15], single-photon optical switches and interaction-induced phase shifts [16, 17, 18, 19, 20] have been demonstrated based on coupling of ensembles of neutral atoms with propagating quantum light fields. Significant progress has also been made in employing Rydberg interactions for entanglement [21, 22, 23], many-body interferometry [24], and quantum simulation in arrays of neutral atoms [25]. All these experiments have relied on quantum coherence between the ground and Rydberg states. Prolonging this coherence lifetime is therefore crucial to further advances in increasing the size and complexity of quantum algorithms and the precision of atomic measurements.

Several physical processes contribute to ground-Rydberg decoherence, including spontaneous decay, black-body radiation, and coupling to stray electric fields [4]. In the majority of experiments to date, however, the loss of coherence can be attributed mainly to motional dephasing, limiting the coherence lifetime to a few microseconds [12, 14, 21, 22, 23, 25]. Motional dephasing can be reduced by tightly confining the atoms in an optical dipole trap. Unfortunately, while typical off-resonant dipole traps are attractive for ground state atoms, they are repulsive for atoms in Rydberg levels. This results in fast decoherence owing to position-dependent differential energy shifts, making it necessary to turn off the trapping fields for the duration of the Rydberg excitation period. To overcome this problem, the trapping fields can be tuned to a so-called "magic" wavelength [26, 27] that results in identical energy shifts for the ground and Rydberg state [15, 28]. The magic wavelength is close to that of the Rydberg level $|ns_{1/2}\rangle$ - intermediate level $|6p\rangle$ transition.

In this work we exploit the use of the magic wavelength to obtain a significant enhancement of ground-Rydberg atomic coherence lifetimes over a range of principal quantum numbers $n = 30 \ldots 70$. This is achieved by confining the atomic sample in a one-dimensional, state-insensitive optical lattice along the axis of propagation of the excitation light fields. We observe damped oscillations of the collective ground-Rydberg atomic coherence in the lattice potential. The anharmonicity of the potential leads to a damping of the visibility of the oscillations, whereas the radiative decay and black-body radiation-driven depopulation of the Rydberg state lead to a damping of the overall signal.

A second component of this paper is the formulation of a theory that can be used to explain the overall features of the experimental data. A first principles calculation of the signal presents considerable challenges, even when interactions between Rydberg atoms can be neglected. The reason for this is that standard methods [29] involving the use of the Maxwell-Bloch equations or a source-field approach are no longer applicable when the atoms undergo quantized motion in the trap potentials. Moreover, if the trap potentials differ for the Rydberg and ground state potentials, any approach assuming classical motion in the potentials fails if the signal depends on the coherence between these levels. There *have* been theories of phased-matched emission from trapped atoms that have been developed in the context of atom interferometry [30], but the formalisms used in those approaches differ somewhat from what is needed in our problem involving excitation of Rydberg levels. More closely related to our calculations are those of Zhao *et al.* [31] and Jenkins *et al.* [32] who considered phase-matched emission from trapped atoms using Raman transitions. Jenkins *et al.* [32] used a model in which the atoms undergo classical motion in a lattice potential. In contrast to these authors, we present a theory that treats the atomic motion in the lattice quantum-mechanically and allows for different Rydberg and ground state potentials. We first present a theoretical formalism that can be used to model our system and then describe its experimental implementation.

7.2 Theory

There are essentially three ingredients needed to calculate the signal. First the ground and Rydberg state potentials produced by the trap fields must be obtained. Second, the contribution to the signal at the detector produced by a single atom needs to be derived. Finally, a weighted sum over the contributions from atoms at different points in the trap potential and an average over the thermal distribution in the sample must be carried out. Each atom is modeled as a three-level system with level 1 corresponding to the ground state, level 2 to the $6p_{3/2}$ state, and level 3 to the ns state, as shown in Fig. 7.1. The atom interacts with both a classical two-photon pulse at time $t = 0$ and a classical readout pulse at time T_s. The applied pulses propagate in the $\pm X$ direction. The first pulse

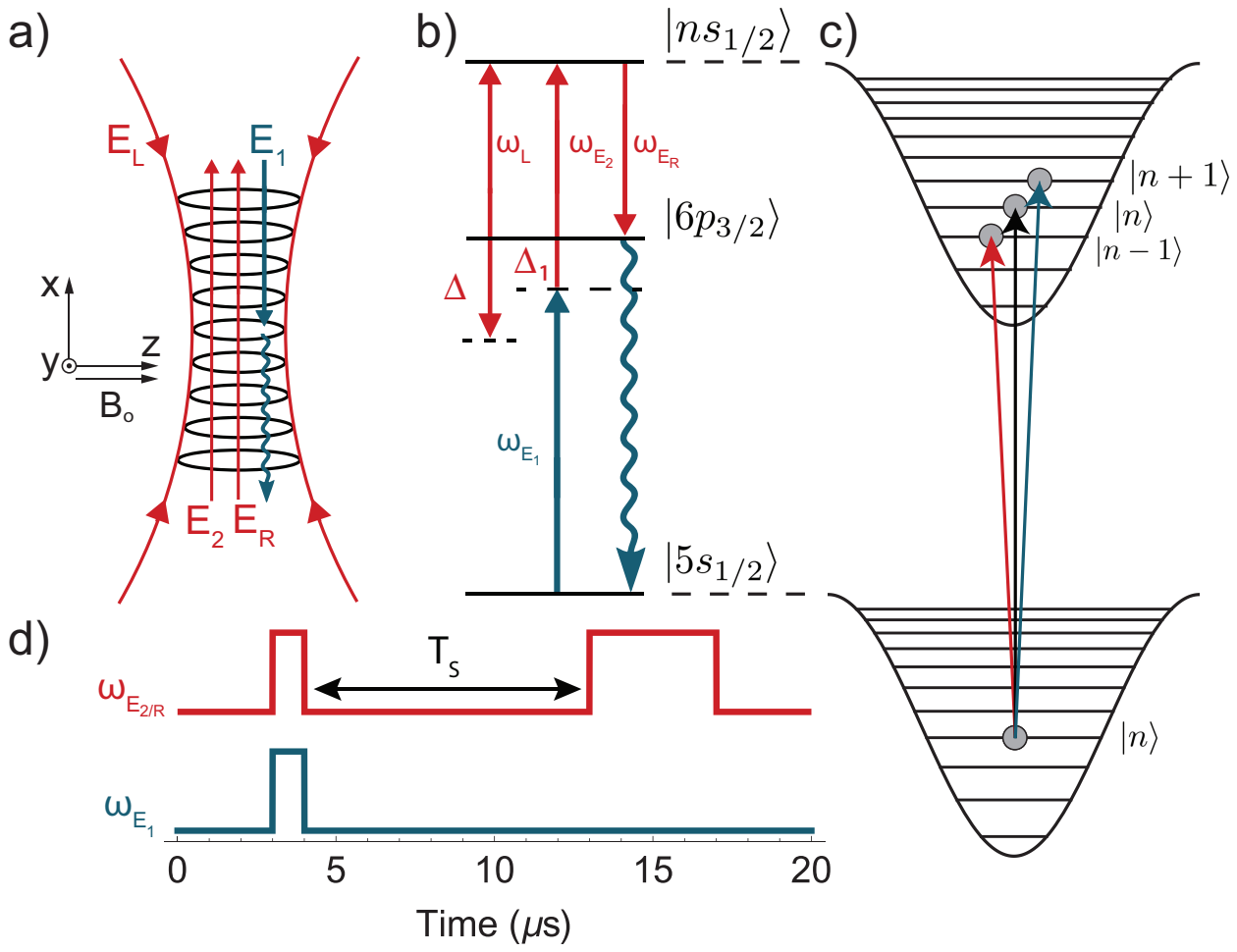

Figure 7.1: (Color online) a) A cold sample of ^{87}Rb gas is trapped in a 0.5-μm-period one-dimensional optical lattice formed by a retro-reflected beam E_L. Two nearly counter-propagating beams, E_1 and E_2 excite a spin wave between the $|5s_{1/2}, F = 2\rangle$ and $|ns_{1/2}\rangle$ levels. After a storage time, T_s, a retrieval pulse, E_R, is applied, creating an array of atomic dipoles which give rise to a phase-matched emission from the sample. The actual geometry used in the experiment differs somewhat from that shown schematically in the figure. b) Relevant ^{87}Rb energy levels and corresponding fields, with $\Delta = \omega_L - \omega_{ns,6p_{3/2}}$ and $\Delta_1 = \omega_{E_2} - \omega_{ns,6p_{3/2}}$. c) Schematic diagram indicating transitions between the ground and excited state motional levels. d) Timing diagram showing the excitation and retrieval pulse sequence.

has effective **k** vector $(k_{E_1} - k_{E_2})\,\mathbf{u}_x$ and effective two-photon frequency $\omega_{E_{31}} = \omega_{E_1} + \omega_{E_2}$, while the readout pulse has **k** vector $-k_R\mathbf{u}_x$ and frequency $\omega_R \approx \omega_{E_2}$. As a result of these interactions and the interaction with the vacuum field, a phase-matched signal is generated from the sample. There is a trap potential formed by fields counterpropagating in the X direction having wavelength $\lambda_L = 2\pi/k_L = 2\pi c/\omega_L$. The detuning of the trap field frequency from the $ns - 6p_{3/2}$ transition frequency is denoted by Δ. The motion of the atoms in the potential wells in the longitudinal

direction is treated quantum-mechanically, while the motion in the transverse trap potential is treated classically. It is assumed that all the atoms are trapped - transitions to continuum states are not taken into account. Moreover, we neglect any modifications of the signal resulting form Rydberg atom - Rydberg atom interactions.

7.2.1 Optical Potentials

We need not consider the optical potential associated with state $|2\rangle$ since it drops out of the calculation of the phase-matched signal. To arrive at expressions for the optical potentials for states $|1\rangle$ and $|3\rangle$, we write the $y-$polarized trap electric field amplitude as

$$\begin{aligned} E(\mathbf{R},t) &= \frac{1}{4}\left[A_+(\rho,X)e^{ik_LX} + A_-(\rho,X)e^{-ik_LX}\right]e^{-i\omega_Lt} \\ &\quad +\text{c.c.}, \end{aligned} \tag{7.1}$$

where

$$A_\pm(\rho,X) = E_{\pm,0}\frac{w_{\pm,0}}{w_\pm(X)}e^{-\rho^2/w_\pm^2(X)}, \tag{7.2}$$

ρ is the coordinate transverse to X, $E_{\pm,0}$ are the field amplitudes for the fields propagating in the $\pm X$ directions that constitute the trap, $w_{\pm,0}$ are the waist radii of these fields,

$$w_\pm(X) = w_{\pm,0}\sqrt{1+\frac{(X-X_{\pm,0})^2}{X_{\pm,r}^2}}, \tag{7.3}$$

$X_{\pm,r,} = \pi w_{\pm,0}^2/\lambda_L$ are Rayleigh lengths, and $X_{\pm,0}$ are the positions of the foci of the $\pm$ beams. We have allowed for unbalanced beams, that is, the beams propagating in the $\pm X$ directions can have different waists and be centered at different positions.

The time-average field intensity is proportional to

$$\left|\bar{E}(\mathbf{R})\right|^2 = \frac{1}{8}\left[4A_+A_-\cos^2(k_LX) + (A_+ - A_-)^2\right]$$

and results in both a transverse ("non-lattice") trap potential that is independent of X and a longitudinal ("lattice") $\cos^2(k_LX)$ trap potential. The non-lattice potential, which trap the atoms transversely, also results in a spatially dependent light shift that limits the coherence time of the signal. The position of the Rydberg electron in a single atom can be taken as $\mathbf{R}+\mathbf{r}$, where $\mathbf{R} = (\rho, X)$ is the center-of-mass position vector of the atom and $\mathbf{r}$ its relative electronic coordinate.

The ground state optical potential, calculated in dipole approximation, is

$$\begin{aligned} U_g &\approx -\frac{1}{2}\alpha_g \left|\bar{E}(\mathbf{R})\right|^2 \\ &= -\frac{1}{16}\alpha_g \left[4A_+A_- \cos^2(k_L X) + (A_+ - A_-)^2\right], \end{aligned} \tag{7.4}$$

where α_g is the ground state polarizability.

To find the optical potential associated with an atom in the Rydberg state ns, we break up the interaction potential into a term representing the $\mathbf{A}\cdot\mathbf{p}$ contribution and one representing the A^2 contribution, where $\mathbf{p}$ is the momentum operator associated with the Rydberg electron and $\mathbf{A} = A(\mathbf{R},t)\mathbf{u}_y$ is the vector potential (which has the same polarization as the electric field) given by

$$\begin{aligned} A(\mathbf{R},t) &= \frac{ie^{-i\omega_L t}}{4\omega_L}\left[A_+(\rho,X)e^{ik_L X} + A_-(\rho,X)e^{-ik_L X}\right] \\ &\quad +\text{c.c.}. \end{aligned}$$

For the $\mathbf{A}\cdot\mathbf{p}$ term can we use the dipole approximation since the major contribution to the sum that determines this contribution originates from the $6p$ intermediate states; however, for the A^2 term we do *not* make the dipole approximation and set

$$\theta_n = \langle \cos(2k_L x)\rangle_{ns} \tag{7.5}$$

and $\langle \sin(2k_L x)\rangle_{ns} = 0$, where the average is over electronic coordinates in the ns state. The total optical potential in the ns state can then be written as [33]

$$\begin{aligned} U_n \approx &-\frac{1}{16}\left[\begin{array}{c} 4A_+(\rho,X)A_-(\rho,X)\cos^2(k_L X) \\ +(A_+ - A_-)^2 \end{array}\right] \\ &\times\frac{e^2}{\hbar}\sum_{m\neq n}\frac{2\left|y_{mn}\right|^2\omega_{mn}}{\omega_{mn}^2-\omega_L^2}\left(\frac{\omega_{mn}}{\omega_L}\right)^2 \\ &+\frac{|\alpha_f|}{16}\left[\begin{array}{c} 4\theta_n A_+A_-\cos^2(k_L X) + (A_+ - A_-)^2 \\ +2A_+A_-(1-\theta_n) \end{array}\right], \end{aligned} \tag{7.6}$$

where the first term is the $\mathbf{A}\cdot\mathbf{p}$ contribution and second the A^2 contribution. The quantity $\alpha_f = -e^2/m\omega_L^2$ is the free electron polarizability. For the detunings $\Delta/2\pi \lesssim 4.5$ GHz used in our experiment, the dominant contribution to the summation appearing in Eq. (7.6) originates from

the intermediate $6p_{3/2}$ levels (the $6p_{3/2} - 6p_{1/2}$ transition frequency is about 2.3 THz). As a consequence, we can approximate

$$\frac{e^2}{\hbar}\sum_{m\neq n}\frac{2\left|y_{mn}\right|^2\omega_{mn}}{\omega_{mn}^2-\omega_L^2}\left(\frac{\omega_{mn}}{\omega_L}\right)^2 \approx \frac{D_n^2}{6\hbar\Delta}, \tag{7.7}$$

where

$$D_n = \left|\langle ns||\hat{d}||6p_{3/2}\rangle\right| \tag{7.8}$$

is a reduced matrix element of the dipole moment operator $\hat{\mathbf{d}}$.

From Eqs. (7.4) and (7.6), it then follows that the lattice potentials for levels 1 and 3 are

$$U_1^{(l)}(\rho,X) \approx -\frac{1}{4}\alpha_g A_+(\rho,X)A_-(\rho,X)\cos^2\left(k_L X\right); \tag{7.9a}$$

$$\begin{aligned} U_3^{(l)}(\rho,X) = &-\frac{1}{4}A_+(\rho,X)A_-(\rho,X)\cos^2\left(k_L X\right) \\ &\times\left[\frac{D_n^2}{6\hbar\Delta}-\left|\alpha_f\right|\theta_n\right]; \end{aligned} \tag{7.9b}$$

and the non-lattice potentials are

$$U_1^{(nl)} = -\frac{\alpha_g}{16}\left(A_+ - A_-\right)^2; \tag{7.10a}$$

$$\begin{aligned} U_3^{(nl)} = &-\frac{D_n^2}{96\hbar\Delta}\left(A_+ - A_-\right)^2 \\ &+\frac{\left|\alpha_f\right|}{16}\left[2A_+A_-\left(1-\theta_n\right)+\left(A_+-A_-\right)^2\right]. \end{aligned} \tag{7.10b}$$

Experimentally, the detuning Δ can be chosen to equate the lattice potentials of the ground and Rydberg levels; that is, ω_L is adjusted such that

$$\frac{D_n^2}{6\hbar\Delta_{m,n}} = \alpha_g + \left|\alpha_f\right|\theta_n, \tag{7.11}$$

where $\Delta_{m,n}$ is the so-called magic detuning for the ns Rydberg level. In this limit, the difference between the Rydberg and ground state non-lattice potentials is

$$U_d^{(nl)} = U_3^{(nl)} - U_1^{(nl)} = \frac{\left|\alpha_f\right|}{16}\left(1-\theta_n\right)\left(A_+^2+A_-^2\right). \tag{7.12}$$

As we shall see, the non-lattice potential leads to a dephasing of the signal.

The amplitudes $E_{0\pm}$ can be related to the power $P_\pm$ in each of the beams via

$$E_{0\pm} = \sqrt{\frac{16c\mu_0 P_\pm}{\pi w_{\pm,0}^2}}, \tag{7.13}$$

obtained by integrating the time-averaged Poynting vector in the $X = X_{\pm,0}$ planes. It is convenient to define

$$U_0 = \frac{1}{4}\alpha_g \frac{16c\mu_0 P}{\pi}\frac{1}{w_+(0)w_-(0)}, \tag{7.14}$$

where $X = 0$ denotes the position of the atomic cloud center, determined by the position of the MOT, and

$$P = \sqrt{P_+ P_-}. \tag{7.15}$$

For matched ground and Rydberg lattice potentials, the ground and Rydberg state lattice potentials can be written in terms of U_0 as

$$\begin{aligned} U_g^{(l)}(\rho, X) \approx -U_0 \frac{w_+(0)w_-(0)}{w_+(X)w_-(X)} \\ \times e^{-\rho^2/w_+^2(X)} e^{-\rho^2/w_-^2(X)} \cos^2(k_L X) \end{aligned} \tag{7.16}$$

and the differential shift resulting from the non-lattice potential as

$$U_d^{(nl)}(\rho, X) = \hbar\omega_d(\rho, X) = \frac{|\alpha_f|\, U_0}{2\alpha_g}(1 - \theta_n)\, \mathcal{I}(\rho, X), \tag{7.17}$$

where

$$\begin{aligned} \mathcal{I}(\rho, X) = \frac{w_+(0)w_-(0)}{2} \\ \times \left[\sqrt{\frac{1}{\xi}}\frac{e^{-2\rho^2/w_+^2(X)}}{w_+^2(X)} + \sqrt{\xi}\frac{e^{-2\rho^2/w_-^2(X)}}{w_-^2(X)}\right] \end{aligned} \tag{7.18}$$

and $\xi = P_-/P_+$ is the ratio of reflected to incident power. For different ground and Rydberg potentials, Eqs. (7.9) and (7.10) must be used for the lattice and non-lattice potentials, respectively.

In our experiment, the atomic cloud is centered at $X = 0$ and

$$\begin{aligned} w_{+,0} = 33\ \mu\text{m}; \quad w_{-,0} = 68\ \mu\text{m}; \\ X_{+,0} = 7.9\ \text{mm}; \quad X_{-,0} = 23.9\ \text{mm}; \\ X_{+,r} = 3.35\ \text{mm}; \quad X_{-,r} = 14.2\ \text{mm}; \\ \lambda_L \approx 1.02\ \mu\text{m}; \quad \xi = 0.73. \end{aligned} \tag{7.19}$$

7.2.2 Signal at the Detector

The signal recorded at a detector located at position $\mathbf{R}_d$ centered at a position along the positive $X-$axis is proportional to the time-integral of the Poynting vector of the phase-matched emission from the sample. The signal S is given roughly by

$$S = 2\epsilon_0 c R_d^2 \int dt \int d\Omega_d \left\langle \mathbf{E}_+(\mathbf{R}_d) \cdot \mathbf{E}_-(\mathbf{R}_d) \right\rangle , \tag{7.20}$$

where the integral is over the solid angle Ω_d subtended by the detector and $\mathbf{E}_\pm(\mathbf{R}_d)$ are the positive and negative frequency components of the electric field operator at the detector. The electric field arises from contributions from all the atoms.

To evaluate S, we must calculate the effects of the excitation field pulse, the retrieval (readout) field pulse, and the vacuum field on each atom and then sum the contribution from all atoms. A weak, two-photon excitation pulse creates an atomic coherence for atom j characterized by a density matrix element $\rho_{31}^{(j)}$ at time $t = 0$. As a result of atomic motion and the non-lattice potential, this coherence undergoes dephasing. At time $t = T_s$, the retrieval pulse, taken as a square pulse that is in resonance with the $3-2$ transition frequency, is applied to create the coherence $\rho_{21}^{(j)}$. The duration of the retrieval pulse is much longer than the lifetime $\tau_2 = 1/\gamma_2$ of level 2. The phase-matched signal emitted by the sample, which results from the interaction of the vacuum field with the atoms, is dependent on the value of $\rho_{21}^{(j)}$ created by the excitation and retrieval fields. If the Rabi frequency of the retrieval field is greater than γ_2, the signal is emitted in a time of order τ_2, which is assumed to be sufficiently short to neglect any dephasing while the signal is being emitted.

Using a calculation based on a source-field approach modified to allow for quantized motion of the atoms in the optical potentials, we find

$$\begin{aligned} S(T_s) = {} & 2\epsilon_0 c \Omega_d \left(\frac{\omega_{21}^2 \mu_{21}}{4\pi\epsilon_0 c^2} \right)^2 \int_0^\infty d\tau \\ & \times \left| \begin{array}{c} \sum_j \sum_{q,q',q''}^{q_{\max}} \left(A_{31}^{(j)}/2 \right) \tilde{Q}^{(j)}(\tau)\, e^{-i\omega_d^{(j)} T_s} \rho_{1q'',1q'}(0) \\ \times M_{1q';3q}^{(j)}(-k\mathbf{u}_x)\, M_{3q;1q''}^{(j)}(k\mathbf{u}_x)\, e^{i\left(\omega_{q'}^{(j1)} - \omega_q^{(j3)}\right) T_s} \end{array} \right|^2 , \end{aligned} \tag{7.21}$$

where $k = (k_{E_1} - k_{E_2})$, μ_{21} is a dipole moment matrix element (it is assumed that the excitation and retrieval pulses are $z-$polarized - the dipole moments that enter are also in the $z-$direction), $A_{31}^{(j)} = \int_{-\infty}^{\infty} \Omega_{31}^{(j)}(t) dt$ is the pulse area of the excitation pulse whose two-photon Rabi frequency is denoted by $\Omega_{31}^{(j)}(t) = \Omega_{E_1}^{(j)}(t)\Omega_{E_2}^{(j)}(t)/(2\Delta_1)$, $\rho_{qq'}(0)$ is an initial density matrix element for the

motional lattice trap states, $\omega_d^{(j)}$ is given by

$$\omega_d^{(j)} = \left[U_3^{(nl)(j)} - U_1^{(nl)(j)}\right]/\hbar, \tag{7.22}$$

$$\tilde{Q}^{(j)}(\tau) = \frac{\Omega_{32}^{(j)}}{\sqrt{\Omega_{32}^{(j)2} - \gamma^2}} e^{-\gamma\tau/2} \sin\left[\frac{\sqrt{\Omega_{32}^{(j)2} - \gamma^2}}{2}\tau\right], \tag{7.23}$$

$$\begin{aligned} M_{3q;1q'}^{(j)}(\mathbf{k}) &= \int dX_j \left[\psi_{3q}(X_j)\right]^* e^{i\mathbf{k}\cdot\mathbf{R}_j} \psi_{1q'}(X_j) \\ &= \left[M_{1q';3q}(-\mathbf{k})\right]^*, \end{aligned} \tag{7.24}$$

$\Omega_{32}^{(j)} = \Omega_R^{(j)}$ is the Rabi frequency of the retrieval pulse, $\psi_{\alpha q}(\mathbf{R}_j)$ is an eigenfunction and $\hbar\omega_q^{(j\alpha)}$ an eigenvalue for atom j moving in the potential $U_\alpha^{(j)}(X)$ ($\alpha = 1, 3$) given in Eqs. (7.9), $U_3^{(nl)(j)}$ ($\alpha = 1, 3$) are the non-lattice potentials given in Eqs. (7.10), and all field strengths and frequencies now include the variation of field strength with location in the sample, indicated by the superscript (j). The sums over q, q', q'' are restricted to (quasibound) states; that is, $q_{\max}$ is the number of bound states in the potential.

7.2.3 Final Expression for the Signal

The numerical calculation of $S(T_s)$ is time-consuming, since the sum over j in Eq. (7.21) must be carried out for each τ, the result squared, and then integrated over τ. To simplify matters, we assume that $\tilde{Q}^{(j)}(\tau)$ can be approximated as a function of τ times $\Omega_{32}^{(j)}$. We have verified that such an an assumption lead to errors of at most 10% in the non-lattice potential contributions to $S(T_s)$ for times $T_s \lesssim 40.\ \mu$s. With this assumption, the signal at time T_s normalized to that at $T_s = 1\ \mu$s, can be written as

$$\eta(T_s) = G(T_s)/G(T_s = 1\mu s); \tag{7.25}$$

where

$$\begin{aligned} G(T_s) &= \left|\int_{-\infty}^{\infty} dX \int_0^{\infty} \rho d\rho f(\rho, X)\mathcal{N}(\rho, X)C(\rho, X, T_s)\right|^2 \\ &\quad \times e^{-T_s/\tau_{eff}}, \end{aligned} \tag{7.26}$$

$$C(X,\rho,T_s) = \sum_{q,q',q''}^{q_{\max}} e^{-i\omega_d(\rho,X)T_s}\rho_{1q'',1q'}(0)$$
$$\times M_{1q';3q}\left[-k\mathbf{u}_x\right] M_{3q;1q''}\left[k\mathbf{u}_x\right] e^{i\left(\omega_{q'}^{(1)}-\omega_q^{(3)}\right)T_s}, \tag{7.27}$$

where $\mathcal{N}(\rho,X)$ and τ_{eff} are the atomic density distribution and the effective lifetime of the Rydberg level, respectively. The frequencies $\omega_{q'}^{(1)}$ and $\omega_q^{(3)}$ are implicit functions of ρ and X. The sum over j has been converted to a spatial integral over the sample.

The distribution $f(\rho,X)$ appearing in Eq. (7.26) is equal to the product of the spatially dependent envelopes of the excitation and retrieval electric field amplitudes, namely

$$f\left(\rho,X\right) = \left(\frac{w_{E_1,0}}{w_{E_1}(X)}\right)\exp\left[-\frac{\rho^2}{w_{E_1}^2(X)}\right]$$
$$\times\left\{\left(\frac{w_{E_2,0}}{w_{E_2}(X)}\right)\exp\left[-\frac{\rho^2}{w_{E_2}^2(X)}\right]\right\}^2, \tag{7.28}$$

where $w_{i,0}$ are the transverse waists of the beams at the foci, $w_i(X) = w_{i,0}\sqrt{1+\left(\frac{X}{X_{ri}}\right)^2}$, and X_{ri} is the Rayleigh length for beam i (we have taken equal Rayleigh lengths for fields E_2 and E_R). In our experiment,

$$w_{E_1,0} = 17\ \mu\text{m}; \qquad w_{E_2,0} = 15\ \mu\text{m}. \tag{7.29}$$

To obtain the Boltzmann factor for the transverse confinement, we need to evaluate the transverse trap potential. The transverse trap potential is actually different for the ground and Rydberg levels. We shall assume that the transverse density distribution is determined by the spatially averaged [that is, with $\cos^2\left(k_L X\right) \to 1/2$] ground state optical potential given in Eq. (7.4),

$$\begin{aligned} U_g\left(\rho,X\right) &\approx -\frac{1}{16}\alpha_g\left[2A_+A_- + \left(A_+ - A_-\right)^2\right] \\ &= -\frac{U_0\mathcal{I}(\rho,X)}{2}, \end{aligned} \tag{7.30}$$

where $\mathcal{I}(\rho,X)$ is given in Eq. (7.18). Moreover, the $\theta \approx 5^\circ$ angle between the excitation beams and the $X-$axis results in an effective length L in the X-direction of the atomic sample that we model using a Gaussian distribution. The transverse and longitudinal effects combine to produce an atomic density profile given by

$$\mathcal{N}\left(\rho,X\right) = \exp\left[\frac{U_0}{2k_BT}\mathcal{I}(\rho,X)\right]\exp\left[-\frac{X^2}{L^2}\right]. \tag{7.31}$$

The factor $C(X,\rho,T_s)$ in Eq. (7.27) is the product of a non-lattice contribution, $e^{-i\omega_d(\rho,X)T_s}$, and

a lattice contribution corresponding to motional dephasing. In principle the motional dephasing term contains ρ and X dependence owing to the spatial dependence of the frequencies $\omega_{q'}^{(1)}$ and $\omega_q^{(3)}$. However for the Rayleigh lengths and waists of the trap fields used in our experiment, it is an excellent approximation to evaluate these frequencies at the center of the sample, $\rho = 0$, $X = 0$. With this approximation the signal factors and can be written as

$$G(T_s) = G_{nl}(T_s) G_l(T_s) e^{-T_s/\tau_{eff}}, \tag{7.32}$$

where

$$G_{nl}(T_s) = \left| \int_{-\infty}^{\infty} dX \int_0^{\infty} \rho d\rho f(\rho, X) \mathcal{N}(\rho, X) e^{-i\omega_d(\rho,X)T_s} \right|^2, \tag{7.33}$$

$$G_l(T_s) = \left| \begin{array}{c} \sum_{q,q',q''}^{q_{\max}} \rho_{1q'',1q'}(0) M_{1q';3q}\left(-k\mathbf{u}_x\right) \\ \times M_{3q;1q''}\left(k\mathbf{u}_x\right) e^{i\left(\omega_{q'}^{(1)} - \omega_q^{(3)}\right)T_s} \end{array} \right|^2, \tag{7.34}$$

and the frequencies $\omega_{q'}^{(1)}$ and $\omega_q^{(3)}$ are obtained as eigenvalues of the potentials

$$U_1^{(l)}(X) = -U_0 \cos^2\left(k_L X\right); \tag{7.35a}$$

$$U_3^{(l)}(X) = -\frac{U_0}{\alpha_g} \cos^2\left(k_L X\right) \times \left[\frac{D_n^2}{6\hbar\Delta} - |\alpha_f|\, \theta_n\right], \tag{7.35b}$$

respectively.

The non-lattice contribution to the signal given in Eq. (7.33) is evaluated numerically. Owing to the fact that ω_d is a function of ρ and X, there is an inhomogeneous broadening in the sample that results in a decrease of $G_{nl}(T_s)$ with increasing T_s. To see the effect of the sample length on $G_{nl}(T_s)$, we plot in Fig. 7.3 (a)

$$g_{nl}(T_s) = G_{nl}(T_s)/G_{nl}(0)$$

for $U_0/k_B = 32$ μK ($U_0/h = 0.666$ MHz), $U_0/k_BT = 2.75$, $|\alpha_f|/\alpha_g = 0.628$, and $L = 1$ μm, 50 μm, 100 μm, 150 μm, and 500 μm. The integral over ρ leads to a decay of $g_{nl}(T_s)$, even for $L = 0$, owing to radial inhomogenities in the non-lattice phase. With increasing L there is an additional contribution to the dephasing from the integral over X. It is evident from the figure that this contribution to the dephasing becomes important for $L \gtrsim 50$ μm.

If the Rayleigh lengths for all the fields are much greater than L and if $w_{\pm}(0) \gg w_{E_{1,2},0}$, it is possible to get an analytic expression for $g_{nl}(T_s)$ that is in excellent agreement with the result

obtained using numerical integration. To do so, we expand

$$\mathcal{I}(\rho, X) \approx \mathcal{I}(0,0) + aX + b\rho^2, \tag{7.36}$$

where

$$a = \left.\frac{d\mathcal{I}(0,X)}{dX}\right|_{X=0}; \tag{7.37a}$$

$$b = \frac{1}{2}\left.\frac{d^2\mathcal{I}(\rho,0)}{d\rho^2}\right|_{\rho=0}, \tag{7.37b}$$

and set $f(\rho, X) \approx f(\rho, 0)$. With these approximations the integrals in Eq. (7.33) can be calculated analytically. In this manner, we find

$$g_{nl}(T_s) \approx e^{-2T_s^2/\tau_X^2} \frac{1}{1 + \frac{T_s^2}{\tau_\rho^2}}, \tag{7.38}$$

where

$$\tau_X = \frac{2}{\frac{|\alpha_f|U_0}{2\alpha_g}(1-\theta_n)\,aL}; \tag{7.39a}$$

$$\tau_\rho = \frac{1}{\frac{|\alpha_f|U_0}{2\alpha_g}(1-\theta_n)\,b} \times \left(\frac{1}{w_{E_1,0}^2} + \frac{2}{w_{E_2,0}^2} - \frac{bU_0}{2k_BT}\right). \tag{7.39b}$$

The Gaussian factor in Eq. (7.38) results from the longitudinal integration and the Lorentzian factor from the transverse integration. Equation (7.38) for $g_{nl}(T_s)$, plotted as the dashed curves in Fig. 7.2(a), is in very good agreement with the values of $g_{nl}(T_s)$ obtained from numerical integration of Eq. (7.33).

From Eqs. (7.39), it follows that the lifetimes decrease with increasing U_0. This feature is seen in Fig. 7.2(b) where $g_{nl}(T_s)$ is plotted for $L = 100$ μm, $|\alpha_f|/\alpha_g = 0.628$, and $U_0/k_B = 5, 10, 20, 40$ μK, with the ratio $U_0/(k_BT) = 2.75$ kept fixed.

The motional dephasing contribution to the signal given in Eq. (7.34) is summed using a thermal ground state distribution

$$\rho_{1q,1q'}(0) = \frac{\exp\left[-\frac{\hbar\omega_q^{(1)}}{k_BT}\right]\delta_{q,q'}}{\sum_{q=0}^{q_{\max}}\exp\left[-\frac{\hbar\omega_q^{(1)}}{k_BT}\right]}, \tag{7.40}$$

where $\delta_{q,q'}$ is a Kronecker delta. The $\omega_q^{(1)}$ are obtained by solving the appropriate Mathieu's equation for the potentials given in Eqs. (7.35), limited to quasi-bound state energies. The matrix elements needed in Eq. (7.34) have been calculated using the corresponding Mathieu wave functions. The values of θ_n used in fitting the data, calculated using a method to be described in the following subsection, are $\theta_n = 0.909, 0.705, 0.334, 0.082, 0.059, -0.013, -0.016$ for $n = 30, 40, 51, 59, 60, 65, 70$.

In Fig. 7.3 we plot

$$g_l(T_s) = G_l(T_s)/G_l(0) \tag{7.41}$$

as a function of $\omega_0 T_s$ for $U_0/k_B = 32$ μK and $U_0/k_B T = 2.75$. The frequency ω_0 is defined by

$$U_0 = \frac{1}{2}\frac{M\omega_0^2}{k_L^2}, \tag{7.42}$$

such that, for large ratios of $U_0/k_B T$ and small values of the trap Lamb-Dicke parameter $\eta_{LD} = k_L\sqrt{\hbar/2M\omega_0}$, the potentials should approximate those of an oscillator. Superimposed on the graph is a plot of $g_l(T_s)$ for oscillator potentials characterized by the same value of ω_0. It can be seen that the anharmonicity both damps the signal and reduces the fringe visibility that which is obtained for harmonic potentials.

The expression for $G_l(T_s)$ can be cast in a suggestive form when the ground and Rydberg potentials are identical. In that limit, Eq. (7.27) reduces to

$$G_l(T_s) = \left|\left\langle e^{-ik\hat{X}(T_s)} e^{ik\hat{X}(0)}\right\rangle\right|^2, \tag{7.43}$$

where $\hat{X}(T_s)$ and $\hat{X}(0)$ are Heisenberg operators and the average is over the quantized motional states of an atom located at cloud center. We can take a classical limit of Eq. (7.43) by ignoring the commutator of $\hat{X}(T_s)$ and $\hat{X}(0)$ and replacing the operators by their classical counterparts, $X(T_s)$ and $X(0)$, to arrive at

$$C_l \sim \left\langle e^{-ik[X(T_s)-X(0)]}\right\rangle, \tag{7.44}$$

where the average is now a classical average over the initial conditions. For our experimental parameters, the classical and quantum results do not differ by more than 10%.

We include three dissipative mechanisms that affect the ground-Rydberg coherence lifetime. The effective population decay lifetime is given by

$$\frac{1}{\tau_{eff}} = \frac{1}{\tau_{6p,n}} + \frac{1}{\tau_n^{(0)}} + \frac{1}{\tau_n^{(bb)}}, \tag{7.45}$$

where $\tau_{6p,n}$, $\tau_n^{(0)}$, and $\tau_n^{(bb)}$ are the contributions from the lattice-induced population decay of the

$6p_{3/2}$ level, Rydberg level decay at zero temperature, and blackbody induced transitions, respectively. Explicitly

$$\begin{aligned}\tau_{6p,n} &= \frac{h\Delta_{m,n}}{U_0}\tau_{6p,0};\\ \tau_n^{(0)} &= \tau^{(0)}(n^*)^{2.94};\\ \tau_n^{(bb)} &= \frac{3\hbar(n^*)^2}{4\alpha_{FS}^3 k_B T},\end{aligned}$$

where $\tau_{6p,0} = 125$ ns, $\tau^{(0)} = 1.43$ ns, $T = 293$ K,

$$n^* = n - 3.13 \tag{7.46}$$

is the effective electronic quantum number, and α_{FS} is the fine structure constant. At low n, the lifetime is limited mainly by spontaneous decay and blackbody transitions. With $n \gtrsim 40$, the dephasing produced by the non-lattice potential begins to reduce the lifetime, an effect that saturates for $n \gtrsim 60$. For still higher values of n, the lattice induced population of the $6p_{3/2}$ begins to play an important role in limiting the coherence lifetime. The reason for this is that the magic detuning $\Delta_{m,n}$ decreases with increasing n.

The data has been fit using Eqs. (7.25), (7.32)-(7.34), (7.40), and (7.45) with $L = 100\mu$m. The potential depth is used as a free parameter to match the oscillation periods of the signals, while the temperature is chosen to match the fringe visibility.

7.2.4 Value of θ_n and Reduced Dipole Moment Matrix Elements

7.2.4.1 Value of θ_n

The polarizability of the Rydberg level is affected by a breakdown of the electric dipole approximation due to the finite size of the Rydberg electron orbital. This landscape factor [33] is calculated by finding the expectation value of the periodic portion of the trap potential $\theta_n = \langle\cos(2k_L x)\rangle$, where k_L is the wave number of the lattice field, and x is the longitudinal position of the electron. To calculate θ_n we perform an expansion of $\cos(2k_L x)$ in spherical Bessel functions to obtain

$$\begin{aligned}\theta_n &= (2l+1)\sum_{l'=even}(2l'^{l'/2-m_z}\begin{pmatrix} l & l' & l\\ -m_z & 0 & m_z\end{pmatrix}\\ &\times\begin{pmatrix} l & l' & l\\ 0 & 0 & 0\end{pmatrix}\int_0^\infty dr_e P_{nl}^2(r_e) j_{l'}(2k_L r_e),\end{aligned}$$

where the $j_{l'}(2k_L r_e)$ are spherical Bessel functions of the first kind and $P_{nl}(r_e)$ are the Rydberg radial wave functions calculated via Numerov integration of the Schrödinger equation using quantum defect potentials. We only consider the $l = 0$ term which simplifies the expression to

$$\theta_n = \int_0^\infty dr_e P_{n,0}^2(r_e) j_0(2kr_e).$$

7.2.4.2 Reduced dipole moment matrix elements

Using Eqs. (7.9), (7.10), and (7.11), we can write the lattice potentials approximately as

$$U_1^{(l)}(X) = -U_0 \cos^2(k_L X); \tag{7.47a}$$

$$U_3^{(l)}(X) = -\frac{U_0}{\alpha_g}\cos^2(k_L X) \times \left[(\alpha_g + |\alpha_f|\,\theta_n)\frac{\Delta_{m,n}}{\Delta} - |\alpha_f|\,\theta_n\right] \tag{7.47b}$$

and the non-lattice potential difference as

$$\begin{aligned}\hbar\omega_d(\rho, X) &= \left[U_3^{(nl)} - U_1^{(nl)}\right] \\ &= \frac{|\alpha_f|\,U_0}{2\alpha_g}(1-\theta_n)\mathcal{I}(\rho, X) \\ &-\frac{U_0}{4}w_+(0)w_-(0)\left(1 + \frac{|\alpha_f|\,\theta_n}{\alpha_g}\right)\left(\frac{\Delta_{m,n}}{\Delta} - 1\right) \\ &\times\left(\xi^{-1/4}\frac{1}{w_+(X)}e^{-\rho^2/w_+^2(X)}{}_+ - \xi^{1/4}\frac{1}{w_-(X)}e^{-\rho^2/w_-^2(X)}\right)^2,\end{aligned} \tag{7.48}$$

where $\Delta_{m,n}$ is the magic detuning for state ns. Owing to the anharmonicity of the potentials and the presence of a non-lattice potential, the local maxima of the signals do not necessarily occur exactly at $\Delta = \Delta_{m,n}$. To extract values for D_n, we find the value of $\Delta_{m,n}$ that gives the best fit to the experimental curves of signal strength versus Δ and then use

$$\frac{1}{6}\frac{D_n^2}{\hbar\Delta_{m,n}} = \alpha_g + |\alpha_f|\,\theta_n. \tag{7.49}$$

to find D_n. The value of D_n is compared with the corresponding value calculated using wave functions obtained using the "Alkali Rydberg Calculator" (ARC) Python package [34]. The ground state polarizability was taken from the paper of Ref. [26].

7.3 Experimental results

The experimental geometry and measurement sequence are shown in Fig. 7.1(a). An optical lattice is formed by a y-polarized, retro-reflected laser field propagating along the x-axis having power $P_+ \approx 0.8$ W. The trap field is generated by a Titanium-Sapphire laser tunable in the 850 nm to 1050 nm range, frequency-locked to an optical cavity. The laser wavelength is measured with a wavemeter calibrated to 10 MHz accuracy using a diode laser locked to Rb 780 nm line. The trap field is detuned from $\omega_{ns,6p_{3/2}}$ by Δ.

Atoms are loaded into the lattice using a magneto-optical trap. The maximum depth of the optical dipole potential at the atoms is $U_0/k_B \approx 40$ μK, with the corresponding axial and radial oscillation frequencies $\{\nu_\rho, \nu_x\} = \{0.3, 86\}$ kHz. The resulting cloud, which has temperature of $T \approx 10$ μK, consists of $\sim 10^5$ ^{87}Rb atoms having radial and axial waists of $\sigma_\rho \approx 50$ μm and $\sigma_X \approx 0.2$ mm respectively. The atoms are optically pumped to the $|5S_{1/2}, F = 2, m_F = 0\rangle$ state in a magnetic bias field $B_0 = 0.5$ mT.

Two nearly counter-propagating, z-polarized fields, E_1 and E_2 excite a spin wave between the $|5s_{1/2}, F = 2\rangle$ and $|ns_{1/2}\rangle$ levels. The fields imprint a spatial phase coherence between the ground and Rydberg states varying as $\propto e^{i(\vec{k}_1+\vec{k}_2)\cdot\vec{R}}$, where $\vec{k}_1$ and $\vec{k}_2$ are the wave-vectors for the fields E_1 and E_2 respectively. Field E_1 has wavelength 420 nm, while field E_2, produced by a laser diode, is tunable in the 1012 nm to the 1026 nm wavelength range to excite Rydberg states with principal quantum numbers $n \geq 30$. Field E_2 is detuned from $\omega_{ns,6p_{3/2}}$ by $\Delta_1 \approx 12$ MHz. The E_1 and E_2 fields are focused onto the atoms with beam waists $w_{E_1,0} \approx 17$ μm and $w_{E_2,0} \approx 15$ μm and Rabi frequencies $\Omega_{E_1}/2\pi \simeq 0.2$ MHz and $\Omega_{E_2}/2\pi \simeq 5$ MHz, respectively. The spin wave is stored for a period T_s varied between 1 and 70 μs. At time T_s the atoms are coherently driven on the $|ns_{1/2}\rangle \leftrightarrow |6p_{3/2}\rangle$ transition by a (z-polarized) retrieval field E_R of Rabi frequency $\Omega_R \approx \Omega_{E_2}$, creating an array of atomic dipoles which give rise to a phase-matched emission from the sample. The emitted light is collected into a single-mode optical fiber coupled to a single-photon detector. To avoid damaging the detectors by the Ω_{E_1} field, a gating acousto-optical modulator is used. The photon transmission and detection efficiency η_{td} is given by $\eta_{td} = \eta_c\eta_o\eta_f\eta_d = 0.13$, where $\eta_c = 0.89$, $\eta_o = 0.39$, $\eta_f = 0.66$ and $\eta_d = 0.55$ are vacuum cell transmission efficiency, optics transmission efficiency (including the gating AOM), fiber coupling efficiency and single photon detection efficiency, respectively. The arrival times of detected photons are recorded, and the number of detected photons per excitation and retrieval cycle is used as our signal.

7.3.1 Magic wavelengths for the $5s - ns$ transition

The normalized retrieval signal $\eta(T_s)$, given by Eq. (7.25), is plotted in Fig. 7.4(a-d) as a function of Δ, along with the experimental data points. The solid green vertical lines represent the values

of the magic detunings $\Delta_{m,n}$ extracted from the fit of the theoretical curves to the data while the dashed red vertical lines represent the values of $\Delta_{m,n}$ obtained using Eq. (7.49) and the ARC values of the dipole matrix elements. The extracted values of $\Delta_{m,n}$ are plotted in Fig. 7.4(e). Consistent with the scaling of dipole matrix elements, $\Delta_{m,n}$ varies approximately as $(n^*)^{-3}$. The values of $D_n(n^*)^{3/2}$ obtained from Eq. (7.49) using the extracted values of $\Delta_{m,n}$ are shown in Fig. 7.4(f), superimposed on the expected values of the matrix elements computed using the ARC values [34]. The 3% standard deviation band is based on comparing our computed values of $|\langle 15s_{1/2}||\hat{d}||np\rangle|$ reduced matrix elements with the values for these matrix elements given in Ref. [26].

7.3.2 Dynamics of the ground-Rydberg coherence

The signal as a function of T_s serves as a measure of the dynamics of the stored spin wave. With $\Delta = \Delta_{m,n}$, the signal as a function of storage time T_s, normalized to its value at $T_s = 1\mu$s, is plotted in Fig. 7.5, along with the theoretical curves. The oscillations result from the nearly periodic motion of the atoms along the optical lattice. The oscillation visibility decreases with time owing to the anharmonic nature of the potential. Moreover the anharmonicity adds a small damping component to the signal and its contribution becoming more pronounced with increasing temperature.

In Fig. 7.6 we compare the $n = 40$ signal with its counterpart obtained by exciting the atoms with 795 nm and 475 nm fields via the $|5p_{1/2}, F = 1\rangle$ intermediate level. The effective two-photon excitation wavelength for the latter $\lambda_{2ph} = 1.2$ μm, longer than $\lambda_{2ph} = 0.72$ μm for the 420 nm-1018 nm excitation. As one would expect, the 795 nm-475 nm excitation exhibits lower visibility of oscillations as a result of decreased motional dephasing for the longer-wavelength spin-wave. The role of trap anharmonicity also decreases with longer spin-wave period, whereas the non-lattice contribution to the dephasing contribution is unaffected by it.

7.4 Conclusion

We have demonstrated ground-Rydberg atomic coherence lifetimes in excess of 20 μs using a state insensitive optical lattice. A theory has been developed to account for the quantized motion of atoms in the trap potentials. The theoretical line shapes that are derived are in good agreement with the experimental results and can be used to extract values for the ns - $6p_{3/2}$ reduced electric dipole matrix elements. Our approach should be of use for precision measurements and quantum information studies involving atomic Rydberg states.

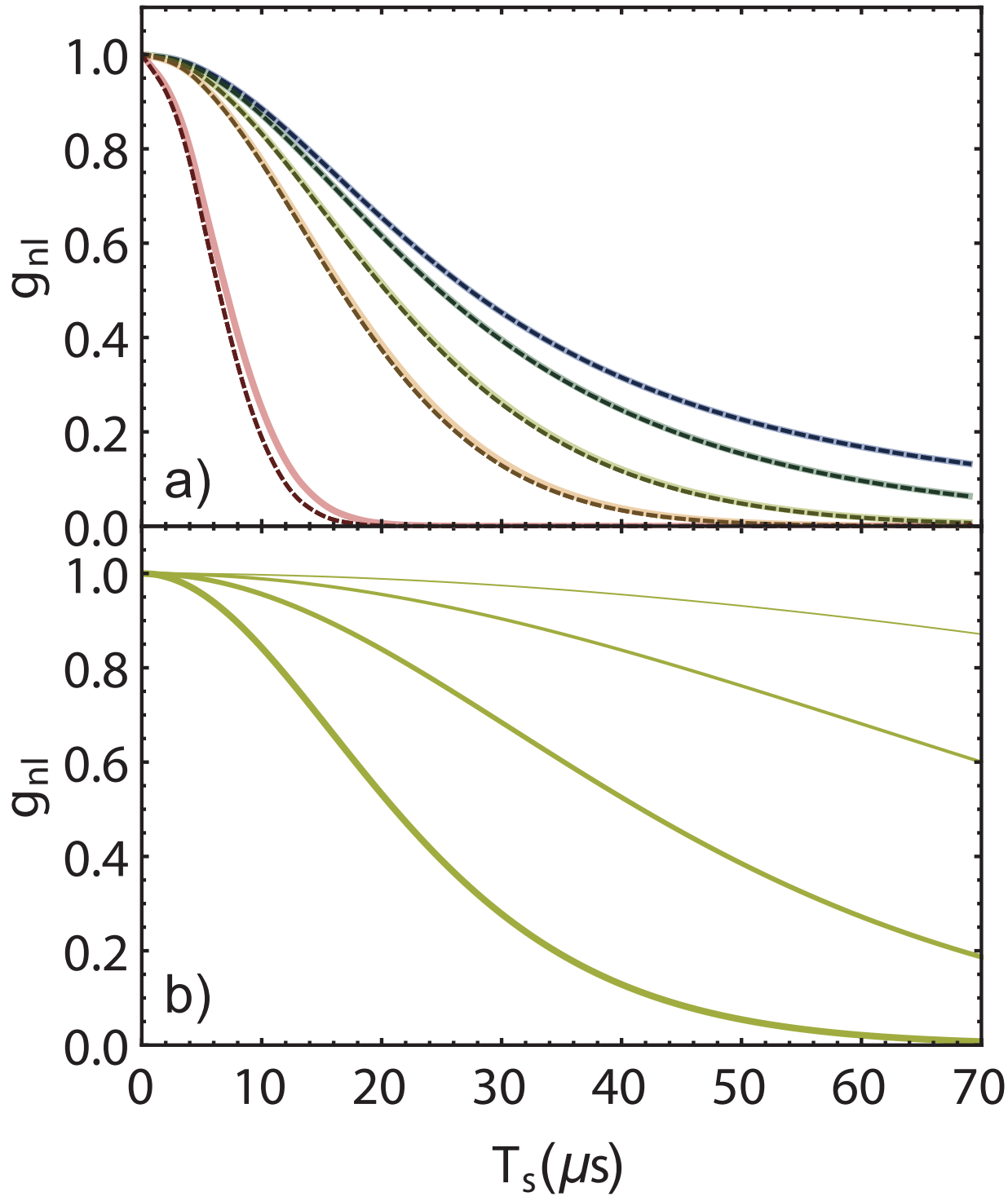

Figure 7.2: (Color online) a) Graphs of the analytic approximation and exact expressions of g_{nl} (dashed and solid respectively) as a function of storage time T_s for $U_0/k_B = 40$ μK and different sample lengths: blue - $L = 1$ μm, dark green - $L = 50$ μm, light green - $L = 100$ μm, orange - $L = 150$ μm, red - $L = 500$ μm. b) Graphs of g_{nl} for sample length $L = 100$ μm and trap depths $U_0/k_B = 5, 10, 20$, and 40 μK, represented by increasing line thickness.

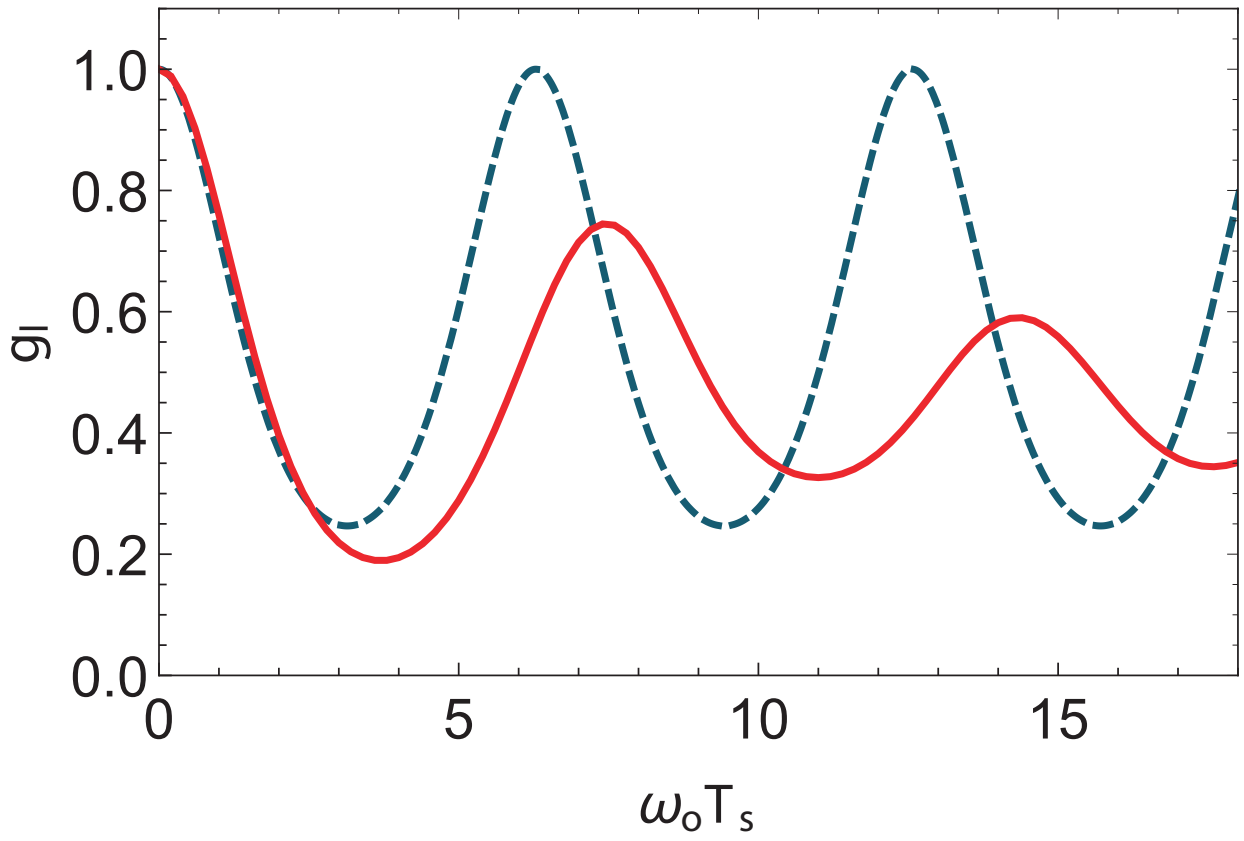

Figure 7.3: Graphs of $g_l(T_s)$ as a function of $\omega_0 T_s$: red, solid curve - $\cos^2(k_L X)$ potential; black, dashed curve - harmonic potential.

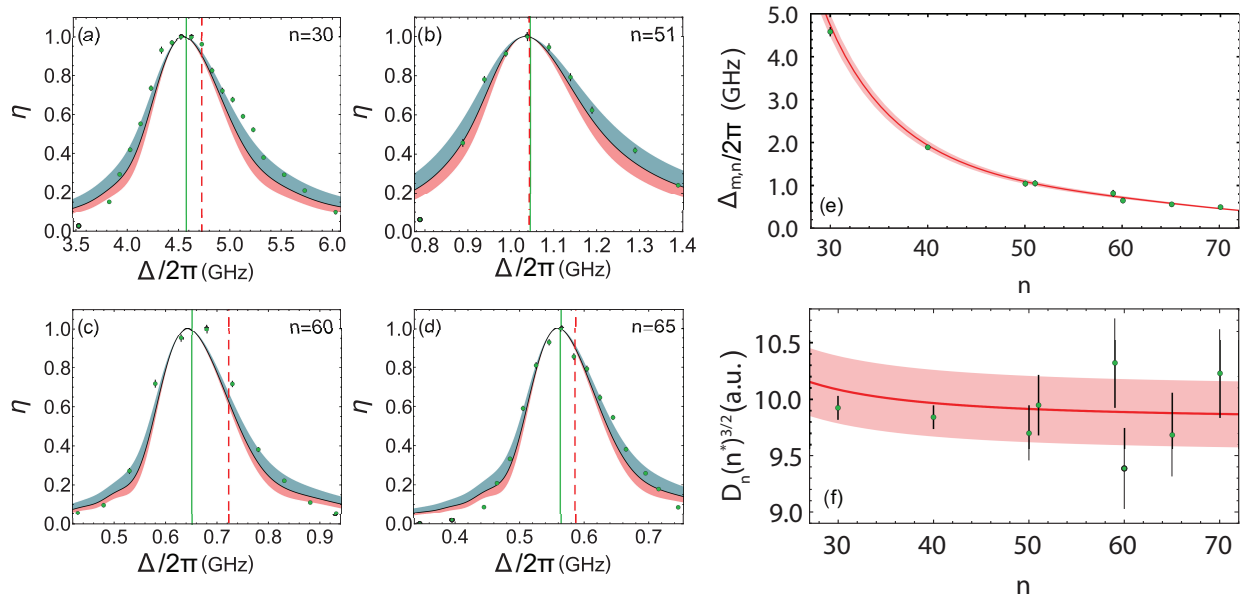

Figure 7.4: (Color online) a)-d) Normalized signal $\eta(T_s)$ at storage time T_s around the first revival ($10 - 12$ μs) as a function of lattice detuning Δ for principal quantum numbers 30, 51, 60, and 65. The solid curves, based on the model described in the text, are used to extract the values of $\Delta_{m,n}$. The dashed red and solid green vertical lines represent the theoretically expected and the extracted values of the magic detuning, respectively. Blue and red bands represent fits using temperatures 20% lower and higher than the best fit value, respectively. (e) $\Delta_{m,n}$ as a function of the principal quantum number n, with the solid curve based on our theoretical model. (f) Extracted values of the scaled reduced matrix elements as a function of n.

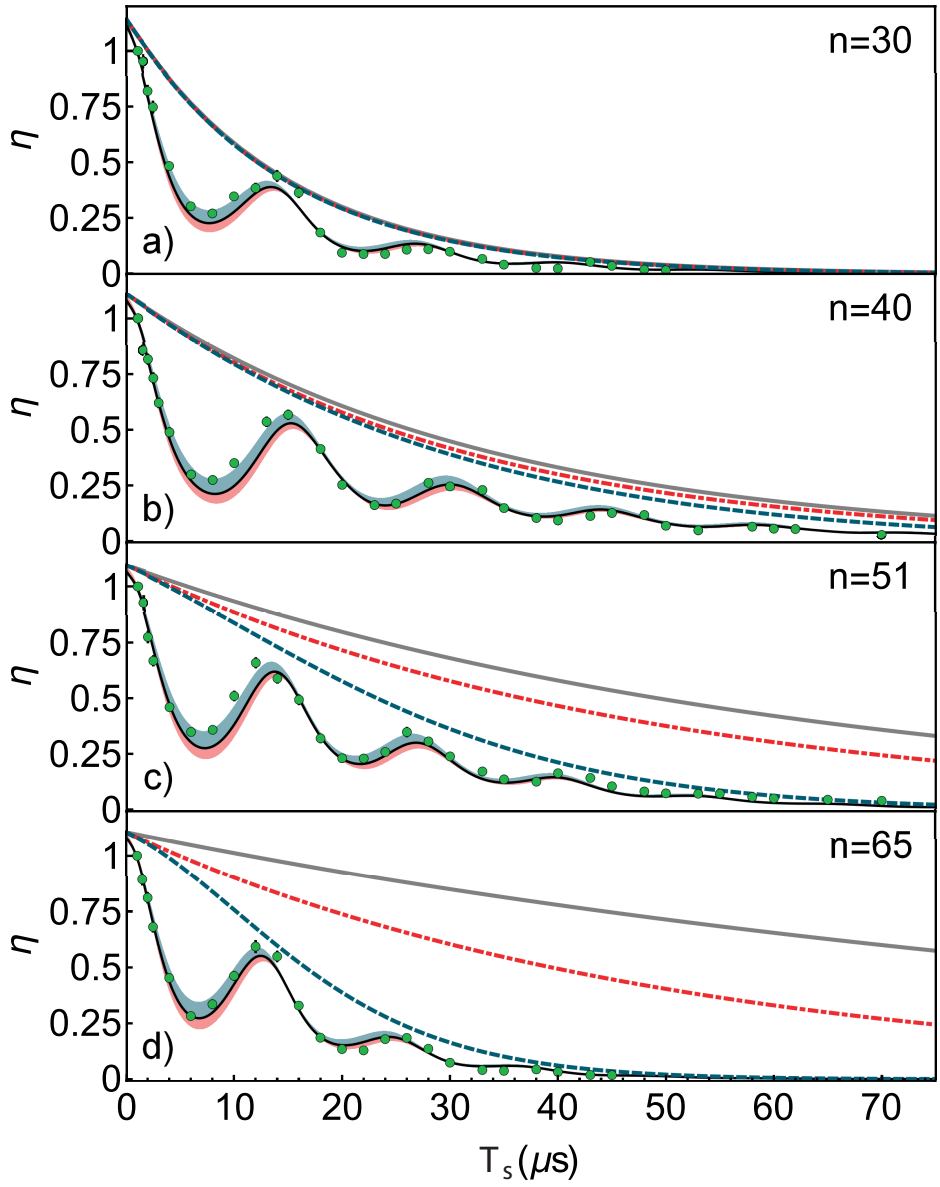

Figure 7.5: (Color online) Normalized signal η as a function of storage time for several principal quantum numbers. The solid black curve is based on our theoretical model. Blue and red bands represent temperatures 20% lower and higher than the best fit value, respectively. The gray curve shows loss attributable to black-body and spontaneous decay from the Rydberg state. The dashed red curve adds in the contribution of spontaneous decay from the $6P$ level. The dashed blue curve additionally includes the dephasing attributable to the non-lattice potential. Most experimental error bars are smaller than the shown markers.

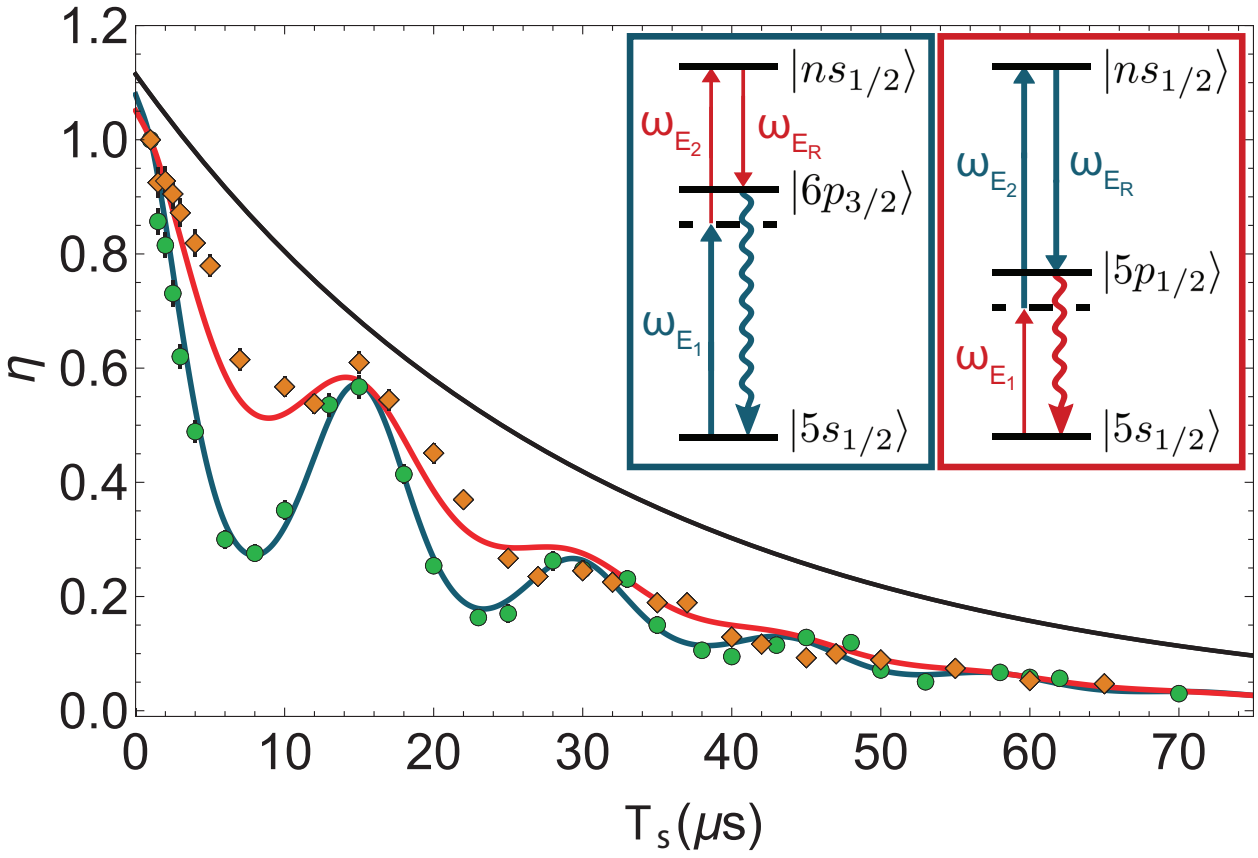

Figure 7.6: (Color online) Normalized signal η as a function of storage time for $n = 40$ for 420 nm - 1018 nm (green circles) and 795 nm-475 nm (orange diamonds) excitation, with the corresponding atomic transitions shown in the inset. The solid curves are the result of a numerical simulation of atomic motion using the model described in the text. The black curve is the same as in Fig. 5. Most experimental error bars are smaller than the shown markers.

CHAPTER 8

Theory of Coherent Optical Transients With Quantized Atomic Motion

8.1 Introduction

Coherent transients provide an important probe of atomic and molecular systems. Historically, the field of coherent transients was developed within the context of nuclear magnetic resonance (NMR). In NMR a series of radio frequency pulses is applied to a spin system [35]. In response to the applied pulses, the sample emits a coherent signal that can be used to measure spin relaxation rates. With the development of laser sources, the coherent transient technique was extended to the optical domain [29]. A series of optical pulses is applied to an atomic or molecular sample, resulting in phase-matched, coherent emission from the sample. Such coherent optical transients (COT) can be used to measure the relaxation rates of the various atomic coherences that are produced by the incident pulses. In both NMR and COT, inhomogeneous variations in the transition frequencies of the spins or atoms can result in significant damping of the generated signals. In NMR, stray magnetic fields modify the separation between spin magnetic sublevels while in COT the Doppler shift associated with atomic motion leads to the inhomogeneities. Spin echoes and photon echoes represent coherent transient techniques that can be used to suppress the effects of magnetic field or Doppler dephasing.

A somewhat more direct way of eliminating Doppler dephasing is to cool atoms. However, even at temperatures of tens of microKelvins that can be achieved using standard laser cooling techniques, Doppler dephasing can still be the dominant factor that limits the lifetimes of long-lived atomic coherences. To further reduce any effects of motional or Doppler dephasing, atoms can be trapped in optical potentials that confine the atoms to distances that are much smaller than the relevant optical wavelengths [36]. This is akin to Dicke narrowing [37], where collisions of atoms with a background buffer gas effectively restrict the atoms to a small volume for the duration of a given experiment. To observe Dicke narrowing, there is a subtle effect that enters. If the collision interaction between the buffer gas and the atoms is state-dependent, that is, if the

collision interaction differs for the two atomic states of an optical transition, then the mechanism responsible for Dicke narrowing can be totally suppressed [29]. In such cases, the atomic center-of-mass motion must be quantized. The same can be said for trapping by optical potentials. If phase-matched emission results from coherence between two atomic levels for which the optical potentials are different, the atomic motion in the trapping potentials must be treated using a fully quantum theory.

Light-matter interfaces and quantum memories based on Raman scattering [38, 39] or excitation to Rydberg levels [5, 40] in atomic ensembles are well-known applications of COT. Such systems have been studied intensely in the past two decades. Much of the experimental and theoretical work in this area was focused on situations in which atoms are not subjected to external forces. On the other hand, there are experiments aimed at achieving long-term ($\geq$ 1 s) quantum state storage that make use of atomic confinement, typically employing far-detuned optical fields [41, 42, 43]. The atomic state dynamics is then governed by the periodic motion in the confining potentials, with a corresponding modulation of the strength of atom-light coupling and memory storage/retrieval efficiencies.

Although there have been numerous papers written related to the interaction of optical fields with trapped atoms in the context of laser cooling [44], light scattering [45], fluorescence [46], and wave packet oscillations [47], there have been only a few articles that addressed phase-matched emission from trapped atoms. Zhao *et al.* [31] and Jenkins *et al.*[32] calculated the phase-matched emission from an ensemble of trapped atoms following a Raman excitation pulse and a readout pulse. Recently, Lampen *et al.* [48] presented both theoretical and experimental results for phase-matched emission from an ensemble of trapped atoms using pulsed, two-photon excitation of a Rydberg level pulse followed by a readout pulse. There are also related calculations carried out within the context of atom interferometry [30]. However, to our knowledge, a general theory of optical coherent transients from trapped atoms based on a source-field approach [29] that includes the effects of quantized motion in state-dependent trapping potentials has not yet been developed.

In this paper, we formulate a general theory of coherent transient spectroscopy that incorporates a quantum description of the atomic center-of-mass motion. In Sec. II, we calculate the change in atomic density matrix elements produced by an optical pulse acting on a generic two-level atomic system. The transfer matrix associated with such a process is the building-block solution from which the more general response of the atoms to a number of pulses can be calculated. In Sec. III, source-field theory [29], modified to include quantized center-of-mass motion for the atoms, is used to calculate the phase-matched coherent transient signal emitted by a sample of atoms. In Secs. IV and V, we present two examples to illustrate the theory. The first involves the creation and probing of ground-Rydberg level coherence in an optical lattice and the second the effect of transit-time loss on Raman coherence between ground state sublevels. For state-dependent optical

potentials, a quantized treatment of the center-of-mass motion is needed. However, under suitable initial conditions, a classical description of the center-of-mass motion can be used, provided the optical potentials are identical for the relevant atomic levels. In this limit, closed form expressions for the radiated signal are obtained with and without the assumption of classical center-of-mass motion. The results are summarized in Sec. VI. The atomic density is assumed to be sufficiently low to neglect all atom-atom interactions.

8.2 Pulsed Excitation - Transfer Matrix

The atoms are subjected to a series of classical optical pulses. In this section, we calculate the response of a generic "two-level" atom (lower level a, upper level c, transition frequency ω_{ca}) to the n-th pulse in this series. The incident fields are assumed to propagate in the X direction and be polarized in the z direction. In a paraxial wave approximation, the electric field of the $n-$th pulse in the sample is given by

$$\mathbf{E}_n(\mathbf{R},t) = \frac{1}{2}\mathbf{u}_z E_n(t) f_n(\mathbf{R}) e^{i(k_n X - \omega_n t)} + \text{c.c.}, \tag{8.1}$$

where $E_n(t)$ is the pulse amplitude at the center of the sample, $f_n(\mathbf{R})$ is the (real) spatial profile of the field in the sample, $\mathbf{u}_z$ is a unit vector in the z direction, $k_n = \omega_n/c$ is a propagation constant, and "c.c." stands for "complex conjugate." The pulse duration T_n is assumed to be sufficiently large to insure that the spatial extent of the pulse is much larger than the sample length L. As a consequence the pulse amplitude $E_n(t)$ reaches its maximum at approximately the same time for all atoms in the sample - this time is denoted by t_n. In other words, it is assumed that the spatial profile of the pulses can be taken to be constant during the atom-field interaction.

In addition to their interaction with the applied field pulses, the atoms are continuously subjected to optical trap fields that result in state-dependent optical potentials. The optical potentials associated with levels a and c are denoted by $V_a(\mathbf{R})$ and $V_c(\mathbf{R})$, respectively. The eigenenergies associated with the potential $V_\alpha(\mathbf{R})$ ($\alpha = a, c$) are denoted by $\hbar\tilde{\omega}_{\alpha q}$, the eigenkets by $|\alpha q\rangle$ and the eigenfunctions by $\psi_{\alpha q}(\mathbf{R})$, where q labels all the quantum numbers associated with the potential $V_\alpha(\mathbf{R})$. The eigenfunctions $\psi_{aq}(\mathbf{R})$ and $\psi_{cq'}(\mathbf{R})$ are *not* orthogonal for $q \neq q'$ if the potential is state-dependent.

In the rotating-wave approximation (RWA), the Hamiltonian is taken as

$$\begin{aligned} H_n = \hbar\omega_a |a\rangle\langle a| + \hbar\omega_c |c\rangle\langle c| + \hbar\tilde{\omega}_{aq} |aq\rangle\langle aq| \\ +\hbar\tilde{\omega}_{cp} |cp\rangle\langle cp| + \frac{\hbar\Omega_{ca}^{(n)}(t)}{2} f_n(\mathbf{R}_j) \begin{bmatrix} e^{ik_n X_j} e^{-i\omega_n t}\sigma_{ca}^{(j)} \\ +e^{-ik_n X_j} e^{i\omega_n t}\sigma_{ac}^{(j)} \end{bmatrix}, \end{aligned} \tag{8.2}$$

where $\Omega_{ca}^{(n)}(t) = -\mu_{ca}E_n(t)/\hbar$ (assumed real) is a Rabi frequency associated with the $a-c$ transition , μ_{ca} is an electric dipole transition matrix element, $\sigma_{ca}^{(j)}$ $\left(\sigma_{ac}^{(j)}\right)$ is a raising (lowering) operator for atom j, and a *summation convention* is adopted, in which repeated indices are summed if they do not appear on both sides of an equation. It is important to recognize that X_j is an *operator* - it is the $X-$component of the position operator of atom j. The field is taken to be resonant with the atomic transition, $\omega_n = \omega_{ca}$.

Our goal is to calculate the change in density matrix elements of atom j resulting from the applied pulse. In this section, we drop the j and n labels, but it is to be understood that all quantities refer to the time evolution of atom j during the $n-$th pulse [for example $f_n(\mathbf{R}_j) \to f(\mathbf{R})$, $\mathbf{k}_n \to \mathbf{k}$, etc.] - these labels will be restored in the Section III. In the Schrödinger representation, density matrix elements obey the time evolution equation

$$\dot{\rho}_{\alpha q;\alpha' q'} = \frac{1}{i\hbar}\left[H,\rho\right]_{\alpha q;\alpha' q'}. \tag{8.3}$$

Defining an interaction representation by

$$\rho_{\alpha q;\alpha' q'} = \rho^I_{\alpha q;\alpha' q'} \exp\left[-i\omega_{\alpha\alpha'}t - i\omega_{\alpha q,\alpha' q'}t\right], \tag{8.4}$$

where

$$\omega_{\alpha\alpha'} = \omega_\alpha - \omega_{\alpha'}; \qquad \omega_{\alpha q,\alpha' q'} = \tilde{\omega}_{\alpha q} - \tilde{\omega}_{\alpha' q'}, \tag{8.5}$$

we find time-evolution equations

$$\dot{\rho}^I_{aq;cp} = -i\frac{\Omega_{ca}(t)}{2}\left[\begin{array}{c} e^{i\omega_{aq,cp'}t}B^\dagger_{aq,cp'}(\mathbf{k})\,\rho^I_{cp';cp} \\ -e^{i\omega_{aq',cp}t}\rho^I_{aq;aq'}B^\dagger_{aq',cp}(\mathbf{k}) \end{array}\right]; \tag{8.6a}$$

$$\dot{\rho}^I_{cp;aq} = -i\frac{\Omega_{ca}(t)}{2}\left[\begin{array}{c} e^{i\omega_{cp,aq'}t}B_{cp,aq'}(\mathbf{k})\,\rho^I_{aq';aq} \\ -e^{i\omega_{cp',aq}t}\rho^I_{cp;cp'}B_{cp',aq}(\mathbf{k}) \end{array}\right]; \tag{8.6b}$$

$$\dot{\rho}^I_{cp;cp'} = -i\frac{\Omega_{ca}(t)}{2}\left[\begin{array}{c} e^{i\omega_{cp,aq}t}B_{cp,aq}(\mathbf{k})\,\rho^I_{aq;cp'} \\ -e^{-i\omega_{cp',aq}t}\rho^I_{cp;aq}B^\dagger_{aq,cp'}(\mathbf{k}) \end{array}\right]; \tag{8.6c}$$

$$\dot{\rho}^I_{aq;aq'} = -i\frac{\Omega_{ca}(t)}{2}\left[\begin{array}{c} e^{i\omega_{aq,cp}t}B^\dagger_{aq,cp}(\mathbf{k})\,\rho^I_{cp;aq'} \\ -e^{-i\omega_{aq',cp}t}\rho^I_{aq;cp}B_{cp,aq'}(\mathbf{k}) \end{array}\right], \tag{8.6d}$$

where $\mathbf{k} = k\mathbf{u}_x$ and

$$B_{cp,aq}(\mathbf{k}) = \int d\mathbf{R} \left[\psi_{cp}(\mathbf{R})\right]^* f(\mathbf{R}) e^{i\mathbf{k}\cdot\mathbf{R}} \psi_{aq}(\mathbf{R}); \tag{8.7a}$$

$$B^\dagger_{aq,cp}(\mathbf{k}) = \int d\mathbf{R} \left[\psi_{aq}(\mathbf{R})\right]^* f(\mathbf{R}) e^{-i\mathbf{k}\cdot\mathbf{R}} \psi_{cp}(\mathbf{R}). \tag{8.7b}$$

If we define an operator

$$M_{ca}(\mathbf{R}, \mathbf{k}, t) = f_n(\mathbf{R}) e^{iV_c(\mathbf{R})t/\hbar} e^{i\mathbf{k}\cdot\mathbf{R}} e^{-iV_a(\mathbf{R})t/\hbar}, \tag{8.8}$$

then Eqs. (8.6) can be written in matrix form as

$$\dot{\rho}^I_{ac} = -i\frac{\Omega_{ca}(t)}{2}\left[M_{ca}(\mathbf{k}, t)^\dagger \rho^I_{cc} - \rho^I_{aa} M_{ca}(\mathbf{k}, t)^\dagger\right]; \tag{8.9a}$$

$$\dot{\rho}^I_{ca} = -i\frac{\Omega_{ca}(t)}{2}\left[M_{ca}(\mathbf{k}, t)\rho^I_{aa} - \rho^I_{cc} M_{ca}(\mathbf{k}, t)\right]; \tag{8.9b}$$

$$\dot{\rho}^I_{cc} = -i\frac{\Omega_{ca}(t)}{2}\left[M_{ca}(\mathbf{k}, t)\rho^I_{ac} - \rho^I_{ca} M_{ca}(\mathbf{k}, t)^\dagger\right]; \tag{8.9c}$$

$$\dot{\rho}^I_{aa} = -i\frac{\Omega_{ca}(t)}{2}\left[M_{ca}(\mathbf{k}, t)^\dagger \rho^I_{ca} - \rho^I_{ac} M_{ca}(\mathbf{k}, t)\right], \tag{8.9d}$$

where each element $\rho^I_{\alpha\alpha'}$ is now a *matrix* having matrix elements $\langle \alpha q| \rho^I_{\alpha\alpha'} |\alpha' q'\rangle$. There is no sum over a or c on the right hand side of these equations - both M_{ca} and $\rho^I_{\alpha\beta}$ are themselves matrices in the center-of-mass basis state, e.g.

$$\left[M_{ca}(\mathbf{k}, t)\right]_{\alpha q;\beta q'} = \langle \alpha q| M_{ca}(\mathbf{R}, \mathbf{k}, t) |\beta q'\rangle, \tag{8.10}$$

for α, β equal to a or c. The pulse duration is sufficiently short to neglect any decay during the pulse. Note that $M_{ca}(\mathbf{R}, \mathbf{k}, t)$ is *not* a unitary operator owing to the factor $f(\mathbf{R})$, but that the operator

$$U_{ca}(\mathbf{R}, \mathbf{k}, t) = e^{iV_c(\mathbf{R})t/\hbar} e^{i\mathbf{k}\cdot\mathbf{R}} e^{-iV_a(\mathbf{R})t/\hbar}, \tag{8.11}$$

is unitary.

In principle, Eqs. (8.9) could be solved numerically as coupled equations for all the matrix elements. However if the pulse duration T is sufficiently short such that $|\omega_{aq,cp}T| \ll 1$ for all relevant q and p (this corresponds to the atomic motion being frozen during the pulse), then the

matrix $M_{ca}(\mathbf{k},t)$ can be evaluated at $t = t_n$ and Eqs. (8.9) reduce to

$$\dot{\rho}^I_{ac} = -i\frac{\Omega_{ca}(t)}{2}\left[M_{ca}(\mathbf{k},t_n)^\dagger \rho^I_{cc} - \rho^I_{aa} M_{ca}(\mathbf{k},t_n)^\dagger\right]; \tag{8.12a}$$

$$\dot{\rho}^I_{ca} = -i\frac{\Omega_{ca}(t)}{2}\left[M_{ca}(\mathbf{k},t_n)\,\rho^I_{aa} - \rho^I_{cc} M_{ca}(\mathbf{k},t_n)\right]; \tag{8.12b}$$

$$\dot{\rho}^I_{cc} = -i\frac{\Omega_{ca}(t)}{2}\left[M_{ca}(\mathbf{k},t_n)\,\rho^I_{ac} - \rho^I_{ca} M_{ca}(\mathbf{k},t_n)^\dagger\right]; \tag{8.12c}$$

$$\dot{\rho}^I_{aa} = -i\frac{\Omega_{ca}(t)}{2}\left[M_{ca}(\mathbf{k},t_n)^\dagger \rho^I_{ca} - \rho^I_{ac} M_{ca}(\mathbf{k},t_n)\right]. \tag{8.12d}$$

Unfortunately, even though $M_{ca}(\mathbf{k},t_n)$ and $M_{ca}(\mathbf{k},t_n)^\dagger$ are time-independent in these equations, there is no simple solution owing to the fact that $M_{ca}(\mathbf{k},t_n)$ is not a unitary matrix. In effect, Eqs. (8.9) must be solved numerically to obtain the $\rho^I_{\alpha q;\beta q'}(t_n^+)$ in terms of $\rho^I_{\alpha q,\beta q'}(t_n^-)$.

There are two limiting cases where a relatively simple solution can be obtained. If the applied field spatial profile is constant over the sample [$f(\mathbf{R}) = 1$ and $M_{ca}(\mathbf{k},t_n) = U_{ca}(\mathbf{k},t_n)$], then we can set

$$\tilde{\rho}_{ac}(\mathbf{k},t,t_n) = \rho^I_{ac}(t)\,U_{ca}(\mathbf{k},t_n); \tag{8.13a}$$

$$\tilde{\rho}_{ca}(\mathbf{k},t,t_n) = U_{ca}(\mathbf{k},t_n)^\dagger \rho^I_{ca}(t); \tag{8.13b}$$

$$\tilde{\rho}_{aa}(\mathbf{k},t,t_n) = \rho^I_{aa}(t); \tag{8.13c}$$

$$\tilde{\rho}_{cc}(\mathbf{k},t,t_n) = U_{ca}(\mathbf{k},t_n)^\dagger \rho^I_{cc}(t)\,U_{ca}(\mathbf{k},t_n), \tag{8.13d}$$

which transforms Eqs. (8.12) into

$$\frac{d\tilde{\rho}_{ac}}{dt} = -i\frac{\Omega_{ca}(t)}{2}\left[\tilde{\rho}_{cc} - \tilde{\rho}_{aa}\right]; \tag{8.14a}$$

$$\frac{d\tilde{\rho}_{ca}}{dt} = -i\frac{\Omega_{ca}(t)}{2}\left[\tilde{\rho}_{aa} - \tilde{\rho}_{cc}\right]; \tag{8.14b}$$

$$\frac{d\tilde{\rho}_{cc}}{dt} = -i\frac{\Omega_{ca}(t)}{2}\left[\tilde{\rho}_{ac} - \tilde{\rho}_{ca}\right]; \tag{8.14c}$$

$$\frac{d\tilde{\rho}_{aa}}{dt} = -i\frac{\Omega_{ca}(t)}{2}\left[\tilde{\rho}_{ca} - \tilde{\rho}_{ac}\right]. \tag{8.14d}$$

The solution of these equations is straightforward [29],

$$\begin{pmatrix} \tilde{\rho}_{ac}\left(t_n^+\right) \\ \tilde{\rho}_{ca}\left(t_n^+\right) \\ \tilde{\rho}_{aa}\left(t_n^+\right) \\ \tilde{\rho}_{cc}\left(t_n^+\right) \end{pmatrix} = \begin{pmatrix} \cos^2\left(\frac{A}{2}\right) & \sin^2\left(\frac{A}{2}\right) & i\frac{\sin A}{2} & -i\frac{\sin A}{2} \\ \sin^2\left(\frac{A}{2}\right) & \cos^2\left(\frac{A}{2}\right) & -i\frac{\sin A}{2} & i\frac{\sin A}{2} \\ i\frac{\sin A}{2} & -i\frac{\sin A}{2} & \cos^2\left(\frac{A}{2}\right) & \sin^2\left(\frac{A}{2}\right) \\ -i\frac{\sin A}{2} & i\frac{\sin A}{2} & \sin^2\left(\frac{A}{2}\right) & \cos^2\left(\frac{A}{2}\right) \end{pmatrix} \times \begin{pmatrix} \tilde{\rho}_{ac}\left(t_n^-\right) \\ \tilde{\rho}_{ca}\left(t_n^-\right) \\ \tilde{\rho}_{aa}\left(t_n^-\right) \\ \tilde{\rho}_{cc}\left(t_n^-\right) \end{pmatrix}, \tag{8.15}$$

where $t_n^{\pm}$ are times just before and after the application of the pulse and

$$A = \int_{t_n^-}^{t_{n+}} dt\Omega_{ca}(t) \tag{8.16}$$

is a pulse area. Equations (8.15) and (8.13) can be used to calculate the change in the atomic density matrix elements in the interaction representation.

The second case where a simple solution is possible is one in which there is a lattice trap potential varying as $-V_0\cos^2(k_{tr}X)$ superimposed on a much more slowly varying trap potential. If the temperature is sufficiently low to insure that all atomic motion can be neglected on the time scale of an experiment *except* that associated with motion in the lattice potential, but is still sufficiently large to insure that motion in the slowly varying trap potential can be treated classically, then $f\left(\mathbf{R}\right)$ can be replaced a classical function $f_{cl}\left(\mathbf{R}\right)$ and the resulting signal averaged over the classical Boltzmann distribution associated with the slowly varying trap potential. In this limit Eqs. (8.13) and (8.15) remain valid, provided that the area A appearing in Eq. (8.15) is replaced by

$$A\left(\mathbf{R}\right) = f_{cl}\left(\mathbf{R}\right)\int_{t_n^-}^{t_n^+} dt\Omega_{ca}(t). \tag{8.17}$$

Although we have taken the $a-c$ transition to be dipole allowed, the formalism can still be used when levels a and c have the same parity and are driven by two-photon excitation. The only change that need be made is to replace $\Omega_{ca}(t)$ by some effective two-photon Rabi frequency that depends on the product of the amplitudes of each of the fields involved in the transition.

8.2.1 Readout Pulse

In some cases, it is necessary to apply a readout pulse to generate the phase-matched signal. For example, consider the level schemes shown in Fig. 8.1. In both cases it is assumed that some

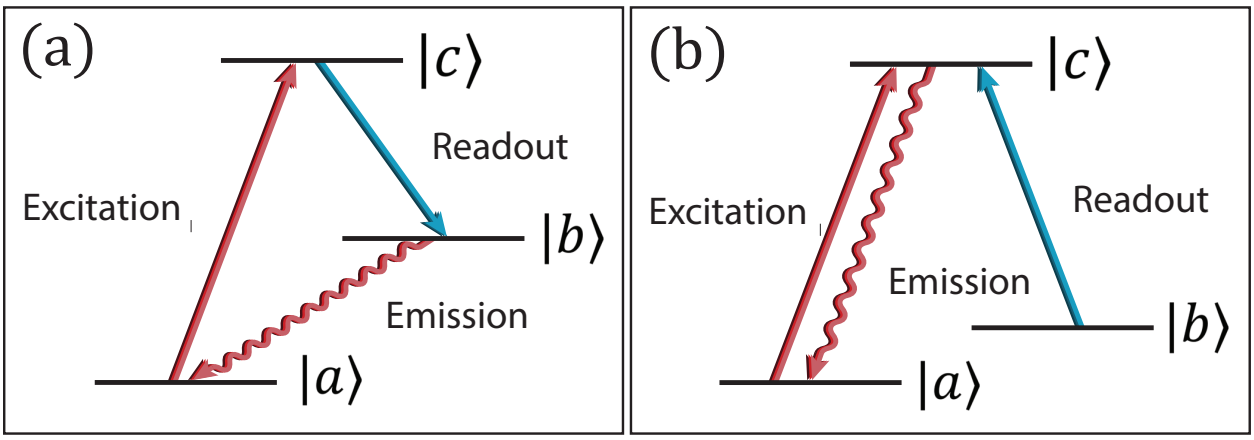

Figure 8.1: Level schemes.

initial two-photon pulse has created a long-lived atomic coherence between levels a and c, both of which have the same parity. In Fig. 8.1 (a), the coherence is between a ground and Rydberg level and, in Fig. 8.1 (b), it is between two-ground state sublevels. To read out the coherence, a pulse is applied that is resonant with the $c-b$ transition and results in phase-matched emission on the $a-b$ transition. We shall assume that the Rabi frequency Ω_{bc}^{out} associated with the readout pulse is greater than the decay rate $\Gamma_b = 2\gamma_b$ of level b. The duration T_{out} of the readout pulse may be greater than Γ_b^{-1}; it is assumed, however, that all motion is frozen on a time scale of $\min\left(\gamma_b^{-1}, T_{out}\right)$.

The calculation proceeds in exactly the same manner as that for the excitation pulse, except it is necessary to use density matrix equations for a three-level lambda scheme [29] with a single field acting on the $c-b$ transition. We find that, for the level scheme of 8.1 (a) and $f(\mathbf{R}) = 1$,

$$\frac{d\tilde{\rho}_{ca}}{dt} = -i\frac{\Omega_{cb}^{out}(t)}{2}\tilde{\rho}_{ba}; \tag{8.18a}$$

$$\frac{d\tilde{\rho}_{ba}}{dt} = -i\frac{\Omega_{cb}^{out}(t)}{2}\tilde{\rho}_{ca} - \gamma_b\tilde{\rho}_{ba}, \tag{8.18b}$$

where

$$\tilde{\rho}_{ca}\left(\mathbf{k}_n, t, t_{out}\right) = U_{cb}\left(\mathbf{k}_{out}, t_{out}\right)^{\dagger}\rho_{ca}^{I}\left(t\right); \tag{8.19a}$$

$$\tilde{\rho}_{ba}\left(\mathbf{k}_n, t, t_{out}\right) = \rho_{ba}^{I}\left(t\right), \tag{8.19b}$$

$\mathbf{k}_{out}$ is the propagation vector of the readout pulse, and t_{out} is the time the readout pulse is applied.

For the level scheme of 8.1 (b) and $f(\mathbf{R}) = 1$,

$$\frac{d\tilde{\rho}_{ca}}{dt} = -i\frac{\Omega_{bc}^{out}(t)}{2}\tilde{\rho}_{ba}; \tag{8.20a}$$

$$\frac{d\tilde{\rho}_{ba}}{dt} = -i\frac{\Omega_{bc}^{out}(t)}{2}\tilde{\rho}_{ca} - \gamma_b\tilde{\rho}_{ba}, \tag{8.20b}$$

where

$$\tilde{\rho}_{ca}(\mathbf{k}_n, t, t_{out}) = U_{cb}(\mathbf{k}_{out}, t_{out})\,\rho_{ca}^{I}(t); \tag{8.21a}$$

$$\tilde{\rho}_{ba}(\mathbf{k}_n, t, t_{out}) = \rho_{ba}^{I}(t). \tag{8.21b}$$

It is a simple matter to solve Eqs. (8.18) or (8.20) numerically (or analytically for a square pulse) and then use Eqs. (8.19) or (8.21) to obtain matrix elements of $\rho_{ca}^{I}(t)$, matrix elements that will be needed in the evaluation of the phase-matched signal. If, instead of taking $f(\mathbf{R}) = 1$, we consider the second limiting case discussed following Eq. (8.12), then $\Omega_{bc}^{out}(t)$ is replaced by $\Omega_{bc}^{out}(t)f_{cl}(\mathbf{R})$ in Eqs. (8.18) and (8.20).

8.3 Source-Field Expression for the Signal

The signal recorded at time t at a point detector located at position $\mathbf{R}_d$ is proportional to a quantity S defined by

$$S = R_d^2 \langle \mathbf{E}_-(\mathbf{R}_d, t) \cdot \mathbf{E}_+(\mathbf{R}_d, t) \rangle, \tag{8.22}$$

where

$$\mathbf{E}_+(\mathbf{R}, t) = i\left(\frac{\hbar\omega_k}{2\epsilon_0\mathcal{V}}\right)^{1/2} e^{i\mathbf{k}\cdot\mathbf{R}} a_{\mathbf{k}_\lambda}(t)\boldsymbol{\epsilon}_{\mathbf{k}}^{(\lambda)}, \tag{8.23}$$

is the positive frequency component of the electric field operator at position $\mathbf{R}_d$, $\mathbf{E}_-(\mathbf{R}_d, t) = [\mathbf{E}_+(\mathbf{R}, t)]^\dagger$, $\omega_k = kc$,

$$\boldsymbol{\epsilon}_{\mathbf{k}}^{(1)} = \cos\theta_k \cos\phi_k \mathbf{u}_x + \cos\theta_k \sin\phi_k \mathbf{u}_y - \sin\theta_k \mathbf{u}_z; \tag{8.24a}$$

$$\boldsymbol{\epsilon}_{\mathbf{k}}^{(2)} = -\sin\phi_k \mathbf{u}_x + \cos\phi_k \mathbf{u}_y, \tag{8.24b}$$

are the field polarization vectors, and $\mathcal{V}$ is the quantization volume. A sum over all field modes and polarizations is implicit in Eq. (8.23), owing to our summation convention. The field operators are written in the Heisenberg representation, but could have equally well been written as time-independent operators in the Schrödinger representation. We will return to this point shortly.

In the problem under consideration a number of classical field pulses give rise to the creation

of previously unoccupied vacuum field modes. In situations such as this, a powerful method for obtaining an expression for $\mathbf{E}_+(\mathbf{R}_d, t)$ is afforded by the so-called source-field approach [29]. In that approach the creation and annihilation operators are written in terms of their initial values and their dependence on atomic operators. For example, consider emission on transitions from level b to a having transition frequency ω_{ba} in an ensemble of atoms whose center-of-mass coordinates are fixed. Level b is taken to be the $m = 0$ sublevel of a $J = 1$ angular momentum state, while level a is taken to be a $J = 0$ angular momentum state. In that case, for an electric dipole interaction of the form

$$V_{af}(\mathbf{R}, t) = -\hat{\boldsymbol{\mu}}(t) \cdot [\mathbf{E}_+(\mathbf{R}, t) + \mathbf{E}_-(\mathbf{R}, t)], \tag{8.25}$$

where $\hat{\boldsymbol{\mu}}(t)$ is the atomic dipole moment operator, the Hamiltonian in the RWA is given by

$$\begin{aligned} H &= \hbar\omega_a |a\rangle \langle a| + \hbar\omega_b |b\rangle \langle b| \\ &+ \left[\hbar g_{\mathbf{k}_\lambda} e^{i\mathbf{k}\cdot\mathbf{R}_j} e^{-i\omega_k t} \sigma_{ba}^{(j)} + \hbar g_{\mathbf{k}_\lambda}^* e^{-i\mathbf{k}\cdot\mathbf{R}_j} e^{i\omega_k t} \sigma_{ab}^{(j)}\right], \end{aligned} \tag{8.26}$$

where

$$g_{\mathbf{k}_\lambda} = -i\mu_{ba} \left(\frac{\omega_k}{2\hbar\epsilon_0 \mathcal{V}}\right)^{1/2} \sin\theta_k \delta_{\lambda,1}, \tag{8.27}$$

$\sigma_{ab}^{(j)}(t')$ [$\sigma_{ba}^{(j)}(t')$] is a lowering [raising] operator for atom j located at position $\mathbf{R}_j$, μ_{ba} is the $z-$component of the dipole moment matrix element (assumed real) between states b and a, and $\delta_{\lambda,1}$ is a Kronecker delta. The annihilation operator at time t can be expressed as

$$\begin{aligned} a_{\mathbf{k}_\lambda}(t) &= a_{\mathbf{k}_\lambda}(0) e^{-i\omega_k t} \\ &- i g_{\mathbf{k}_\lambda}^* e^{-i\mathbf{k}\cdot\mathbf{R}_j} \int_0^t dt' \sigma_{ab}^{(j)}(t') e^{-i\omega_k (t-t')}. \end{aligned} \tag{8.28}$$

The second term in Eq. (8.28) is the contribution to the field operator that can be traced to the atoms - the so-called source-field term. Including only the source-field contribution in Eq. (8.23), it is straightforward to show that the field operator can be written in a form that mirrors the classical expression for the electric field produced by an ensemble of electric dipoles. In particular, assuming that the detector is located in the radiation zone of the atomic dipoles, one finds [29]

$$\mathbf{E}_+(\mathbf{R}_d, t) = -\left(\frac{\omega_{ba}^2}{4\pi\epsilon_0 c^2 R_d}\right) \mu_{ba} \sin\theta_d \sigma_{ab}^{(j)}(t_r^{(j)}) \mathbf{u}_{\theta_d}, \tag{8.29}$$

where θ_d is the polar angle of the detector, $\mathbf{u}_{\theta_d}$ is a unit vector in the direction of increasing θ_d and

$$t_r^{(j)} = t - \frac{|\mathbf{R}_d - \mathbf{R}_j|}{c} \tag{8.30}$$

is a retarded time.

If the center-of-mass motion of the atoms can be treated *classically*, it is a simple matter to extend the source-field result to include the effects of atomic motion. Equation (8.29) remains valid provided that $t_r^{(j)}$ is defined as the solution of

$$t_r^{(j)} = t - \frac{\left|\mathbf{R}_d - \mathbf{R}_j\left(t_r^{(j)}\right)\right|}{c} \tag{8.31}$$

where $\mathbf{R}_j(t)$ is the position of atom j at time t. On the other hand, if the center-of-mass motion of the atoms is quantized, $\mathbf{R}_j(t)$ becomes a Heisenberg *operator* and there is no obvious manner in which to generalize Eq. (8.29).

To make some progress in the case where the center-of-mass motion is quantized, we can still use the Heisenberg representation, but it is necessary to delay the sum over field modes that lead to the final source-field expression. In other words, we use Eq. (8.28) to write the source field contribution to the signal as

$$\begin{aligned}
S &= R_d^2 \left\langle \mathbf{E}_-(\mathbf{R}_d, t) \cdot \mathbf{E}_+(\mathbf{R}_d, t) \right\rangle \\
&= R_d^2 \left(\frac{\hbar\omega_{k'}}{2\epsilon_0 \mathcal{V}}\right)^{1/2} \left(\frac{\hbar\omega_k}{2\epsilon_0 \mathcal{V}}\right)^{1/2} e^{i(\mathbf{k}-\mathbf{k}')\cdot\mathbf{R}_d} \\
&\times \left\langle a^\dagger_{\mathbf{k}'\lambda'}(t) a_{\mathbf{k}\lambda}(t) \right\rangle \boldsymbol{\epsilon}^{(\lambda')}_{\mathbf{k}'} \cdot \boldsymbol{\epsilon}^{(\lambda)}_{\mathbf{k}} \\
&= \mu_{ba}^2 R_d^2 \left(\frac{\hbar\omega_{k'}}{2\epsilon_0 \mathcal{V}}\right) \left(\frac{\hbar\omega_k}{2\epsilon_0 \mathcal{V}}\right) \\
&\times \sin\theta_k \sin\theta_{k'} e^{i(\mathbf{k}-\mathbf{k}')\cdot\mathbf{R}_d} \boldsymbol{\epsilon}^{(1)}_{\mathbf{k}'} \cdot \boldsymbol{\epsilon}^{(1)}_{\mathbf{k}} \\
&\times \int_0^t dt' \int_0^t dt'' \left\langle e^{i\mathbf{k}'\cdot\hat{\mathbf{R}}_{j'}(t'')} \sigma_{ba}^{(j')}(t'') \sigma_{ab}^{(j)}(t') e^{-i\mathbf{k}\cdot\hat{\mathbf{R}}_j(t')} \right\rangle \\
&\times e^{i\omega_{k'}(t-t')} e^{-i\omega_k(t-t')},
\end{aligned} \tag{8.32}$$

where $\hat{\mathbf{R}}_j(t)$ is a Heisenberg operator. Note that $\left[\hat{\mathbf{R}}_j(t), \sigma^{(j)}_{\alpha\beta}(t)\right] = 0$, but that $\left[\hat{\mathbf{R}}_j(t), \sigma^{(j)}_{\alpha\beta}(t')\right] \neq 0$, in general.

Qualitatively, there are two types of terms that enter the double summation over j and j' in Eq. (8.32). Terms with $j = j'$ are difficult to calculate using this approach, but such terms contribute negligibly to the phase-matched signal. For completeness, a method for treating the $j = j'$ terms is discussed in the Appendix. The remaining terms involve products of operators corresponding to different atoms, implying that the average of the product is equal to the product of the averages. In other words, for such terms we can write Eq. (8.32) as

$$S = \left|G(\mathbf{R}_d, t)\right|^2, \tag{8.33}$$

where

$$G(\mathbf{R}_d,t)=\mu_{ba}R_d\left(\frac{\hbar\omega_k}{2\epsilon_0\mathcal{V}}\right)\times\int_0^t dt'\left\langle\sigma_{ab}^{(j)}(t')e^{-i\mathbf{k}\cdot\hat{\mathbf{R}}_j(t')}\right\rangle e^{-i\omega_k(t-t')}. \tag{8.34}$$

Written in this form, the signal contains extra terms since terms with $j=j'$ are not excluded; however for a large number of atoms N in the sample, the $j=j'$ terms can be neglected since they scale as N, whereas the phase-matched signal scales as N^2.

The average in Eq. (8.34) can be written as

$$\begin{aligned}F_j&=\left\langle\sigma_{ab}^{(j)}(t')e^{-i\mathbf{k}\cdot\hat{\mathbf{R}}_j(t')}\right\rangle=\mathrm{Tr}\left[\rho(0)\sigma_{ab}^{(j)}(t')e^{-i\mathbf{k}\cdot\hat{\mathbf{R}}_j(t')}\right]\\&=\mathrm{Tr}\left[\rho^{(j)}(t')\left|a\right\rangle\left\langle b\right|e^{-i\mathbf{k}\cdot\hat{\mathbf{R}}_j}\right],\end{aligned} \tag{8.35}$$

where $\rho^{(j)}(t)$ is the density matrix for atom j at time t and the trace is over motional states. The trace is very difficult to carry out using Heisenberg operators, but relatively simple to evaluate using Schrödinger operators. Explicitly we find

$$\begin{aligned}F_j&=\rho_{bq;aq'}^{(j)}(t')\left\langle aq'\right|e^{-i\mathbf{k}\cdot\hat{\mathbf{R}}_j}\left|bq\right\rangle\\&=\rho_{bq;aq'}^{I(j)}(t')\left\langle aq'\right|e^{-i\mathbf{k}\cdot\hat{\mathbf{R}}_j}\left|bq\right\rangle e^{-i\omega_{bq;aq'}t'}e^{-i\omega_{ba}t'}\\&=\int d\mathbf{R}_j\left[\psi_{aq'}\left(\mathbf{R}_j\right)\right]^*e^{-i\mathbf{k}\cdot\mathbf{R}_j}\psi_{bq}\left(\mathbf{R}_j\right)\rho_{bq;aq'}^{I(j)}(t')\\&\quad\times e^{-i\omega_{bq;aq'}t'}e^{-i\omega_{ba}t'}.\end{aligned} \tag{8.36}$$

The key point is that the $\mathbf{R}_j$ appearing in Eq. (8.36) is no longer an operator. As a consequence,when this expression is substituted back into Eq. (8.34), the sum over field modes can be carried out as in normal source field theory. In this manner, we find

$$\begin{aligned}G(\mathbf{R}_d,t)=-\mu_{ba}\left(\frac{\omega_{ba}^2\sin\theta_d}{4\pi\epsilon_0c^2}\right)\int d\mathbf{R}_j\left[\psi_{aq'}\left(\mathbf{R}_j\right)\right]^*\\\times\rho_{bq;aq'}^{I(j)}\left(t-\frac{|\mathbf{R}_d-\mathbf{R}_j|}{c}\right)\\\times\exp\left[-i\omega_{bq;aq'}\left(t-\frac{|\mathbf{R}_d-\mathbf{R}_j|}{c}\right)\right]\\\times\exp\left[-i\omega_{ba}\left(t-\frac{|\mathbf{R}_d-\mathbf{R}_j|}{c}\right)\right]\psi_{bq}\left(\mathbf{R}_j\right).\end{aligned} \tag{8.37}$$

Since $R_d\gg R_j$ we can set $|\mathbf{R}_d-\mathbf{R}_j|=R_d$ *except* in the exponential containing ω_{ba}, since ω_{ba}

corresponds to an optical frequency. In that term, we set

$$|\mathbf{R}_d - \mathbf{R}_j| \approx R_d - \frac{\mathbf{R}_d \cdot \mathbf{R}_j}{R_d} \tag{8.38}$$

and Eq. (8.37) reduces to

$$G(\mathbf{R}_d, t) = -\mu_{ba} \left(\frac{\omega_{ba}^2 \sin\theta_d}{4\pi\epsilon_0 c^2} \right) e^{ik_{ba}R_d} e^{-i\omega_{ba}t} \rho_{bq;aq'}^{I(j)}(t_r) \times \int d\mathbf{R}_j \left[\psi_{aq'}(\mathbf{R}_j)\right]^* e^{-i\omega_{bq;aq'}t_r} e^{-i\mathbf{k}_{ba}\cdot\mathbf{R}_j} \psi_{bq}(\mathbf{R}_j), \tag{8.39}$$

where

$$\mathbf{k}_{ba} = \frac{\omega_{ba}}{c} \frac{\mathbf{R}_d}{R_d} \tag{8.40}$$

and

$$t_r = t - R_d/c. \tag{8.41}$$

Equation (8.39) can be written in the more compact form as

$$G(\mathbf{R}_d, t) = -\mu_{ba} \left(\frac{\omega_{ba}^2 \sin\theta_d}{4\pi\epsilon_0 c^2} \right) e^{ik_{ba}R_d} e^{-i\omega_{ba}t} \mathrm{Tr}\left[\rho_{ba}^{I(j)}(t_r) U_{ba}(\mathbf{k}_{ba}, t_r)^\dagger \right], \tag{8.42}$$

where both $\rho_{ba}^{I(j)}(t_r)$ and $U_{ba}(\mathbf{k}, t_r)^\dagger$ are matrices in the motional states. Recall that $U_{ba}(\mathbf{k}, t_r)$ is defined in Eq. (8.11). The trace in Eq. (8.42) is over center-of-mass states.

In principle, the calculation is now complete. One calculates $\rho_{ba}^{I(j)}(t_r)$ by piecing together the various transfer matrices calculated using the method outlined in Sec. II and then carries out the trace needed in Eq. (8.42). As specific examples, we now calculate the signal associated with the level schemes of Fig. 8.1.

8.4 Specific Example: Ground Level - Rydberg Level Coherence in an Optical Lattice

We consider first the level scheme of Fig. 8.1 (a) in which level a is a $J = 0$ ground state, level c is a $J = 0$ Rydberg level, and level b is a $J = 1$ excited state. Trap fields, counter-propagating in the $X-$direction and polarized in the $y-$direction, confine the atoms in the transverse direction

and provide attractive lattice potentials

$$V_\alpha(X) = -V_\alpha \cos^2(k_{tr}X); \quad \alpha = a, c \tag{8.43}$$

in the longitudinal (X) direction for levels a and c. Any additional contributions to the trap potentials, such as those associated with a breakdown of the dipole approximation in calculating the Rydberg potentials [33], are ignored. The trap fields can also give rise to a repulsive potential for level b, but we will see that the potential for level b is unimportant for the pulse sequence under consideration. At $t = 0$, a two-photon pulse resonantly excites atomic coherences $\rho_{ca}^{(j)}$. As a result of atomic motion, these coherences undergoes dephasing. At time $t = T_{21}$, a readout pulse that is resonant with the $c - b$ transition frequency is applied and creates the coherences $\rho_{ba}^{(j)}$. The phase-matched signal emitted by the sample, which results from the interaction of the vacuum field with the atoms, is dependent on the value of $\rho_{ba}^{(j)}$ created by the excitation and readout fields.

The excitation and readout pulses are all $z-$polarized and propagate in the $\pm X$ direction. The two-photon excitation pulse consists of two fields having propagation vectors $\mathbf{k}_1 = k_1\mathbf{u}_x$ and $\mathbf{k}_2 = -k_2\mathbf{u}_x$. The excitation pulse has an effective propagation vector $\mathbf{k}_e = \mathbf{k}_{12} = k_{12}\mathbf{u}_x$, where

$$k_{12} = k_1 - k_2, \tag{8.44}$$

an effective two-photon frequency $\omega_e = (|k_1| + |k_2|)\, c = \omega_{ca}$, and an effective two-photon Rabi frequency $\Omega_{ca}(t)$, while the readout pulse has propagation vector $\mathbf{k}_{out}$, frequency $\omega_{out} = \omega_{cb}$, and Rabi frequency $\Omega_{cb}(t)$. The waists of the excitation and readout pulses are centered at the center of the atomic cloud at times $t = 0$ and $t = T_{21}$, respectively. The trap fields are also centered at the center of the atomic cloud. It is assumed that the radial extent of the excitation field is much smaller than that of the trap fields. As a consequence, the trap fields can be taken to be constant over the excitation volume. Moreover, we assume that the atoms are sufficiently cold that any *transverse* motion can be neglected on a time scale equal to T_{21}. For example, if the atoms are cooled to 10 μK, they move a distance of order 1.8 μm in 40 μsec. For T_{21} of order 40 μsec, the transverse motion can be neglected if the waist of the excitation pulse is much greater than 1.8 μm. The pulse durations are sufficiently short to neglect *all* motion during the pulses. With these simplifying assumptions, the atomic density can taken to be constant over the excitation volume and the spatial profiles of the excitation and readout pulses, $f_e(\mathbf{R}_j)$ and $f_{out}(\mathbf{R}_j)$ can be considered as *classical* functions of atomic position.

The problem effectively reduces to a one-dimensional problem for quantized motion in poten-

tials

$$V_\alpha(X) = -V_\alpha \cos^2(k_{tr}X) = -V_\alpha + V_\alpha \sin^2(k_{tr}X);$$
$$\alpha = a, c. \tag{8.45}$$

It proves convenient to set

$$V_\alpha = \frac{1}{2}\frac{M\tilde{\omega}_\alpha^2}{k_{tr}^2}; \quad \alpha = a, c, \tag{8.46}$$

where M is the mass of the atoms - with this definition the motion near the bottom of the wells is approximately harmonic with frequency $\tilde{\omega}_\alpha$. We assume that all the atoms in the excitation volume are trapped in the lattice wells - transitions out of the wells are not included. As such the motional quantum numbers are simply those associated with the bound (or quais-bound) states of the lattice potential. It is now a simple matter to piece together the signal.

Using Eq. (8.15), we find that the excitation pulse results in a density matrix

$$\tilde{\rho}_{ca}^{(j)}\left(0^+\right) = -i\frac{\sin\left[A_e\left(\mathbf{R}_j\right)\right]}{2}\tilde{\rho}_{aa}^{(j)}\left(0^-\right), \tag{8.47}$$

where

$$A_e\left(\mathbf{R}_j\right) = f_e\left(\mathbf{R}_j\right)\int_{0^-}^{0^+} dt\Omega_{ca}(t) \tag{8.48}$$

and $f_e\left(\mathbf{R}\right)$ is the (classical) spatial profile of the excitation pulse. From Eqs. (8.13b,8.13c), it then follows that

$$\rho_{ca}^{I(j)}\left(0^+\right) = U_{ca}(k_{12}\mathbf{u}_x, 0)\tilde{\rho}_{ca}^{(j)}\left(0^+\right). \tag{8.49}$$

Between $t = 0$ and $t = T_{21}$ this coherence decays as a result of loss of population from level c with rate Γ_c, such that

$$\rho_{ca}^{I(j)}\left(T_{21}^-\right) = e^{-\gamma_c T_{21}}\rho_{ca}^{I(j)}\left(0^+\right), \tag{8.50}$$

where $\gamma_c = \Gamma_c/2$. At time $t_{out} = T_{21}$ the readout pulse transforms the $c - a$ coherence into a $b - a$ coherence which can be calculated using Eqs. (8.15) and (8.19) as

$$\rho_{ba}^{I(j)}\left(T_{21}^+\right) = \tilde{\rho}_{ba}^{(j)}\left(T_{21}^+\right) = -i\frac{\sin\left[A_{out}\left(\mathbf{R}_j\right)\right]}{2}\tilde{\rho}_{ca}^{(j)}\left(T_{21}^-\right)$$
$$= -i\frac{\sin\left[A_{out}\left(\mathbf{R}_j\right)\right]}{2}U_{cb}\left(-k_2\mathbf{u}_x, T_{21}\right)^\dagger \rho_{ca}^{I(j)}\left(T_{21}^-\right) \tag{8.51}$$

where

$$A_{out}\left(\mathbf{R}_j\right) = f_{out}\left(\mathbf{R}_j\right)\int_{T_{21}^-}^{T_{21}^+} dt\Omega_{cb}(t). \tag{8.52}$$

and $f_{out}(\mathbf{R})$ is the spatial profile of the readout pulse. For times $t > T_{21}^{+}$,

$$\rho_{ba}^{I(j)}(t) = e^{-\gamma_b (t-T_{21})} \rho_{ba}^{I(j)}\left(T_{21}^{+}\right), \tag{8.53}$$

where $\gamma_b = \Gamma_b/2$ and Γ_b is the rate at which the level b population decays.

The detector is located at position $\mathbf{R}_d = R_d \mathbf{u}_x$, which is in the direction of phase-matched emission. As a consequence, the vector $\mathbf{k}_{ba}$ appearing in Eq. (8.39) is

$$\mathbf{k}_{ba} = (\omega_{ba}/c)\,\mathbf{u}_x = k_1 \mathbf{u}_x. \tag{8.54}$$

To achieve phase-matching, it is necessary that $|k_2 - k_{out}|\, L \ll 1$, as is assumed. By combining Eqs. (8.33), (8.42), (8.47)-(8.54), we find that the phase-matched signal emitted on the $b-a$ transition at a time $\tau = t - T_{21}$ following the readout pulse is given by

$$S(T_{21}, \tau) = e^{-\Gamma_c T_{21}} e^{-\Gamma_b \tau_r} J^2 \Theta(\tau_r) \left|C(T_{21})\right|^2 \tag{8.55}$$

where

$$J = \frac{\mu_{ba}}{4}\left(\frac{\omega_{ba}^2}{4\pi\epsilon_0 c^2}\right) \int d\mathbf{R} \sin\left[A_e(\mathbf{R})\right] \sin\left[A_{out}(\mathbf{R})\right], \tag{8.56}$$

$$\tau_r = \tau - \frac{R_d}{c} = t - T_{21} - \frac{R_d}{c}, \tag{8.57}$$

Θ is a Heaviside function, and

$$\begin{aligned} C(T_{21}) &= \mathrm{Tr}\left[U_{ba}(k_1\mathbf{u}_x, T_{21})^{\dagger}\, \rho_{ba}^{I}\left(T_{21}^{+}\right)\right] \\ &= \mathrm{Tr}\left[\begin{array}{c} U_{ba}(k_1\mathbf{u}_x, T_{21})^{\dagger}\, U_{cb}(-k_2\mathbf{u}_x, T_{21})^{\dagger} \\ \times U_{ca}[k_{12}\mathbf{u}_x, 0]\, \rho_{aa}(0) \end{array}\right] \\ &= \mathrm{Tr}\left[U_{ca}(k_{12}\mathbf{u}_x, T_{21})^{\dagger}\, U_{ca}(k_{12}\mathbf{u}_x, 0)\, \rho_{aa}(0)\right] \\ &= e^{-i\omega_{cq';aq} T_{21}} B_{aq;cq'}^{\dagger}(k_{12}\mathbf{u}_x)\, B_{cq';aq''}(k_{12}\mathbf{u}_x)\, \rho_{q''q}(0). \end{aligned} \tag{8.58}$$

The matrices B and $B^{\dagger}$ are defined in Eqs. (8.7). The matrix $U_{ba}(\mathbf{k}_{ba}, t_r)^{\dagger}$ appearing in Eq. (8.42) has been evaluated at $t_r = T_{21}$, based on the assumptions that the atomic center-of-mass motion is frozen during the readout pulse and that $|\omega_{bq;aq'}|\, R_d/c \ll 1$. Note that state b has dropped out of the calculation. Equation (8.58) can be evaluated for various trap potentials. A normalized signal that depends only on T_{21} and the nature of the lattice potentials can be defined by

$$\tilde{S}(T_{21}) = \frac{S(T_{21}, \tau)}{S(0, \tau)} = e^{-\Gamma_c T_{21}} \left|C(T_{21})\right|^2. \tag{8.59}$$

8.4.1 State-independent potentials

In general, Eq. (8.58) must be used to calculate $C(T_{21})$, with matrix elements given by Eqs. (8.7). However, for *state-independent* potentials, the *internal* state does not have to be specified in calculating the matrix elements. In that case,

$$\begin{aligned} C(T_{21}) &= \langle q| \, e^{iV_aT_{21}/\hbar}e^{-ik_{12}X}e^{-iV_cT_{21}/\hbar}e^{ik_{12}X} \, |q'\rangle \, \rho_{q'q}\,(0) \\ &= \left\langle e^{-ik_{12}\hat{X}(T_{21})}e^{ik_{12}\hat{X}(0)} \right\rangle \end{aligned} \tag{8.60}$$

where $\hat{X}(T_s)$ and $\hat{X}(0)$ are Heisenberg operators. Of course, Eq. (8.60) is all but impossible to evaluate except for free atoms or for atoms moving in a harmonic potential. For our specific choice of potentials, we have

$$V_a(X) = V_c(X) = V(X) = -V_0 + V_0 \sin^2\left(k_{tr}X\right), \tag{8.61}$$

with

$$V_0 = \frac{1}{2}\frac{M\omega^2}{k_{tr}^2}. \tag{8.62}$$

8.4.1.1 Harmonic potential

In the harmonic approximation, that is, when the level a and c potentials are replaced by

$$V(X) \sim -V_0 + \frac{1}{2}M\omega^2X^2, \tag{8.63}$$

it is possible to evaluate Eq. (8.60) directly, without reverting to Eq. (8.58). For Eq. (8.63) to be a good approximation, a necessary condition is

$$\frac{V_0}{\hbar\omega} = \frac{1}{2}\frac{M\omega^2}{\hbar\omega k_{tr}^2} = \frac{1}{4\zeta_{tr}^2} \gg 1, \tag{8.64}$$

where

$$\zeta_{tr} = k_{tr}\sqrt{\frac{\hbar}{2M\omega}} \tag{8.65}$$

is the trap field Lamb-Dicke parameter.

In the harmonic approximation

$$\begin{aligned} k_{12}\hat{X}(T_{21}) &= k_{12}\left[\hat{X}(0)\cos\left(\omega T_{21}\right) + \frac{\hat{P}(0)}{M\omega}\sin\left(\omega T_{21}\right)\right] \\ &= \zeta\left[ae^{-i\omega T_{21}} + a^\dagger e^{i\omega T_{21}}\right], \end{aligned} \tag{8.66}$$

where

$$\zeta = k_{12}\sqrt{\frac{\hbar}{2M\omega}} \tag{8.67}$$

is the effective Lamb-Dicke parameter for the excitation field,

$$a = \frac{\hat{\xi} + i\hat{\nu}}{\sqrt{2}}; \tag{8.68a}$$

$$a^\dagger = \frac{\hat{\xi} - i\hat{\nu}}{\sqrt{2}}, \tag{8.68b}$$

$$\hat{\xi} = \sqrt{\frac{M\omega}{\hbar}}\hat{X}(0); \tag{8.69a}$$

$$\hat{\nu} = \frac{1}{\sqrt{\hbar M\omega}}\hat{P}(0), \tag{8.69b}$$

such that

$$\begin{aligned} C(T_{21}) &= \left\langle e^{-i\zeta\left[ae^{-i\omega T_{21}} + a^\dagger e^{i\omega T_{21}}\right]} e^{i\zeta\left[a + a^\dagger\right]} \right\rangle \\ &= e^{-i\zeta^2 \sin(\omega T_{21})} \left\langle e^{\sigma(T_{21})a^\dagger - \sigma(T_{21})^* a} \right\rangle . \end{aligned} \tag{8.70}$$

with

$$\sigma\left(T_{21}\right) = i\zeta\left[1 - e^{i\omega T_{21}}\right]. \tag{8.71}$$

The evaluation of the characteristic function

$$\left\langle e^{\sigma(T_{21})a^\dagger - \sigma(T_{21})^* a} \right\rangle$$

for various initial states can be found in standard texts [49].

For atoms prepared in a coherent state $|\alpha\rangle$,

$$C(T_{21}) = e^{-i\zeta^2 \sin(\omega T_{21})} e^{-|\sigma(T_{21})|^2/2} e^{\sigma(T_{21})\alpha^* - \sigma(T_{21})^*\alpha}, \tag{8.72}$$

and

$$|C(T_{21})| = e^{-|\sigma(T_{21})|^2/2}, \tag{8.73}$$

with

$$\left|\sigma\left(T_{21}\right)\right|^2 = 2\zeta^2\left[1 - \cos\left(\omega T_{21}\right)\right]. \tag{8.74}$$

There is minimal dephasing for a small Lamb-Dicke parameter. This dephasing is a pure quantum

effect, which vanishes in the limit that $\hbar \to 0$. In the analogous classical problem, $|C(T_{21})| = 1$, since all atoms have the same initial conditions.

If the atoms are prepared in a state having density matrix elements that are diagonal in the number representation,

$$\rho_{nn'}(0) = P_n \delta_{n,n'}, \tag{8.75}$$

then

$$\begin{aligned} C(T_{21}) &= P_n e^{-i\zeta^2 \sin(\omega T_{21})} \left\langle n \right| e^{\sigma(T_{21}) a^\dagger - \sigma(T_{21})^* a} \left| n \right\rangle \\ &= e^{-i\zeta^2 \sin(\omega T_{21})} e^{-|\sigma(T_{21})|^2/2} P_n \\ &\times \left\langle n \right| \frac{\left[\sigma(T_{21}) a^\dagger\right]^q \left[-\sigma(T_{21})^* a\right]^p}{q! p!} \left| n \right\rangle . \end{aligned} \tag{8.76}$$

Only terms with $p = q$ enter the sum; moreover

$$a^p \left| n \right\rangle = \begin{cases} \sqrt{\frac{n!}{(n-p)!}} \left| n - p \right\rangle & p \le n \\ 0 & p > n \end{cases} , \tag{8.77}$$

such that

$$\begin{aligned} C(T_{21}) &= e^{-i\zeta^2 \sin(\omega T_{21})} e^{-|\sigma(T_{21})|^2/2} \\ &\times \sum_{n=0}^{\infty} P_n \sum_{q=0}^{n} \frac{n!}{(n-q)!} \frac{(-1)^q \left|\sigma(T_{21})\right|^{2q}}{(q!)^2} \\ &= e^{-i\zeta^2 \sin(\omega T_{21})} e^{-|\sigma(T_{21})|^2/2} \sum_{n=0}^{\infty} P_n L_n \left(\left|\sigma(T_{21})\right|^2 \right) , \end{aligned} \tag{8.78}$$

where $L_n(z)$ is a Laguerre polynomial.

If the atoms are prepared in a number state, $P_q = \delta_{q,n}$

$$|C(T_{21})| = e^{-|\sigma(T_{21})|^2/2} L_n \left(\left|\sigma(T_{21})\right|^2 \right) . \tag{8.79}$$

The value of $C(T_{21})$ is identical for an initial coherent state and an initial vacuum state since the spatial widths of both packets are identical and do not change in time. For a thermal state with

$$P_n = \left(1 - e^{-\beta}\right) e^{-n\beta}; \qquad \beta = \frac{\hbar\omega}{k_B T}, \tag{8.80}$$

$$|C(T_{21})| = e^{-|\sigma(T_{21})|^2/2}\left(1-e^{-\beta}\right)\sum_{n=0}^{\infty} e^{-n\beta} L_n\left(|\sigma(T_{21})|^2\right)$$
$$= e^{-\frac{1}{2}|\sigma(T_{21})|^2\coth(\beta/2)} = e^{-\zeta^2[1-\cos(\omega T_{21})]\coth(\beta/2)}. \tag{8.81}$$

For a Poissonian distribution,

$$P_n = e^{-\bar{n}}\frac{\bar{n}^n}{n!}, \tag{8.82}$$

$$|C(T_{21})| = e^{-|\sigma(T_{21})|^2/2} e^{-\bar{n}} \sum_{n=0}^{\infty} \frac{\bar{n}^n}{n!} L_n\left(|\sigma(T_{21})|^2\right), \tag{8.83}$$

which must be evaluated numerically. For large $\bar{n}$, the result is similar to the result for a number state having $n = \bar{n}$. For a squeezed vacuum with squeeze parameter $z = re^{i\theta}$,

$$|C(T_{21})| = \left|\langle 0|\, e^{g(T_{21})a^\dagger - g(T_{21})^* a}\,|0\rangle\right| = e^{-|g(T_{21})|^2/2}, \tag{8.84}$$

where

$$g\left(T_{21}\right) = \sigma(T_{21})\cosh r + \sigma^*(T_{21})e^{i\theta}\sinh r \tag{8.85}$$

For a squeezing parameter $r \gg 1$, $|C(T_{21})| \ll 1$, in general. Of course, $C(T_{21}) = 1$ at the revival times when ωT_{21} is an integral multiple of 2π. However, there is an *additional* time during each period when there is a complete revival, occurring when $\omega T_{21} = \theta \pm (2n+1)\,\pi$. For example, when θ equals zero, additional revivals occur for values ωT_{21} that are odd integral multiples of π. In this case, from Eq. (8.66),

$$k_{12}\left[\hat{X}(T_{21} = \pi/\omega)\right] = -k_{12}\hat{X}(0). \tag{8.86}$$

Since the momentum operator no longer appears, the signal can be optimized by squeezing the spatial distribution. For values $\omega T_{21} = \theta \pm (2n+1)\,\pi$, it is some combination of the momentum and coordinate distributions that is squeezed.

In Fig. 8.2, we plot $|C(T_{21})|^2$ as a function of ωT_{21} for initial pure number state and Poissonian distributions, with $\zeta = 0.23$. It is seen that if $\bar{n}$ of the Poissonian distribution equals n of the number state distribution, the two results do not differ by much. In Fig. 8.3, we plot $|C(T_{21})|^2$ as a function of ωT_{21} for initial coherent state (solid red curve) and squeezed vacuum state distributions (dashed blue and solid black curves), with $\zeta = 0.23$. The dashed blue curve is for squeezing parameters $r = 1.5, \theta = 0$ and the solid black for $r = 4, \theta = 0$. The extra peaks at $\omega T_{21} = (2n+1)\,\pi$ are a clear signature of the quantum nature of the initial motional state associated with the squeezed vacuum.

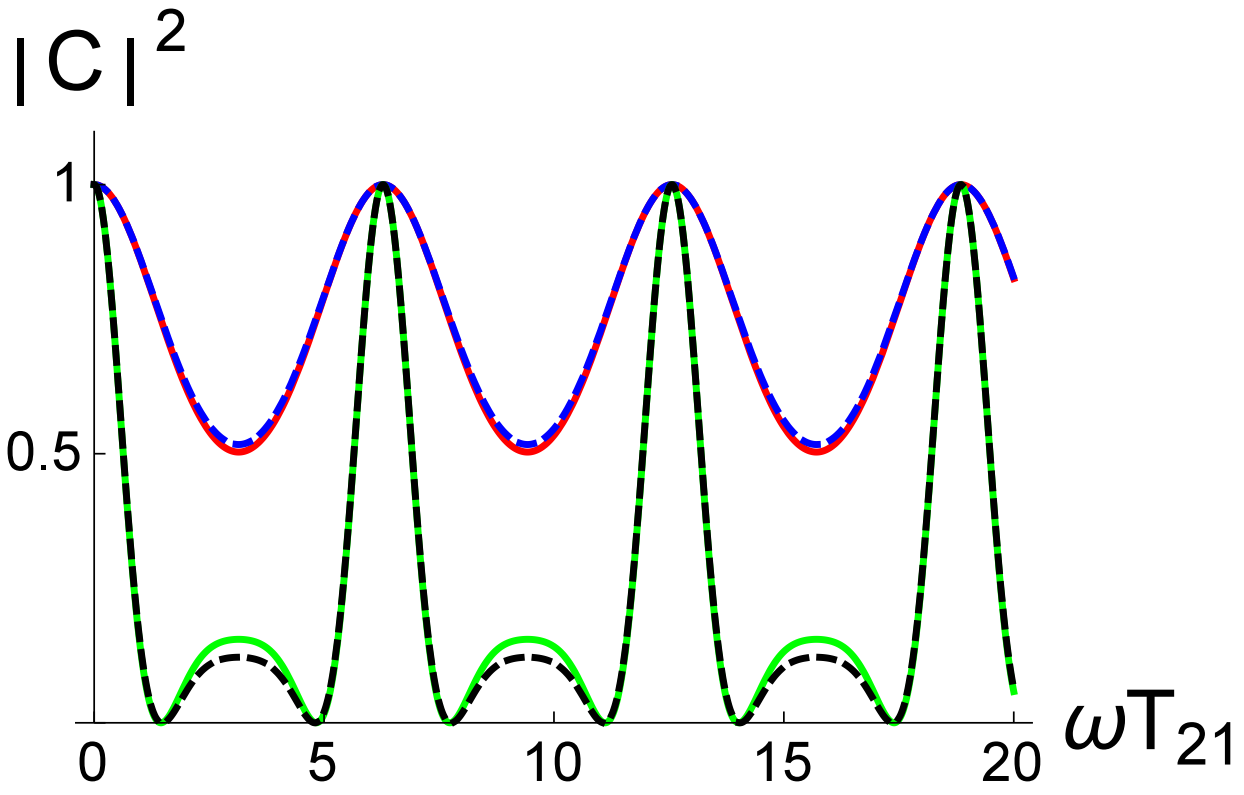

Figure 8.2: Plots of $|C(T_{21})|^2$ as a function of ωT_{21} for a state-independent, harmonic lattice potential and for initial number state and Poissonian distributions, with $\zeta = 0.23$ The solid red and green curves are for initial number state distributions with $n = 1$ and 15, respectively. The dashed blue and black curves are for initial Poissonian distributions with $\bar{n} = 1$ and 15, respectively.

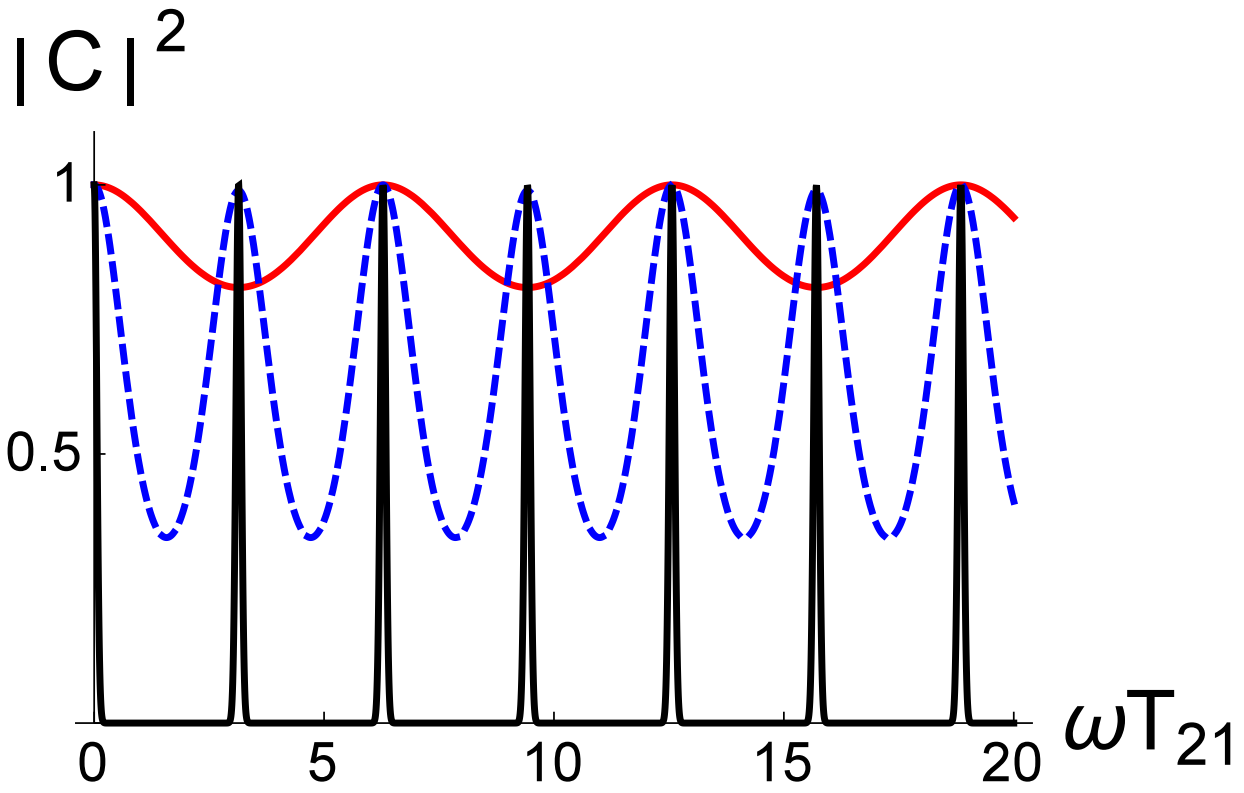

Figure 8.3: Plots of $|C(T_{21})|^2$ as a function of ωT_{21} for a state-independent, harmonic lattice potential and for initial coherent state (solid red curve) and squeezed vacuum state distributions (dashed blue curve - $r = 1.5$, solid black curve - $r = 4$), with $\zeta = 0.23$.

Classical limit We can take a classical limit of Eq. (8.60) by ignoring the commutator of $\hat{X}(T_s)$ and $\hat{X}(0)$ and replacing the operators by their classical counterparts to arrive at

$$\begin{aligned} C_{cl}(T_{21}) &\sim \left\langle e^{-ik_{12}[X(T_{21})-X(0)]} \right\rangle \\ &= \left\langle e^{-ik_{12}[X_0[\cos(\omega T_{21})-1]+(v_0/\omega)\sin(\omega T_{21})]} \right\rangle , \end{aligned} \tag{8.87}$$

where the average is now a classical average over the distribution of initial conditions. For a thermal distribution,

$$W_0\left(X_0, v_0\right) = \frac{M\omega}{2\pi k_B T} \exp\left[-\frac{1}{2}\frac{Mv_0^2 + M\omega^2 X_0^2}{k_B T}\right], \tag{8.88}$$

we find

$$\begin{aligned} |C_{cl}(T_{21})| &= e^{-2\zeta^2[1-\cos(\omega T_{21})]/\beta} \\ &= \exp\left[-\frac{k_B T}{2V_0}\frac{k_{12}^2}{k_{tr}^2}[1-\cos\left(\omega T_{21}\right)]\right], \end{aligned} \tag{8.89}$$

independent of $\hbar$. The classical [Eq. (8.89)] and quantum [Eq. (8.81)] results agree for $\beta \ll 1$ (high temperature limit). Somewhat remarkably, even for $\beta = 1$, the difference between the classical and quantum predictions is small if the Lamb-Dicke parameter is less than or of order unity. For $\beta \gg 1$ (low temperature limit), $|C_{cl}(T_{21})| \sim 1$, whereas $|C(T_{21})| \sim e^{-\frac{1}{2}|\sigma(T_{21})|^2}$. A comparison of the classical and quantum results is shown in Fig. 8.4, with $\zeta = 0.23$. The solid curves are the quantum results and the dashed curves the classical results. It is seen that, even for $\beta = 0.5$, the two results practically overlap. On the other hand, for very cold atoms, $\beta = 10$, the classical result is almost equal to unity, whereas the quantum result still exhibits dephasing owing to the spread of momentum in the ground state wave function.

8.4.1.2 Anharmonic motion

If the potential is not sufficiently deep for the harmonic approximation to be valid, it is necessary to use the eigenfunctions and eigenenergies for a potential that varies as $V_0 \sin^2\left(k_{tr}X_0\right)$ (the $-V_0$ part of the potential can be dropped since it plays no role in this calculation). The periodic eigenfunctions and eigenvalues for a $\sin^2\left(k_{tr}X_0\right)$ potential are the so-called A_n and B_{n+1} Mathieu functions [50]. As long as the potential is sufficiently deep and the temperature sufficiently low, the only eigenfunctions of importance are those associated with the quasi-bound states of the potentials for which the A_n and B_{n+1} Mathieu functions are nearly identical, as are the eigenenergies associated with these eigenfunctions. This is the only limit we will consider.

The calculation of Eq. (8.58) must now be carried out numerically. For $\zeta = 0.23$ and $\zeta_{tr} = 0.16$,

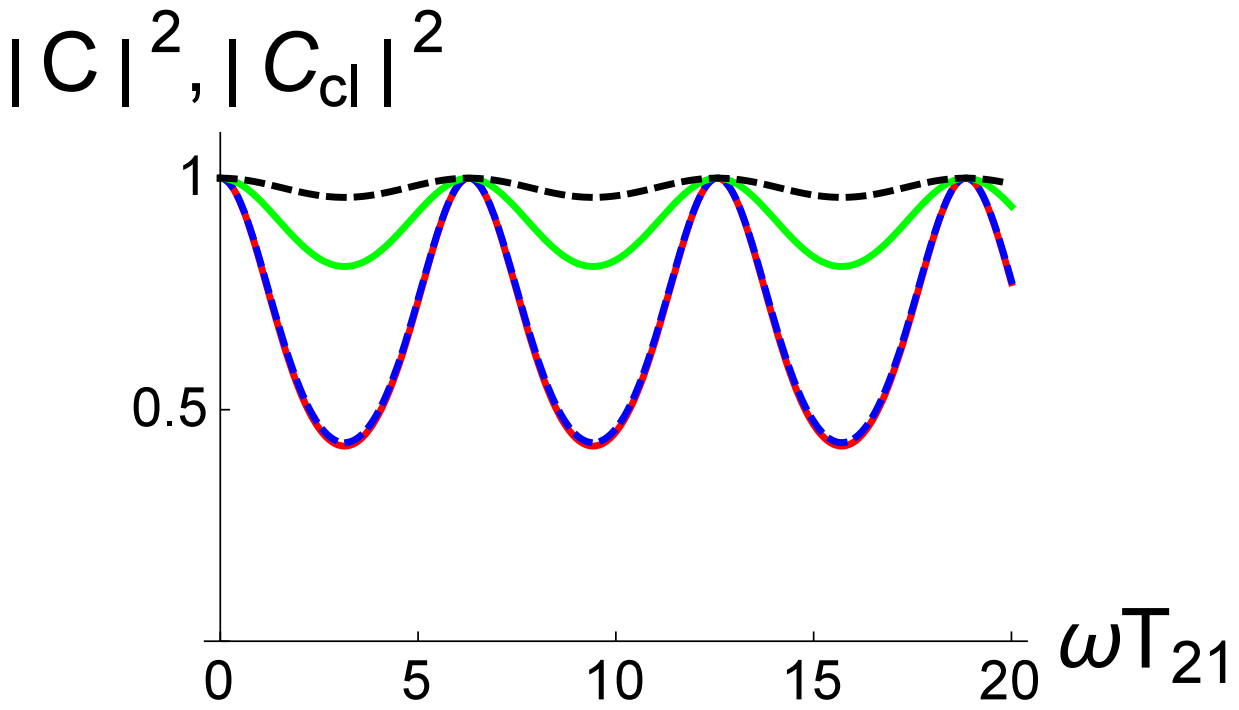

Figure 8.4: Plots of $|C(T_{21})|^2$ and $|C_{cl}(T_{21})|^2$ as a function of ωT_{21} for a state-independent, harmonic lattice potential and for initial thermal distributions, with $\zeta = 0.23$. The solid red and green curves are the quantum results with $\beta = 0.5$ and 10, respectively. The dashed blue and black curves are the corresponding classical results.

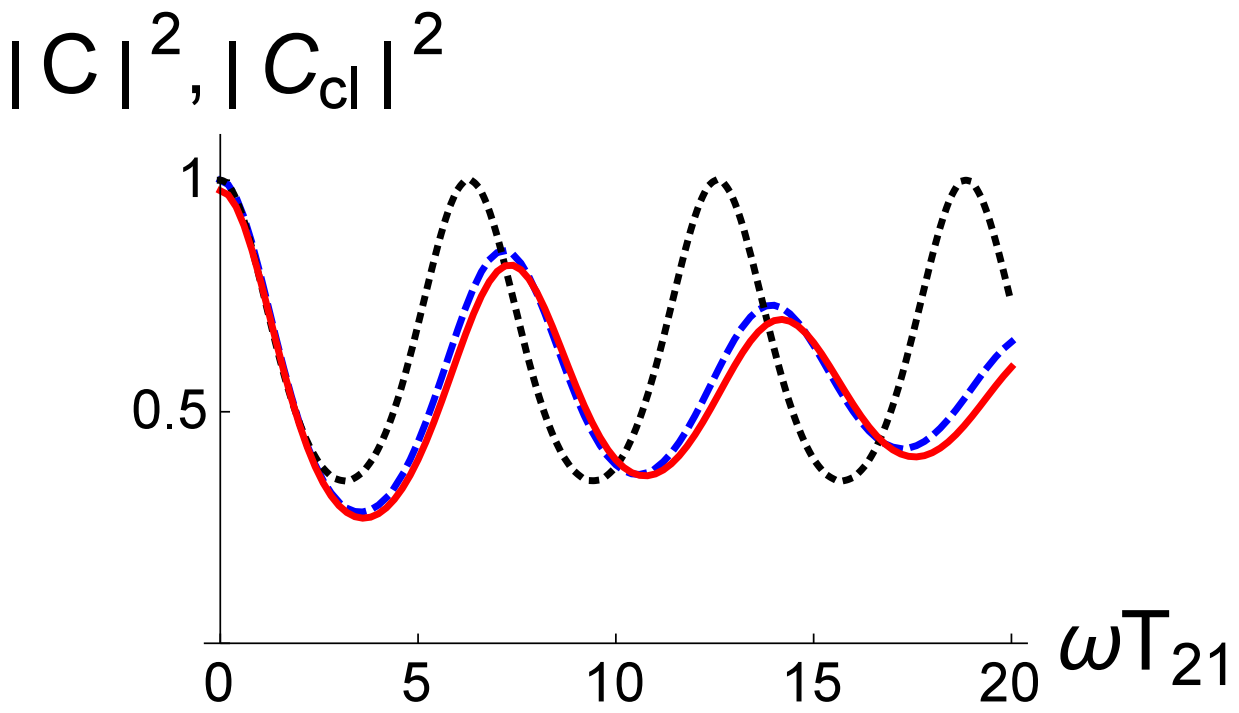

Figure 8.5: Plots of $|C(T_{21})|^2$ and $|C_{cl}(T_{21})|^2$ as a function of ωT_{21} for a state-independent, anharmonic lattice potential and for an initial thermal distribution with $\zeta = 0.23$, $\zeta_{tr} = 0.16$, and $\beta = 0.41$. The solid red curve is the quantum result, the dashed blue curve is the classical result, and the dotted black curve is the quantum result for the corresponding harmonic potential.

results are shown in Figs. 8.5 and 8.6 as the solid red curves for $\beta = 0.41$ and $\beta = 3$, respectively. The anharmonicity leads to a reduction of the amplitude of oscillation, as well as a decay of the signal, owing to the continuous range of frequencies present in the response. For comparison the results for the corresponding harmonic potential are shown as the dotted black curves in the figures. Even in the case of cold atoms, $\beta = 3$, when the harmonic approximation is expected to be good, the anharmonic and harmonic results begin to diverge at longer times, owing to the fact that small changes in frequency can still lead to significant phase shifts for sufficiently long times.

Classical limit The fact that the classical and quantum results for a harmonic potential are nearly identical for $\beta \lesssim 1$ when $\zeta < 1$ suggests that the quantum and classical results for a potential that varies as $V_0 \sin^2(k_{tr}X)$ might also be nearly identical. The total energy associated with the center-of-mass motion of an atom can be written as

$$E = \frac{1}{2}\left[M\left(\frac{dX}{dt}\right)^2 + \frac{M\omega^2}{k_{tr}^2}\sin^2(k_{tr}X)\right] \tag{8.90}$$

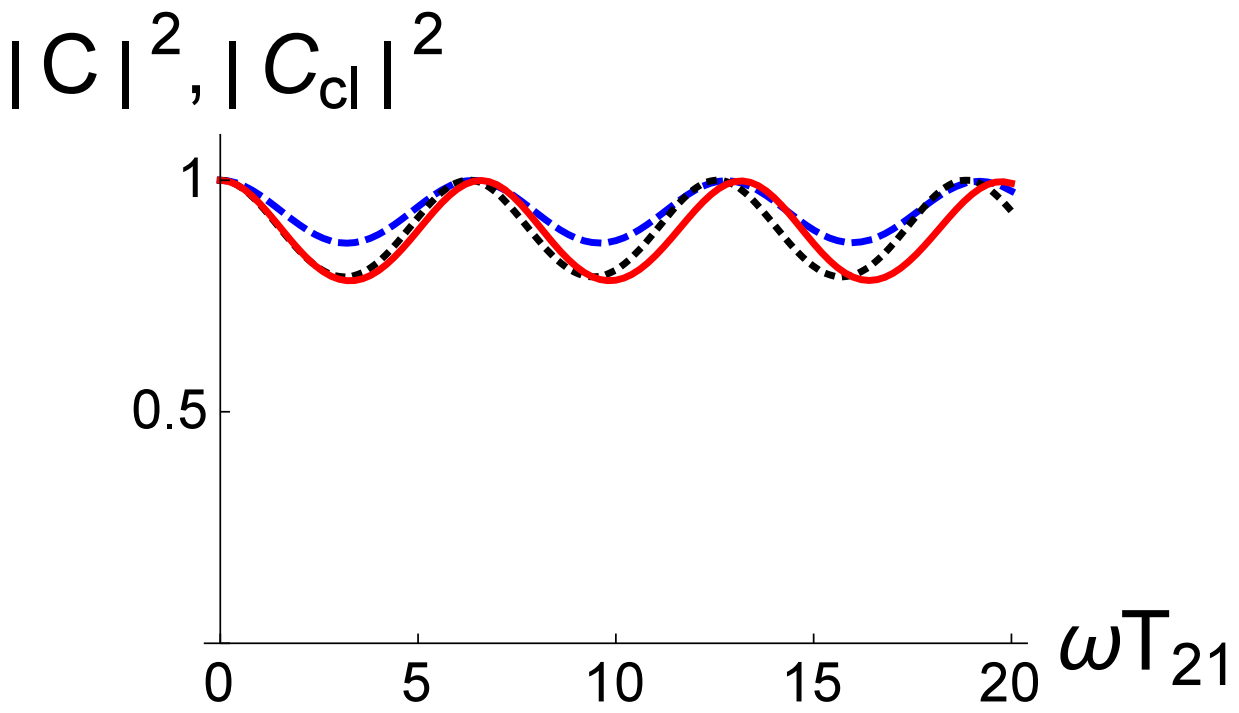

Figure 8.6: Same as Fig. 8.5, but with $\beta = 3$.

where ω is defined by Eq. (8.62), and X and dX/dt are the position and velocity of the atom. Setting $k_{tr}X = z$ and $\omega t = \tau$, and using Eqs. (8.67) and (8.80), we can rewrite the energy as

$$E = \frac{\beta k_B T}{4\zeta_{tr}^2}\left(\dot{z}^2 + \sin^2 z\right), \tag{8.91}$$

where the dot signifies differentiation with respect to τ.

The equation of motion for an atom moving in this potential is

$$\ddot{z} = -\frac{\sin z}{2}. \tag{8.92}$$

The solution of this equation can be written as

$$z(\tau) = \text{JacobiAmplitude}\left[\begin{array}{c}\text{EllipticFunctionF}\left(z_0; \frac{1}{\epsilon}\right) \\ +\sqrt{\epsilon}\tau, \frac{1}{\epsilon}\end{array}\right], \tag{8.93}$$

where

$$\epsilon = \left(\dot{z}_0^2 + \sin^2 z_0\right), \tag{8.94}$$

$z_0 = z(0)$, and $\dot{z}_0 = \dot{z}(0)$, and JacobiAmplitude and EllipticFunctionF are built in functions in

Mathematica. It then follows that, for a thermal distribution with E given by Eq. (8.91),

$$|C_{cl}\left(T_{21}\right)|^2 = \frac{\begin{array}{c}\int_{-\pi/2}^{\pi/2} dz_0 \int_{-\sqrt{1-\sin^2 z_0}}^{\sqrt{1-\sin^2 z_0}} d\dot{z}_0 \\ \times e^{-\frac{\beta}{4\zeta_{tr}^2}\left(\dot{z}_0^2+\sin^2 z_0\right)-i[z(\omega T_{21})-z_0]}\end{array}}{\begin{array}{c}\int_{-\pi/2}^{\pi/2} dz_0 \int_{-\sqrt{1-\sin^2 z_0}}^{\sqrt{1-\sin^2 z_0}} d\dot{z}_0 \\ \times e^{-\frac{\beta}{4\zeta_{tr}^2}\left(\dot{z}_0^2+\sin^2 z_0\right)}\end{array}}, \tag{8.95}$$

where the integrals have been restricted to bound state motion. The integrals can be evaluated numerically. In Figs. 8.5 and 8.6, $|C_{cl}\left(T_{21}\right)|^2$ is plotted as the dashed blue curves for $\beta = 0.41$ and $\beta = 3$, respectively. As can be seen, the classical and quantum results are in good agreement for $\beta = 0.41$, but differ somewhat for cold atoms, $\beta = 3$, when the classical picture is expected to fail.

8.4.2 State-dependent potentials

When the potentials are state-dependent, it is necessary to revert to Eq. (8.58). We consider only harmonic potentials. From Eq. (8.58), it is seen that, for incommensurable frequencies $\tilde{\omega}_a$ and $\tilde{\omega}_c$ of the motional states of the level a and c potentials defined in Eq. (8.46), there are no complete revivals of the signal. On the other hand, if $\tilde{\omega}_c = (m/n)\,\tilde{\omega}_a$, where both m and n are integers and n is the least common denominator, then revivals occur at integral multiples of $\tilde{\omega}_a T_{21} = 2n\pi$. In Figs. 8.7 and 8.8, we plot $|C(T_{21})|^2$ as a function of $\tilde{\omega}_a T_{21}$ for a thermal initial state with $\zeta = 0.23$, $\beta = 3$ or 0.41, and several values of $s = \tilde{\omega}_c/\tilde{\omega}_a$.

For cold atoms, $\beta = 3$, most of the initial population is in the ground state and only the frequencies associated with the lowest transitions in both wells appear in the signal (Fig. 8.7). For $s = 1.05$, these frequencies are not resolved and we see a slight damping of the signal. For $s = 1.5$ and $s = \sqrt{2}$, both frequencies are evident, as is the complete revival of the signal at $\tilde{\omega}_a T_{21} = 4\pi$ for $s = 1.5$. For $s = 1.05$ there is a complete revival (not shown) at $\tilde{\omega}_a T_{21} = 40\pi$.

The situation changes for hotter atoms, $\beta = 0.41$, since many transitions contribute to the signal and tend to wash out the signal, as shown in Fig. 8.8. For $s = 1.05$, the signal is damped - a complete revival would occur at $\tilde{\omega}_a T_{21} = 40\pi$. For $s = 1.5$, the complete revival is seen at $\tilde{\omega}_a T_{21} = 4\pi$. Somewhat surprisingly, there is a *partial* revival for incommensurate frequencies, $s = \sqrt{2}$. It is not difficult to understand why this occurs. If we write $s = 1 + \sigma$ and insert this into Eq. (8.58), we see that, for times $\tilde{\omega}_a T_{21} = 2n\pi/\sigma$, the expression reduces to that for a *state-independent harmonic potential* having frequency $\tilde{\omega}_a$. The value of $|C(T_{21})|^2$ for a state-independent potential is calculated using Eq. (8.81) as $\exp\left\{-2\zeta^2\left[1-\cos\left(\tilde{\omega}_a T_{21}\right)\right]\coth(\beta/2)\right\}$. For $\beta = 0.41$ and $\zeta = 0.23$, $|C(T_{21})|^2 \geq 0.35$ so a partial revival is seen at integral multiples of

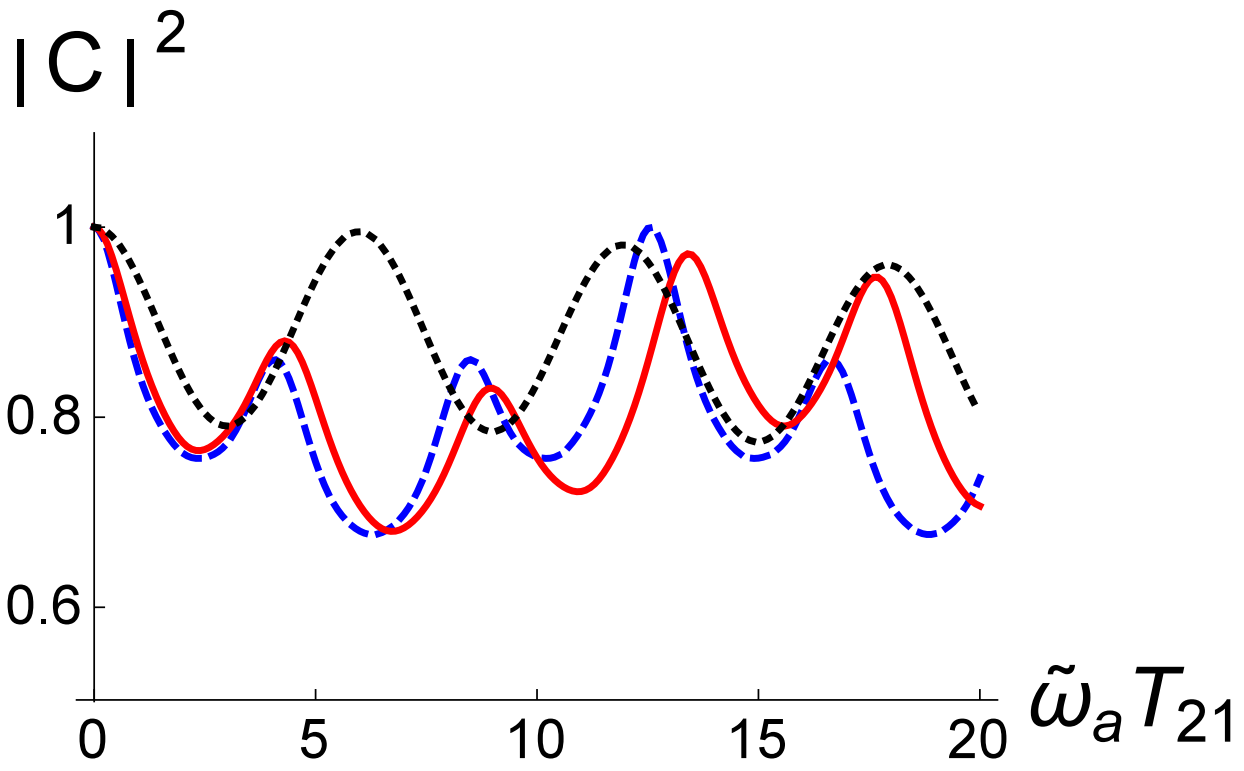

Figure 8.7: Graphs of $|C(T_{21})|^2$ as a function of $\tilde{\omega}_a T_{21}$ for a state-dependent, harmonic lattice potential and for a thermal initial state with $\zeta = 0.23$, $\beta = 3$, and $s = 1.05$ (black, dotted curve), $s = \sqrt{2}$ (blue, dashed curve) and $s = 1.5$ (red, solid curve).

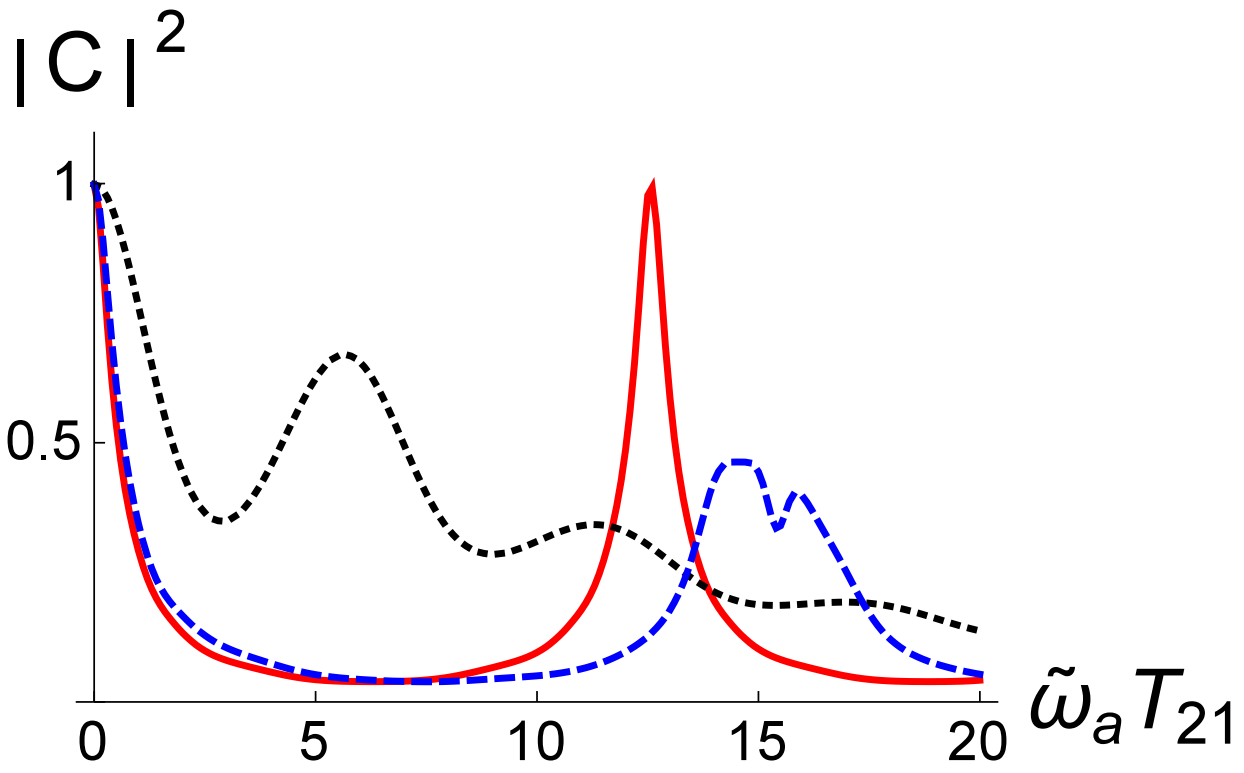

Figure 8.8: Graphs of $|C(T_{21})|^2$ as a function of $\tilde{\omega}_a T_{21}$ for a state-dependent, harmonic lattice potential and for a thermal initial state with $\zeta = 0.23$, $\beta = 0.41$, and $s = 1.05$ (black, dotted curve), $s = \sqrt{2}$ (blue, dashed curve) and $s = 1.5$ (red, solid curve).

$\tilde{\omega}_a T_{21} = 2\pi/\sigma$.

An additional effect enters the calculation that is not present for state-independent potentials. Owing to the difference in the values of V_α the energy levels in the harmonic potentials are displaced by different amounts. In other words, we have set

$$V_\alpha(\mathbf{R}) \approx -V_\alpha + \frac{1}{2} M \tilde{\omega}_\alpha^2 X^2; \qquad \alpha = a, c, \tag{8.96}$$

and have assumed that both $\tilde{\omega}_\alpha$ and V_α are independent of the transverse coordinate ρ. If this assumption is not valid for V_α, $C(T_{21})$ must be multiplied by an additional factor, $\exp\{-i\left[V_c(\rho) - V_a(\rho)\right] T_{21}/\hbar\}$ and included in the average over the excitation field spatial profiles. This would result in a damping of the signal with increasing T_{21}, making it difficult to observe the revivals when the potentials differ significantly.

8.5 Specific Example: Raman Coherence - Transit-time Effects

We now turn our attention to the level scheme if Fig. 8.1 (b) and assume co-propagating excitation fields with $k_1 \approx k_2$. In this limit we can ignore the spatial phase factors in Eqs. (8.7). We assume that we need only take into account transverse effects. As such, the only net effect that we study in this section is one of *transit-time* loss and revival. The excitation fields carve out an excitation volume, but atomic motion takes atoms out of this volume, an effect that is monitored by the readout pulse. In essence, this is a quantum treatment of transit-time effects, which can be compared with the classical results for free atoms [51] or atoms in traps. We consider only harmonic traps and state-independent, harmonic potentials having characteristic frequency ω. The readout field and two fields comprising the excitation field are assumed to have the same waist, w_e.

8.5.1 Classical Limit

We consider first the classical limit, for which the normalized signal can be written as

$$\tilde{S}\left(T_{21}\right) = \frac{S\left(T_{21}, \tau\right)}{S\left(0, \tau\right)} = \tilde{S}_{cl}\left(T_{21}\right), \tag{8.97}$$

where

$$\tilde{S}_{cl}\left(T_{21}\right) = \left| \frac{C_{cl}\left(T_{21}\right)}{C_{cl}\left(0\right)} \right|^2, \tag{8.98}$$

$$C_{cl}\left(T_{21}\right)=\frac{1}{4}\left\langle \sin\left[A_e e^{-2\rho(0)^2/w_e^2}\right] \times \sin\left[A_{out} e^{-\rho(T_{21})^2/w_e^2}\right]\right\rangle, \tag{8.99}$$

$$\boldsymbol{\rho}(0)=\boldsymbol{\rho}_0; \tag{8.100a}$$

$$\boldsymbol{\rho}(t)=\boldsymbol{\rho}_0\cos\left(\omega t\right)+\frac{\mathbf{v}_0}{\omega}\sin\left(\omega t\right), \tag{8.100b}$$

and the average is taken with the classical Maxwell-Boltzmann distribution given in Eq. (8.88). With a change of variables to dimensionless coordinates, we find

$$\begin{aligned} C_{cl}\left(T_{21}\right) &= \frac{1}{16\pi^2}\int_{-\infty}^{\infty}dy\int_{-\infty}^{\infty}dv_y\int_{-\infty}^{\infty}dz\int_{-\infty}^{\infty}dv_z \\ &\times e^{-(y^2+v_y^2)/2}e^{-(z^2+v_z^2)/2}\sin\left(A_e e^{-\kappa^2\left(y^2+z^2\right)}\right) \\ &\times\sin\left[A_{out}\exp\left\{-\frac{\kappa^2}{2}\left[\begin{array}{c}\left(y^2+z^2\right)\cos^2\left(\omega T_{21}\right)\\ +\left(v_y^2+v_z^2\right)\sin^2\left(\omega T_{21}\right)\\ +\left(yv_y+zv_z\right)\sin\left(2\omega T_{21}\right)\end{array}\right]\right\}\right], \end{aligned} \tag{8.101}$$

where

$$\kappa=\sqrt{\frac{2k_BT}{M\omega^2w_e^2}}=\frac{w_{th}}{w_e}, \tag{8.102}$$

and

$$w_{th}=\sqrt{\frac{2k_BT}{M\omega^2}} \tag{8.103}$$

is the spatial width associated with the classical Boltzmann distribution at temperature T.

If the $\sin$ functions are expanded, all the integrals can be evaluated analytically and the result expressed as

$$\begin{aligned} C_{cl}\left(T_{21}\right) &= \frac{1}{4}\sum_{n,m=0}^{\infty}\frac{(-1)^{n+m}A_e^{(2n+1)}A_{out}^{(2m+1)}}{(2n+1)!\,(2m+1)!} \\ &\times\frac{1}{1+\kappa^2\left(3+2m+4n\right)+2\kappa^4\left(2n+1\right)\left(2m+1\right)\sin^2\left(\omega T_{21}\right)}. \end{aligned} \tag{8.104}$$

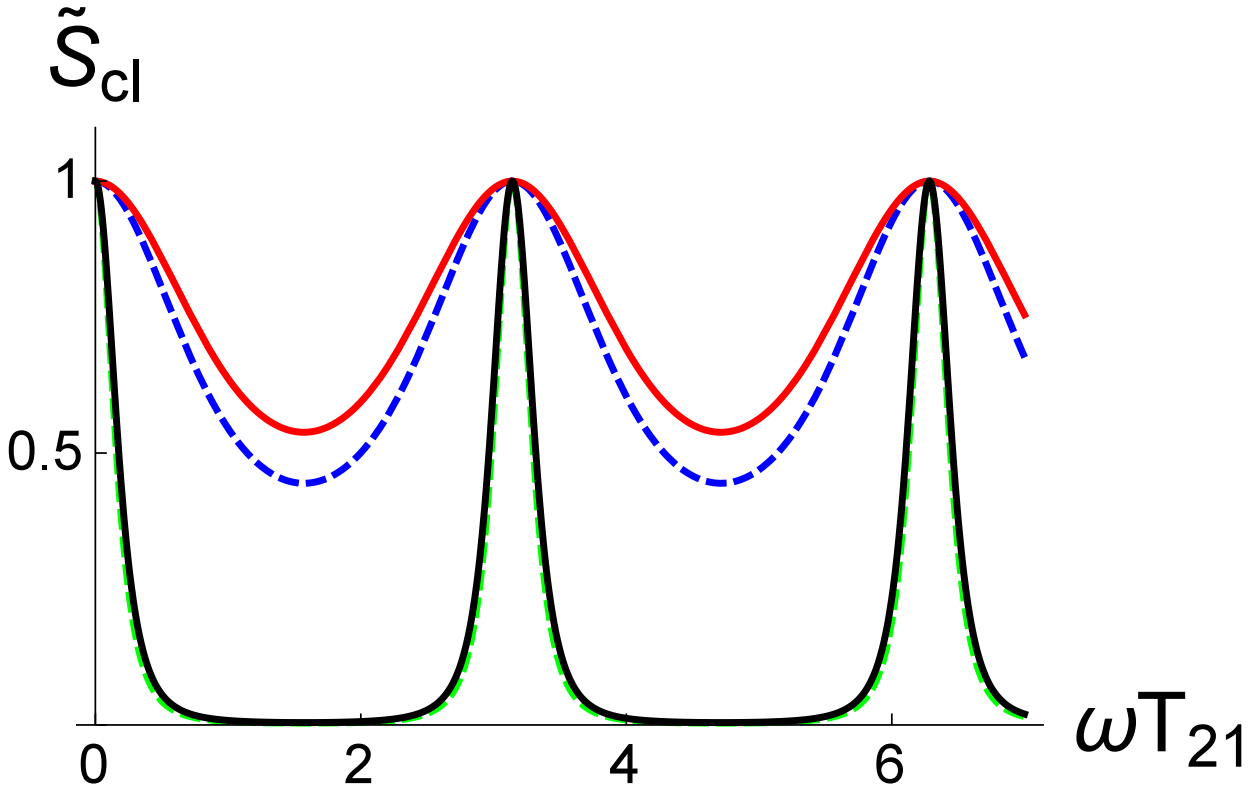

Figure 8.9: Plots of $\tilde{S}_{cl}\left(T_{21}\right)$ as a function of ωT_{21} for a state-independent, transverse harmonic potential with $\beta = 0.1$ and $\kappa = 1$ (red and blue curves) ; $\kappa = 5$ (black and green curves). The solid curves are for pulse areas $(A_1, A_2) = (0.1, 0.1)$ and the dashed curves for $(A_1, A_2) = (\pi/2, \pi/2)$.

In the perturbation theory limit, $A_e, A_{out} \ll 1$,

$$C_{cl}\left(T_{21}\right) \sim \frac{A_e A_{out}/4}{1 + 3\kappa^2 + 2\kappa^4 \sin^2\left(\omega T_{21}\right)} \tag{8.105}$$

and

$$\tilde{S}_{cl}\left(T_{21}\right) \sim \left[1 + \frac{2\kappa^4 \sin^2\left(\omega T_{21}\right)}{1 + 3\kappa^2}\right]^{-2}. \tag{8.106}$$

In Fig. 8.9, $\tilde{S}_{cl}\left(T_{21}\right)$ is plotted as a function of ωT_{21} for $\beta = 0.1$, $\kappa = 1, 5$ and $(A_1, A_2) = (0.1, 0.1)\,, (\pi/2, \pi/2)$. The signal decays owing to transit time effects, but eventually revives for $\omega T_{21} = n\pi$; that is, any atoms that leave the excitation volume return to it after each half-period of oscillation. There is not much difference in the *normalized* signal for weak pulses and (optimal) $\pi/2$ pulses. The transit time regime is shown in Fig. 8.10 for $\kappa = 3, 8$ and $(A_1, A_2) = (0.1, 0.1)\,, (\pi/2, \pi/2)$. To a good approximation the perturbation theory result for $\kappa^2 \gg 1$ and $\omega T_{21} \ll 1$ is the square of a Lorentzian,

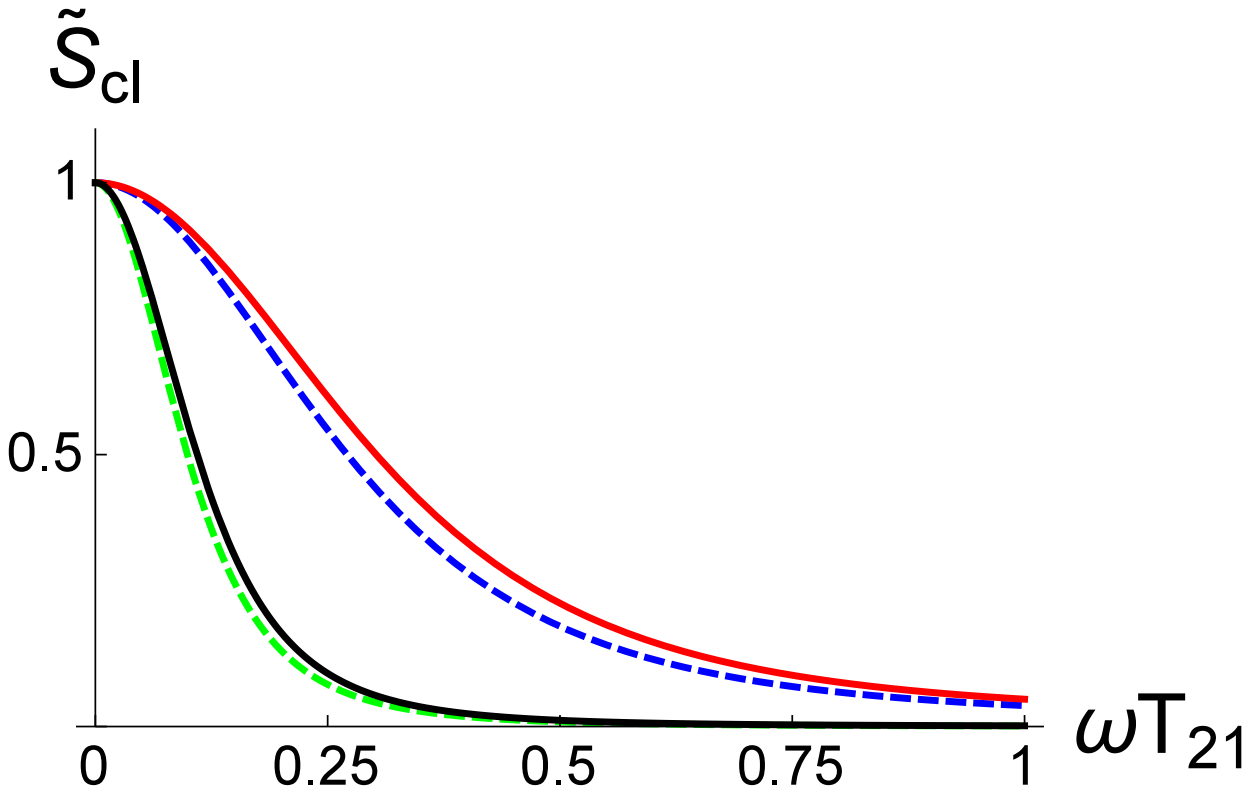

Figure 8.10: Plots of $\tilde{S}_{cl}\,(T_{21})$ illustrating transit-time decay as a function of ωT_{21} for a state-independent, transverse harmonic potential with $\beta = 0.1$ and $\kappa = 3$ (red and blue curves) ; $\kappa = 8$ (black and green curves). The solid curves are for pulse areas $(A_1, A_2) = (0.1, 0.1)$ and the dashed curves for $(A_1, A_2) = (\pi/2, \pi/2)$.

$$\tilde{S}_{cl}\left(T_{21}\right) \sim \frac{1}{\left[1+\frac{2\kappa^2(\omega T_{21})^2}{3}\right]^2}, \tag{8.107}$$

having half width

$$\omega T_{21} = \frac{\sqrt{3\left(\sqrt{2}-1\right)/2}}{\kappa}. \tag{8.108}$$

The classical results can be given a simple interpretation. In this picture involving classical center-of-mass motion, any atom j that is in the initial excitation volume has a coherence $\rho_{ac}^{(j)}$ created by the excitation field. When probed by the readout field, atom j will contribute to the phase matched signal, provided it is *still* in the excitation volume at the time of the readout pulse. The time it takes an atom to leave the excitation volume is of order $t_{cl} = w_e/u_{th}$, where

$$u_{th} = \sqrt{\frac{2k_BT}{M}} \tag{8.109}$$

is the velocity width associated with the classical Boltzmann distribution at temperature T. Therefore, we would expect a transit time width of order

$$\omega t_{cl} = \omega w_e/u_{th} = 1/\kappa, \tag{8.110}$$

which is what we found. Of course, at half-integral multiples of the trap period, any atom that was excited initially is back in the excitation volume.

The quantity w_{th} is the width of the Boltzmann distribution. For $\kappa^2 \ll 1$, the excitation field width w_e is much larger than w_{th}; as a consequence almost *all* the atoms are excited by the field. The Maxwellian velocity distribution results in some loss of population from the excitation volume as time progresses, but this is a minimal loss since very few atoms move outside this large excitation volume in a trap period, implying that $\tilde{S}_{cl}\left(T_{21}\right) \sim 1$. For $1 < \kappa^2 \ll 10$, about a half to a quarter of the atoms are excited by the first pulse. The velocity distribution of the chosen atoms is still given by the initial Maxwellian distribution since there is no velocity selection in the excitation process. Between the revival times a significant percentage of this population migrates out of the excitation region, leading to a signal loss that depends on T_{21}. For $\kappa^2 \gg 10$ only a very small fraction of the atoms are excited and they quickly migrate out of the excitation volume. The signal in this case is a series of spikes of unit amplitude at the revival times, with virtually no signal between those times.

8.5.2 Quantum Calculation

We want to derive the corresponding results for a quantum thermal distribution. We expect that a quantum description is needed if either of two conditions are not met. First, when $\beta \gg 1$, most of the initial state population is in the quantum ground state, which introduces quantum corrections. That is, the quantum and classical results will differ whenever $\beta \gg 1$, even though these differences may be small in an absolute sense if $\kappa \ll 1$. The second condition can be inferred from Eq. (8.81), where, even for $\beta \ll 1$, there are quantum corrections of order $\beta\zeta^2$. In the transit-time calculation, ζ is replaced by $\zeta_e = \sqrt{\hbar/2M\omega w_e^2}$ and

$$\beta\zeta^2 \to \beta\zeta_e^2 = \beta^2\kappa^2/4. \tag{8.111}$$

Thus we can expect quantum corrections to contribute when $\beta\kappa > 1$, even if $\beta \ll 1$. This is related to the fact that the narrow spatial distribution that is excited when $\kappa \gg 1$ can lead to uncertainties in the momentum distribution (owing to the uncertainty principle) that are larger than those already present in the thermal momentum distribution.

Since the *normalized* signal does not depend strongly on the pulse areas, it suffices to calculate $S(T_{21})$ in the quantum case assuming pulse areas much less than unity. The normalized signal, written using dimensionless coordinates, factors into equal contributions from each of the transverse coordinates. As a consequence, we can write

$$\tilde{S}(T_{21}) = \left|\frac{C(T_{21})}{C(0)}\right|^4 \tag{8.112}$$

where

$$\begin{aligned} C(T_{21}) = {} & e^{-i\omega_{cq';aq}T_{21}} \langle q| e^{-\beta\kappa^2\xi^2} |q'\rangle \langle q'| e^{-\beta\kappa^2\xi^2/2} |q''\rangle \\ & \times \rho_{aq'';aq}(0), \end{aligned} \tag{8.113}$$

ξ is a dimensionless coordinate and the q's are quantum numbers of a one-dimensional oscillator potential. Transit time effects enter implicitly through the exponential time factors. The needed matrix elements can be evaluated explicitly using

$$\begin{aligned} \langle q| e^{-g^2\xi^2} |q'\rangle = {} & \frac{(-2g^2)^{\frac{q+q'}{2}} \Gamma\left(\frac{1+q+q'}{2}\right)}{\sqrt{\pi q! q'!}\,(1+g^2)^{\frac{1+q+q'}{2}}} \\ & \times {}_2F_1\left(-q, -q', \frac{1-q-q'}{2}, \frac{1+g^2}{2g^2}\right), \end{aligned} \tag{8.114}$$

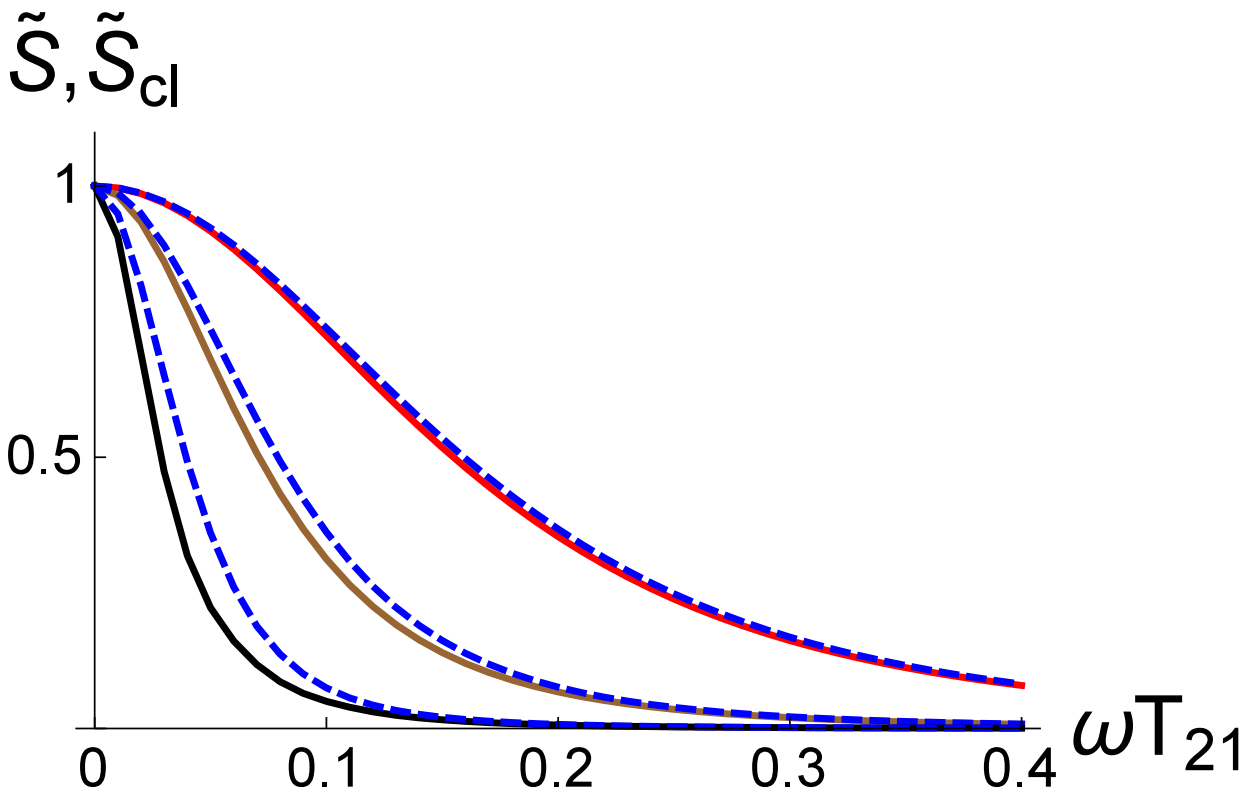

Figure 8.11: Plots of $S_{cl}\left(T_{21}\right)$ and $\tilde{S}_{cl}\left(T_{21}\right)$ for perturbative fields as a function of ωT_{21} for $\beta = 0.1$ and $\kappa = 5$ (red curve) ; $\kappa = 10$ (brown curve), and $\kappa = 20$ (black curve). The dashed blue curves are the classical results for the same parameters.

where Γ is the gamma function and ${}_2F_1$ is a hypergeometric function.

In the initial density matrix is diagonal,

$$\rho_{qq'}(0) = P_q \delta_{q,q'}, \tag{8.115}$$

then

$$C\left(T_{21}\right) = P_q e^{-i(q'-q)\omega T_{21}} \left\langle q\right| e^{-\beta\kappa^2\xi^2} \left|q'\right\rangle \left\langle q'\right| e^{-\beta\kappa^2\xi^2/2} \left|q\right\rangle . \tag{8.116}$$

For a thermal state with $P_q = \left(1 - e^{-\beta}\right) e^{-q\beta}$ ($\beta = \hbar\omega/k_B T$), Eq. (8.116) is evaluated numerically using Eq. (8.114) for different values of β and κ^2.

In Fig. 8.11, $\tilde{S}\left(T_{21}\right)$ is plotted as a function of ωT_{21} for $\beta = 0.1$ and $\kappa = 5$; $(\beta\kappa = 0.5)$, $\kappa = 10$; $(\beta\kappa = 1)$, and $\kappa = 20$ $(\beta\kappa = 2)$, along with the classical result, $\tilde{S}_{cl}\left(T_{21}\right)$. With increasing values of $\beta\kappa$, the classical and quantum results begin to deviate.

In Fig. 8.12, $\tilde{S}\left(T_{21}\right)$ is plotted as a function of ωT_{21} for $\kappa = 1$ and $\beta = 1, 5, 10$, along with the classical result, $\tilde{S}_{cl}\left(T_{21}\right)$. With increasing β, the signal deviates significantly from the classical result. We can estimate the signal for $\beta \gg 1$. In the limit of large β, $P_q \approx \delta_{q,0}$ and the sum in Eq.

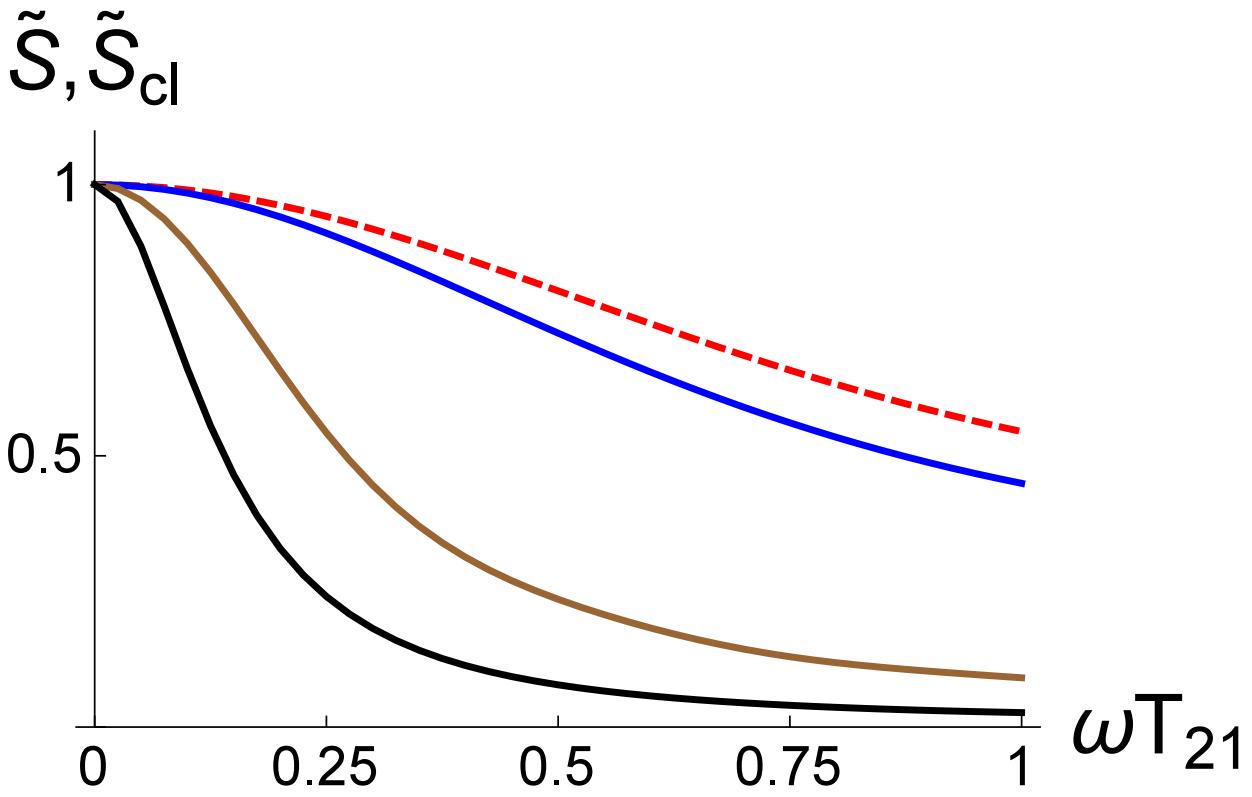

Figure 8.12: Plots of $S_{cl}\left(T_{21}\right)$ and $\tilde{S}_{cl}\left(T_{21}\right)$ for perturbative fields as a function of ωT_{21} for $\kappa = 1$ and $\beta = 1$ (blue curve) ; $\beta = 5$ (brown curve), and $\beta = 10$ (black curve). The dashed red curve is the classical result which is the same for all β if κ is held fixed.

(8.116) can be carried out analytically. Using Eqs. (8.112)-(8.116), we find

$$\tilde{S}\left(T_{21}\right) \sim \frac{1}{1+\frac{4\sin^2(\omega T_{21})(\beta^4\kappa^8+3\beta^3\kappa^6+2\beta^2\kappa^4)}{(2+3\beta\kappa^2)^2}}. \tag{8.117}$$

The result depends only on powers of $\beta\kappa^2$, whereas the classical result, Eq. (8.112), depends only on powers of κ. If $\kappa \geq 1$, $\beta \gg 1$ and $\omega T_{21} \ll 1$,

$$\tilde{S}\left(T_{21}\right) \sim \frac{1}{1+\frac{4(\omega T_{21})^2\beta^2\kappa^4}{9}} \tag{8.118}$$

which is a Lorentzian having half-width $3/\left(2\beta\kappa^2\right)$.

8.6 Summary

We have presented a theory of coherent transients in which a sequence of optical pulses is incident on a sample of trapped atoms and gives rise to phase-matched emission from the sample. The trapping potential for the atoms is state-dependent, in general, necessitating a quantum treatment of the center-of-mass motion. To carry out the calculation we used a source-field approach, modified to account for the quantized motion of the atoms. In the simplest version of the theory, all atomic motion is frozen during the excitation pulses and during the time in which the signal is emitted. For state-independent potentials, a comparison was made with a theory in which the motion is treated classically.

Coherent transients from trapped atoms differ in a fundamental way from those for free atoms. In the case of free atoms, the Doppler phase accumulated by the various coherences in the problem are linear functions of time. As a result it is possible to use echo techniques to effectively eliminate effects related to inhomogeneous broadening. With trapped atoms, no such methods can be used since the motional phases are not linear in time. As such, the general use of coherent transients in trapped atoms is to establish a long-lived coherence between two atomic levels that is only marginally affected by the motion in the trapping potentials. In this manner, quantum coherence can be stored in the sample and read out at a later time. Any deterioration of the signal resulting from motional effects can be calculated using the techniques developed in this paper.

Two examples were given. In the first, a long-lived coherence was established between a ground and Rydberg level for atoms trapped in a lattice potential. Phase-matched emission is produced with the use of a readout pulse. The coherence loss produced by harmonic, anharmonic, and state-dependent potentials was investigated. In the second example, a long-lived coherence was established between two, ground state sublevels for atoms in a dipole trap, and also probed by a

readout pulse. The dynamics of transit-time loss was probed in this example.

This work was supported by the ARL Center for Distributed Quantum Information, AFOSR, and the National Science Foundation.

Appendix

We would like to return to the non-phase matched contribution to the signal give with $j = j'$ in Eq. (8.32). This term can be written as

$$\begin{aligned} S_{npm} &= R_d^2 \left\langle \mathbf{E}_-(\mathbf{R}_d, t) \cdot \mathbf{E}_+(\mathbf{R}_d, t) \right\rangle \\ &= N\mu_{ba}^2 R_d^2 \left(\frac{\hbar\omega_{k'}}{2\epsilon_0 \mathcal{V}}\right)\left(\frac{\hbar\omega_k}{2\epsilon_0 \mathcal{V}}\right) \\ &\times \sin\theta_k \sin\theta_{k'} e^{i(\mathbf{k}-\mathbf{k}')\cdot\mathbf{R}_d} \boldsymbol{\epsilon}_{\mathbf{k}'}^{(1)} \cdot \boldsymbol{\epsilon}_{\mathbf{k}}^{(1)} \\ \times \int_0^t dt' \int_0^t dt'' &\left\langle e^{i\mathbf{k}'\cdot\hat{\mathbf{R}}(t'')} \sigma_{ba}(t'') \sigma_{ab}(t') e^{-i\mathbf{k}\cdot\hat{\mathbf{R}}(t')} \right\rangle \\ &\times e^{i\omega_{k'}(t-t')} e^{-i\omega_k(t-t')}, \end{aligned} \tag{8.119}$$

where N is the number of atoms. We have dropped the label j since all atoms contribute equally to the signal - $\hat{\mathbf{R}}(t'')$ and $\sigma_{ba}(t'')$ and Heisenberg operators of a given atom. It is not simple to evaluate this expression in the Heisenberg representation if quantized motion must be taken into account. In fact, the best method for evaluating this term is to use a Schrödinger equation approach [29].

Going back one step in the calculation, we write

$$\begin{aligned} S_{npm} &= N R_d^2 \left(\frac{\hbar\omega_k}{2\epsilon_0 \mathcal{V}}\right)^{1/2} \left(\frac{\hbar\omega_{k'}}{2\epsilon_0 \mathcal{V}}\right)^{1/2} \\ &\times \boldsymbol{\epsilon}_{\mathbf{k}}^{(1)} \cdot \boldsymbol{\epsilon}_{\mathbf{k}'}^{(1)} \left\langle a_{\mathbf{k}}^\dagger a_{\mathbf{k}'} \right\rangle e^{-i(\mathbf{k}-\mathbf{k}')\cdot\mathbf{R}_d}. \end{aligned} \tag{8.120}$$

We have anticipated the fact that only the $\lambda = 1$ polarization enters the calculation for the $z-$polarized excitation and readout pulses we are using. Only states that are diagonal in the atomic quantum numbers contribute to the average value of $\left\langle a_{\mathbf{k}}^\dagger a_{\mathbf{k}'} \right\rangle$; moreover, in the RWA, the only non-vanishing terms involve the ground internal states,

$$\left\langle a_{\mathbf{k}}^\dagger a_{\mathbf{k}'} \right\rangle \equiv \rho_{aq,\mathbf{k};aq,\mathbf{k}'}(t) e^{-i\omega_{kk'}t} \equiv \rho^I_{aq,\mathbf{k};aq,\mathbf{k}'}(t) e^{-i\omega_{kk'}t}, \tag{8.121a}$$

where $\omega_{kk'} = \omega_k - \omega_{k'}$.

The Hamiltonian is

$$\begin{aligned} H &= \hbar\omega_a \left|a\right\rangle \left\langle a\right| + \hbar\omega_b \left|b\right\rangle \left\langle b\right| \\ &+ \hbar\omega_{aq} \left|aq\right\rangle \left\langle aq\right| + \hbar\omega_{bp} \left|bp\right\rangle \left\langle bp\right| \\ &+ \left[\hbar f_{\mathbf{k}} e^{i\mathbf{k}\cdot\mathbf{R}} e^{-i\omega_k t} \sigma_{ba} a_{\mathbf{k}} + \hbar f_{\mathbf{k}}^* e^{-i\mathbf{k}\cdot\mathbf{R}_j} e^{i\omega_k t} a_{\mathbf{k}}^\dagger \sigma_{ab}\right], \end{aligned} \tag{8.122}$$

where

$$f_{\mathbf{k}} = -i\mu_{ba} \left(\frac{\omega_k}{2\hbar\epsilon_0 \mathcal{V}}\right)^{1/2} \sin\theta_k. \tag{8.123}$$

From Schrödinger's equation, it then follows that[29]

$$\begin{aligned} \dot{\rho}^I_{aq,\mathbf{k};aq,\mathbf{k}'} &= i f_{\mathbf{k}'} U_{bp;aq}\left(\mathbf{k}'\right) e^{i(\omega_0 - \omega_{k'})t} e^{i\omega_{bp;aq}t} \rho^I_{aq,\mathbf{k};bp,0} \\ &\quad - i f^*_{\mathbf{k}} U^\dagger_{aq,bp}\left(\mathbf{k}\right) e^{-i(\omega_0 - \omega_k)t} e^{i\omega_{aq;bp}t} \rho^I_{bp,0;aq,\mathbf{k}'}; \end{aligned} \tag{8.124a}$$

$$\begin{aligned} \dot{\rho}^I_{bp,0;aq,\mathbf{k}'} &= -\gamma_b \rho^I_{bp,0;aq,\mathbf{k}'} + i f_{\mathbf{k}'} U_{bp',aq}\left(\mathbf{k}'\right) \\ &\quad \times e^{i(\omega_0 - \omega_{k'})t} e^{i\omega_{bp';aq}t} \rho^I_{bp,0;bp',0}, \end{aligned} \tag{8.124b}$$

along with the complex conjugates of these equations. In these equations, the zero subscript stands for the vacuum state of the field, ω_0 is the $b - a$ transition frequency, and

$$U_{bp,aq}\left(\mathbf{k}\right) = \int d\mathbf{R} \left[\psi_{bp}\left(\mathbf{R}\right)\right]^* e^{i\mathbf{k}\cdot\mathbf{R}} \psi_{aq}\left(\mathbf{R}\right); \tag{8.125a}$$

$$U^\dagger_{aq,bp}\left(\mathbf{k}\right) = \int d\mathbf{R} \left[\psi_{aq}\left(\mathbf{R}\right)\right]^* e^{-i\mathbf{k}\cdot\mathbf{R}} \psi_{bp}\left(\mathbf{R}\right), \tag{8.125b}$$

such that

$$U_{bp,aq}\left(\mathbf{k}\right) U^\dagger_{aq,bp'}\left(\mathbf{k}\right) = U^\dagger_{bp,aq}\left(\mathbf{k}\right) U_{aq,bp'}\left(\mathbf{k}\right) = \delta_{p,p'}. \tag{8.126}$$

Equations (8.124) are in a form that is identical to the equations in Ref. [29] and can be solved iteratively and substituted back into Eq. (8.120) as in that paper. The only difference is that the matrix elements of U must be left in the form of Eqs. (8.125). In this manner, we obtain [see Eqs.

(22), (23a), and (25) of Ref. [29]],

$$
\begin{aligned}
S_{npm} = & N\left(\frac{\mu_{ba}\omega_0^2\sin\theta}{4\pi\epsilon_0 c^2}\right)^2\Theta\left(\tau\right) \\
& \times\int d\mathbf{R}\int d\mathbf{R}'\left[\psi_{bp'}\left(\mathbf{R}\right)\right]^*\psi_{aq}\left(\mathbf{R}\right) \\
& \times\left[\psi_{aq}\left(\mathbf{R}'\right)\right]^*\psi_{bp}\left(\mathbf{R}'\right)e^{-\gamma_b\left(t_{\mathbf{R}'}-t_{\mathbf{R}}\right)} \\
& \times e^{i\omega_0 t_{\mathbf{R}}}e^{i\omega_{bp';aq}t_{\mathbf{R}}}\rho^I_{bp,0;bp',0}\left(t_{\mathbf{R}}\right)e^{-i\omega_0 t_{\mathbf{R}'}}e^{i\omega_{aq;bp}t_{\mathbf{R}'}} \\
& + \text{c.c.},
\end{aligned}
\tag{8.127}
$$

where

$$
t_{\mathbf{R}} = t - t_{out} - \frac{|\mathbf{R}_d - \mathbf{R}|}{c} \approx \tau + \frac{\mathbf{R}_d\cdot\mathbf{R}}{R_d c}; \tag{8.128}
$$

$$
t_{\mathbf{R}'} = t - t_{out} - \frac{|\mathbf{R}_d - \mathbf{R}'|}{c} \approx \tau + \frac{\mathbf{R}_d\cdot\mathbf{R}'}{R_d c}; \tag{8.129}
$$

$$
\tau = t - t_{out} - \frac{R_d}{c} \tag{8.130}
$$

When these equations are substituted into Eq. (8.127) and the terms involving the dot products are retained only in the exponential terms containing ω_0, we obtain

$$
\begin{aligned}
S_{npm} = & 2N\left(\frac{\mu_{ba}\omega_0^2\sin\theta}{4\pi\epsilon_0 c^2}\right)^2\Theta\left(\tau\right) \\
\times & U_{bp';aq}\left(\mathbf{k}_d,\tau\right)U^\dagger_{aq;bp}\left(\mathbf{k}_d,\tau\right)e^{i\left(\omega_{bp'}-\omega_{bp}\right)\tau}\rho^I_{bp,0;bp',0}\left(\tau\right),
\end{aligned}
\tag{8.131}
$$

where

$$
\mathbf{k}_d = \omega_0\mathbf{R}_d/c \tag{8.132}
$$

and

$$
U_{bp';aq}\left(\mathbf{k}_d,\tau\right) = \left\langle bp'\right| e^{iV_b(\mathbf{R})\tau/\hbar}e^{i\mathbf{k}_d\cdot\mathbf{R}}e^{-iV_a(\mathbf{R})\tau/\hbar}\left|aq\right\rangle; \tag{8.133}
$$

$$
U^\dagger_{aq;bp}\left(\mathbf{k}_d,\tau\right) = \left\langle aq\right| e^{iV_a(\mathbf{R})\tau/\hbar}e^{-i\mathbf{k}_d\cdot\mathbf{R}}e^{-iV_b(\mathbf{R})\tau/\hbar}\left|bp\right\rangle. \tag{8.134}
$$

Finally, using Eq. (8.126), we arrive at

$$
S_{npm} = 2N\left(\frac{\mu_{ba}\omega_0^2\sin\theta}{4\pi\epsilon_0 c^2}\right)^2\rho_{bb}\left(\tau\right)\Theta\left(\tau\right), \tag{8.135}
$$

where $\rho_{bb}\left(\tau\right)$ is the total population of level b at the retarded time. Equation (8.135) is a somewhat

intuitive result - since the atomic motion is constrained to distances that are much less than R_d, any *retardation* effects related to different motional states are not important and the non-phased matched signal arises only from the total population in level b at time τ. Although this result is intuitive, we have not found a way to derive it using the Heisenberg representation.

CHAPTER 9

Differential Nuclear-Spin-Dependent Light Shifts and State Mixing of Rydberg Atoms

9.1 Introduction

A promising platform for quantum information processing is based on the excitation of ultra-cold atoms to Rydberg states [5]. Achieving long-lived ground-Rydberg atomic coherence is one of the cornerstones of this approach. To suppress the effects of motional dephasing on this coherence, the atoms can be confined in optical potentials that are identical for the ground and Rydberg states [26, 27, 52, 53, 15, 28, 48]. However, in addition to confining the atoms, the optical trap fields also mix and shift the Rydberg energy levels. As a consequence, the energy level spacing within a given Rydberg manifold results from a complicated combination of optical field potentials, hyperfine interactions, and interactions of the atoms with any external magnetic bias fields. A complete understanding of this level structure is needed to maximize the fidelities for quantum information protocols using trapped Rydberg atoms.

In this paper we present a theoretical and experimental study of ^{87}Rb Rydberg atoms confined in an optical lattice potential and subjected to an external magnetic field. For a given n, the frequency of the lattice fields is chosen so as to match the light shift potentials for the ground and ns Rydberg levels [15, 48]. Actually, it is not possible to match the ground state lattice potential to that of *all* the hyperfine sublevels in a given ns level. For example, an ns level of ^{87}Rb contains eight sublevels. In general, the trapping potential differs for each of these levels and must be accounted for in a complete analysis. Moreover, since the atoms are trapped in these potentials, it becomes necessary to use a fully quantum theory for the atomic motion.

The trapped atoms are subjected to a two-photon pulse that excites the atoms to a targeted Rydberg level, followed by a time-delayed readout pulse that leads to phase-matched emission from the sample. By a proper choice of excitation field polarization, the output signal, measured as a function of the time delay, contains components that oscillate at the frequency separations of the ns Rydberg sublevels.

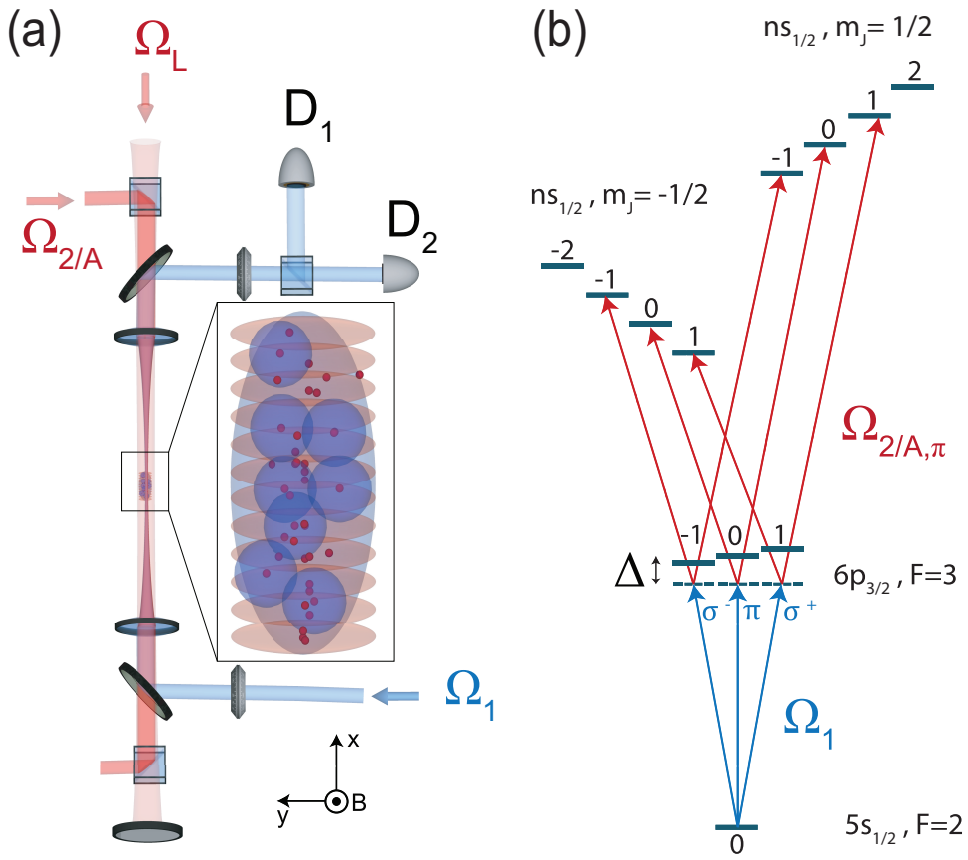

Figure 9.1: (a) Experimental setup. An ultra-cold sample of ^{87}Rb gas is trapped in a "magic" one-dimensional optical lattice formed by a retro-reflected lattice beam Ω_L that is directed along the x axis and polarized in the y direction. Two excitation beams, Ω_1 (420 nm) and Ω_2 (varying between 1013 nm and 1026 nm) counter-propagate along the x axis and are focused at the position of the atomic sample cloud with ($\frac{1}{e^2}$) waists of 17 and 15 μm, respectively. After a time delay T_s following the excitation pulse, a retrieval field Ω_A generates a phase-matched output signal. The polarization of field Ω_2 and the retrieval field Ω_A is fixed in the z-direction, whereas the polarization of field Ω_1 has both y and z components that are adjusted to optimize the modulation depth of the output signal. The output signal has both y- and z- components which are mixed with a half-wave plate, split by a polarizing beam splitter, and measured by single-photon detectors $D_{1(2)}$. (b) Atomic level diagram showing the initial ($|5s_{1/2}, F = 2, m = 0\rangle$) state, intermediate ($|6p_{3/2}\rangle$), and Rydberg $|ns_{1/2}\rangle$ sublevels. The final state manifold consists of two, spectrally resolved Zeeman sub-manifolds, each containing four levels. Even in the presence of light shifts, $m_F = m_J + m_I$ remains a good quantum number. For this excitation scheme, the $m_F = 0, \pm 1$ levels in each electronic Zeeman manifold are populated.

These frequency separations contain contributions arising from the magnetic field interaction, hyperfine interaction and light shift potentials. To isolate these effects, we calculate the eigenkets and eigenenergies of the Rydberg levels in the *absence* of light shifts and then determine to what

extent the light shifts modify them. The light shifts themselves are composed of near-resonance and ponderomotive contributions. The ponderomotive contribution, which includes effects related to the breakdown of the dipole approximation [53], is a function of n, but for a given n, is the same for all the sublevels. The near-resonance contribution both shifts and couples the sublevels. Rather remarkably, we find that coupling of hyperfine – magnetic field eigenkets is almost negligible for the range of our experimental parameters, although there was no *a priori* reason to believe that this should be the case when the lattice field polarization is orthogonal to the magnetic field. As a result, the only effect of the optical potential is to provide a differential shift for the Rydberg sublevels. We are able to assess the role played by these differential light shifts and to determine what effect, if any, they have on the atomic motion. In this way we determine the hyperfine constant A from the measured frequency intervals for n ranging from 30 to 65. Previously, A values were measured for low values of n using direct optical spectroscopy [54, 55]. In these experiments, residual Doppler broadening resulted in a spectral resolution to about 100 kHz, limiting the method to $n \leq 27$. Millimeter-wave spectroscopy has been used for high-n states of atomic Cs, with kHz-level resolution achieved using ultra-cold atoms [56]. In this work we achieve a resolution as low as several kHz.

9.2 Experiment

The experimental setup and level diagram for one of our excitation schemes are shown in Fig. 1. For the most part, the experimental setup is identical to the one used in our previous work Ref.[48]. The major difference is that the polarization of the field Ω_1 in the current experiment has both y and z components whereas it was z-polarized in the previous experiment. An ultra-cold sample of Rb atoms is loaded into a one-dimensional optical lattice formed by counter-propagating optical fields polarized along the y-axis. The measurements are made using a magnetic field $B = 5$ Gauss for which the electronic Zeeman splitting is much greater than the hyperfine separations of the ns levels being studied, the so-called hyperfine Paschen-Back regime. In this case the $ns_{1/2}$ Rydberg level splits into two manifolds, characterized by $m_J = \pm 1/2$, separated in frequency by ≈ 14 MHz, with each manifold consisting of four m_I-components. The ~ 1 MHz two-photon excitation bandwidth $\delta\nu$ is much smaller than the frequency separation between the two manifolds. The lattice wavelength $\lambda \simeq 1012 - 1027$ nm is tuned to near-resonance with the $|6p_{3/2}\rangle \leftrightarrow |ns_{1/2}\rangle$ atomic transition, the specific value chosen to match the optical potentials for the ground state and the $m_F = m_J + m_I = 0$ component of the Rydberg Zeeman manifold.

The ensemble is driven resonantly to the Rydberg state $|ns_{1/2}\rangle$ using counter-propagating, $T_e = 1$ μs-long, pulses of a 420 nm field Ω_1 and a (nominally) 1012 nm field Ω_2. The polarization of Ω_1, controlled by half-wave plate oriented at an angle $\theta_i/2$ with respect to z-axis, is a linear

combination of the y- and z-polarizations, while Ω_2 is purely z-polarized. In this way three m_I-components in a given electronic Zeeman manifold of $|ns\rangle$ are excited. After a storage period T_s, the atoms are coherently driven by a (z-polarized) 10 μs-long retrieval field Ω_A whose frequency is resonant with the $|ns\rangle \leftrightarrow |6p_{3/2}\rangle$ transition . The ensuing cooperative emission on the $|6p_{3/2}\rangle \leftrightarrow |5s_{1/2}\rangle$ transition is directed through a half-wave plate and polarizing beam splitter. Each of the output polarization modes is collected into a single-mode fiber and directed onto a single-photon detector.

9.3 Theory

The theoretical analysis is carried out in two stages. First we calculate the energy of the sublevels of an ns Rydberg state of ^{87}Rb subjected to a magnetic field $\mathbf{B}$ along z and a y-polarized optical trap field whose frequency is nearly resonant with the $|ns\rangle \leftrightarrow |6p_{3/2}\rangle$ transition frequency. We then use this result to obtain an expression for the phase-matched signal as a function of delay between excitation and retrieval pulses. The details of the calculation are presented in the Appendix. Here we summarize some of the results.

In the absence of all but the Coulomb interaction, there are 8 degenerate states in an ns manifold that can be labeled as $|nLSJIFm_F\rangle$ with $S = 1/2$ and $I = 3/2$. The energy levels in a given Rydberg ns manifold are determined by the hyperfine interaction, the magnetic field interaction, and the optical potentials produced by the trap field. In a given basis, these interactions result in a shift and coupling of the various Rydberg sublevels. In principle, it is necessary to diagonalize the Hamiltonian associated with a given ns manifold to obtain the eigenenergies and eigenkets. For our experimental parameters, however, the eigenkets that are obtained are approximately those in which the optical potentials are set equal to zero. As such, $m_F = m_J + m_I$ corresponds to an approximate constant of the motion. We denote the zero field hyperfine separation of the ns state by $h\nu_{hfs}$ (the n label is suppressed). It is a simple matter to obtain the eigenkets and eigenfrequencies ω_{nsm_F} of the ns levels in the absence of the trap field.

The optical potentials produced by the trap field can be broken down into two contributions. First there is the ponderomotive potential associated with the A^2 ($\mathbf{A}$ is the vector potential of the trap field) contribution to the Hamiltonian and is the same for all the levels in the ns Rydberg manifold. In addition, there is also the $\mathbf{A} \cdot \mathbf{p}$ contribution. Although the trap field is in near-resonance with the $|ns\rangle \leftrightarrow |6p_{3/2}\rangle$ transition, the detuning of the trap field frequency from the $|ns\rangle \leftrightarrow |6p_{3/2}\rangle$ transition frequency is *not* sufficiently large to justify the neglect of the hyperfine splitting of the $6p_{3/2}$ sublevels. This results in optical potentials that are dependent on the m_F values of the ns Rydberg sublevels.

For magic wavelength lattices, one matches the ground and excited state trap potentials by a

proper choice of the trap field detuning. In our case. it is *not* possible to simultaneously match the potentials for *all* the Rydberg sublevels. With an external magnetic field strength of about 5 Gauss, an ns manifold consists of two Zeeman sub-manifolds (corresponding to $m_s = \pm 1/2$) separated by about 14 MHz, each containing four of the eight sublevels of the ns Rydberg levels. As such, the excitation fields can be chosen to excite only one of these Zeeman sub-manifolds (see Fig. 1). For a given Zeeman sub-manifold, we match the $m_F = 0$ potential to the ground state potential. The trap potential for the other Zeeman sublevels will then differ from the ground state potential.

Both the near-resonant and ponderomotive components of the Rydberg optical potentials, as well as the ground state optical potential, contain both lattice and non-lattice contributions. The lattice contributions are responsible for trapping the atoms longitudinally in the wells of the potential. The remaining non-lattice contributions to the optical potentials trap the atoms in the transverse direction and give rise to a spatially inhomogeneous shift of the levels owing the transverse spatial dependence of the trap fields. The lattice potentials determine the center-of-mass motion of the atoms. Since these potentials are state-dependent, the motion must be treated quantum mechanically. The spatial dependence of the non-lattice potentials results in a dephasing that degrades the output signal with increasing time delay between the excitation and retrieval pulses.

The atoms are optically pumped into a *single* magnetic sublevel having angular momentum $F = 2$ and magnetic quantum number $m_F = 0$. Pulsed, counter-propagating fields incident along the $x-$direction drive a two-photon transition from this ground state to the Zeeman manifolds of an ns Rydberg level. The first excitation field propagates in the $\mathbf{u}_x$ direction, has polarization given by $\cos\theta_i \mathbf{u}_z + \sin\theta_i \mathbf{u}_y$, and is nearly resonant (but still far enough from resonance to neglect any saturation effects) with the transition from the ground state to a single hyperfine state of either the $6p_{3/2}$ or $5p_{1/2}$ manifolds (manifolds specified by the symbol p_J), depending on the excitation scheme. The detuning Δ in Figure 1(b) is of order $\Delta/2\pi \approx 12$ MHz and the frequency spacing of adjacent $6p_{3/2}(F = 3)$ magnetic sublevels is ≈ 4.7 MHz. The second, counter-propagating field couples each intermediate state magnetic sublevel labeled by m_F to a single level in either the upper ($m_J = 1/2$) or lower ($m_J = -1/2$) Zeeman sub-manifold having the same value of m_F.

The excitation pulses create coherence between the $F = 2$, $m_F = 0$ ground level and the Rydberg sublevels. To monitor this coherence, a retrieval pulse, polarized in the z direction and propagating in the $-\mathbf{u}_x$ direction is applied at a time T_s following the excitation pulses. The field is resonant with the same Rydberg - intermediate state transition used in the excitation process. The excitation, readout, and vacuum fields combine to produce a phase-matched output field in the $\mathbf{u}_x$ direction that has both y and z polarization components. These components are mixed on a half-wave plate to produce new vertical and horizontal components which are then separated by a polarizing beam splitter and measured in two detectors.

It is shown in the Appendix that the signal at time T_s normalized to that at $T_s = 1$ μs, the

vertical signal component can be written as

$$\eta_V(T_s) = S_V(T_s)/S_V(T_s = 1\mu s); \tag{9.1}$$

where

$$\begin{aligned} S_V(T_s) &= \left| \int_{-\infty}^{\infty} dX \int_0^{\infty} \rho d\rho \Lambda(\rho, X) \mathcal{N}(\rho, X) C_V(\rho, X, T_s) \right|^2 \\ &\times e^{-\Gamma_{ns} T_s}, \end{aligned} \tag{9.2}$$

$$\begin{aligned} C_V(\rho, X, T_s) = &\sum_{m_F=-1}^{2} \sum_{q,q'}^{q_{\max}} e^{-i\omega_{nsm_F} T_s} Q^{(V)}_{p_J nsm_F} \\ &\times e^{-2\pi i \tilde{D}^{(j)}_{nsm_F}(\rho,X) T_s} M_{gq;nsm_F q'}(-k) \\ &\times M_{nsm_F q';gq}(k)\, e^{i\left(\omega_q^{(g)} - \omega_{q'}^{(nsm_F)}\right) T_s} \rho_{1q,1q}(0), \end{aligned} \tag{9.3}$$

$\Lambda(\rho, X)$ is proportional to the product of the spatially dependent Rabi frequencies of the excitation and retrieval pulses and $\mathcal{N}(\rho, X)$ is the atomic density distribution. A loss factor, $e^{-\Gamma_{ns} T_s/2}$, has been added to allow for decay between the excitation and retrieval pulses owing to spontaneous emission, black-body radiation, and decay from the intermediate state.

The factor $C_V(\rho, X, T_s)$ reflects the contributions to the signal from different initial motional states in the ground state lattice potential, represented by density matrix elements $\rho_{1q,1q}(0)$. Here ω_{nsm_F} are eigenfrequencies of the Hamiltonian that account for differential light shifts, in addition to the magnetic and hyperfine interactions. The frequencies $\omega_q^{(g)}$ and $\omega_{q'}^{(nsm_F)}$ are those associated with the ground and nsm_F lattice potentials, respectively, while $\tilde{D}^{(j)}_{nsm_F}(\rho, X)$ is the spatially dependent difference in non-lattice potentials between nsm_F and ground state levels. The matrix elements $M_{nsm_F q';gq}(k)$ represent the coupling between the ground and Rydberg motional states, while the function $Q^{(V)}_{p_J nsm_F}$ incorporates all the excitation and retrieval dynamics. The sums over q, q', q'' are restricted to (quasibound) states; that is, $q_{\max}$ is the number of bound states in the potential.

9.4 Analysis of retrieved signal

Let us first consider the data for $n = 40$. As a function of delay time T_s between the excitation and readout pulses, the overall signal decays, primarily as a result of blackbody-induced transitions and

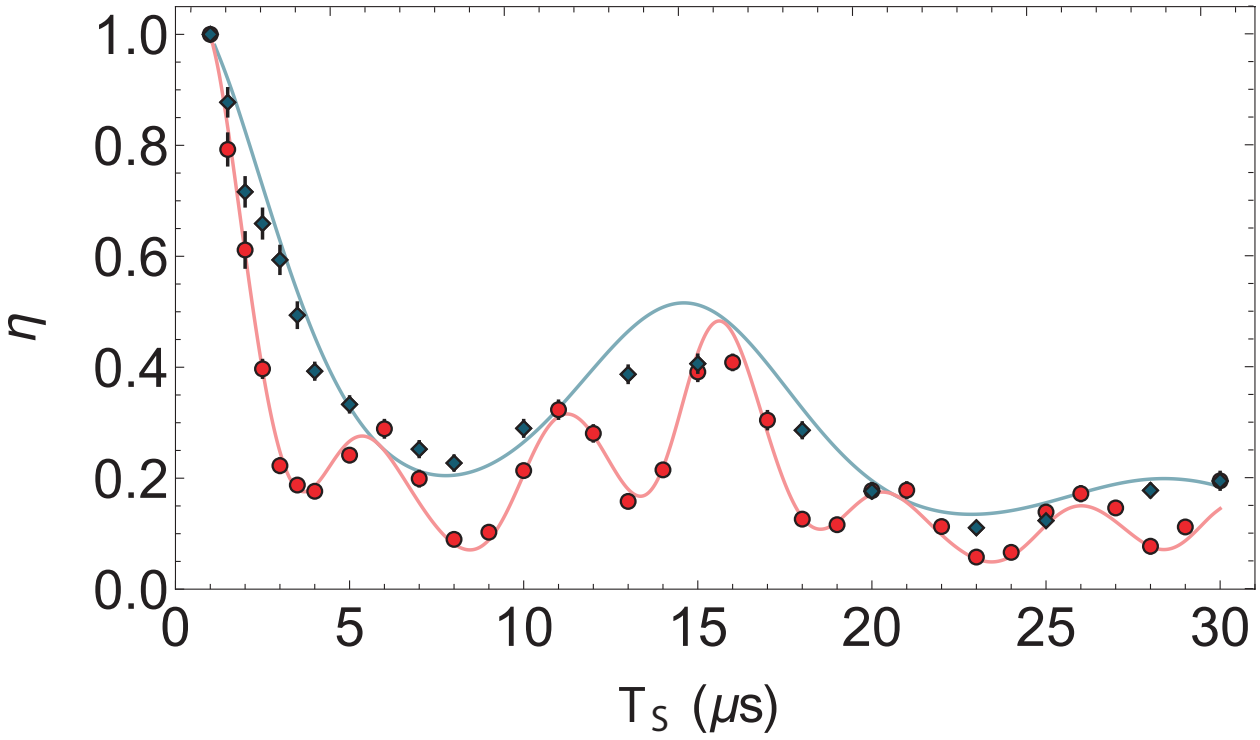

Figure 9.2: Normalized signal $\eta \equiv F(T_s)/F(T_s = 1\ \mu s)$ as a function of storage time for principal quantum number $n = 40$ with fitted trap depth $U_0/k_B = 31\ \mu K$ and temperature $T = 10\ \mu K$ for a single excited state (blue) and a triplet of states (red) using (θ_i, θ_d)=$(0°, 24°)$ and $(32°, 24°)$ respectively. Solid curves are based on our theoretical model.

spontaneous decay. In addition to the overall decay, the signal exhibits an oscillatory behavior. If the trap potentials are purely harmonic characterized by frequency ω and if the ground and Rydberg potentials are matched, for a ground state thermal distribution,

$$\rho_{1q,1q}(0) = \left(1 - e^{-\beta}\right) e^{-q\beta}; \qquad \beta = \frac{\hbar\omega}{k_B T}, \tag{9.4}$$

the quantity C_V in Eq. (9.3) can be written in the form [57]

$$\begin{aligned} |C_V(T_{21})| &\approx e^{-2\zeta^2[1-\cos(\omega T_s)]/\beta} \\ &\times \left|1 + Q_1 e^{-i\omega_{10}T_s} + Q_{-1} e^{-i\omega_{-10}T_s}\right|, \end{aligned} \tag{9.5}$$

where

$$\zeta = k_{12}\sqrt{\frac{\hbar}{2M\omega}} \tag{9.6}$$

is the Lamb-Dicke parameter for the excitation field (k_{12} is the effective propagation constant for the two-photon excitation field and M is the atomic mass) and ω_{m0} ($m = -1, 1$) is the frequency

difference between the Zeeman Rydberg sublevel having total magnetic quantum number m from the level having $m = 0$. For $n = 40$, the quantity ω_{m0} results primarily from the hyperfine and Zeeman interactions. For $n = 40$ the light shifts for the Rydberg sublevels can be neglected as they have an insignificant effect on the signal. The frequency ω is determined by the depth of the trap potential U_0.

To fit our data we need to know the value of the trap depth U_0 and the temperature T. We obtain values for these quantities by fitting our data with the half-wave plate angle controlling the polarization of the first excitation field to $\theta_i = 0$. In this case, both the fields that constitute the two-photon excitation scheme are z-polarized, and $Q_{\pm 1} = 0$ in Eq. (9.5). The retrieved signal in this case, displayed as blue diamonds in Fig. 9.2 exhibits the oscillatory behavior predicted by the exponential term in Eq. (9.5), which can be attributed to the center-of-mass motion of the atom within the optical lattice trap potential. In fitting the data to theory, however, we allow for trap anharmonicity [see Eq. (9.3)] and extract values for U_0 and T from the frequency and visibility of the oscillations, respectively. A theoretical curve using the best-fit value of $U_0/k_B = 31\ \mu K$ and $T = 10\ \mu K$ is displayed in the figure as a solid blue curve. If the potential were purely harmonic, the signal would rephase at integral multiples of the trap frequency; however owing to the trap anharmonicity, the oscillations are no longer purely periodic. Trap anharmonicity also adds slightly to the decay of the signal.

Having obtained values of U_0 and T, we switch the half-wave plate angle to an angle $\theta_i \neq 0$. In that case the signal oscillates at the beat frequency between the different Rydberg sublevels. Fitting the signal to the full theoretical expression given in Eq. (9.3) using the best-fit values of U_0 and T found previously allows us to extract the hyperfine splitting ν_{hfs}, treated as a free parameter. The quantities $Q^{(V)}_{nsm_F}$ appearing in Eq. (9.3) are also treated as adjustable parameters in the fitting procedure to account for the uncertainties in the bandwidths, detunings and strengths of the excitation and retrieval pulses. A representative output signal in one of the detectors is shown in Fig. 9.2 with experimental data points displayed as red circles and theory as the solid red curve. We find agreement between the experimental data and the best-fit models obtained via Markov Chain Monte Carlo fitting. The input and output polarization angles $\theta_i = 32^\circ$ and $\theta_i = 24^\circ$ were empirically chosen to maximize the visibility of the Rydberg Zeeman beat frequency oscillations.

We have also used an alternative excitation scheme with a smaller value of k_{12} that leads to a diminished amplitude of the oscillations attributed to motion in the traps (see the dashed gray curves in Figure 3). In this scheme atoms are optically pumped into the $\left|5s_{1/2}, F = 2, m_F = 2\right\rangle$ ground state and using the $5p_{1/2}$ level as the intermediate state for two-photon excitation with fields Ω_1 and Ω_1 having wavelengths of 795 nm and 475 nm. The signal in this case is shown in Fig. 3 for $T = 4\ \mu K$ and trap depths $U_0/k_B = 22$, 18, and $14\ \mu K$.

For $n = 40$, the light shifts do not significantly contribute to the separation between the three

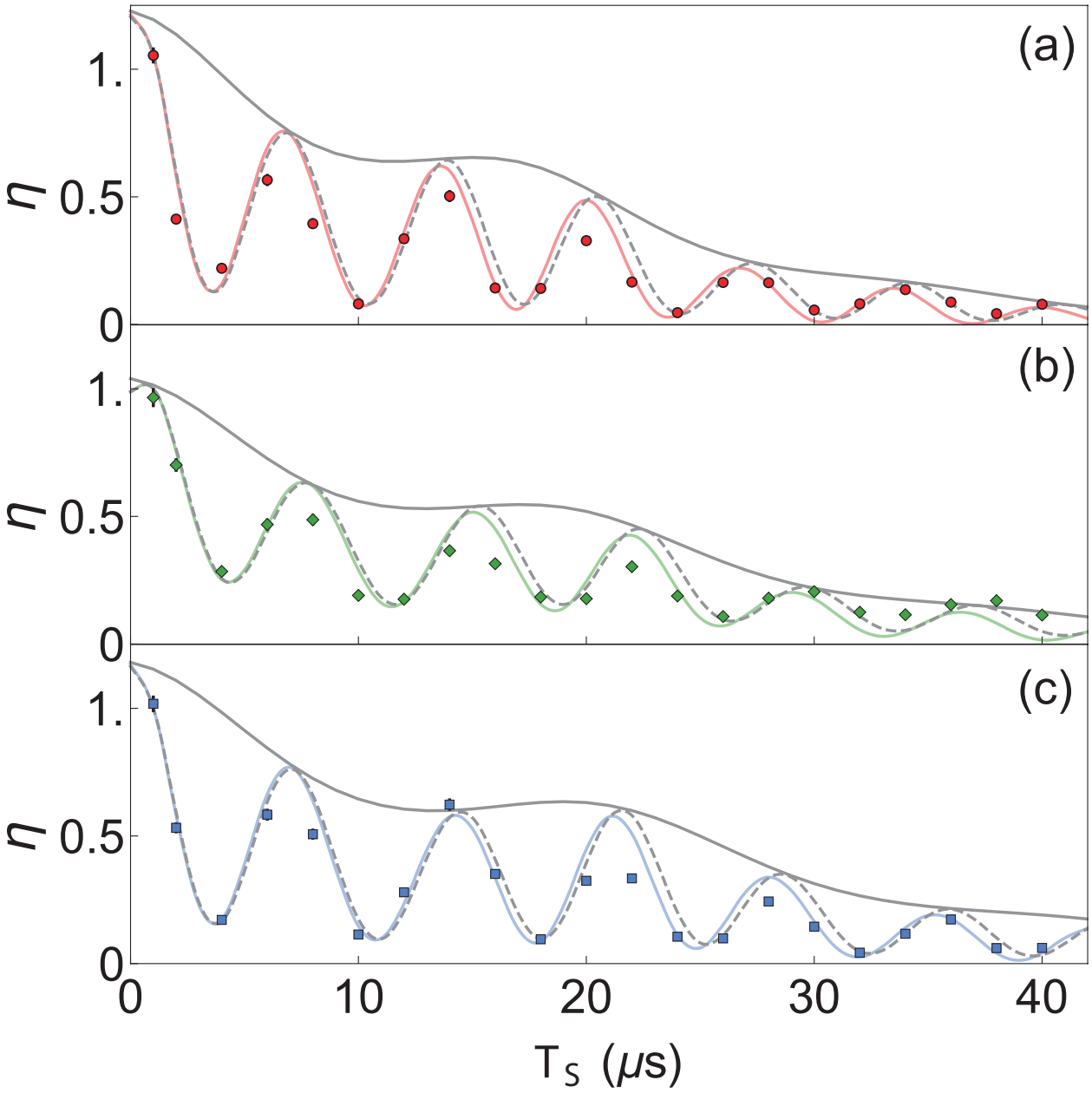

Figure 9.3: Normalized signal η utilizing the alternative excitation scheme via the intermediate $|5p_{1/2}\rangle$ state and $(\theta_i, \theta_d) = (32°, 24°)$ for the $m_J = -1/2$ electronic Zeeman component and principal quantum number $n = 60$. Experimental data with best-fit values of temperature of $4\ \mu K$ and trap depths of $U_o/k_B = 22, 18$ and $14\ \mu K$ are shown as red circles, green diamonds, and blue squares, respectively, along with color-coded curves that represent the predictions of a theoretical model that take into account the state-dependence of the optical potentials. The dashed gray curves correspond to a theory in which this state dependence is neglected and a single optical potential is used (that of the $m_F = 0$ sublevel). The solid gray theory curves correspond to an excitation scheme in which field Ω_1 is z-polarized.

m_F Rydberg sublevels that are excited. Moreover, the *differential* optical potentials for the three states are sufficiently small to result in approximately the same motional states for the three levels. This is no longer the case for higher values of n. For example, the theoretical curves shown in Fig. 3 for $n = 60$, exhibit differences between the models assuming a single state independent potential (that associated with the $m_F = m_J + m_I = 0$ level) and the true state-dependent potentials. In addition, for higher values of n, effects of spontaneous decay from the $|6p_{3/2}\rangle$ state, which is coupled to the Rydberg levels by the trap fields adds to the signal decay rate. Moreover, the dephasing associated with the breakdown of the dipole approximation in calculating the contributions of the ponderomotive potential to the light shifts also increases the decay of the signal [53]. Experimental data for $n = 60$ shown in Fig. 3 do not allow us to distinguish definitively between the state-independent and state-dependent potential models.

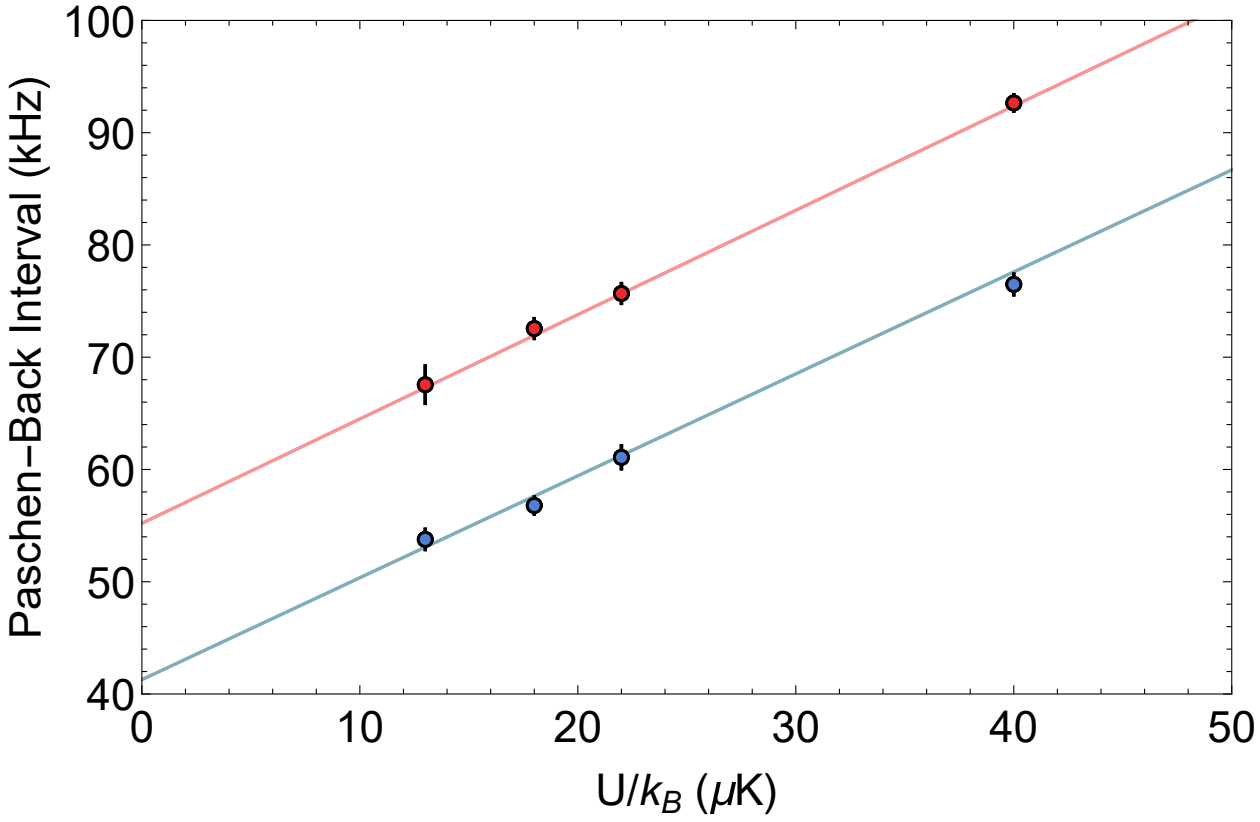

Figure 9.4: Average frequency separation between adjacent nuclear-spin states within the same m_J manifold for the $n = 60$ Rydberg level as a function of trap depth for the upper ($m_J = \frac{1}{2}$), blue circles) and lower ($m_J = -\frac{1}{2}$, blue circles) electronic Zeeman manifold.

The measured frequency intervals as a function of trap depths are displayed in Fig. 9.4 for the two electronic Zeeman components of the $|60s_{1/2}\rangle$ level, together with linear fits based on Eqs. (9.12,9.32). The two intervals differ by the nuclear Zeeman interaction. The intervals in the absence of the trapping potential are determined by the intercepts of the fits with the ordinate.

Using Eq. (9.12) the value of the hyperfine splitting $\nu_{hfs} = 193 \pm 5$ kHz for the $n = 60$ Rydberg state is determined.

For other values of n, fits similiar to those in Fig. 9.2 are made for a single value of the trap depth. Each value of ν_{hfs} constitutes a weighted average of values obtained over up to three runs using data recorded by the two detectors. The mean value ν_{hfs} is computed as a weighted average of $\nu_{hfs}^{(i)}$, with the weights being their inverse variances extracted from the individual fits.

The two main sources of uncertainty for ν_{hfs} are 1) the statistical which is evaluated as weighted sum of the individual values, and 2) the uncertainty in the determination of the trap depth which translates into an error of the inferred differential light shifts for the hyperfine Paschen-Back states. The $\nu_{hfs} \sim n^{-3}$, while differential light shifts scale as $\sim n^3$. As a result, the statistical uncertainty is the dominant one for $n = 30$ and 40, whereas the error due to the uncertainty of the trap depth is the larger one for states of $n \geq 51$. The data are shown in Figure 5(a) along with a fit using $\nu_{hfs} = C(n - 3.13)^{-3}$ with C as an adjustable parameter. In the inset to Figure 5 we plot the scaled hyperfine constant $A_{ns} \equiv \nu_{hfs}(n - 3.13)^3$. The weighted average $\overline{A}_{ns} = 35.71 \pm 0.18$ GHz is plotted as a dashed line together with a corresponding 95% confidence region. Also shown are the results of prior measurements of A_{ns} [58, 54, 55, 59, 60].

9.5 Conclusions

In summary, we have analyzed nuclear-spin manifolds associated with the ns Rydberg levels of ^{87}Rb atoms placed in magnetic and optical lattice fields. Using the eigenvalues and eigenkets for the Rydberg manifold, we have investigated the dynamics of phase-matched emission following illumination of an ensemble of cold atoms with excitation and readout laser pulses. In this way, Rydberg state-dependent light shifts and hyperfine splittings for principal quantum numbers between $n = 30$ and $n = 65$ have been determined. Our results have relevance to implementations of optically-trapped Rydberg qubits allowing for high-fidelity quantum gates.

This work was supported by the ARL Center for Distributed Quantum Information, AFOSR, and the National Science Foundation.

9.6 Theoretical Details

9.6.1 Basis Set and Hamiltonian

We consider an ns Rydberg level of ^{87}Rb subjected to a magnetic field $\mathbf{B}$ along z and a y-polarized optical trap field nearly resonant with the $|ns\rangle \leftrightarrow |6p_{3/2}\rangle$ transition frequency, as shown in Fig. 1. The trap fields counter-propagate in the x direction. The atom-field detuning between the trap field

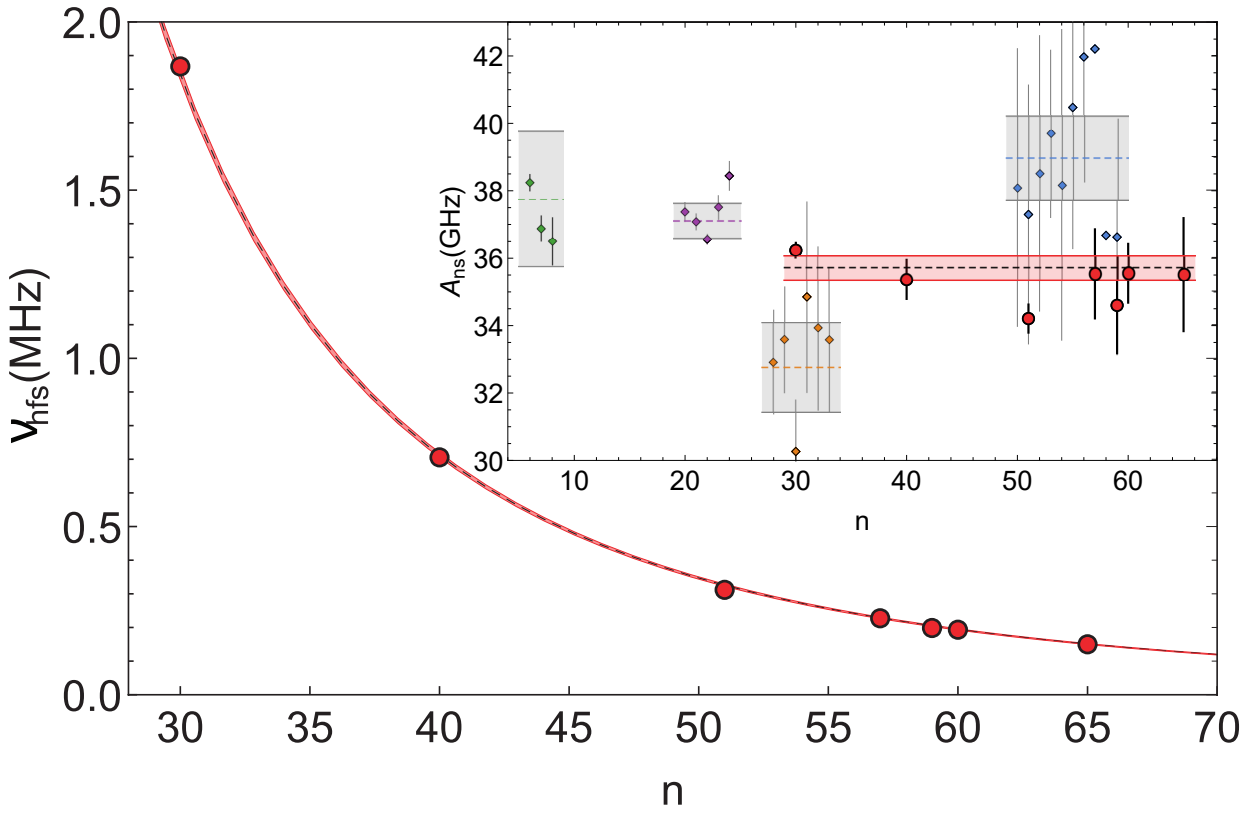

Figure 9.5: Hyperfine frequency ν_{hfs} as a function of principal quantum number n. The inset depicts the same data after removing the $(n-3.13)^{-3}$ dependence. The red band represents a 95% confidence interval for our fitted value. Gray intervals are data from Corney 2010 (green), Tauschinsky et al. 2013 (purple), Li et al. 2003 (orange), and Meschede 1987(blue).

frequency and the $|ns\rangle \leftrightarrow |6p_{3/2}\rangle$ transition frequency is much larger than the Zeeman splitting of the $6p_{3/2}$ or ns sublevels. We use the $|nLSJIFm_F\rangle$ basis throughout with $S = 1/2$ and $I = 3/2$. To simplify the notation we write the state kets for the ns states as $|nFm_F\rangle$, since $L = 0$ and $J = 1/2$ for these states. We denote the zero field hyperfine separation of the ns state by $h\nu_{hfs}$ (the n label is suppressed).

In the absence of all but the Coulomb interaction, there are 8 degenerate levels in an ns manifold, each having energy $E_n^{(0)} = \hbar\omega_{ns}$ - we neglect this contribution to the Hamiltonian since it is the same for all the levels. Next there is the contribution to the Hamiltonian from the hyperfine interaction, denoted by H_{hf}. In the $|nFm_F\rangle$ basis, this contribution is diagonal and given in frequency units by

$$\frac{\langle nF'm'_F|\, H_{hf}\, |nFm_F\rangle}{h} = \nu_{hfs} \begin{cases} \frac{3}{8}\delta_{F,2} \\ -\frac{5}{8}\delta_{F,1} \end{cases} \delta_{F,F'}\delta_{m_F,m'_F}, \tag{9.7}$$

where $\delta_{a,b}$ is a Kronecker delta. Finally, there is the magnetic field interaction contribution,

$$H_B = -\frac{\beta_0 B}{\hbar}\left(g_s S_z + g_I \frac{m_e}{m_p} I_z\right), \tag{9.8}$$

where β_0 is the Bohr magneton and $g_I = -0.995 \times 10^{-3}$ [61] is the nuclear $g-$factor. In frequency units,

$$\begin{aligned} \frac{H_B}{h} &= \frac{\beta_0 B}{h}\left(2S_z + g_I \frac{m_e}{m_p} I_z\right)/\hbar \\ &= 1.40(\text{MHz}) B(\text{Gauss})\left(2\frac{S_z}{\hbar} + 0.995 \times 10^{-3}\frac{I_z}{\hbar}\right). \end{aligned} \tag{9.9}$$

The interaction Hamiltonian H_B is *not* diagonal in the $|nFm_F\rangle$ basis, with matrix elements given by

$$\langle nF'm'_F| H_B |nFm_F\rangle /h = \nu_B \sum_{m_s,m_I} \begin{bmatrix} \frac{1}{2} & \frac{3}{2} & F' \\ m_s & m_I & m_F \end{bmatrix} \tag{9.10}$$

$$\times \begin{bmatrix} \frac{1}{2} & \frac{3}{2} & F \\ m_s & m_I & m_F \end{bmatrix} \left(2m_s + 0.995 \times 10^{-3} m_I\right) \delta_{m_F,m'_F}, \tag{9.11}$$

where $\nu_B = \beta_0 B/h$ is the Larmor frequency in Hz and the quantity in square brackets is a *Clebsch-Gordan* coefficient. The modification to the eigenvalues from the nuclear term must be included because of the sensitivity of the experiment to the shift produced by this term, but the eigenkets can be calculated neglecting this contribution.

It is simple to diagonalize $H_{hf} + H_B$ since it is block-diagonal. The eigenfrequencies are equal

to

$$\begin{aligned}
\nu_{n8} &= \frac{3\nu_{hfs}}{8} + \nu_B \quad m_F{=}\,2 \\
\nu_{n7,n1} &= \frac{-\nu_{hfs} \pm 4\sqrt{\nu_{hfs}^2 + 2\nu_{hfs}\nu_B + 4\nu_B^2}}{8} \quad m_F{=}\,1 \\
\nu_{n6,n2} &= \frac{-\nu_{hfs} \pm 4\sqrt{\nu_{hfs}^2 + 4\nu_B^2}}{8} \quad m_F{=}\,0 \\
\nu_{n5,n3} &= \frac{-\nu_{hfs} \pm 4\sqrt{\nu_{hfs}^2 - 2\nu_{hfs}\nu_B + 4\nu_B^2}}{8} \quad m_F{=}\,-1 \\
\nu_{n4} &= \frac{3\nu_{hfs}}{8} - \nu_B \quad m_F{=}\,-2
\end{aligned} \tag{9.12}$$

and the eigenkets can be written as $|n\nu_{ni}m_F\rangle$, where i labels the frequency ν_{ni} of each level (these eigenkets are not written explicitly). In the limit that $\nu_B \gg \nu_{hfs}$, approximately satisfied in our experiment (Pashen-Back region), one recovers the $|m_s m_I\rangle$ eigenkets with associated energy levels $\pm h\nu_B$, corrected by $h\nu_{hfs}m_s m_I/2$ (spacing about $h\nu_{hfs}/4$). In the upper Zeeman sub-manifold the energy order (from highest to lowest) is $m_F = 2, 1, 0, -1$ and in the lower Zeeman sub-manifold it is $m_F = -2, -1, 0, 1$.

9.6.2 Optical Potentials

We now need to calculate the contributions to the Hamiltonian arising from the trap field. In a paraxial approximation, the trap electric field, $\mathbf{E}(\mathbf{R}, t) = E(\mathbf{R}, t)\mathbf{u}_y$, is taken as

$$\begin{aligned}
E(\mathbf{R}, t) &= \frac{1}{4}\left[E_+(\rho, X)e^{ik_L X} + E_-(\rho, X)e^{-ik_L X}\right] e^{-i\omega_L t} \\
&\quad +\text{c.c.},
\end{aligned} \tag{9.13}$$

where

$$E_\pm(\rho, X) = E_{\pm,0}\frac{w_{\pm,0}}{w_\pm(X)}e^{-\rho^2/w_\pm^2(X)}, \tag{9.14}$$

ρ is the coordinate transverse to X, $E_{\pm,0}$ are the field amplitudes for the trap fields propagating to the right and left, $w_{\pm,0}$ are the waist radii of these fields,

$$w_\pm(X) = w_{\pm,0}\sqrt{1 + \frac{(X - X_{\pm,0})^2}{X_{\pm,r}^2}}, \tag{9.15}$$

$X_{\pm,r} = \pi w_{\pm,0}^2/\lambda_L$ are Rayleigh lengths, $X_{\pm,0}$ are the positions of the foci of the beams, and $\lambda_L = 2\pi/k_L = 2\pi c/\omega_L$ is the wavelength of the trap beam. We have allowed for unbalanced beams,

that is, the beams propagating in the $\pm X$ directions can have different waists and be centered at different positions.

The detuning of the trap field frequency from all the ground to excited state transition frequencies is sufficiently large to insure that the optical potential is the same for all ground state sublevels. The ground state optical potential is

$$U_g = -\frac{1}{2}\alpha_g \left|\bar{E}(\mathbf{R})\right|^2 \tag{9.16}$$

where

$$\left|\bar{E}(\mathbf{R})\right|^2 = \frac{1}{8}\left[\begin{array}{c} 4E_+(\rho,X)E_-(\rho,X)\cos^2(k_L X) \\ +\left[E_+(\rho,X)-E_-(\rho,X)\right]^2 \end{array}\right] \tag{9.17}$$

and α_g is the ground state polarizabilty. The trap depth $U_0(\rho,X)$ of the ground state optical potential is given by

$$U_0(\rho,X) = h\tilde{U}_0(\rho,X) = \frac{1}{4}\alpha_g E_+(\rho,X)E_-(\rho,X), \tag{9.18}$$

where

$$\tilde{U}_0(\rho,X) = \frac{1}{4h}\alpha_g E_+(\rho,X)E_-(\rho,X) \tag{9.19}$$

is the trap depth in frequency units. Therefore we can write

$$\begin{aligned} \tilde{U}_g(\rho,X) &= U_g(\rho,X)/h \\ &= -\tilde{U}_0(\rho,X)\left[\cos^2(k_L X) + \frac{\left[E_+(\rho,X)-E_-(\rho,X)\right]^2}{4E_+(\rho,X)E_-(\rho,X)}\right]. \end{aligned} \tag{9.20}$$

The optical potential associated with an ns Rydberg level has been calculated previously [48, 57] and consists of two parts. First there is the ponderomotive potential associated with the A^2 ($\mathbf{A}$ is the vector potential of the trap field) contribution to the Hamiltonian and is the same for all the levels in the ns Rydberg manifold. Explicitly the ponderomotive potential is given by

$$U_n^{pon}(\rho,X) = -\frac{|\alpha_f|}{16}\left[\begin{array}{c} 4\theta_n E_+(\rho,X)E_-(\rho,X)\cos^2(k_L X) \\ +\left[E_+(\rho,X)-E_-(\rho,X)\right]^2 \\ +2E_+(\rho,X)E_-(\rho,X)\left(1-\theta_n\right) \end{array}\right] \tag{9.21}$$

where

$$\alpha_f = \left(-\frac{e^2}{m_e\omega_L^2}\right) \tag{9.22}$$

is the free electron polarizability, and θ_n is a "landscape" factor [53].

In addition to the ponderomotive contribution to the Hamiltonian, there is also the $\mathbf{A}\cdot\mathbf{p}$ contribution. Although the $\mathbf{A}\cdot\mathbf{p}$ contribution contains a sum over all intermediate states, the trap field

is in near-resonance with the $|ns\rangle \leftrightarrow |6p_{3/2}\rangle$ transition and we can restrict the the sum to only the hyperfine states in the $6p_{3/2}$ manifold. In that limit it makes no difference whether we use the $\mathbf{A}\cdot\mathbf{p}$ or $\mathbf{E}\cdot\mathbf{r}$ form of the interaction potential. However, the detuning of the trap field frequency from the $|ns\rangle \leftrightarrow |6p_{3/2}\rangle$ transition frequency is *not* sufficiently large to justify the neglect of the hyperfine splitting of the $6p_{3/2}$ sublevels. This results in optical potentials that are dependent on the m_F values of the ns Rydberg sublevels.

The interaction Hamiltonian associated with this nearly resonant contribution is denoted by H_r, having matrix elements in frequency units given by [62]

$$\frac{\langle nF'm'_F|\, H_r\, |nFm_F\rangle}{h} = \sum_{K,Q} S_{F'F}\left(K\right) \begin{bmatrix} F' & K & F \\ m'_F & Q & m_F \end{bmatrix} \varepsilon_Q^K, \tag{9.23}$$

where

$$\begin{aligned} S_{F'F}\left(K\right) = \sum_H & \frac{\left(-1\right)^{F'+H+K} \chi^{+}_{H;nF}(\rho,X)\chi^{-*}_{H;nF'}(\rho,X)}{2\pi\Delta_{ns,H}} \\ & \times \left[\left(2K+1\right)/\left(2F+1\right)\right]^{1/2} \begin{Bmatrix} F & F' & K \\ 1 & 1 & H \end{Bmatrix} \\ & \times \left[\cos^2\left(k_L X\right) + \frac{\left[E_+(\rho,X) - E_-(\rho,X)\right]^2}{4E_+(\rho,X)E_-(\rho,X)}\right], \end{aligned} \tag{9.24}$$

$$\chi^{\pm}_{H;nF}(\rho,X) = -\mu_{H;nF}E_{\pm}(\rho,X)/2\hbar, \tag{9.25}$$

μ_{HF} is the reduced matrix element of the dipole moment operator between hyperfine states H of the $6p_{3/2}$ level and the nsF Rydberg level, the quantity in braces is a 6-J symbol,

$$\Delta_{ns,H} = \omega_L - \omega_{ns,H} \tag{9.26}$$

is an atom-field detuning for the transition between hyperfine states H of the $6p_{3/2}$ level and the Rydberg level ns,

$$\varepsilon_Q^K = \sum_{q,q'} \left(-1\right)^{q'} \epsilon_q \left(\epsilon_{-q'}\right)^* \begin{bmatrix} 1 & 1 & K \\ q & q' & Q \end{bmatrix}, \tag{9.27}$$

e_q are spherical components of the polarization ϵ, and

$$\epsilon_{\pm1} = \mp\frac{\epsilon_x \pm i\epsilon_y}{\sqrt{2}}; \quad \epsilon_0 = \epsilon_z. \tag{9.28}$$

Note that the sum over H consists of the 4 hyperfine levels of the $6p_{3/2}$ state ($H = 0, 1, 2, 3$). For a y- polarized field ($\epsilon_x = \epsilon_z = 0; \epsilon_y = 1$) ,

$$\epsilon_{\pm 1} = -\frac{i}{\sqrt{2}}; \quad \epsilon_0 = 0, \tag{9.29}$$

and

$$\begin{aligned} \epsilon_Q^K(y) = & -\frac{1}{\sqrt{3}}\delta_{K,0}\delta_{Q,0} \\ & -\delta_{K,2}\left[\frac{1}{\sqrt{6}}\delta_{Q,0} + \frac{1}{2}\left(\delta_{Q,2} + \delta_{Q,-2}\right)\right]. \end{aligned} \tag{9.30}$$

The reduced Rabi frequency $\chi_{H;nF}$ can be written in terms of that in the J basis as

$$\begin{aligned} \chi_{H;nF} &= \chi_{6p_{3/2},ns_{1/2}}(-1)^{F+1}\sqrt{(2F+1)(2H+1)} \\ &\quad \times \begin{Bmatrix} \frac{3}{2} & 1 & \frac{1}{2} \\ F & \frac{3}{2} & H \end{Bmatrix}, \end{aligned} \tag{9.31}$$

implying that the optical potential for each sublevel is proportional to

$$\chi^{+}_{6p_{3/2},ns_{1/2}}(\rho, X)\chi^{-*}_{6p_{3/2},ns_{1/2}}(\rho, X).$$

9.6.3 Rydberg Level Eigenfrequencies

In principle, we should now diagonalize the entire ns subspace. It turns out, however, that the effects of the optical potential can be treated using first order perturbation theory if the basis eigenkets associated with the eigenvalues given in Eq. (9.12) are used. That is when we transform the optical potential to this basis, it is effectively diagonal for our experimental parameters. Using such a procedure we can write the near-resonant contribution to the energy of each level ν_{ni} of the manifold as

$$\begin{aligned} U^r_{\nu_{ni}}(\rho, X) &\approx -hb_{\nu_{ni}}(\rho, X) \\ &\times \left[\cos^2(k_L X) + \frac{\left[E_+(\rho, X) - E_-(\rho, X)\right]^2}{4E_+(\rho, X)E_-(\rho, X)}\right], \end{aligned} \tag{9.32}$$

where $b_{\nu_{ni}}$ is in frequency units. The values of $b_{\nu_{ni}}$ are the diagonal elements of the H_r contribution to the Hamiltonian, when the $|nFm_F\rangle$ eigenkets are expanded in terms of the $|n\nu_{ni}m_F\rangle$ eigenkets associated with the eigenfrequencies given in Eq. (9.12). The $b_{\nu_{ni}}$ values depend on the detuning of the of the trap fields from each of the hyperfine levels of the $6p_{3/2}$ manifold as well as the matrix

elements connecting these hyperfine levels to the ground and Rydberg levels - as a consequence of the different matrix elements, the $b_{\nu_{ni}}$ are different for each of the Rydberg sublevels. The ponderomotive contribution to the energy is given in Eq. (9.21).

Both the near-resonant and ponderomotive components of the Rydberg optical potentials, as well as the ground state optical potential, contain both lattice [terms proportional to $\cos^2(k_L X)$] and non-lattice contributions. The lattice potentials can result in a differential level shift for the Rydberg levels, owing to the fact that the trap depth differs for the different Rydberg sublevels. To account for this differential shift, we write $\cos^2(k_L X) = 1 - \sin^2(k_L X)$. The resulting terms that are proportional to $\sin^2(k_L X)$ constitute the lattice potential and "1" contributes to the non-lattice potential.

For our magnetic field strength of about 5 Gauss, the two Zeeman sub-manifolds, each containing four of the eight sublevels of the ns Rydberg level, are separated by about 14 MHz. As such, the excitation fields can be chosen to excite only one of the Zeeman sub-manifolds. Thus we need consider only the optical potentials of four levels at a time. For magic wavelength lattices, one matches the ground and excited state trap potentials by a proper choice of the trap field detuning. In our case. it is *not* possible to simultaneously match the potentials for *all* the Rydberg sublevels. For a given Zeeman sub-manifold, we match the $m_F = 0$ potential. Using Eqs. (9.20), (9.21), and (9.32), we find the matching condition is

$$b_{ns,m_F=0}(\rho, X) = \tilde{U}_0(\rho, X)\left(1 + \frac{|\alpha_f|}{\alpha_g}\theta_n\right), \tag{9.33}$$

where the m_F value now uniquely labels the energy of a level in each Zeeman sub-manifold. Then the differences in the non-lattice part of excited and ground state potentials, written in frequency units, are

$$\begin{aligned}\tilde{D}_{nsm_F}(\rho, X) &= \tilde{U}_{nsm_F}(\rho, X) - \tilde{U}_g(\rho, X) \\ &= \tilde{U}_0(\rho, X)\frac{|\alpha_f|}{2\alpha_g}(1 - \theta_n)\left[1 + 2r(\rho, X)\right] \\ &- \left[b_{nsm_F}(\rho, X) - b_{ns,m_F=0}(\rho, X)\right]\left[r(\rho, X) + 1\right],\end{aligned} \tag{9.34}$$

where

$$r = \frac{(E_+ - E_-)^2}{4E_+E_-}. \tag{9.35}$$

The spatial variations of $\tilde{U}_0(\rho, X)$ at the different atomic positions lead to a dephasing which degrades the output signal.

The ground and excited state lattice potentials are approximated by

$$\tilde{U}_g(\rho, X) = \tilde{U}_{ns0}(X) \approx \tilde{U}_0(0,0)\sin^2(k_L X)\,; \tag{9.36a}$$

$$\tilde{U}_{nsm_F}(X) \approx \frac{b_{nsm_F}(0,0)}{b_{ns,m_F=0}(0,0)}\tilde{U}_0(0,0)\sin^2(k_L X)_. \tag{9.36b}$$

The lattice potentials determine the center-of-mass motion of the atoms. Since these potentials are state-dependent, the motion must be treated quantum mechanically. The spatial dependence of $\tilde{U}_0$ is neglected in calculating the motional states - that is, $\tilde{U}_0$ is evaluated at the center of the atomic cloud. The justification for this approximation is traced to the fact that the transverse width of the excitation fields is much less than that of the trap fields - the trap potential is approximately constant over the excitation volume. Even though $\tilde{U}_0$ does not vary that much over the excitation volume, it still can have an effect when it appears in *phases* for sufficiently long times - that is why such effects must be included in $\tilde{D}_{nsm_F}$.

9.6.4 Excitation Scheme

The atoms are optically pumped into a *single* magnetic sublevel having angular momentum quantum number G and magnetic quantum number m_G. Counter-propagating fields incident along the $x-$direction drive a two-photon transition from this ground state to the Zeeman manifolds of an ns Rydberg level. We consider only transitions into the four levels of the upper Zeeman manifold ($m_J = 1/2$). These are spectrally isolated from the lower Zeeman manifold. Transitions to the lower manifold can be treated by the same formalism. The two-photon transition is via *one* of the hyperfine levels (labeled by its angular momentum quantum number H) of an intermediate np state. The first of the excitation fields is nearly resonant (but still far enough from resonance to neglect any saturation effects) with the ground to intermediate state transition and has polarization given by $\cos\theta_i \mathbf{u}_z + \sin\theta_i \mathbf{u}_y$. The second field completes the transition to the Rydberg sublevels and is polarized in the z direction. At this point in the calculation, we neglect any motion of the atoms; that is we assume the atoms are at fixed positions. The expressions to be derived will then be generalized to account for the motion of the atoms in the trap potentials.

9.6.4.1 First step

In perturbation theory and in an interaction representation, the intermediate state amplitudes evolve

approximately as

$$c_{p_J H m_H} = \frac{\Omega_1(\rho, X) f_1(t) e^{-i\Delta_{m_H,m_G} t}}{2\sqrt{2H+1}\Delta_{m_H,m_G}} P(m_G, m_H, \theta_i), \tag{9.37}$$

where

$$P(m_G, m_H, \theta) = \begin{pmatrix} \cos\theta \begin{bmatrix} G & 1 & H \\ m_G & 0 & m_H \end{bmatrix} \\ +\frac{i\sin\theta}{\sqrt{2}} \begin{bmatrix} G & 1 & H \\ m_G & 1 & m_H \end{bmatrix} \\ +\frac{i\sin\theta}{\sqrt{2}} \begin{bmatrix} G & 1 & H \\ m_G & -1 & m_H \end{bmatrix} \end{pmatrix}, \tag{9.38}$$

$$\Omega_1(\rho, X) = -\frac{E_1(\rho, X)}{\hbar} \langle p_J H \| \mu \| G \rangle, \tag{9.39}$$

$$\Delta_{m_H,m_G} = \omega_{L_1} - \omega_{m_H,m_G} \tag{9.40}$$

$\langle p_j H || \mu || G \rangle$ is a reduced matrix element, p_J is a label for the intermediate state, ω_{m_H,m_G} is the frequency difference between the m_H hyperfine level and the m_G ground state level, ω_{L_1} is the frequency of the first excitation field, $E_1(\rho, X)$ its amplitude, and $f_1(t)$ is its envelope function. It is assumed that the field is in near resonance with a single hyperfine level H of either the $p_J = 6p$ or $p_J = 5p$ manifolds, depending on the excitation scheme. Although in near-resonance, the detunings Δ_{m_H,m_G} satisfy $\Delta_{m_H,m_G} T_{pe} \gg 1$ and $\gamma_H / (2\Delta_{m_H,m_G}) \ll 1$, where T_{pe} is the excitation pulse duration and γ_H is the decay rate of the intermediate state; as a consequence of the first inequality, the intermediate state amplitude adiabatically follows the field amplitude. Note that Δ_{0,m_G} corresponds to Δ in Figure 1(b). In our experiment, $\Delta/2\pi \approx 12$ MHz, $T_{pe} \approx 1.0$ μs, and the frequency spacing between the adjacent $6p_{3/2}(H = 3)$ magnetic sublevels is ≈ 4.7 MHz.

9.6.4.2 Second Step

The second excitation field, which is applied simultaneously with the first, couples each intermediate state magnetic sublevel labeled by m_H to a single level in the upper Zeeman ($m_J = 1/2$) sub-manifold having the same value, $m_F = m_H$, which remains a good quantum number. Since the final states are approximate eigenstates of I_z and J_z (Paschen-Back region), it is convenient to

use the $m_J m_I$ basis for these final excited states. Thus, we write

$$\dot{c}_{ns,1/2,m_I} = \frac{iE_2(\rho,X)f_2(t)}{2\hbar} c_{p_J H m_H}(t) \times \sum_{m_H} e^{-i\Delta_{m_J m_I, H m_H} t} \langle ns, m_J = 1/2, m_I | \mu_z | p_J H m_H \rangle , \tag{9.41}$$

where

$$\Delta_{m_J m_I, m_H} = \omega_{L_2} - \omega_{m_J m_I, m_H}, \tag{9.42}$$

$\omega_{m_J m_I, m_H}$ is the frequency difference between the $ns m_J m_I$ Rydberg level and the m_H hyperfine level, ω_{L_2} is the frequency of the second excitation field, $E_2(\rho, X)$ its amplitude, and $f_2(t)$ is its envelope function. The kets $|p_J H m_H\rangle$ are expanded as

$$|p_J H m_H\rangle = \sum_{m'_I, m'_J} \begin{bmatrix} J_p & 3/2 & H \\ m'_J & m'_I & m_H \end{bmatrix} |p_J, m'_J, m'_I\rangle . \tag{9.43}$$

and substituted into Eq. (9.41). In the resulting expression, only those matrix elements having $m'_J = m_J = 1/2$ and $m'_I = m_I$ contribute in Eq. (9.41); as a consequence, we find

$$\dot{c}_{ns,1/2,m_I} = -i\frac{\Omega_2(\rho,X)\Omega_1(\rho,X)f_1(t)f_2(t)}{4\sqrt{2p_J+1}\sqrt{2H+1}} \times e^{-i\Delta_{m_J m_I, m_G} t} \sum_{m_H} \frac{P(m_G, m_H, \theta_i)}{\Delta_{m_H, m_G}} \times \begin{bmatrix} J_p & 1 & 1/2 \\ 1/2 & 0 & 1/2 \end{bmatrix} \begin{bmatrix} J_p & 3/2 & H \\ 1/2 & m_I & m_H \end{bmatrix}, \tag{9.44}$$

where J_p is the angular momentum of the intermediate p state,

$$\Omega_2(\rho, X) = -\frac{E_2(\rho,X)}{\hbar} \langle ns_{1/2} \| \mu \| p_J \rangle , \tag{9.45}$$

$$\Delta_{m_J m_I, m_G} = \omega_{L_1} + \omega_{L_2} - \omega_{m_J m_I, m_G}, \tag{9.46}$$

$\omega_{m_J m_I, m_G}$ is the frequency difference between the $nsm_J m_I$ Rydberg level and the m_G ground level, and we have used Eq. (9.37). If we define

$$K\left(m_G, m_H, m_J, m_I\right) = \frac{P(m_G, m_H, \theta_i)}{\Delta_{m_H, m_G}} \times \int_{-\infty}^{\infty} dt f_1(t) f_2(t) e^{-i\Delta_{m_J m_I, m_G} t}, \tag{9.47}$$

then

$$c_{1/2,m_I}(0^+) = -\frac{i\Omega_2(\rho, X)\Omega_1(\rho, X)}{4\sqrt{2H+1}\sqrt{2J_p+1}} \times \sum_{m_H} K\left(m_G, m_H, 1/2, m_I\right) \begin{bmatrix} J_p & 1 & 1/2 \\ 1/2 & 0 & 1/2 \end{bmatrix} \begin{bmatrix} J_p & 3/2 & H \\ 1/2 & m_I & m_H \end{bmatrix}, \tag{9.48}$$

where $0+$ is a time immediately following the excitation pulses. Only a single term, one having $m_H = 1/2 + m_I$ enters the sum - that is, each intermediate state is coupled only to a single final state in the upper Zeeman manifold having the same value of m_F. A specific example is given below in Sec. 9.6.7.

9.6.5 Retrieval Pulse

The excitation pulses create coherence $\rho_{Gm_G, nsm_J m_I}$ between the ground Gm_G level and the $nsm_J m_I$ Rydberg sublevels. The relative values of $\rho_{Gm_G; nsm_J m_I}$ for different $m_J m_I$ is determined by the polarization of the excitation fields. To monitor this coherence, a retrieval pulse, polarized in the z direction and propagating in the same direction as the second excitation field is applied at a time T_s following the excitation pulses. The field is resonant with the the same Rydberg - intermediate state transition used in the excitation process . The retrieval pulse creates coherences $\rho_{Gm_G; p_J H m_H}$ which lead to phase matched emission on the ground to intermediate state transition in the same direction as the first excitation field. In general, this emission will have polarization components in both the y and z directions

The retrieval pulse drives transitions between states having the same value of m_F. The appropriate equations of motion are

$$\begin{aligned} \dot{c}_{p_J H m_H} &= -\frac{\gamma_H}{2} c_{p_J H m_H} \\ &\quad + \frac{iE_r(\rho, X) f_r(t - T_s)}{2\hbar} e^{i\Delta^r_{m_H; 1/2, m_I} t} \\ &\quad \times \langle p_J H m_H | \, \mu_z \, | nsm_J m_I \rangle \, c_{m_J m_I}, \end{aligned} \tag{9.49}$$

where

$$\Delta^r_{m_H,m_J m_I} = \omega_{L_r} - \omega_{m_J m_I, m_H}. \tag{9.50}$$

ω_{L_r} is the frequency of the of the retrieval pulse, $E_r(\rho, X)$ its amplitude, and $f_r(t - T_s)$ is its envelope function. The field frequency can be chosen to insure that $\Delta^r_{m_H,m_J m_I} = 0$ for a given value of m_H but, owing to the Zeeman splitting in the intermediate state, it cannot be equal to zero for *all* values of m_H.

Following the same procedure we used for the excitation field, we find

$$\begin{aligned}\dot{c}_{p_J H m_H} &= -\frac{\gamma_H}{2} c_{p_J H m_H} \\ &-i\frac{\Omega_r(\rho, X)}{2\sqrt{2J_p+1}} f_r(t - T_s) e^{i\Delta^r_{m_H;1/2,m_H-1/2}t} \\ \times &\begin{bmatrix} J_p & 1 & 1/2 \\ 1/2 & 0 & 1/2 \end{bmatrix} \begin{bmatrix} J_p & 3/2 & H \\ 1/2 & m_H{-}1/2 & m_H \end{bmatrix} c_{ns,1/2,m_H-1/2},\end{aligned} \tag{9.51}$$

where

$$\Omega_r(\rho, X) = -\frac{E_r(\rho, X)}{\hbar} \left\langle p_J \right\| \mu \left\| n s_{1/2} \right\rangle. \tag{9.52}$$

In contrast to the excitation pulse, the duration of retrieval pulse is greater than γ_H^{-1}; moreover, its Rabi frequency is typically larger than γ_H so as to collect the output signal on a time scale of order γ_H^{-1}. As such a perturbation treatment is no longer valid and Eq. (9.51) must be solved numerically along with the corresponding equation for $\dot{c}_{nsm_J m_I}$. This solution provides values for $c_{p_J H m_H}(t)$ in terms of $c_{nsm_J m_I}(0^+)$, which can be used to calculate the radiated signal. Since we are considering only a single Zeeman sub-manifold with $m_J = 1/2$ and a single value of H, there is no sum in Eq. (9.51). Only a single value of H and $m_I = m_H - 1/2$ are present in the equation. If we write

$$\begin{aligned}\Delta^r_{m_H;1/2,m_H-1/2} t &= \Delta^r_{m_H;1/2,m_H-1/2} T_s \\ &+\Delta^r_{m_H;1/2,m_H-1/2} (t - T_s),\end{aligned} \tag{9.53}$$

then the formal solution of Eq. (9.51) is given by

$$\begin{aligned}c_{p_J H m_H}(t) &= R_{p_J H m_H; n s m_J m_I}(t - T_s) \\ &\times e^{i\Delta^r_{m_H;1/2,m_H-1/2} T_s} \\ &\times c_{nsm_J m_I}(0^+) \delta_{m_J,1/2} \delta_{m_I,m_H-1/2}.\end{aligned} \tag{9.54}$$

In all but the perturbation theory limit, $R_{p_J H m_H; n s m_J m_I}(t - T_s)$ is a nonlinear function of Ω_r. The

interaction representation density matrix element,

$$\rho^I_{p_J H m_H; G m_G}(t) \approx c_{p_J H m_H}(t), \tag{9.55}$$

since the initial state amplitude is unchanged in lowest order perturbation theory.

So far the calculations have been carried out for an atom located at $X = 0$. To generalize Eq. (9.55) for an atom located at $X = X_j$, we set

$$\rho^{I(j)}_{p_J H m_H; G m_G}(t) \approx c_{p_J H m_H}(t) e^{i k_0 X_j}, \tag{9.56}$$

where $k_0 = \omega_{HG}/c = \omega_{L_r}/c$.

9.6.6 Signal

The excitation, readout, and vacuum fields combine to produce a phase-matched emission in the $\mathbf{u}_x$ direction. The output electric field in the phase-matched direction has both y and z polarization components. These components are mixed on a half-wave plate oriented at an angle $\theta_d/2$ from the z axis to produce new vertical and horizontal components given by

$$\begin{aligned} E_V &= E_z \cos\theta_d + E_y \sin\theta_d; \\ E_H &= E_y \cos\theta_d - E_z \sin\theta_d, \end{aligned} \tag{9.57}$$

which are then separated by a polarizing beam splitter and measured in two detectors. We discuss only the vertical component signal - the horizontal component signal can be obtained by interchanging $\cos\theta_d$ with $-\sin\theta_d$ and $\sin\theta_d$ with $\cos\theta_d$ in the final result.

The time-integrated phase-matched signal recorded at the vertical detector is proportional to a quantity S_V defined by

$$S_V(T_s) = X_d^2 \int dt \, \langle E_{V+}(X_d, t) E_{V-}(X_d, t) \rangle \, , \tag{9.58}$$

where $E_{V\pm}(X_d, t)$ are the positive and negative frequency components of the vertical component of the electric field operator evaluated at some arbitrary point X_d in the radiation zone to the right of the half-wave plate. Using source-field theory [29], it then follows that

$$S_V(T_s) = \int_0^\infty dt \, |G_V(X_d, t)|^2 \tag{9.59}$$

where

$$
\begin{aligned}
G_V(X_d,t) &= \frac{\omega_0^2}{4\pi\epsilon_0 c^2}\sum_{m_H} e^{-i\omega_{m_H m_G}(t-X_d/c)} \\
&\times \langle Gm_G|\left(\mu_z\cos\theta_d+\mu_y\sin\theta_d\right)|p_J H m_H\rangle \\
&\times \sum_{j=1}^{N}\rho^{I(j)}_{p_J H m_H, G m_G}\left(t-X_d/c\right)e^{-ik_0 X_j} \\
&= \left(\frac{\omega_0^2}{4\pi\epsilon_0 c^2}\right)\frac{\langle p_J H\|\,\mu\,\|G\rangle^*}{\sqrt{2H+1}} \\
&\times \sum_{m_I=-3/2}^{3/2} e^{i\left(\omega_{L_r}-\omega_{1/2,m_I;m_G}\right)T_s}P(m_G,m_I{+}1/2,\theta_d) \\
&\times \sum_{j=1}^{N} R^{(j)}_{p_J H m_I+1/2;ns,1/2,m_I}(t-T_s-X_d/c) \\
&\times e^{-i\omega_{H,m_I+1/2;Gm_G}(t-T_s-X_d/c)}c^{(j)}_{ns,1/2,m_I}(0^+),
\end{aligned}
\tag{9.60}
$$

and Eqs. (9.54) and (9.56) have been used. The spatial phase factors of the excitation fields have been accounted for in Eq. (9.56), so that the only spatial dependence of $c^{(j)}_{ns,1/2,m_I}(0^+)$ on j is related to the fact that the excitation field envelopes, $E_{1,2}(\rho,X)$ are a function of position in the atomic cloud. By combining the numerical solution leading to Eq. (9.54) with Eq. (9.48), it is the possible to calculate $G_V(X_d,t)$ and $S_V(T_s)$.

9.6.6.1 Modifications resulting from the trap potentials

The trap potentials lead to a number of qualitatively different effects that modify the signal intensity. Of primary concern to us is the motional dephasing that occurs between the excitation and readout pulses. By using matched trap potentials for both the ground and Rydberg levels, the motional dephasing can be reduced significantly from a case in which the atoms undergo force-free motion. Since it is not possible to match all the Rydberg sublevel potentials to the ground state potential, there is some slight dephasing that results from the potential differences as a result of the spatial dependence of the fields in the atomic cloud. This is in addition to a similar dephasing that occurs for high n Rydberg levels associated with the ponderomotive potential.

To generalize the result to include the effects of the trap potentials, we make a number of simplifying assumptions. First, we assume that atomic motion is frozen during the excitation and retrieval pulses. For our trap depths and temperatures, this is generally a very good approximation. Second, we approximate the energy levels in each potential as those associated with the quasibound states of the corresponding Mathieu equation problem [50]. Although we use the Mathieu equation

quasibound eigenenergies (since they appear in phases), we calculate transition matrix elements using harmonic oscillator wave functions, assuming the atoms are sufficiently cold to be localized near the bottom of the wells. As was already mentioned, we neglect any spatial variations of the field in calculating the quasibound states in the potentials - all fields are evaluated at cloud center, but we include the spatial variations of the fields insofar as they affect light shifts of the Rydberg levels relative to those of the ground state.

With these approximations and assuming an initial density matrix that is diagonal with respect to the motional states, we find [48, 57] that $G_V(X_d,t)$ can be written as

$$\begin{aligned} G_V(X_d,t) &= e^{i\left(\omega_{L_r}+\omega_{Gm_G}\right)T_s} e^{-\Gamma_{ns}T_s/2}\Theta(t-T_p-X_d/c) \\ &\times \sum_{m_F=-1}^{2}\sum_{q,q'}^{q_{\max}}\sum_{j=1}^{N} Q^{(V)(j)}_{p_JHm_H=m_F;nsm_F}(t-T_p-X_d/c) \\ &\times e^{-2\pi i\tilde{D}^{(j)}_{nsm_F}T_s} M_{gq;nsm_Fq'}(-k) \\ &\times M_{nsm_Fq';gq}(k)\, e^{i\left(\omega_q^{(g)}-\omega_{q'}^{(nsm_F)}\right)T_s}\rho_{1q,1q}(0), \end{aligned} \tag{9.61}$$

where

$$\begin{aligned} M_{nsm_Fq;gq'}(k) &= \int dX\left[\psi_{nsm_Fq}(X)\right]^* e^{ikX}\psi_{gq'}(X) \\ &= \left[M_{gq';nsm_Fq}(-k)\right]^*, \end{aligned} \tag{9.62}$$

$\psi_{\alpha q}(X)$ is a ground state eigenfunction and $\omega_q^{(g)}$ an eigenfrequency for an atom moving in the potential $U_g(0,0)$, $\psi_{nsm_Fq}(X)$ is an eigenfunction and $\omega_q^{(nsm_F)}$ an eigenfrequency for an atom moving in the potential $U_{nsm_F}(0,0)$, and $\tilde{D}^{(j)}_{nsm_F}$ is given by Eq. (9.34). The function $Q^{(V)(j)}_{p_JHm_H;nsm_F}(t)$ incorporates all the excitation and retrieval dynamics. The sums over q, q', q'' are restricted to (quasibound) states; that is, $q_{\max}$ is the number of bound states in the potential. A loss factor, $e^{-\Gamma_{ns}T_s/2}$, has been added to allow for decay between the excitation and retrieval pulses owing to spontaneous emission, black-body radiation, and decay from the intermediate state. The sum over j actually corresponds to an integral over X and ρ, taking into account the spatial dependence of the excitation and retrieval fields, weighted with the atomic density distribution.

For the polarizations of our excitation fields, the sum over m_F consists of at most three terms, $m_F = m_G, m_{G\pm1}$. Experimentally, we optically pump the initial state into $m_G = 0$, so only Rydberg levels having $m_F = 0, \pm1$ are populated.

The numerical calculation of $S_V(T_s)$ is time-consuming, since the sum over j in Eq. (9.59) must be carried out for each $\tau = t - T_p - X_d/c$, the result squared and then integrated over τ from

zero to infinity. To simplify matters, we assume that

$$Q^{(V)(j)}_{p_J H m_H = m_F; n s m_F}(\tau) \approx Q^{(V)}_{p_J n s m_F} g(\tau) \Lambda(\rho, X), \tag{9.63}$$

where $g(\tau)$ is a state independent function of τ and

$$\Lambda(\rho, X) = \Omega_r(\rho, X)\Omega_2(\rho, X)\Omega_1(\rho, X). \tag{9.64}$$

While this approximation is not justified in general, it should not seriously affect the dependence of the *normalized* signal on T_s. With this assumption, the signal at time T_s normalized to that at $T_s = 1$ μs, can be written in the form given in Eqs. (9.1)-(9.3). In those expressions, the sum over j has been converted to a spatial integral over the sample.

For example, if $G = 2$ and $m_G = 0$, the basic structure consists of the absolute square of the sum of three terms oscillating at the frequencies of the $m_F = 0, \pm 1$ Rydberg levels. The signal then oscillates at the difference frequencies of these levels. With our knowledge of the potential, we are then able to extract the hyperfine constant from the signal.

9.6.7 Perturbation Theory Calculation of $C_V(\rho, X, T_s)$

In this section, we give perturbation theory expressions for $c_{m_J m_I}(0^+)$, $c_{p_J H m_H}(t)$, and $C_V(\rho, X, T_s)$ when $G = 2$, $m_G = 0$, $J_p = 3/2$, $m_J = 1/2$, and $H = 3$ (values appropriate to one of the excitation schemes in our experiment). For these values, it follows from Eqs. (9.48) and (9.66) that

$$\begin{aligned}
c_{1/2,1/2}(0^+) &= -\frac{\Omega_2(\rho, X)\Omega_1(\rho, X)}{40\sqrt{7}} \\
&\quad \times K\left(1/2\right)\sin\theta_i \\
c_{1/2,-1/2}(0^+) &= \frac{3i\Omega_2(\rho, X)\Omega_1(\rho, X)}{80\sqrt{7}} \\
&\quad \times K\left(-1/2\right)\cos\theta_i \\
c_{1/2,-3/2}(0^+) &= -\frac{\Omega_2(\rho, X)\Omega_1(\rho, X)}{40\sqrt{21}} \\
&\quad \times K\left(-3/2\right)\sin\theta_i,
\end{aligned} \tag{9.65}$$

where

$$K\left(m_I\right) = \frac{\int_{-\infty}^{\infty} dt f_1(t) f_2(t) e^{-i\Delta_{1/2,m_I;0}t}}{\Delta_{m_I+1/2,0}}. \tag{9.66}$$

If all the $K's$ were equal [which would be the case if the Zeeman splitting of the intermediates state is much larger than the detuning $\Delta_{m_H,0}$ and if $\left|\Delta_{1/2,m_I;0}T_{pe}\right| \ll 1$, as it is for most of the n in

our experiment] then

$$\begin{aligned} c_{1/2,-3/2}(0^+) &= c_{1/2,1/2}(0^+)/\sqrt{3}; \\ c_{1/2,-1/2}(0^+) &= -3i\cot\theta_i c_{1/2,1/2}(0^+)/2. \end{aligned} \tag{9.67}$$

Note that the relative coherence between the $c_{1/2,-3/2}$ and $c_{1/2,-1/2}$ is important since it leads to the y-polarized signal in the phase-matched direction.

We next solve Eq. (9.51) using perturbation theory for a square envelope retrieval pulse for which

$$f_r(\tau) = \begin{cases} 0 & \tau < 0 \text{ and } \tau > T_{pr} \\ 1 & 0 < \tau < T_{pr} \end{cases}, \tag{9.68}$$

assuming that $\gamma_H T_{pr} \gg 1$ (T_{pr} is the retrieval pulse duration), to obtain

$$\begin{aligned} c_{p_J H m_H}(t) \approx -i\frac{\Omega_r(\rho,X)}{4}\frac{e^{i\Delta^r_{p_J H m_H;ns,1/2.m_H-1/2}T_s}}{\frac{\gamma_H}{2}+i\Delta^r_{p_J H m_H;ns,1/2.m_H-1/2}} \\ \times \begin{bmatrix} 3/2 & 1 & 1/2 \\ 1/2 & 0 & 1/2 \end{bmatrix} \begin{bmatrix} 3/2 & 3/2 & 3 \\ 1/2 & m_H-1/2 & m_H \end{bmatrix} c_{ns,1/2,m_H-1/2}(0^+). \end{aligned} \tag{9.69}$$

Using Eqs. (9.59)-(9.64), we then find that the normalized signal, as defined in Eq. (9.1), is given by Eq. (9.2) with

$$\begin{aligned} C_V(\rho,X,T_s) = \sum_{m_F=-1}^{1}\sum_{q,q'}^{q_{\max}} e^{-i\omega_{nsm_F}T_s} Q^{(V)}_{p_J nsm_F} \\ \times e^{-2\pi i\tilde{D}^{(j)}_{nsm_F}(\rho,X)T_s} M_{gq;nsm_Fq'}(-k) \\ \times M_{nsm_Fq';gq}(k)\, e^{i\left(\omega^{(g)}_q-\omega^{(nsm_F)}_{q'}\right)T_s}\rho_{1q,1q}(0), \end{aligned} \tag{9.70}$$

and

$$\begin{aligned} Q^{(V)}_{p_J nsm_F} = \frac{K(m_F-1/2)}{\frac{\gamma_H}{2}+i\Delta^r_{p_J H m_H;nsm_F}} \\ \times \begin{pmatrix} \sin\theta_i\sin\theta_d\delta_{m_F,1} \\ -\frac{9\cos\theta_i\cos\theta_d}{4}\delta_{m_F,0} \\ +\frac{\sin\theta_i\sin\theta_d}{3}\delta_{m_F,-1} \end{pmatrix}. \end{aligned} \tag{9.71}$$

Note that, owing to the definition given in Eq. (9.1), we were able to remove any spatially inde-

pendent common factors in writing the expression for $Q^{(V)}_{pjnsm_F}$.

CHAPTER 10

Hanbury Brown-Twiss Correlations for a Driven Super-Atom

In his 1917 paper [63], Einstein introduced his famous A and B coefficients, with the A coefficient associated with spontaneous emission and the B coefficient to either absorption or stimulated emission (both referred to as *changes of state due to irradiation* by Einstein). While there may not be a universal definition as to what constitutes stimulated emission, any definition describes processes in which atom-field interactions lead to an increase in the intensity of an input field. There have been a number of both theoretical analyses and experimental implementations involving parametric down-conversion (e.g., Refs. [64, 65, 66, 67, 68, 69]) which have been interpreted in terms of stimulated emission and/or amplification. In all of these cases, coincidence counts involving both signal and idler modes are measured when a single-photon or a weak coherent probe pulse is sent into a crystal, so that it propagates collinearly with the signal mode. A two-fold increase in the time-integrated coincidence counts occurs for overlapping probe and signal field pulses, compared to the case of non-overlapping pulses. The increase in coincidence counts was interpreted in terms of probe-induced stimulated emission in the crystal. The analyses supporting this assertion are based on a perturbative calculation of the evolution of the state vector associated with an effective Hamiltonian involving third-order nonlinear susceptibilities.

We have carried out an experiment that, in some ways, is analogous to the down-conversion experiments. Instead of a nonlinear crystal, our active medium consists of a gas of cold rubidium atoms, Figure 1(a). Following their release from an optical trap, the atoms are subjected to an excitation/de-excitation pulse sequence, leading to phase-matched emission in the x direction having central frequency ω_A. A weak probe pulse having central frequency ω_P is also sent into the sample in the x direction and can be delayed relative to the phase-matched emission pulse. The output field, containing contributions from both the input field and the field radiated by the atoms, is sent to a beam splitter and coincidence counts are recorded as a function of the delay time. As in the down-conversion experiments, we can observe an increase in coincidence counts by a factor of two when the probe field overlaps with the field radiated by the atoms.

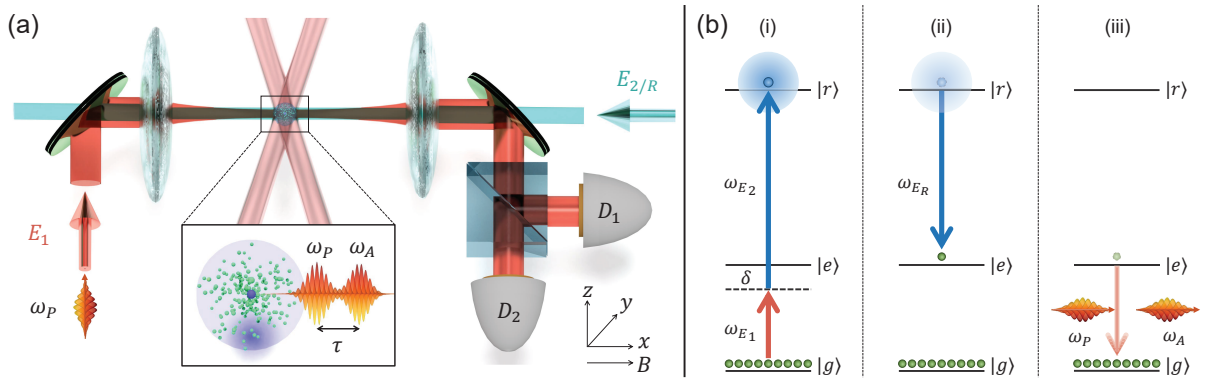

Figure 10.1: Outline of the experiment. (a) Experimental setup: ultracold atomic gas is prepared in a crossed pair of focused YAG laser beams. A pair of lenses focuses E_1 and E_2 laser fields to drive a two-photon transition from the ground state $|g\rangle$ to the Rydberg state $|r\rangle$. A retrieval laser pulse E_R leads to emission of atomic field which is split on a beam-splitter and directed onto photodetectors D_1 and D_2. A probe laser field with controllable frequency and delay is aligned into the spatial mode of the atomic emission. (b) Three main steps of the protocol: (i) an atomic ensemble is excited into a Rydberg atomic state $|r\rangle$; (ii) after a delay T_s, the atoms are driven into intermediate state $|e\rangle$, leading to emission on the $|e\rangle \leftrightarrow |g\rangle$ transition, with propagation direction determined by the phase-matching condition; (iii) an incoming probe field and atomic emission fields, with controllable delay between the two fields, are directed towards HBT measurement.

What is the origin of this increase in coincidence counts? Can it be traced to stimulated emission as is claimed in down-conversion experiments, or are there other mechanisms at play here? To help answer these questions, we prepare our atomic ensemble in two distinct fashions, one involving a single excitation ("super-atom" or Dicke [70] state) and the other a factorized initial state. We are able to do this by choosing different Rydberg states in the excitation schemes. The results are analyzed using source-field theory [71]. In the case of the Dicke state preparation, there is a single excitation shared by N atoms and the incoming probe pulse can drive a stimulated transition between the Dicke state and the ground state. The coupling strength between the two collective states is enhanced by a factor $\sqrt{N}$. As a consequence, one might associate the increased coincidence counts with stimulated emission. On the other hand, for a factorized initial atomic state, such an interpretation is no longer tenable since the incident probe field is actually absorbed by the medium. In both cases however an increase in coincidence counts is observed. We present experimental results and a theoretical analysis that leads us to conclude that stimulated emission is *not* responsible for the increase in coincidence counts. Instead, the increase in coincidence counts can be attributed to Hanbury Brown and Twiss (HBT) interference [72], which we claim is also responsible for the increase in coincidence counts measured in the down-conversion experiments, see Supplementary Material.

To illustrate the underlying physics, we consider first a single-photon probe pulse incident on

a two-level atom (lower level g and excited level e) that is prepared in its excited state at time $t = 0$. The wave front of the probe pulse, which has cross-sectional area A greater than the pulse's central wavelength λ, arrives at the atom at time $\tau \geq 0$. In source-field theory [29], the positive frequency component of the field operator for this system can be written as $E_+(\mathbf{R}, t) = E_+^{(0)}(\mathbf{R}, t) + E_+^{(S)}(\mathbf{R}, t)$, where $E_+^{(0)}(\mathbf{R}, t)$ is the free-field operator and $E_+^{(S)}(\mathbf{R}, t)$ is the source field operator associated with the field radiated by the atoms in the sample. Two types of measurements can be envisioned. Either (1) the integrated field intensity is measured or (2) the time-integrated number of coincidence counts is recorded as a function of τ after the field is sent through a beam splitter. The detection volume is restricted to a small angle in the forward direction.

For $A > \lambda$, a *weak coupling* approximation can be made - the interaction between the atoms and the input pulse can be neglected to lowest order, owing to the fact that $\max[\Omega_p/\gamma_e \ll 1, \Omega_p T_p \ll 1]$, where Ω_p is the probe Rabi frequency, T_p is the probe pulse duration, and γ_e is the excited state decay rate. It is then rather easy to analyze the two measurement scenarios, which are sensitive to different physical processes. The total field can be viewed as a sum of the collimated input field, the spherical wave spontaneously emitted field from the atom, and the field scattered by the atom.

The integrated field intensity is sensitive to the *amplitudes* of the three contributions to the total field. Stimulated emission or absorption is associated with the interference of the scattered field with the (unperturbed) input field [73]. Whether stimulated emission or absorption occurs depends on both the spectral width of the input pulse and the time delay τ. In contrast, the time-integrated number of coincidence counts N_c is insensitive to the relative phase of the input and source fields - it depends only on field *intensities*. Moreover, in the weak coupling approximation, the scattered field has a negligible effect on the value of N_c. When measured as a function of τ, N_c exhibits a "bump" for $\tau = 0$ that can then be interpreted as HBT interference between the input field and the field spontaneously emitted from the atoms, in exact analogy with the HBT increase in the second order correlation function for two independent light sources. In other words, although both stimulated emission and HBT interference can both be described in terms of interference, they correspond to fundamentally different physical processes. The HBT coincidence count bump is *not* linked to stimulated emission - it occurs even if the input field is attenuated. Moreover, in the weak coupling approximation, any absorption or stimulated emission of the input pulse is negligibly small - the output field intensity is approximately equal to the sum of the input and atomic field intensities, considered as independent sources.

The same formalism can be used to model our experiment involving phase-matched emission from an ensemble of atoms, Figure 1(b). The three-level atoms (ground state $|g\rangle = |5S_{1/2}, F = 2, m_F = 2\rangle$, intermediate state $|e\rangle = |5P_{3/2}, F = 3, m_F = 3\rangle$, and Rydberg state $|r\rangle = |nS_{1/2}, m_J = 1/2\rangle$) are prepared in a phase-matched superposition of ground and Rydberg

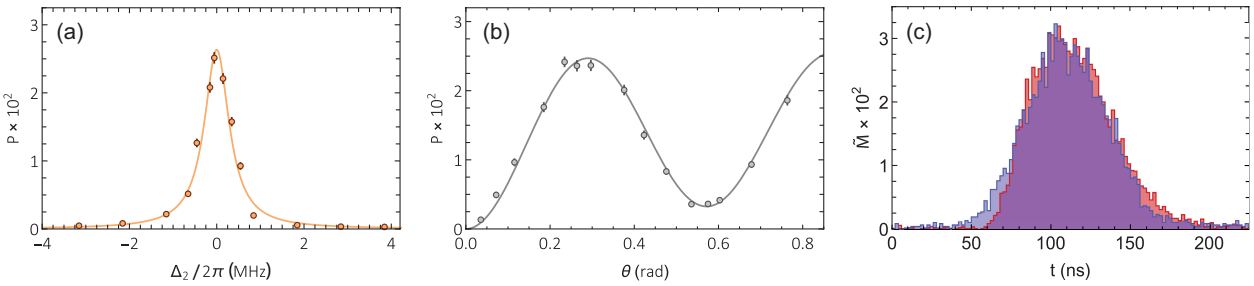

Figure 10.2: Probing a collective (super-atom) state. (a) Probability of photoelectric detection event per trial P as a function of two-photon detuning $\Delta_2 = \omega_{rg} - (\omega_{E_1} + \omega_{E_2})$ for the Rydberg state $|r\rangle = |87S_{1/2}\rangle$. The solid curve is a Lorentzian fit. The 0.8 MHz (FWHM) width of the peak is determined by the 1 μs excitation pulse duration; (b) P as a function of the collective Rabi angle θ displaying a period of a many-body (super-atom) Rabi oscillation. Solid curve is a theory curve for a collective Rabi oscillation with $\Omega_2/2\pi = 1.5$ MHz and $\Omega_1/2\pi$ varied between 2 and 20 MHz. The best fit between theory and the data occurs for the number of atoms $N = 234$; (c) Normalized photocounts $\widetilde{M}$ as a function of time t for the probe pulse (red) and the atomic emission (blue). The error bars represent $\pm$ one standard deviation ($\sqrt{M}$) for M photoelectric counting events.

states using an excitation pulse of duration $T_E = 1$ μs, consisting of two counter-propagating laser pulses E_1 and E_2 having central wavelengths 780 nm and 480 nm, respectively. Field E_1 drives the $|g\rangle \leftrightarrow |e\rangle$ transition with Rabi frequency Ω_1 and field E_2 drives the $|e\rangle \leftrightarrow |r\rangle$ transition with Rabi frequency Ω_2. Field E_1 is detuned by an amount $\delta = -2\pi \times 90$ MHz from ω_{eg}. For a high-n Rydberg state [4], excitation of more than one atom into the Rydberg state can be suppressed, with the atomic ensemble being coherently driven between the collective ground state $|G\rangle$ and a singly-excited (so-called super-atom) collective state $|R\rangle$ at a frequency $\Omega_N = \sqrt{N}\Omega_1\Omega_2/(2\delta)$ [74, 75, 14, 21, 76, 22]. After a delay $T_s \approx 0.5$ μs following the excitation pulse, a readout pulse E_R, centered at 480 nm is applied that is resonant with the $|r\rangle \leftrightarrow |e\rangle$ transition frequency and leads to phase-matched emission with $\omega_A = \omega_{eg}$.

Figure 2(a) displays the probability of photoelectric detection P as a function of two-photon detuning Δ_2 between $(\omega_{E_1} + \omega_{E_2})$ and ω_{rg}. The maximum probability of a photoelectric detection per trial is $P_{max} \approx 2.5 \times 10^{-2}$ for a chosen value of $\theta \equiv \Omega_N T_E \simeq \pi$. Figure 2(b) shows P as a function of θ. Accounting for a factor of $\zeta = 0.27$ transmission and detection efficiency, there is a maximum probability $p_f \approx 0.09$ for a single-photon to be emitted into the spatial mode defined by the single-mode fiber used for collection. A probe pulse whose temporal profile matches that of the phase-matched emission and whose spatial mode corresponds to the detector acceptance mode, is also sent into the medium. In the absence of any Rydberg excitation, the transmission coefficient for the probe pulse is 0.45 ± 0.01. Figure 2(c) shows measured intensity profiles (normalized photocounts $\widetilde{M}$ vs time t) for the probe pulse and the phase-matched atomic emission. The profiles are

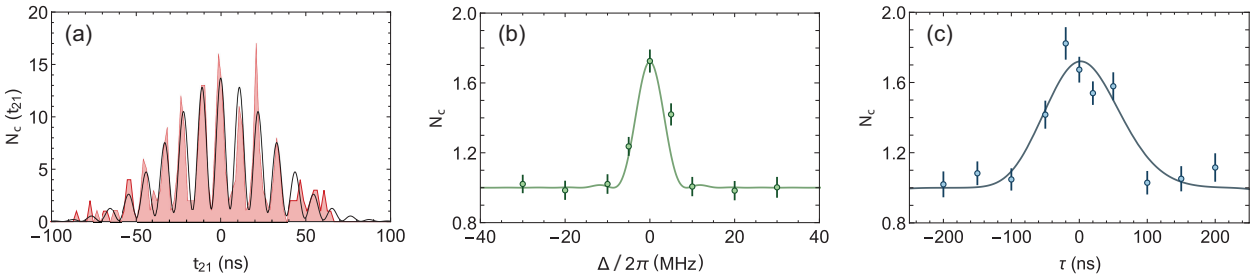

Figure 10.3: Two-photon statistics for the upper atomic state $|r\rangle = |87S_{1/2}\rangle$. (a) Coincidences in a 2-ns window $N_c(t_{21})$ as a function of t_{21} for detuning $\Delta/2\pi = -80$ MHz between the probe field and the field emitted by the atoms. (b) Normalized integrated coincidences N_c as a function of the detuning Δ between the probe pulse and the pulse from the ensemble. (c) N_c as a function of the delay τ between the probe pulse and the pulse from the ensemble. Solid curves in (a)-(c) are obtained using our theoretical model.

matched by adjusting both the readout and probe pulses, with their overlap integral being 0.97 for a 0.5 μs integration window and greater than 0.98 for a 0.1 μs integration window centered on their peak values. The value of the time-integrated second-order correlation function for atomic emission in the absence of the probe pulse is $g_A^{(2)} = 0.04$. The probe pulse can be delayed by a time τ relative to the phase-matched emission and the probe frequency ω_P can be detuned by an amount Δ from ω_A.

The total output field is sent into a beam splitter and detectors in the output mode of the beam splitter record coincidence counts. In the weak coupling approximation, any contribution to coincidence counts due to stimulated emission constitutes a small effect, of order $1/\left(Nk_0^2A\right) \simeq 10^{-6}$, where $k_0 = \omega_{21}/c$ and A is the cross-sectional area of the probe pulse. In fact, instead of being amplified by the medium, the output field intensity in the presence of Rydberg excitation is actually decreased by $\simeq 10^{-2}$.

The probe pulse is a weak, coherent state pulse having energy less than or of order $\hbar\omega_{eg}$. The atoms are prepared either into (1) a state consisting of a single phase-matched excitation by choosing an upper atomic state $|r\rangle = |87S_{1/2}\rangle$ with strong interactions [12, 13, 15], or (2) an upper atomic state $|r\rangle = |50S_{1/2}\rangle$, which leads to a factorized atomic state having on average $N_r \approx 1.5$ Rydberg excitations in the sample. In case (1), assuming that the spatial profiles of the probe and phase-matched emission pulses are identical, the number of photo-counts separated in time by t_{21} is given by

$$N_c(t_{21}) = \int_{-\infty}^{\infty} dt\, \widetilde{I}(t)\widetilde{I}(t+t_{21})\left[1 + V_1(K)\cos\left(\Delta t_{21}\right)\right], \tag{10.1}$$

where $\widetilde{I}(t)$ is proportional to the intensity profile of the probe field, K is the ratio of integrated intensities for the input probe pulse and phase-matched emission, and $V_1(K) = 2K/(K^2 + 2K +$

$g_A^{(2)}$) is the fringe visibility, allowing for a non-zero value of $g_A^{(2)}$. As was the case for a two-level atom, Eq. (10.1) is derived assuming that atom-field interactions are negligibly small, that is no effects related to stimulated emission are included. In Figure 3(a), we plot measured values of $N_c(t_{21})$ for $K = 0.21$. The theory curve is obtained assuming a Gaussian profile for $\widetilde{I}(t)$ and an expected value of $V_1(0.21) = 0.83$.

The normalized time-integrated coincidence counts are given by

$$N_c = 1 + 2K|J|^2/[K^2 + 2K + g_A^{(2)}], \tag{10.2}$$

where $S(t)$ and $f(t)$ are the (real) scaled amplitudes of the phase-matched field and the probe pulse, respectively, normalized such that $\int_{-\infty}^{\infty} dt\, S^2(t) = 1$, $\int_{-\infty}^{\infty} dt\, f^2(t) = 1$, $J \equiv \int_{-\infty}^{\infty} e^{-i\Delta t} S(t - \tau) f(t) dt$ is the overlap integral of the two fields. In this case we allow for a slight difference between the intensity profiles of the probe field and atomic emission. If the intensity envelopes are identical and if $K \ll 1$ and $g_A^{(2)} \ll 1$, the time-integrated coincidence counts are doubled provided $\Delta = 0$ and $\tau = 0$, from the case where $|\Delta| / \gamma_e \gg 1$ or $\gamma_e \tau \gg 1$.

In Fig. 3(b), N_c is plotted as a function of Δ for $\tau = 0$ and N_c is plotted as a function of τ for $\Delta = 0$ in Fig. 3(c). The Eq.(10.2) is strictly valid only under an assumption of an optically thin medium in which the fraction of energy radiated by the atoms in the phase-matched direction $p_f \ll 1$. Including corrections of order $p_f \approx 0.06$ we estimate the value of $N_c \simeq 1 + 2(1 - p_f)K|J|^2/(K^2 + 2K + g_A^{(2)})$. In Figs. 3(b) and 3(c), the theoretical curves are drawn using $\{K = 0.46, |J|^2 = 0.98\}$ [$N_c(\Delta = 0) = 1.72$] and $\{K = 0.35, |J|^2 = 0.94\}$ [$N_c(\tau = 0) = 1.72$], respectively.

When a Rydberg blockade is operative, the problem can be reduced to an effective two-level problem involving transitions between the Dicke state and the ground state. As such, it is possible to envision a situation in which there is total inversion of the system. Although the probe field can produce stimulated emission on the inverted system, the observed factor of two increase in coincidence counts is *not* a consequence of stimulated emission. Rather, it is an indication of both the non-classical nature of the atomic Dicke state and HBT interference.

As further evidence of the fact that the increase in coincidence counts results from HBT interference and not stimulated emission, we next consider a factorized initial atomic state for which $g^{(2)} = 1$ and there is no inversion. Assuming that there is no temporal coherence between the input pulse and the phase-matched emission and that $f(t) = S(t)$, $N_c(t_{21})$ is given by

$$N_c(t_{21}) = \int_{-\infty}^{\infty} dt\, \widetilde{I}(t)\widetilde{I}(t + t_{21}) \left[1 + V_2(K) \cos\left(\Delta t_{21}\right)\right],$$

where $V_2(K) = 2K/(1 + K)^2$ is the fringe visibility. In Figure 4(a), we plot values of $N_c(t_{21})$

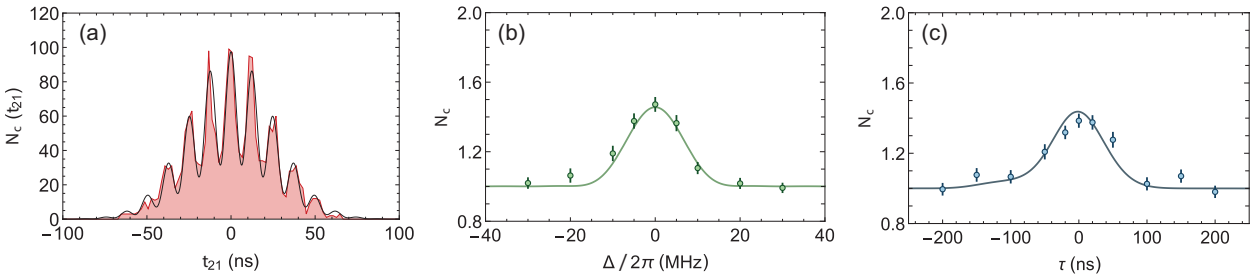

Figure 10.4: Data and curves analogous to those shown in Fig. 3, but for the upper atomic state $|r\rangle = |50S_{1/2}\rangle$.

for the Rydberg state $|r\rangle = |50S_{1/2}\rangle$ and with $K = 0.98$. The solid curve is theory, with fringe visibility $V_2(0.98) \approx 0.50$. The fringe visibility of 1/2 is consistent with HBT interference between two coherent-state pulses, a situation that is mirrored by our choice of a factorized atomic state and a coherent-state probe pulse. For $K = 1$, the normalized time-integrated coincidence counts are given by $N_c = 1 + \frac{1}{2}|J|^2$. It is seen that in this case, for $f(t) = S(t)$, the time-integrated coincidence rates are increased by a factor of $3/2$ provided $\Delta = 0$ and $\tau = 0$, from the case where $|\Delta|/\gamma_e \gg 1$ or $\gamma_e \tau \gg 1$. Figures 4(b,c) show N_c as a function of pulse detuning and delay respectively, together with theory curves for which the enhancement factor $N_c \simeq 1 + 2(1 - p_f)|J|^2 K/(1 + K)^2$. In Figs. 4(b) and 4(c), the theoretical curves are drawn using $\{K = 0.90, |J|^2 = 0.97\}$ [$N_c(\Delta = 0) = 1.46$] and $\{K = 1.00, |J|^2 = 0.93\}$ [$N_c(\tau = 0) = 1.44$], respectively. Again, although stimulated emission is absent, there is an enhancement in coincidence counts when the probe pulse overlaps with the phase-matched atomic emission.

In conclusion, the interaction between the incident probe field with the atoms experiments such as ours and in Refs. [64, 65, 66, 67, 68, 69] can be treated in a weak coupling approximation. In that limit the increase in coincidence counts can be fully described by HBT-type interference between the incident field and the field radiated by the medium. There is no direct connection with stimulated emission.

This work was supported by the ARL Center for Distributed Quantum Information, Air Force Office of Scientific Research, and the National Science Foundation.

CHAPTER 11

Phase Matching in Lower Dimensions

Beginning with the pioneering demonstrations of second-harmonic generation [77, 78] and photon echoes [79], phase-matching has played a critical role in nonlinear and quantum optics. When N atoms are excited in free-space, collective emission can result in a number of ways, some of which are discussed by Dicke [70] in his seminal paper. One type of collective emission, which we refer to as superradiance, is produced when two-level atoms are prepared in a completely inverted or phase-matched initial state in an ensemble for which the so-called cooperativity parameter is greater than or of order unity. A second type of collective emission, on which we focus here, is simply phase-matched emission from an array of non-interacting atoms, that is, a limiting case where the field radiated be a given atom has a negligible effect on the dynamics of the other atoms. This is the type of interference effect typically encountered in optical coherent transients [29]. Yet a third type of collective emission is somewhat of a hybrid of the first two. Atoms are prepared in a collective, phased single-excitation state using a single-photon pulse [38, 80, 81]. The atoms do not acquire a dipole moment, but the emission pattern can mirror that of phase-matched emission. In this and related schemes in which the dimensions of the excitation volume are large compared with the wavelength of the excitation field(s), the $\mathbf{k}$-vector of the phase-matched emission satisfies a momentum conservation condition involving the $\mathbf{k}$-vectors of the excitation fields. For example, in a four-wave mixing process with incident field $\mathbf{k}$-vectors $\mathbf{k}_1$, $\mathbf{k}_2$, and $\mathbf{k}_3$, a possible phase-matched outgoing field propagates in the $\mathbf{k}_s = \mathbf{k}_1 - \mathbf{k}_2 + \mathbf{k}_3$ direction. The signal results from an average over the distribution of positions of individual atomic emitters and does not require a specific spatial arrangement of the atoms in the sample, in contrast to Bragg scattering.

In an experimental situation involving a *single* cw excitation field incident on a low density atomic vapor, collective scattering still occurs, but its signature is very different from that in the 4-wave mixing experiment. The collectively scattered light is phase-matched only in the direction of the input field and it interferes with the incident light to diminish the incident field's intensity. In order to get constructive interference in other directions, a specific atomic array is needed, rather than a disordered vapor. This type of collective emission is nothing more than Bragg scattering and it has been demonstrated using chains of trapped ions [82, 83, 84], two-dimensional Mott insulators

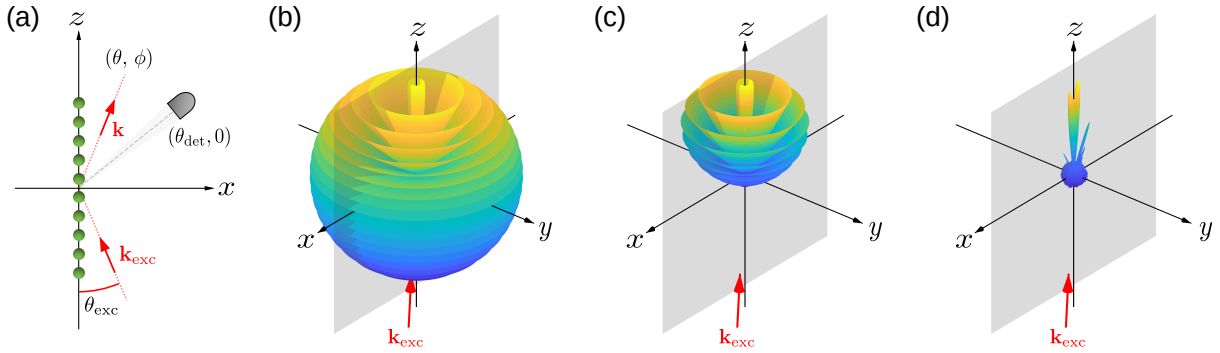

Figure 11.1: Bragg scattering from a one-dimensional atomic chain. (a) A linear chain with $N = 10$ atoms separated by $d = 7.49\,\mu\mathrm{m}$ is aligned along the z axis. An excitation laser with wave vector $\mathbf{k}_{\mathrm{exc}}$ is directed onto the chain at an angle $\theta_{\mathrm{exc}} = 4^\circ$ with respect to the z axis. The scattered light with wave vector $\mathbf{k}$ is detected as a function of spherical angles $(\theta,\, \phi)$. (b) Structure factor $S(\theta,\, \phi)$ for case of equal separation of atoms, and (c) in the presence of disorder of atomic positions with standard deviations $(\sigma_x, \sigma_y,\, \sigma_z) = (0,\, 0,\, 0.3\lambda)$, and (d) $(\sigma_x, \sigma_y,\, \sigma_z) = (0.3\lambda,\, 2.4\lambda,\, 0.3\lambda)$. Gray panels represent the x-z plane in which the excitation laser propagates. To measure the scattered signal, we use a detector whose axis has polar angles $(\theta_{\mathrm{det}}, 0)$.

[85], and ensembles of atoms in 1D and 3D lattices [86, 87]. In Bragg scattering, it is necessary to localize each emitter to well within the wavelength of the incident radiation. Deviations from perfect localization wash out any constructive interference and reduce the fidelity of associated quantum protocols.

Diverse applications of quantum information require interconnected quantum nodes that are capable of local processing and error correction. Integration of local processing and memory enhances performance of quantum repeaters over lossy channels, enables distributed quantum processing and sensing, and allows for entanglement resources to be shared within the network. In prior work with a single atomic qubit per node, entanglement between an atomic qubit and a photon [39, 88, 89, 15] and entanglement between remote atomic qubits [90, 91, 92] have been realized. High-fidelity one-qubit gates [93, 94] and pairwise entanglement of neighboring and next-to-nearest neighbor sites [95, 96] in 1-D and 2-D arrays have also been demonstrated. However, the integration of communication and processing capabilities remains an outstanding challenge. High-quality interference for light emitted from a reconfigurable array of trapped neutral atoms is essential for using such arrays in a way that combines processing and mapping between atomic and photonic states [97].

In this work we propose and demonstrate non-collinear phase-matching geometries that have suppressed sensitivity to particle localization. In the first geometry, there is a single atomic chain whose axis makes a small angle θ_{exc} with the propagation vector of the incident field [Fig. 1(a)]. In

the second geometry, two atomic chains are used to observe interference fringes having near-unity visibility. The ability to obtain high-quality phase-matched scattering from an array of individually controllable atoms represents an important step toward the realization of scalable atom-photon interfaces.

The central idea for achieving this goal is the observation that, as the dimensionality of the system decreases, new directions for phase matching appear even for a disordered atomic array. The origin of this effect can be understood by considering a structure factor $S(\theta,\,\phi) = \sum_{j,j'=1}^{N} e^{-i\Phi_{jj'}}$ for scattering of off-resonant radiation from independent atoms. The scattered intensity is proportional to S, with

$$\begin{aligned}\Phi_{jj'} &= kX_{jj'}\left(\sin\theta\cos\phi + \sin\theta_{\rm exc}\right) + kY_{jj'}\sin\theta\sin\phi \\ &\quad + kZ_{jj'}\left(\cos\theta - \cos\theta_{\rm exc}\right),\end{aligned}$$

being an overall phase for the scattering, $\mathbf{k}_{\rm exc} = k\left(-\sin\theta_{\rm exc}\hat{\mathbf{x}} + \cos\theta_{\rm exc}\hat{\mathbf{z}}\right)$ the incident field propagation vector, (θ, ϕ) polar and azimuthal scattering angles, $\mathbf{R}_j = X_j\hat{\mathbf{x}} + Y_j\hat{\mathbf{y}} + Z_j\hat{\mathbf{z}}$ the position vector for atom j, and $\mathbf{R}_{jj'} = \mathbf{R}_j - \mathbf{R}_{j'}$. For phase-matching from a disordered atomic array, the phase $\Phi_{jj'}$ must vanish for *all* $\mathbf{R}_{jj'}$. In three-dimensions, phase matching is possible only in the direction of the incident field, $(\theta = \theta_{\rm exc}, \phi = \pi)$. However, if the atoms are confined to the $y-z$ plane, there is perfect *reflective* phase matching in the plane of incidence provided $\theta = \theta_{\rm exc}$ and $\phi = 0$. If the dimensionality is further reduced to a chain of atoms along the $z-$axis, there is phase matching in a *cone* with polar angle $\theta_{\rm exc}$. Deviations from perfect phase-matching arising from excursions out of the plane or chain can be reduced by taking $\theta_{\rm exc} \ll 1$.

We first consider an ideal situation in which N atoms are confined to a one-dimensional chain in the z - direction with fixed spacing d between the atoms. In this limit, as illustrated in Fig. 1(b) for our experimental parameters ($d \approx 7.49\,\mu{\rm m},\ \lambda \approx 780.24\,{\rm nm}, \theta_{\rm exc} \approx 4^\circ$), there is constructive conical collective scattering for several values of θ satisfying the Bragg condition. In our experiment, the confinement and separation of the trapped atoms is somewhat disordered, owing to imperfect positioning of the traps, finite atomic temperature, and random filling of trap sites. When effects of atom position deviations along the z axis are included, the number of Bragg scattering cones diminishes, Fig. 1(c). Non-zero values of X_j and Y_j further restrict the emission pattern to a single cone about the symmetry axis having maxima at $\phi = 0$, $\phi = \pi$, Fig. 1(d) and Supplementary Material.

We use cold $^{87}{\rm Rb}$ atoms confined in an array formed by holographic optical microtraps. Once N atoms are prepared in an array containing $N_{\rm t}$ traps, we image these atoms to determine the number of traps that are filled. We then apply a magnetic field of $B \approx 2.0\,{\rm G}$ along the excitation laser axis and employ a gated probing-cooling sequence. During this sequence, the

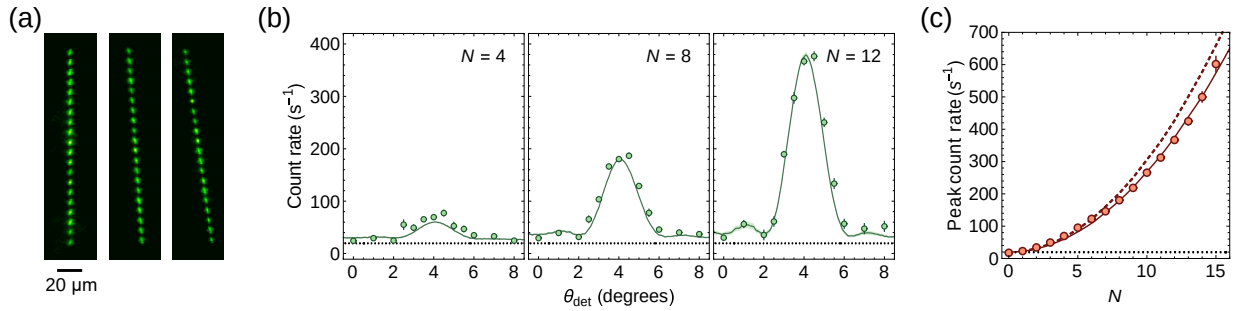

Figure 11.2: Phase-matched emission from a single chain. (a) Averaged atomic fluorescence images of a linear chain containing $N_{\rm t} = 20$ traps. The left image shows a configuration in which the atoms are aligned along with the detection mode axis, i.e. $\theta_{\rm det} = 0°$. For the middle (right) image, the chain is prepared such that $\theta_{\rm det} \approx 4°(8°)$. (b) The measured photocount rate as a function of $\theta_{\rm det}$ for $N = 4, 8, 12$. Each point is an average of randomly filled chains with a given N. Error bars represent one standard deviation of the observed photoelectric counting events. The green lines are the numerical results based on the Monte Carlo simulation with 1,000 runs. The shading on the line represents the standard deviation of the simulation divided by the square root of the averaged number of trials in the experiments. (c) The peak count rate as a function of N. Each point and its error bar represent the observed value at $\theta_{\rm det} = \theta_0 = 4°$. For the single-shot measurement of $N = 15$, we associate a $\sqrt{M}$ Poissonian error for M photoelectric count events. The solid (dashed) line represents the numerical simulation with (without) displacement of atomic positions due to imperfect positioning of the traps and finite temperature effects. The black dotted lines in (b, c) show the detection background measured without loading atoms.

excitation laser and cooling beams are switched on and off in an alternating manner with durations of $0.9\,{\rm ms}$ and $2.2\,{\rm ms}$, respectively. The scattered light is detected with an avalanche photodiode (APD) gated on only during the excitation period. The excitation laser, propagating along the magnetic field, is σ^+-polarized and red-detuned by $\delta/(2\pi) \approx 62\,{\rm MHz}$ from the $|g\rangle = \left|5S_{1/2},\, F = 2,\, m_F = 2\right\rangle \leftrightarrow |e\rangle = \left|5P_{3/2},\, F' = 3,\, m_{F'} = 3\right\rangle$ transition. The beam waist of the excitation laser is $\sim 0.1\,{\rm mm}$. The scattered light is collected by an achromatic doublets lens with focal length $f = 150\ {\rm mm}$ and coupled into a single-mode fiber directed toward the APD. The detector axis has polar angles $(\theta_{\rm det}, 0)$, see Figure 1 (a). The detection mode has a waist of $\approx 13.3\,\mu{\rm m}$. After a total of 1,200 cycles of the gated probing-cooling sequence with repetition rate of $\approx 300\,{\rm Hz}$, an additional imaging of the traps is taken to determine the final number of atoms $N_{\rm f}$ in the array. For the data analysis, only experimental samples with $N_{\rm f} = N$ are post-selected to remove atom loss effects. We repeat this entire sequence in determining a photon count rate averaged over atomic configurations in the array for a given N.

In the first geometry, we use a linear chain with $N_{\rm t} = 20$ traps separated by $d \approx 7.49\,\mu{\rm m}$. To experimentally find a reflective phase-matching condition, both $\theta_{\rm det}$ and $\theta_{\rm exc}$ are varied by rotating the chain axis with $\theta_0 = (\theta_{\rm det} + \theta_{\rm exc})/2$ kept fixed at $\approx 4°$. Figure 11.2(a) displays

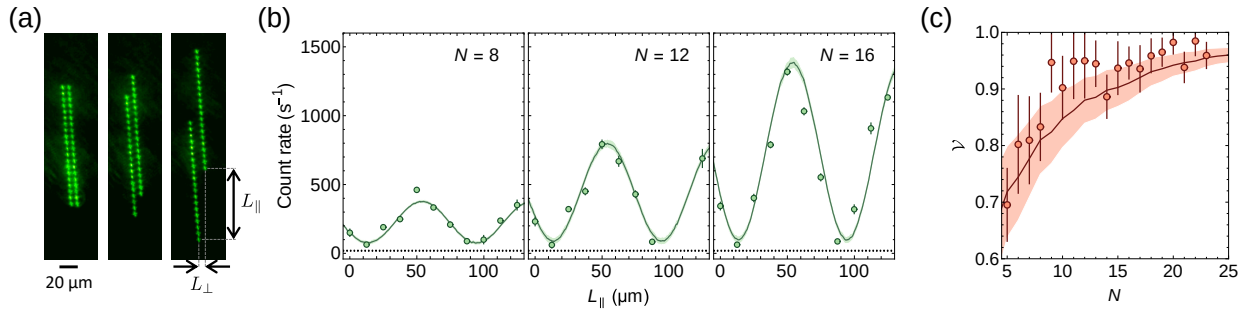

Figure 11.3: Observation of constructive and destructive Bragg scattering from two chains. (a) Averaged fluorescence images of two linear chains under three different values of the chain separation $L = L_\parallel \sin\theta_0 + L_\perp \cos\theta_0$. (b) Measured photon count rate as a function of $L_\parallel$ for $N = 4, 8, 12$. Error bars represent one standard deviation for M photoelectric counting events. The green lines are the numerical simulation based on the Monte Carlo simulation with 1,000 runs. The shading on the line represents the standard deviation of the simulation divided by the square root of the averaged number of trials in the experiments. The black dotted lines show the detection background which is measured without loading atoms. (c) The observed scaling of the interference visibilities $\mathcal{V}$ as a function of the total number of atoms N. Each point is obtained by fitting the observed fringe by a sinusoidal function. Error bars indicate the fitting errors with 68% confidence intervals. The solid line is the result of the numerical simulation together with the standard error of the mean (shaded area).

averaged fluorescence images of the chain for three different $\theta_{\rm det}$. For $\theta_{\rm det} = 0°$ (left image) the chain is oriented along the detection mode, while for $\theta_{\rm det} = 2\theta_0 \approx 8°$ (right image) the chain is aligned along the axis of the excitation field. Reflective phase-matching is expected to appear when $\theta_{\rm det} = \theta_0 \approx 4°$ (middle image). The measured photon count rates as a function of $\theta_{\rm det}$ for various N are shown in Fig. 11.2(b), where the horizontal axis is zeroed within the calibration error of $\pm 0.11°$. We observe an enhanced photon count rate, attributed to the reflective phase-matching emission, for each N at around the expected value of $\theta_{\rm det}$.

The experimental data is offset from the background signal [represented by the black dotted lines in Fig. 2(b)]. The origin of this offset can be traced to (1) deviations from perfect periodicity of the trap potentials, (2) temperature effects, (3) random filling of the traps, and (4) inelastic scattering of the incident field [98].

For our experimental conditions, the theoretical expression for the scattered light intensity in steady-state can be written as

$$I(\mathbf{r}) \propto |\mathbf{F}_{\rm sc}(\mathbf{r})|^2 \left(\sum_j^N \rho_{ee}^{(j)} + \sum_{j \neq j'}^N \rho_{ge}^{(j)} \rho_{eg}^{(j')} e^{-i\Phi_{jj'}} \right), \tag{11.1}$$

where $\mathbf{F}_{\rm sc}$ is a σ^+ dipole radiation field amplitude, $\rho_{ee}^{(j)}$ is an excited state population, and $\rho_{ge}^{(j)}$

denotes the single atom coherence between $|g\rangle$ and $|e\rangle$. Both $\rho_{ee}^{(j)}$ and $\rho_{ge}^{(j)}$ are obtained as a function of Ω, δ from the solution of the steady-state optical Bloch equations. We do not measure the intensity per se, rather we measure the absolute square of the scattered field *amplitude* projected onto the detection mode (see Supplementary Information). To include the effects of disorder, we compute a signal averaged over different atomic configurations. For each atomic configuration, traps for a given N atoms are randomly chosen from a chain with $N_{\rm t}$ traps. The displacement of position of atom j originates from imperfect positioning of the traps and from the finite temperature T. In these simulation the Rabi frequency and θ_0 are taken to be free parameters to fit the data for $2 \leq N \leq 15$. We obtain $\Omega/(2\pi) = 3.24(4)\,\mathrm{MHz}$ and $\theta_0 = 4.19(2)^\circ$ without the calibration error. The results of the numerical simulations displayed as solid lines in Fig. 11.2(b) successfully reproduce the entire shape of the observed signal.

Under conditions of phase-matching, the relative phase $\Phi_{jj'}$ is insensitive to position disorder along the y and z axes, that is $\partial\Phi_{jj'}/\partial Y_{jj'} = \partial\Phi_{jj'}/\partial Z_{jj'} = 0$. Therefore, random filling of the traps by the atoms does not affect the peak signal. However, there is a small sensitivity of the peak signal to displacements along the x axis, since $\partial\Phi_{jj'}/\partial X_{jj'} = 2k\sin\theta_0 \equiv q_x$. Therefore, even for fully coherent scattering, averaging of the peak signal with a Boltzmann distribution of positions in the x direction reduces the structure factor from N^2 to $f_{\rm DW}N^2 + (1 - f_{\rm DW})N$, where $f_{\rm DW}$ is a Debye-Waller factor [99] given by $\left\langle e^{-i\Phi_{jj'}}\right\rangle \approx e^{-q_x^2\sigma_x^2}$ and $\langle\cdots\rangle$ denotes the average over the Boltzmann distributions. In Fig. 11.2(c) the observed peak count rate (red points) is displayed together with a theoretical curve for an equally spaced chain without any position disorder (dashed line). The fact that the curves almost overlap is consistent with the Debye-Waller factor of $f_{\rm DW} \approx 0.93$. The maximum scattered intensity is also diminished by an N independent factor of about 10% resulting from the projection onto the detector mode.

In the second geometry, we extend the system to two chains, each composed of $N_{\rm t}/2 = 20$ equally spaced traps. The chain axes are chosen to satisfy the reflective phase-matched condition $\theta_{\rm det} = \theta_{\rm exc} = \theta_0$ measured in the first geometry. The two chains are separated by a distance $L_\perp$ in the direction orthogonal to the detection axis that is chosen equal to the spacing d between the adjacent traps [left image in Fig. 3(a)]. To observe interference of reflective phase-matched emissions from the two chains, each chain is displaced by $L_\parallel/2$ in the direction away from each other along the detection axis [middle and right images in Fig. 11.3(a)]. Therefore, the shortest distance between the two chains can be written by $L = L_\parallel\sin\theta_0 + L_\perp\cos\theta_0$.

Figure 3(b) displays the measured photon count rates as a function of the chain separation $L_\parallel$ for $N = 8,\ 12,$ and 16. These results show constructive and destructive Bragg scattering, and they are analyzed using sinusoidal fits. These interference fringes provide information about geometrical parameters of the experimental setup. According to Bragg's Law: $2L\sin\theta_0 = m\lambda$, the expected interference period is $\Delta L_\parallel = \lambda/(2\sin^2\theta_0)$ and m-th order constructive emission appears

at $L_{\parallel}^{(m)} = m\Delta L_{\parallel} - L_{\perp}\cot\theta_0$. Taking into account the observed period and 2nd order peak position $(\Delta L_{\parallel},\, L_{\parallel}^{(2)}) = (10.56(5),\, 6.92(2))d$ averaged over $5 \leq N \leq 23$, we obtain $d = 7.49(11)\,\mu\mathrm{m}$ and $\theta_0 = 4.01(4)^{\circ}$.The solid lines in Fig. 11.3(b) are the results of the numerical simulations with the obtained values of d, θ_0.

In Figure 11.3(c) we show the measured interference visibility $\mathcal{V} = (I_{\max} - I_{\min})/(I_{\max} + I_{\min})$ as a function of the total number of atoms N. When averaged over the range $20 \leq N \leq 23$, the background-subtracted $\mathcal{V}$ we obtain is $0.97(2)$, significantly higher than that reported in prior studies of multi-atom Bragg scattering [82, 83, 84, 85, 86, 87]. The clear reduction in visibility for smaller numbers of atoms N is due mostly to an increased imbalance in the atom number between the two chains. It can be understood as follows: for constructive interference, the relative phase $\Phi_{jj'}$ is zero for any two atoms in the same chain and a multiple of 2π for any two atoms in different chains. Therefore the maximum fringe intensity $I_{\max}$ is insensitive to an imbalance in the number of atoms between the individual chains and scales as $\sim N^2$. On the other hand, for *complete* destructive interference, the relative phase between atoms in different chains must be a odd multiple of π *and* the number of atoms in each chain must be the same. For unequal numbers of atoms in the two chains, destructive interference cannot be complete. The solid line in Figure 11.3(c) is based on our numerical simulations which include random filling of traps, inelastic scattering, and atomic position disorder, see Supplementary Material.

It is well-known that restricting the dimensionality of a quantum system can radically alter its global properties, as well as inter-particle interactions and, in doing so, allow for new applications that do not occur in higher dimensions. Frequently in such settings, many-body effects play a critical role. In contrast, our work demonstrates that the reduced dimensionality of a quantum system can be important in a situation with no strong inter-particle correlations. Specifically, we have demonstrated phase-matched coherent scattering for 1- and 2-dimensional geometries of a single-atom qubit array suitable for storage and processing of quantum information. High-visibility interference fringes are observed for two atomic chains as a function of their separation. Atom arrays connected to photonic channels can provide a technology foundation for future quantum networks with efficient multi-partite scaling. Networks using such arrays as quantum nodes would offer a variety of schemes to encode, transfer, and manipulate quantum information within and between the nodes of the network for distributed quantum computation, communication, and sensing [97]. A logical extension of this work could involve the creation of multi-atom entangled states in a setting where the atoms can be individually addressed and their various combinations chosen for entangled state generation.

11.1 Supplementary material

We use cold $^{87}\mathrm{Rb}$ atoms confined in an array formed by holographic optical microtraps. The trapping beam is generated by a $1064\,\mathrm{nm}$ fiber-based amplifier seeded by a single-mode fiber laser. The trap field intensity is stabilized by measurement and feedback via an acousto-optic modulator. The resulting beam is diffracted by a spatial light modulator (SLM) that imprints a phase on the trapping beam, as shown in Fig. S11.4 (a). The diffracted beam passes through a $2:3$ telescope and is then strongly focused by a high-numerical-aperture (NA) objective lens ($\mathrm{NA} \approx 0.55$) into an ultra-high vacuum (UHV) glass cell to form an array of optical microtraps centered on what we define as our z axis. Each trap has a waist of $\approx 1.7\,\mu\mathrm{m}$, a depth $U_0/k_\mathrm{B} \approx 2.3\,\mathrm{mK}$, and trap frequencies $(\omega_x,\, \omega_y,\, \omega_z) \approx 2\pi \times (91.2,\, 13.0,\, 91.2)\,\mathrm{kHz}$.

To load atoms into an array of microtraps, the array is spatially overlapped with a magneto-optical trap (MOT) which is loaded from a background Rb vapor in the UHV glass cell. After the loading phase, we turn off the magnetic field gradient of the MOT and then shine an imaging beam onto the trapped atoms. The imaging beam contains two laser beams, one is red-detuned by about $20\,\mathrm{MHz}$ from the in-trap D2 $F = 2 \leftrightarrow F' = 3$ transition and the other is a repumper beam resonant with the in-trap D2 $F = 1 \leftrightarrow F' = 2$ transition. The imaging beam is retro-reflected in a one-dimensional lin$\perp$lin configuration which provides a Sisyphus cooling mechanism. The fluorescence from the trapped atoms is collected by the objective lens and directed onto a cooled electron-multiplying CCD (EMCCD) camera by a dichroic mirror (DM). To count the number of atoms, the detected photon statistics is analyzed for each trap. The statistics exhibit bimodal structure which indicates the trap has either zero or one atom due to a collisional blockade mechanism [100]. The total number of atoms N in an array with N_t traps is varied in a range of $N/N_t \lesssim 0.5$ by changing the duration of the loading phase. The atomic temperature is $T \approx 248\,\mu\mathrm{K}$ which yields disorder of atomic positions with standard deviations of $\sigma_x = \sigma_z \approx 0.3\lambda$, $\sigma_y \approx 2.4\lambda$.

Figure S11.4 (b) shows the geometry used in this work. An excitation laser propagating along the magnetic field direction results in scattering from the atoms. The scattered light is collected by a lens whose aperture is much larger than that of the detection mode $\lambda/(\pi w_{d,\,0}) \approx 1.07^\circ$, where $w_{d,\,0} \approx 13.3\,\mu\mathrm{m}$ is the spot size of the detection mode and $\lambda = 780.24\,\mathrm{nm}$ is wavelength of the scattered light. The lens axis coincides with the detector axis. The collected light passes two optical band-pass filters having a central wavelength of $780\,\mathrm{nm}$ to suppress stray light, and is then coupled into a single-mode fiber directed to an avalanche photodetector (APD). The total transmission efficiency of the UHV glass cell, the lens, and the filters is $\eta_\mathrm{T} \approx 0.88$ and the quantum efficiency of the APD is $\eta_\mathrm{APD} \approx 0.56$. The excitation laser is detuned by $\delta/(2\pi) \approx 62\,\mathrm{MHz}$ from the $|g\rangle = \left|5S_{1/2},\, F = 2,\, m_F = 2\right\rangle \leftrightarrow |e\rangle = \left|5P_{3/2},\, F' = 3,\, m_{F'} = 3\right\rangle$ transition of atoms located at the center of a trap. The light shift induced by the π-polarized trapping beam is extracted by

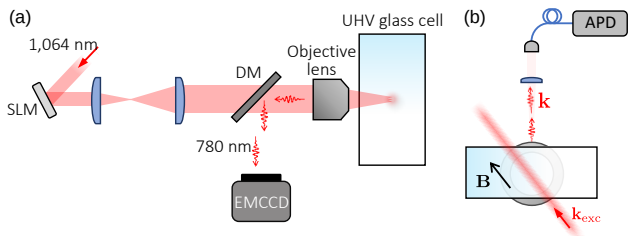

Figure 11.4: Experimental layout for holographic arrays of optical microtraps (a) and an excitation laser and a detection mode (b).

measuring atomic loss as a function of detuning of the excitation laser from the resonance in free-space. The value of the light shift averaged over all sites is $89\,\mathrm{MHz}$, with the standard deviation $\sigma_{\mathrm{LS}}/(2\pi) \approx 6.5\,\mathrm{MHz}$ resulting in a $\sigma_{\mathrm{LS}}/\delta \approx 0.10$ fractional variation in the detuning. To reduce heating loss of trapped atoms during measurements of scattered light, a gated probing-cooling sequence is applied (see the main text), where the imaging beam is used as the cooling beam. The survival probability after 1200 cycles of the gated probing-cooling sequence with repetition rate of $\approx 300\,\mathrm{Hz}$ is about 95% per atom which is mainly limited by finite lifetime of trapped atoms. To extract experimental samples in which there is no atomic loss, we use post-selection to compare the number of atoms recorded before and after the gated-probing sequence. To measure the angle θ_{det} between the detection axis and the trap chain, we direct a laser field having wavelength $810\,\mathrm{nm}$ backwards through the detector mode volume into the interaction volume. This field forms a far-off-resonance optical trap (FORT). The angle θ_{det} is calibrated by analyzing fluorescence images of atoms trapped in the microtrap chain and the FORT. The calibration error is ± 0.11 degrees limited by the EMCCD resolution and capture range.

Theoretical methods

In general, the total electric field $\mathbf{E}_{\mathrm{tot}}(\mathbf{R})$ at any position in space is a superposition of the excitation field $\mathbf{E}_{\mathrm{exc}}(\mathbf{R})$ and the field scattered by the atoms $\mathbf{E}_{\mathrm{sc}}(\mathbf{R})$,

$$\mathbf{E}_{\mathrm{tot}}(\mathbf{R}) = \mathbf{E}_{\mathrm{exc}}(\mathbf{R}) + \mathbf{E}_{\mathrm{sc}}(\mathbf{R}). \tag{11.2}$$

There are three axes defined in our experiment (see Fig. 1 (a) of main text). The z axis is taken along the atomic chain(s). The propagation vector of the excitation field lies in the x-z plane and defines a second axis that makes an angle θ_{exc} with the negative z axis. This field is circularly polarized with respect to its own axis. Finally, there is the detector axis, having polar angles $(\theta_{\mathrm{det}}, 0)$. A collection lens having a diameter of 1" is centered on this axis at a distance $R \approx 150$ mm from the origin. The plane of the lens lies roughly in the θ direction, having some extent in

both the θ and ϕ directions. The spatial mode of the single-mode fiber used to measure the signal is also centered on the detection axis. In our experiment, the angular separation $2\theta_0 \approx 8^\circ$ between the detection and excitation axes is kept fixed as the direction of the atomic chains is varied. There is never any overlap of the excitation and scattered fields in our measurements, so we restrict our discussion to the scattered field.

11.1.1 Scattered field from an atomic array

It is easiest to write an expression for the scattered field using polar angles (θ_e, ϕ_e) relative to the *excitation* axis. Relative to this axis, it follows from source-field theory that the positive frequency component of the electric field operator can be written as

$$\hat{\mathbf{E}}^{+}_{\text{sc}}(R,\, \theta_e,\, \phi_e; \theta, \phi; t) = \mathbf{F}_{\text{sc}}(R, \theta_e, \phi_e) e^{-i\omega t} \sqrt{\frac{\hbar \omega \gamma_e}{2\epsilon_0 c}} \times \sum_j^N e^{-i(\mathbf{k}-\mathbf{k}_{\text{exc}})\cdot \mathbf{R}_j} \hat{S}^{(j)}_{-}, \tag{11.3}$$

where $\hat{S}^{(j)}_{-} = |g_j\rangle \langle e_j|$ ($\hat{S}^{(j)}_{+} = |e_j\rangle \langle g_j|$) is the lowering (raising) for an atom at position $\mathbf{R}_j$, γ_e is the excited state decay rate,

$$\mathbf{k} = \sin\theta\cos\phi\hat{\mathbf{x}} + \sin\theta\sin\phi\hat{\mathbf{y}} + \cos\theta\hat{\mathbf{z}}; \tag{11.4a}$$

$$\mathbf{k}_{\text{exc}} = -\sin\theta_{\text{exc}}\,\hat{\mathbf{x}} + \cos\theta_{\text{exc}}\,\hat{\mathbf{z}} \tag{11.4b}$$

and

$$\mathbf{F}_{\text{sc}}(R, \theta_e, \phi_e) = -\frac{e^{ikR}}{R} e^{i\phi_e} \sqrt{\frac{3}{8\pi}} \left(\frac{\cos\theta_e \hat{\boldsymbol{\theta}}_e + i\hat{\boldsymbol{\phi}}_e}{\sqrt{2}} \right) \tag{11.5}$$

is a function that gives the radiation pattern of a single atom, normalized such that

$$R^2 \int \|\mathbf{F}_{\text{sc}}(R, \theta_e, \phi_e)\|^2 \; d\Omega_e = 1. \tag{11.6}$$

We note that the angles (θ_e, ϕ_e) are implicit functions of $(\theta, \phi, \theta_{\text{exc}})$.

11.1.2 Detection mode

The detection mode corresponds to a circularly polarized TEM_{00} relative to the *detection* axis that is focused to a waist having radius $w_{d,\,0} \approx 13.3\ \mu\text{m}$ at the center of the atomic array. We specify the spherical angles relative to the detector axis by (θ_d, ϕ_d). For our experimental parameters, $\theta_d \ll 1$

and the Rayleigh length $z_{\rm R} = \pi w_{d,0}^2/\lambda \approx 712$ μm is much less than R, enabling us to write the incoming vector spatial mode pattern on a spherical surface intersecting the collection lens as

$$\begin{aligned}\mathbf{F}_{\rm det}(R,\theta_d,\phi_d) &\approx \left(\frac{\cos\theta_d\hat{\boldsymbol{\theta}}_d - i\hat{\boldsymbol{\phi}}_d}{\sqrt{2}}\right) e^{-i\phi_d}\sqrt{\frac{kz_R}{\pi}}\frac{e^{-ikR}}{R} \\ &\quad\times e^{-kz_{\rm R}\theta_d^2/2} e^{-ikR\theta_d^4/8},\end{aligned} \tag{11.7}$$

which, for $kz_R \gg 1$, is normalized such that

$$R^2\int \|\mathbf{F}_{\rm det}(R,\theta_d,\phi_d)\|^2\, d\Omega_d = 1. \tag{11.8}$$

We note that the angles (θ_d,ϕ_d) are implicit functions of $(\theta,\phi,\theta_{\rm det})$.

11.1.3 Count Rate

With the adopted normalization, the photoelectric count rate is given by

$$C_N = \mathcal{I}\eta + C_0, \tag{11.9}$$

where $\eta = \eta_{\rm T}\,\eta_{\rm APD}$, C_0 is the experimentally determined background count rate, and

$$\mathcal{I} = \frac{2\epsilon_0 cR^4}{\hbar\omega}\left\langle \int \hat{\mathbf{E}}_{\rm sc}^- \cdot \mathbf{F}_{\rm det}^*\, d\Omega_{\rm lens} \int \hat{\mathbf{E}}_{\rm sc}^+ \cdot \mathbf{F}_{\rm det}\, d\Omega_{\rm lens}\right\rangle \tag{11.10}$$

is the intensity projected onto the fiber mode. The angular integrals can be restricted to the solid angle of the lens since the detection mode acts as a spatial filter whose acceptance angle $\sqrt{2/kz_{\rm R}} = \lambda/(\pi w_{d,0}) \approx 0.019$ radians is much less than the angular acceptance of the lens, which is 0.084 radians. In acting as a spatial filter, the detection mode increases the visibility of the interference fringes observed with two chains of atoms as a function of the separation of the chains.

When Eq. (11.3) is substituted into Eq. (11.10), we find that $\mathcal{I}$ can be expressed in terms of density matrix elements as

$$\begin{aligned}\mathcal{I} = &\sum_j^N \left[\rho_{ee}^{(j)} - \left|\rho_{eg}^{(j)}\right|^2\right]\left|\int \mathbf{F}_{\rm sc}\cdot\mathbf{F}_{\rm det}\, e^{-i\Phi_j} d\Omega_{\rm lens}\right|^2 \\ &+ \left|\sum_{j=1}^N \rho_{ge}^{(j)} \int \mathbf{F}_{\rm sc}\cdot\mathbf{F}_{\rm det}\, e^{-i\Phi_j} d\Omega_{\rm lens}\right|^2,\end{aligned} \tag{11.11}$$

where

$$\Phi_j(\theta,\phi) = (\mathbf{k} - \mathbf{k}_{\text{exc}}) \cdot \mathbf{R}_j, \tag{11.12}$$

$$\rho_{ee}^{(j)} = \frac{s_j}{2(1+s_j)},\ \rho_{eg}^{(j)} = \frac{i\Omega_j}{2(\gamma_e/2 - i\delta_j)(1+s_j)}, \tag{11.13}$$

and

$$s_j = \frac{\Omega_j^2/2}{\delta_j^2 + \gamma_e^2/4}. \tag{11.14}$$

is the saturation parameter associated with the jth atom - field interaction. The saturation parameter is a function of the Rabi frequency Ω_j and the detuning δ_j.

11.1.4 Numerical simulation

We account for (a) disorder in atomic positions resulting from temperature and from imperfect trap positioning, (b) random filling of N_t trap sites by N atoms, and (c) the effects of an inhomogenous distribution of trap depths, by using Monte Carlo simulations to average over these effects. The photoelectric count rate C_N from an array consisting of N atoms is calculated using the following procedure:

1. The coordinates for each of the N_{t} traps in the absence of experimental imperfections are defined using the geometric parameters d, $L_{\parallel}$ and $L_{\perp}$ (see Fig. 2 (a) of main text).

2. Each site in the array is randomly assigned a deviation from the ideal trap position to account for irregularities arising from the finite spatial resolution of the SLM. The distribution is assumed as a normal distribution with the measured standard deviation of $\approx 0.10\ \mu\text{m}$.

3. A value of in-trap detuning is randomly assigned to each site in the array to account for the nonuniform distribution of trap depths. The values of detuning follow a normal distribution centered at δ with a standard deviation σ_{LS}.

4. To model the stochastic loading process associated with the collisional blockade mechanism, N of the N_{t} the traps are randomly chosen to be filled.

5. Due to finite atomic temperature, atomic positions $\mathbf{R}_j$ are randomly sampled from Gaussian Boltzmann distributions in each dimension having spatial waists $\sigma_i = \sqrt{k_{\text{B}}T/(m\omega_i^2)}$, where m is the atomic mass. Atomic temperature T and trap frequencies ω_i are measured by release and recapture techniques [101, 102]. The temperature remains approximately constant during the excitation process due to our gated probing-cooling sequence, allowing us to neglect any motional effects and any changes in the resonant frequency resulting from recoil heating.

6. The count rate for the particular configuration of atomic positions, Rabi frequency, and in-trap detuning is calculated using Eq. (11.9).

To match the theory to the experimental data, we perform simultaneous fits of peak count rates

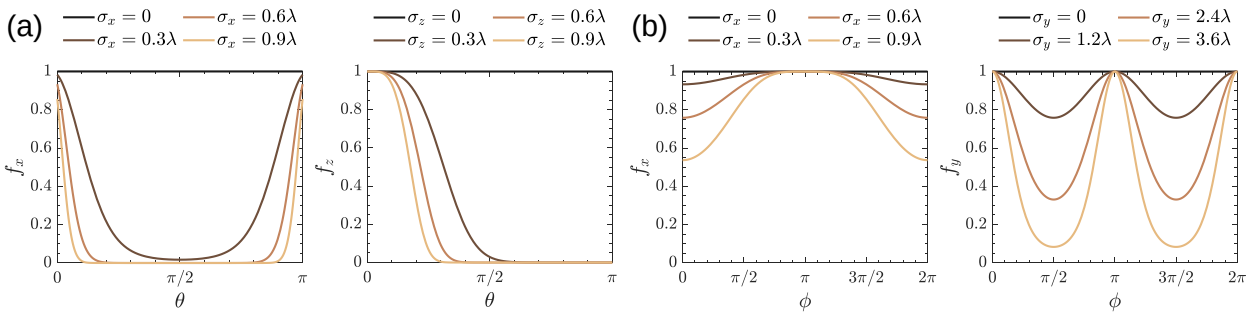

Figure 11.5: Angular dependence of the Debye-Waller factors. (a) f_i as a function of θ for various values of disorder σ_i ($i = x,\ z$) for $\phi = 0$ and $\theta_{\rm exc} = 4^\circ \approx 0.022\pi$, (b) f_i as a function of ϕ for various values of disorder σ_i ($i = x,\ y$) with $\theta = \theta_{\rm exc}$.

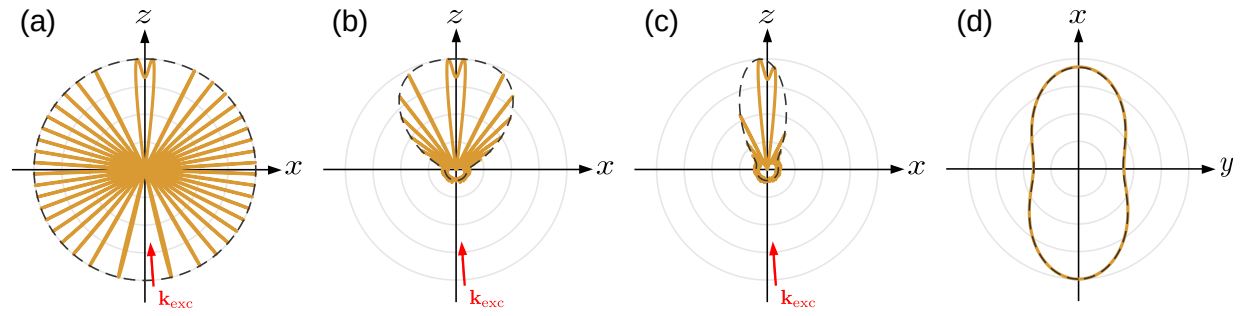

Figure 11.6: Bragg scattering from a one-dimensional atomic chain with $N = 10$ atoms. Two dimensional structure factor $S(\theta,\ 0)$ for (a) case of equal separation of atoms, (b) in the presence of disorder of atomic positions with standard deviations $(\sigma_x, \sigma_y,\ \sigma_z) = (0,\ 0,\ 0.3\lambda)$, and (c) $(\sigma_x, \sigma_y,\ \sigma_z) = (0.3\lambda,\ 2.4\lambda,\ 0.3\lambda)$. They correspond to the emission patterns in the x-z plane displayed in Fig. 1 (b-d) of the main text. (d) the structure factor in a single cone $S(\theta_{\rm exc}, \phi)$. The solid lines are the results of the Monte Carlo simulation in which each atomic position is randomly sampled with the standard deviations $(\sigma_x,\ \sigma_y,\ \sigma_z)$. The dashed lines represent the envelope of the maximum intensity obtained from $N + f_{\rm DW} N(N-1)$.

for all values of N, using the Rabi frequency Ω as an adjustable parameter. The measurements at the value of $\theta_{\rm det} = 4^\circ$ ($L_\parallel \approx 50\ \mu$m) serve as representative points for the single (double) chain geometry. To generate the theoretical curves shown in Figures 2 and 3 of the main text, we average over 1000 realizations of the Monte Carlo simulation using the best fit values of $\Omega/2\pi = 3.24(4)$ MHz and $\Omega/2\pi = 5.05(8)$ MHz respectively.

11.1.5 Disorder in atomic position

In this section we want to see how thermal averaging of position affects Bragg scattering from an equally spaced single atomic chain, with one atom per site. The atoms are aligned along the z axis and the excitation beam makes an angle $\theta_{\rm exc} = 4^\circ \approx 0.07$ radians with the z axis. The detector

axis can be placed at any $\theta_{\rm det} = \theta$. For this geometry and with a saturation parameter much less than unity, the scattered signal is proportional to the structure factor $S = \left\langle \sum_{j,\,j'=1}^{N} e^{-i\Phi_{jj'}} \right\rangle$, where $\Phi_{jj'} = \Phi_j - \Phi_{j'}$ and the brackets denote a thermal average. The structure factor can be written as

$$S = N\,(1 - f_{\rm DW}) + f_{\rm DW} \frac{\sin^2\left[Nkd(\cos\theta - \cos\theta_{\rm exc})/2\right]}{\sin^2\left[kd(\cos\theta - \cos\theta_{\rm exc})/2\right]} \tag{11.15}$$

where d is the chain spacing and

$$f_{\rm DW} = \left| \left\langle e^{-i(\mathbf{k}-\mathbf{k}_{\rm exc})\cdot\mathbf{R}_j} \right\rangle \right|^2 \tag{11.16}$$

is a Debye-Waller factor. The average is over the thermal Boltzmann distribution associated with atom j. Disorder of atomic positions results in a reduction of the peak height of Bragg scattering and an offset of the Bragg minima from zero. It can also wash out Bragg diffraction peaks. For atoms confined in harmonic potentials, $f_{\rm DW} \approx f_x f_y f_z$, with

$$\begin{aligned} f_x &= \exp[-k^2(\sin\theta\cos\phi + \sin\theta_{\rm exc})^2\,\sigma_x^2] \\ f_y &= \exp[-k^2(\sin\theta\sin\phi)^2\,\sigma_y^2] \\ f_z &= \exp[-k^2(\cos\theta - \cos\theta_{\rm exc})^2\,\sigma_z^2]. \end{aligned} \tag{11.17}$$

In Fig. S11.5 (a), f_x and f_z are plotted as a function of θ for $\phi = 0$, $\theta_{\rm exc} = 4^\circ$ and several values of σ_x/λ and σ_z/λ. It is seen that disorder reduces the range of θ for which phase matching can occur. In Fig. S11.5 (b), f_x and f_y are plotted as a function of ϕ for $\theta = \theta_{\rm exc} = 4^\circ$ and several values of σ_x/λ and σ_y/λ. The product of f_x and f_y is equal to unity at $\phi = 0, \pi$, and is reduced somewhat for other values of ϕ. Regardless of disorder, phase matching is always perfect in the direction of the excitation beam, $\theta = \theta_{\rm exc}$, $\phi = \pi$.

To see how disorder reduces the number of Bragg peaks, first consider the case when all the $\sigma_i = 0$. In that case the structure factor equals N^2 whenever $kd(\cos\theta - \cos\theta_{\rm exc}) = n\pi$. For $\lambda = 780.24$ nm and $d = 7.49$ μm, $kd = 60.3$, Bragg peaks occur for 20 values of θ. Since the Bragg condition is independent of ϕ, each value of θ gives rise to a cone of phase-matched emission, resulting in the 20 cones seen in Fig. 1 (b) of the main text. Figure S11.6 represents a cross section of these cones in the x-z plane ($\phi = 0, \pm\pi/2$). In the presence of disorder in the z direction alone with $\sigma_z = 0.3\lambda$, conical emission at angles other than $\theta = \theta_{\rm exc}$ are reduced by a factor f_z [Fig. S11.6 (b)]. From Fig. S11.5 (a), you can deduce that $f_z < 0.01$ for $\theta > \pi/2$. As a consequence the number of phase-matched cones is reduced to 6 for $\sigma_z = 0.3\lambda$. When disorder along the x and y directions is also included [$\sigma_x = 0.3\lambda$, $\sigma_y = 2.4\lambda$], Bragg scattering is reduced primarily to a single cone having $\theta = \theta_{\rm exc}$ [Fig. S11.6 (c)]. Moreover, the disorder in the

y direction results in a ϕ dependence that is a maximum at $\phi = \pi$ (forward scattering along the negative x axis) and has a secondary maximum at $\phi = 0$ (reflective scattering along the positive x axis) [Fig. S11.6 (d)].

11.1.6 Random Filling

To isolate the effects of random filling on the signal, we neglect any effects of disorder. In this case, for a single chain with spacing d, the structure factor is given by

$$S = N + 2 \sum_{j,\, j'=1;\, j'<j}^{N} \cos\left[(j - j')\alpha\right], \tag{11.18}$$

where

$$\alpha = kd\left[\cos\left(2\theta_0 - \theta\right) - \cos\theta\right] \tag{11.19}$$

and we must place the N atoms at random in N_t traps, with at most one atom in each trap. In turns out that it is possible to get an analytic expression for $\langle S \rangle$, where the average is now over all possible configurations. Explicitly, [103]

$$\begin{aligned} \bar{S}\left(\alpha\right) &= \frac{\langle S \rangle}{N^2} = \frac{1}{N} + \frac{2}{N^2 \binom{N_t}{N}} \sum_{m=1}^{N_t - 1} W(m) \cos(m\alpha); \\ W(m) &= \sum_{i=1}^{N-1} \sum_{j=i+1}^{N} \sum_{q=1}^{N_t - N + j - m} \binom{q-1}{i-1} \\ &\quad \times \binom{m-1}{j-i-1} \binom{N_t - q - m}{N - j}. \end{aligned} \tag{11.20}$$

The quantity $W(m)$ gives the number of configurations for which atom j and atom i ($j > i$) are separated by $md = (j - i)d$. In Fig. S11.7, $\bar{S}$ is plotted as a function of θ for $\theta_0 = 4^\circ$, $kd = 60.3$, $N_t = 20$, and $N = 4, 8, 12$. As can be seen, the main effect of random filling is to produce an offset in the signal, which becomes less important with increasing N.

For two chains the normalized structure factor is

$$\bar{S} = \frac{1}{N^2} \left\langle \sum_{j,j'=1}^{N} e^{iq_z Z_{jj'} + iq_x X_{jj'}} \right\rangle, \tag{11.21}$$

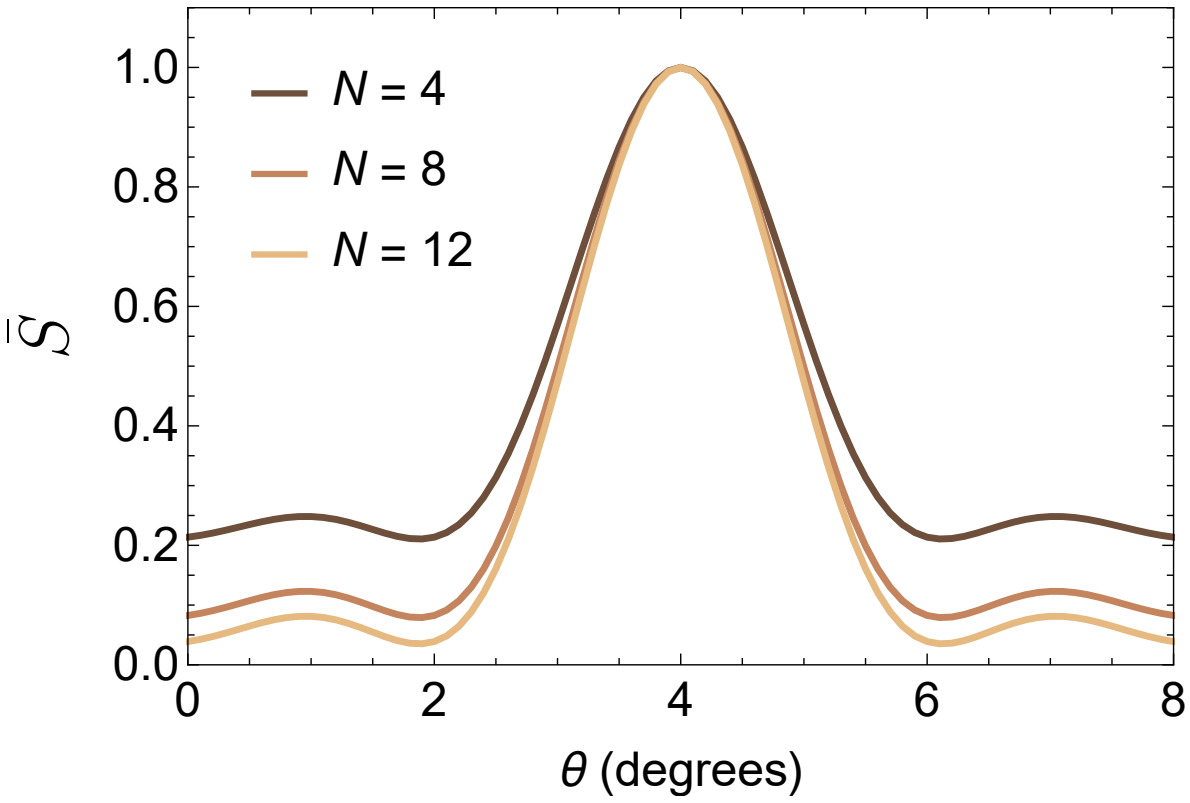

Figure 11.7: Effect of random filling for a single chain. The normalized structure factor is plotted as a function of θ for 20 traps and $N = 4, 8, 12$ atoms.

where

$$\begin{aligned} Z_j &= jd\Theta\left(N_t/2 - j\right) \\ &\quad + \left(j - N_{\mathrm{t}}/2\right) d\Theta\left(j - N_t/2 - 1\right); \qquad \text{(11.22a)} \\ X_j &= X_0\Theta\left(j - N_t/2 - 1\right), \qquad \text{(11.22b)} \end{aligned}$$

$$\begin{aligned} q_z &= k\left[\cos\left(2\theta_0 - \theta\right) - \cos\theta\right]; \qquad \text{(11.23a)} \\ q_x &= k\left[\sin\left(2\theta_0 - \theta\right) + \sin\theta\cos\phi\right], \qquad \text{(11.23b)} \end{aligned}$$

and $\Theta(x)$ is the Heaviside function defined by $\Theta(x) = 1$ for $x \geq 0$ and $\Theta(x) = 0$ for $x < 0$. In other words, there are now two chains of particles separated by X_0 in the x direction and an even number N_t of traps, with half the traps in each chain. Again, there is no more than one atom per trap, but it is possible to end up with all the atoms in one chain if $N < N_t/2$. That is, there is no restriction that forces the number of atoms in each chain to be the same - indeed, N can be odd. In

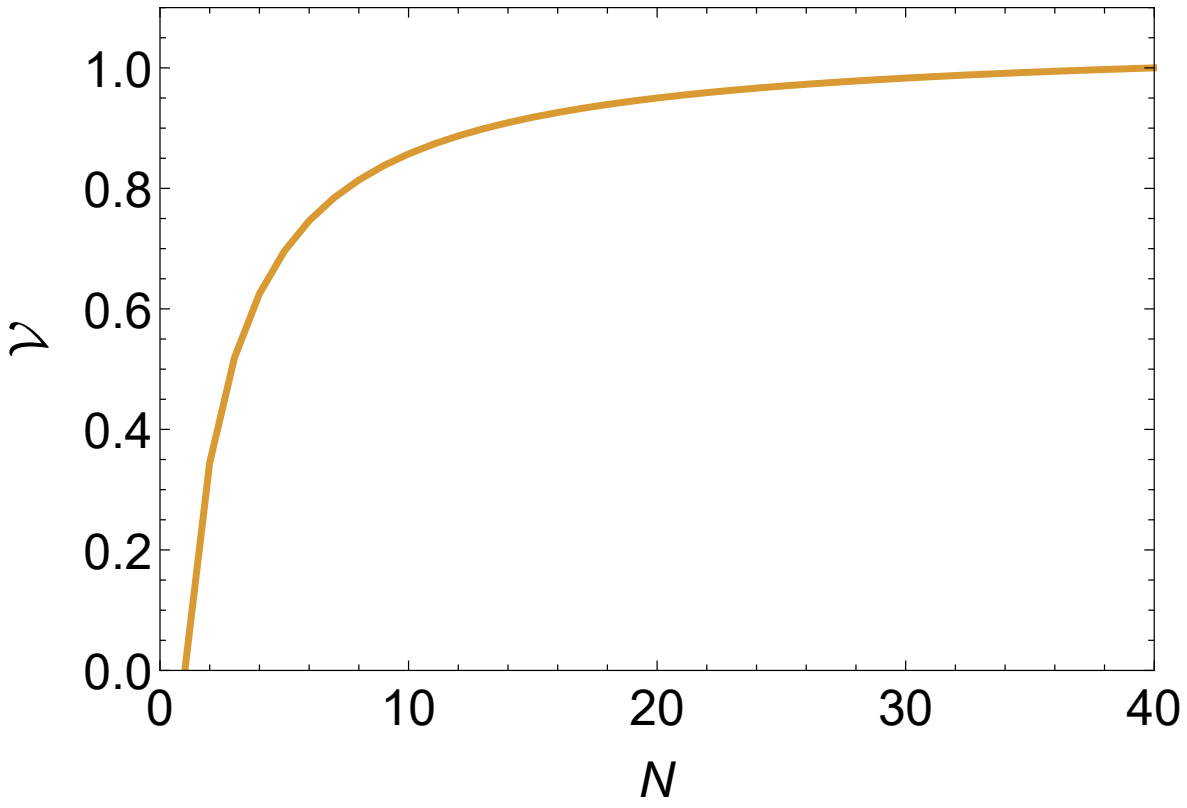

Figure 11.8: Effect of random filling on the visibility for two chains as a function of N for 40 traps.

this case, when $\theta = \theta_0/2 = \theta_{\text{exc}}$ and $\phi = 0$,

$$\bar{S}(\beta) = \frac{1}{N} + \frac{2}{N^2\binom{N_t}{N}} \sum_{m=N_t/2}^{N_t-1} W(m)\cos\beta$$
$$+\frac{2}{N^2\binom{N_t}{N}} \sum_{m=1}^{N_t/2-1} m\binom{N_t-2}{N-2}(\cos\beta - 1) + W(m), \tag{11.24}$$

where $\beta = 2kX_0 \sin\theta_{\text{exc}}$. In Fig. S11.8, the fringe visibility,

$$V = \frac{\bar{S}(0) - \bar{S}(\pi)}{\bar{S}(0) + \bar{S}(\pi)} = \frac{1 - \bar{S}(\pi)}{1 + \bar{S}(\pi)}, \tag{11.25}$$

is plotted as a function of N for $N_t = 40$. As can be seen, the main effect of random filling is to reduce the fringe visibility, an effect which becomes less important with increasing N.

CHAPTER 12

Theory of Rydberg Blockade With Multiple Intermediate State Excitations

12.1 Introduction

As a consequence of the dipole-dipole interaction between highly excited Rydberg atoms, it is possible to suppress multiple Rydberg excitations in an atomic ensemble when the atoms are driven by optical fields. The suppression mechanism produces a "dipole or Rydberg blockade" that can be used to entangle a large number of atoms. As proposed originally by Lukin et al [6], such a Rydberg blockade can be used as an important element in quantum computing and quantum information protocols. Experimental confirmation of the Rydberg blockade has been reported for both two-atom [104] and many-atom [105] systems.

In the simplest theoretical modeling of the Rydberg blockade, the ensemble of atoms is taken to consist of two collective states, the ground state and a fully symmetric state involving a single Rydberg excitation. Excitation of the collective Rydberg state is often accomplished via two-photon excitation via an off-resonant intermediate state. In the two-level model, the intermediate state does not appear explicitly in the formalism, having been adiabatically eliminated in some fashion. In such treatments, it is not clear whether or not there are multiple collective excitations of the intermediate state and to what extent off-resonant excitation of the intermediate states results in light shifts. The light shifts can modify the resonance condition for excitation of the blockade. In this paper, we fully account for multiple intermediate state excitations.

The collective states that are excited in the Rydberg blockade can be related to Dicke states [70]. There is a vast literature on both Dicke states and the Rydberg blockade. In a comprehensive article containing many references, Shammah et al [106] reviewed the Dicke state dynamics for an ensemble of non-interacting two-level atoms. If the atoms are non-interacting, the Dicke formalism, while interesting, simply makes a theoretical analysis of the problem much more complex, since the expectation value of any physical observable for non-interacting atoms is simply N times that of a single atom. On the other hand, when the blockade is operational, the Dicke formalism

offers distinct advantages, especially if decay is negligible and the field amplitudes are constant over the atomic ensemble. In that limit, the state vector describing the atomic ensemble is restricted to a limited subspace, namely the fully symmetric Dicke states. Although there are many papers devoted to the state dynamics of the symmetric states in the Rydberg blockade [107], far fewer consider the role intermediate state excitations [108]. Moreover these papers often focus on the role of spontaneous decay rather than the modifications of the Rydberg dynamics in the absence of decay.

The goals of this paper are several-fold: (1) to provide formal justification for the use of the two-level approximation in the theory of the dipole blockade, (2) to examine the changes in the blockade that occur when there are multiple intermediate state excitations, (3) to develop a dressed state theory of the blockade that can be used for both constant amplitude and adiabatic input pulses, (4) to underline the advantages of the dressed state approach, (5) to calculate the probability of the collective Rydberg population produced in the blockade as a function of pulse duration, (6) to compare this response for both constant amplitude and adiabatic input pulses, and, finally, (7) to connect our results with those that can be obtained using a form of the Holstein-Primakoff transformation [109]. We shall see that multiple intermediate state excitations can lead to an overall modulation of the Rydberg state population for constant amplitude fields that is absent when adiabatic pulses are used.

The paper is organized as follows: In Sec. II, the basic model is presented. A theory based on "bare" states is developed in Sec. III, allowing us to calculate the probability for excitation of the collective Rydberg state as a function of pulse duration. The analogous theory using a dressed-state basis is developed in Sec. IV for constant amplitude and adiabatic pulses. In Sec. V, a form of the Holstein-Primakoff transformation is used to reproduce the results that were obtained for adiabatic pulse excitation of the blockade.

12.2 General Considerations

Each atom is modeled as a three-level atom with lower state 1 (ground state), intermediate state 2, and upper state 3 (Rydberg level), as shown in Fig. 12.1. The atoms are assumed to be cold - motion of the atoms is neglected. There are two fields present,

$$\boldsymbol{E}_1(\boldsymbol{R},t) = \frac{1}{2}E_1(t)\boldsymbol{\epsilon}_1 e^{i\boldsymbol{k}_1\cdot\boldsymbol{R}-i\omega_1 t} + \text{c.c.}, \tag{12.1a}$$

$$\boldsymbol{E}_2(\boldsymbol{R},t) = \frac{1}{2}E_2(t)\boldsymbol{\epsilon}_2 e^{i\boldsymbol{k}_2\cdot\boldsymbol{R}-i\omega_2 t} + \text{c.c.}, \tag{12.1b}$$

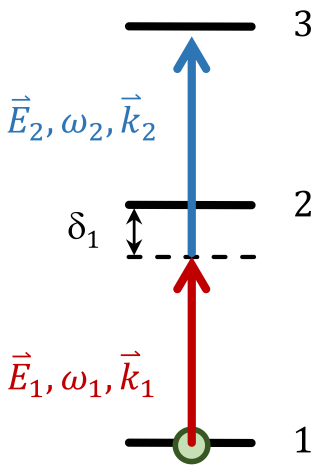

Figure 12.1: Level scheme. The detuning $\delta_2 = \omega_{32} - \omega_2$ is not indicated explicitly in the figure.

where c.c. stands for "complex conjugate." Field $\boldsymbol{E}_1(\boldsymbol{R}, t)$ $[\boldsymbol{E}_2(\boldsymbol{R}, t)]$ has propagation vector $\boldsymbol{k}_1$ $[\boldsymbol{k}_2]$, frequency $\omega_1 = k_1 c$ $[\omega_2 = k_2 c]$, and polarization $\boldsymbol{\epsilon}_1$ $[\boldsymbol{\epsilon}_2]$. We define detunings

$$\delta_1 = \omega_{21} - \omega_1; \quad \delta_2 = \omega_{32} - \omega_2, \tag{12.2}$$

where ω_{21} is the intermediate state to ground state frequency and ω_{32} is the Rydberg state to intermediate state frequency. It is assumed that $|\delta_1| \gg |\delta_1 + \delta_2|$. In drawing the figures in this paper, we assume that $\delta_1 > 0$. Field $\boldsymbol{E}_1(\boldsymbol{R}, t)$ drives the $1 - 2$ transition and field $\boldsymbol{E}_2(\boldsymbol{R}, t)$ drives the $2 - 3$ transition with associated Rabi frequencies

$$\Omega_1(t) = 2\chi_1(t) = -\frac{\boldsymbol{\mu}_{12} \cdot \boldsymbol{\epsilon}_1 E_1(t)}{\hbar}, \tag{12.3a}$$

$$\Omega_2(t) = 2\chi_2(t) = -\frac{\boldsymbol{\mu}_{23} \cdot \boldsymbol{\epsilon}_2 E_2(t)}{\hbar}, \tag{12.3b}$$

where $\boldsymbol{\mu}_{12}$ and $\boldsymbol{\mu}_{23}$ are dipole matrix elements. It is assumed that both $\chi_1(t)$ and $\chi_2(t)$ are real and positive.

Two pulse amplitude envelopes are considered, square profiles having duration T for which

$$\chi_{1,2}(t) = \chi_{1,2}\Theta\left(t\right)\Theta\left(T - t\right), \tag{12.4}$$

where $\Theta\left(t\right)$ is a Heaviside function, and Gaussian profiles,

$$\chi_{1,2}(t) = \chi_{1,2} e^{-t^2/T_p^2}, \tag{12.5}$$

with

$$T_p = T/\sqrt{\pi}, \tag{12.6}$$

chosen such that the pulse areas of the square and Gaussian pulses are equal. For the most part, it is assumed that the detunings satisfy

$$\frac{\chi_1^2}{\delta_1^2} \ll 1; \quad \frac{\chi_2^2}{\delta_1^2}, \frac{\chi_2^2}{\delta_2^2} \ll 1, \tag{12.7}$$

and that

$$|\delta_1|\, T_p \approx |\delta_2|\, T_p \gg 1. \tag{12.8}$$

Condition (12.7) guarantees that the intermediate state population of a single atom is much less than unity while condition (12.8) insures that the Gaussian pulses are adiabatic.

It is assumed that the Rydberg blockade is totally functional. That is, in an ensemble of N atoms, there is at most one collective Rydberg excitation in the sample. On the other hand, there can be *several* collective intermediate state excitations. The average number of level 2 excitations is of order

$$n_2 = \frac{N\Omega_1^2}{\delta_1^2} \ll N. \tag{12.9}$$

Decay of levels 2 and 3 is neglected, based on the assumptions that

$$\frac{(\chi_1^2 + \chi_2^2)}{\delta_1^2}\gamma_2 T \ll 1, \tag{12.10a}$$

$$\gamma_3 T \ll 1 \tag{12.10b}$$

where γ_j is the decay rate of state j [110]. Although decay is neglected, the light shifts, which are of order $\chi_1^2/\delta_1, \chi_2^2/\delta_1$, can modify the atomic response to the applied fields if

$$\frac{\chi_1^2 T}{|\delta_1|} \gtrsim 1 \ \text{ or } \ \frac{\chi_2^2 T}{|\delta_1|} \gtrsim 1. \tag{12.11}$$

The ensemble will undergo enhanced Rabi oscillations between the ground and collective Rydberg state with rate

$$\chi_{RN} = \sqrt{N}\frac{\chi_1\chi_2}{|\delta_1|} \equiv \frac{\Omega_{RN}}{2}. \tag{12.12}$$

To observe m Rabi oscillations, it is necessary that $\chi_{RN}T > m\pi$. On this time scale, the light shifts will be negligible provided that

$$\frac{\chi_1 m\pi}{\chi_2\sqrt{N}} \ll 1; \quad \frac{\chi_2 m\pi}{\chi_1\sqrt{N}} \ll 1. \tag{12.13}$$

We assume that $N \gg 1$.

12.3 Bare Atom Basis

12.3.1 Single Atom

For a single atom, the wave function in a field interaction representation [29] can be written as

$$|\psi(t)\rangle = a_1 |1\rangle + a_2 |2\rangle e^{i\boldsymbol{k}_1 \cdot \boldsymbol{R}_1 - i\omega_1 t} + a_3 |3\rangle e^{i\boldsymbol{k}_1 \cdot \boldsymbol{R}_1 - i\omega_1 t} e^{i\boldsymbol{k}_2 \cdot \boldsymbol{R}_1 - i\omega_2 t}, \tag{12.14}$$

where $\boldsymbol{R}_1$ is the position of the atom. The state amplitudes evolve as

$$\dot{a}_1 = -i\chi_1(t) a_2, \tag{12.15a}$$

$$\dot{a}_2 = -i\chi_1(t) a_1 - i\chi_2(t) a_3 - i\delta_1 a_2, \tag{12.15b}$$

$$\dot{a}_3 = -i\chi_2(t) a_2 - i\left(\delta_1 + \delta_2\right) a_3, \tag{12.15c}$$

with initial condition, $a_1(0) = 1$. It is straightforward to solve these equations numerically. For square pulses the solution for the vector $\boldsymbol{a}(t) = (a_1(t), a_2(t), a_3(t))$ is

$$\boldsymbol{a}(t) = \exp\left(-i\boldsymbol{H}t/\hbar\right) \boldsymbol{a}(0) \tag{12.16}$$

where

$$\boldsymbol{H} = \hbar \begin{pmatrix} 0 & \chi_1 & 0 \\ \chi_1 & \delta_1 & \chi_2 \\ 0 & \chi_2 & \delta_1 + \delta_2 \end{pmatrix} \tag{12.17}$$

is the effective Hamiltonian in a field interaction representation.

For adiabatic Gaussian pulses, it is possible to eliminate the intermediate state using

$$a_2(t) \approx -\frac{\left[\chi_1(t) a_1(t) + \chi_2(t) a_3(t)\right]}{\delta_1} \tag{12.18}$$

to arrive at

$$\dot{a}_1 \approx i\frac{\chi_1(t)\chi_2(t)}{\delta_1} a_3 + i\frac{\left[\chi_1(t)\right]^2}{\delta_1} a_1 \tag{12.19a}$$

$$\dot{a}_3 \approx i\frac{\chi_1(t)\chi_2(t)}{\delta_1} a_1 + i\frac{\left[\chi_2(t)\right]^2}{\delta_1} a_3 - i\left(\delta_1 + \delta_2\right) a_3 \tag{12.19b}$$

Even though there is a very small probability for the atom to be in level 2 following the pulse, these

equations give the sum of level 1 and level 3 populations equal to unity. In other words, adiabatic elimination leads to an error that is exponentially small in the parameter $|\delta_1| T_p$. This is true of any asymptotic expansion - it misses only exponentially small corrections.

There is an effective net detuning from two-photon resonance given by

$$\Delta(t) = \delta_1 + \delta_2 - \frac{[\chi_2(t)]^2}{\delta_1} + \frac{[\chi_1(t)]^2}{\delta_1} \tag{12.20}$$

which implies that the light shifts can be larger than or comparable with the two-photon coupling rate

$$\chi(t) = \frac{\chi_1(t)\chi_2(t)}{\delta_1}. \tag{12.21}$$

The light shifts can be somewhat compensated by taking a non-zero two-photon detuning, but it is impossible to compensate for the light shifts at *all* times.

12.3.2 N Atoms

Once the dipole-dipole interaction between different atoms in Rydberg level 3 is included, the calculation becomes very difficult. Even if the blockade is fully functional, as we assume, there can be several level 2 excitations. There is no obvious simple way to eliminate the intermediate states, in general. In other words, there is no formal justification for considering the problem as an effective 2-level problem involving the ground and collective Rydberg states.

A more formal justification begins with the neglect of Rydberg-Rydberg interactions. We assume the field amplitude is constant over the sample. Then the ensemble wave function is given simply by

$$|\psi(t)\rangle = \prod_{j=1}^{N} \left(a_1 |1\rangle_j + a_2 |2\rangle_j e^{i\boldsymbol{k}_1 \cdot \boldsymbol{R}_j - i\omega_1 t} + a_3 |3\rangle_j e^{i\boldsymbol{k}_1 \cdot \boldsymbol{R}_j - i\omega_1 t} e^{i\boldsymbol{k}_2 \cdot \boldsymbol{R}_j - i\omega_2 t} \right). \tag{12.22}$$

where $\boldsymbol{R}_j$ is the position of the atom j. When expanded, this gives a state vector that can be written as the sum of fully symmetric orthonormal phased basis kets $|N; n, q\rangle$ that have n excitations of level 2 and q excitations of level 3; that is

$$|N; n, q\rangle = \frac{1}{\sqrt{C_n^N C_q^{N-n}}} \left| S_{nq}^N \right\rangle, \tag{12.23}$$

where the $\left|S_{nq}^N\right\rangle$ are fully symmetric, *unnormalized* phased states. In other words,

$$\begin{aligned}|\psi(t)\rangle &= \sum_{n,q} a_1^{N-n-q} a_2^n a_3^q \left|S_{nq}^N\right\rangle \\ &= \sum_{n,q} c_{nq}^N(t) \left|N; n, q\right\rangle, \end{aligned} \tag{12.24}$$

where n and q can vary from 0 to N with $n + q \leq N$. It then follows immediately that

$$c_{nq}^N = \sqrt{C_n^N C_q^{N-n}} a_1^{N-n-q} a_2^n a_3^q. \tag{12.25}$$

The $|N; n, 0\rangle$ are not Dicke states [70], but can be related to the Dicke states if we set $n = m_{Dicke} + N/2$ and $N = 2J_{Dicke}$. Using Eqs. (12.25) and (12.15), we obtain the evolution equations

$$\begin{aligned}\dot{c}_{nq}^N = &-i\left[n\delta_1 + q\left(\delta_1 + \delta_2\right)\right] c_{nq}^N - i\chi_1(t)\sqrt{n\left(N - n - q + 1\right)} c_{n-1,q}^N \\ &- i\chi_1(t)\sqrt{(n+1)\left(N - n - q\right)} c_{n+1,q}^N - i\chi_2(t)\sqrt{n\left(q+1\right)} c_{n-1,q+1}^N \\ &- i\chi_2(t)\sqrt{q(n+1)} c_{n+1,q-1}^N, \end{aligned} \tag{12.26}$$

subject to the initial conditions

$$c_{nq}^N(0) = \delta_{n,0}\delta_{q,0}, \tag{12.27}$$

where $\delta_{i,j}$ is a Kronecker delta. Of course, for our factorized state, if you want to calculate any physical observable's expectation value, it will simply be N times the single atom expectation value.

To go from a factorized state to the blockade, we limit the values of q to be 0 or 1. Then there are two ladders of levels, the first of which has $N+1$ steps ($q = 0$ and $0 \leq n \leq N$) and the second N steps ($q = 1$ and $0 \leq n \leq N-1$). These ladders are represented schematically in Fig. 12.2 for the case when $\delta_1 + \delta_2 = 0$. The equations for the state amplitudes in these two chains are

$$\begin{aligned}\dot{c}_{n0}^N = &-in\delta_1 c_{n0}^N - i\chi_1(t)\sqrt{n\left(N - n + 1\right)} c_{n-1,0}^N \\ &- i\chi_1(t)\sqrt{(n+1)\left(N - n\right)} c_{n+1,0}^N - i\chi_2(t)\sqrt{n} c_{n-1,1}^N, \end{aligned} \tag{12.28a}$$

$$\begin{aligned}\dot{c}_{n1}^N = &-i\left[n\delta_1 + \left(\delta_1 + \delta_2\right)\right] c_{n1}^N - i\chi_1(t)\sqrt{n\left(N - n\right)} c_{n-1,1}^N \\ &- i\chi_1(t)\sqrt{(n+1)\left(N - n - 1\right)} c_{n+1,1}^N - i\chi_2(t)\sqrt{(n+1)} c_{n+1,0}^N. \end{aligned} \tag{12.28b}$$

Field 1 produces strong coupling up and down each ladder when N is large, as is assumed. There is coupling between adjacent ladder states for n differing by one with a coupling constant $\sqrt{(n+1)}\chi_2$. The maximum population in each ladder occurs for $n \approx n_2/2$, where n_2 is given by

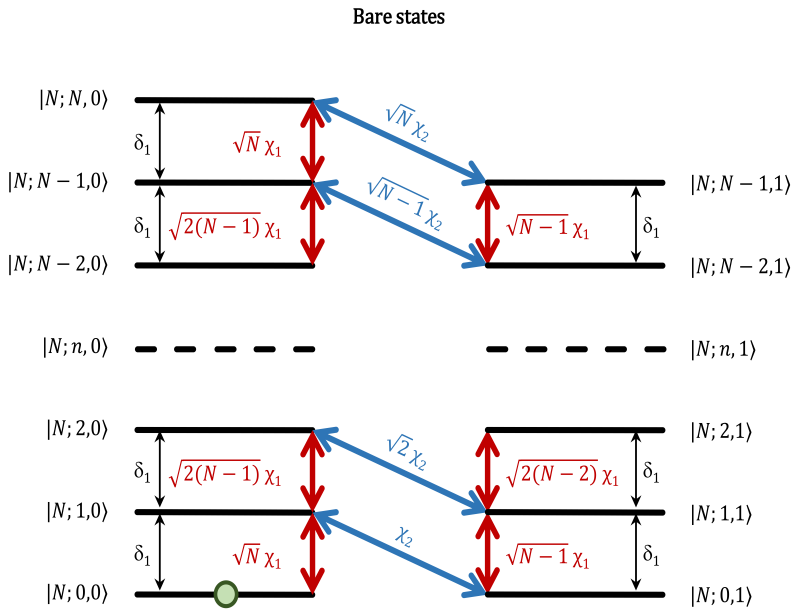

Figure 12.2: Fully-symmetric collective bare states. The left ladder consists of states $|N; n, 0\rangle$ containing zero Rydberg excitations and up to $n = N$ level 2 excitations. The right ladder consists of states $|N; n, 1\rangle$ containing one Rydberg excitation and up to $n = (N-1)$ level 2 excitations. Coupling strengths are shown. Initially the atoms are in the ground state $|N; 0, 0\rangle$. The ladders are drawn for $\delta_1 + \delta_2 = 0$.

Eq. (12.9), and approximately n_2 states are populated significantly. Thus, only the lower states of the ladders get populated in the limit that $\Omega_1^2/\delta_1^2 \ll 1$. In the case of square pulses, the solution of Eqs. (12.28) at time $t = T$ can be expressed formally as

$$\boldsymbol{c}_{nq}^N(t) = e^{-i\boldsymbol{H}_{bare}t/\hbar}\boldsymbol{c}_{nq}^N(0), \tag{12.29}$$

where $\boldsymbol{H}_{bare}$ is a $(2N+1) \times (2N+1)$ matrix and $\boldsymbol{c}_{nq}^N$ is a $(2N+1)$ column vector. The matrix exponential function needs to be calculated numerically, in general. For time-dependent Rabi frequencies (pulsed fields), Eqs. (12.28) must be solved numerically.

If $n_2 = N\Omega_1^2/\delta_1^2 \ll 1$, it is a good approximation to include only the two lowest states of each ladder (at least two steps must be included since the lowest states of each ladder are not coupled in

this bare state calculation). The truncated equations with $n \leq 1$ and $q \leq 1$ are

$$\dot{c}_{00}^N = -i\chi_1(t)\sqrt{N}c_{10}^N, \tag{12.30a}$$

$$\dot{c}_{10}^N = -i\delta_1 c_{10}^N - i\chi_1(t)\sqrt{N}c_{00}^N - i\chi_2(t)c_{01}^N, \tag{12.30b}$$

$$\dot{c}_{01}^N = -i\left(\delta_1 + \delta_2\right)c_{01}^N - i\chi_2(t)c_{10}^N - i\chi_1(t)\sqrt{N-1}c_{11}^N, \tag{12.30c}$$

$$\begin{aligned}\dot{c}_{11}^N &= -i\left(2\delta_1 + \delta_2\right)c_{11}^N - i\chi_1(t)\sqrt{N-1}c_{01}^N, \\ &\approx -i\delta_1 c_{11}^N - i\chi_1(t)\sqrt{N-1}c_{01}^N.\end{aligned} \tag{12.30d}$$

For adiabatic pulses [111]

$$c_{10}^N(t) \approx -\frac{\chi_1(t)\sqrt{N}c_{00}^N(t) + \chi_2(t)c_{01}^N(t)}{\delta_1}, \tag{12.31a}$$

$$c_{11}^N(t) \approx -\frac{\chi_1(t)\sqrt{N-1}}{\delta_1}c_{01}^N(t), \tag{12.31b}$$

which, when substituted into the original equations, yields

$$\dot{c}_{00}^N \approx \frac{iN\left[\chi_1(t)\right]^2}{\delta_1}c_{00}^N + \frac{i\sqrt{N}\chi_1(t)\chi_2(t)}{\delta_1}c_{01}^N, \tag{12.32a}$$

$$\begin{aligned}\dot{c}_{01}^N \approx& -i\left(\delta_1 + \delta_2\right)c_{01}^N + \frac{i\left[\chi_2(t)\right]^2}{\delta_1}c_{01}^N \\ &+ \frac{i\left(N-1\right)\left[\chi_1(t)\right]^2}{\delta_1}c_{01}^N + \frac{i\sqrt{N}\chi_1(t)\chi_2(t)}{\delta_1}c_{00}^N.\end{aligned} \tag{12.32b}$$

If we let

$$c_{00}^N = \tilde{c}_{00}^N \exp\left[i\frac{N}{\delta_1}\int_{-\infty}^{t}\left[\chi_1(t')\right]^2 dt'\right], \tag{12.33a}$$

$$c_{01}^N = \tilde{c}_{01}^N \exp\left[i\frac{N}{\delta_1}\int_{-\infty}^{t}\left[\chi_1(t')\right]^2 dt'\right], \tag{12.33b}$$

then

$$d\tilde{c}_{00}^N/dt = \frac{i\sqrt{N}\chi_1(t)\chi_2(t)}{\delta_1}\tilde{c}_{01}^N, \tag{12.34a}$$

$$d\tilde{c}_{01}^N/dt = \frac{i\sqrt{N}\chi_1(t)\chi_2(t)}{\delta_1}\tilde{c}_{00}^N - i\Delta(t)\tilde{c}_{01}^N, \tag{12.34b}$$

which are the effective two-level equations, including the light shifts, with $\Delta(t)$ defined by Eq. (12.20).

For *constant amplitude* pulses and $n_2 \ll 1$, Eqs. (12.34) can still provide a very good approx-

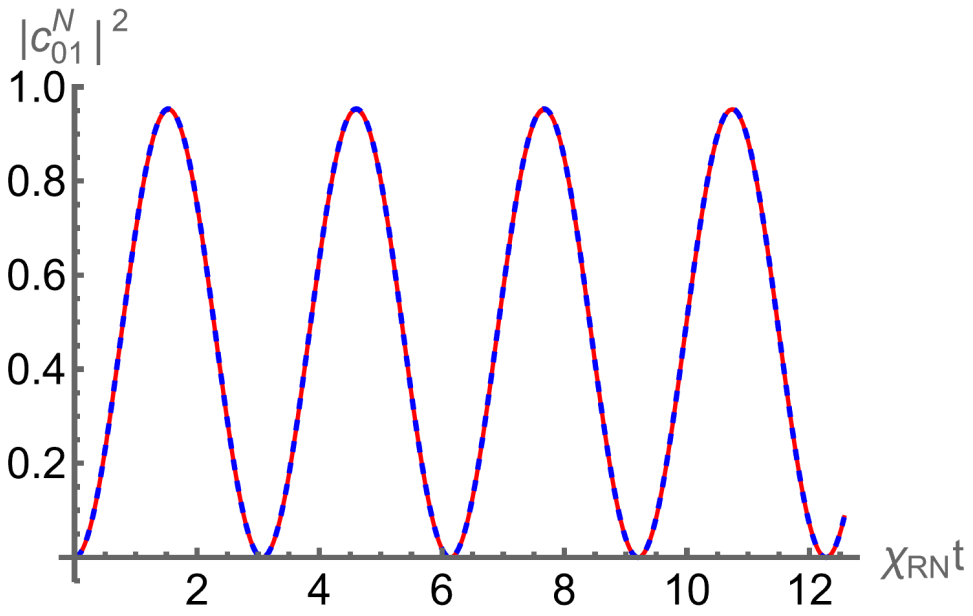

Figure 12.3: Population of the lowest state of the Rydberg ladder as a function of $\chi_{RN}t$ for $\chi_1 = 1$, $\chi_2 = 10$, $\delta_1 = -\delta_2 = 1000$, and $N = 500$. The solid red curve is the exact result and the dashed blue curve is the two-level result given by Eq. (12.35a). For these parameters the two curves overlap.

imation to the exact result provided that $\chi_2/\delta_1 \ll 1$. The solution of Eqs. (12.34) with constant amplitude fields is

$$\left|c_{01}^N(t)\right|^2 = \frac{4\chi_{RN}^2}{\Delta^2 + 4\chi_{RN}^2} \sin^2\left[\sqrt{\Delta^2 + 4\chi_{RN}^2}\, t/2\right], \tag{12.35a}$$

$$\left|c_{00}^N(t)\right|^2 = 1 - \left|c_{01}^N(t)\right|^2, \tag{12.35b}$$

where Δ is given by Eq. (12.20) and χ_{RN} by Eq. (12.12). With increasing χ_2/δ_1, Eqs. (12.34) may fail to reproduce the nonadiabatic effects associated with the sudden turn-on of the fields. In Figs. 12.3 and 12.4, we plot $\left|c_{01}^N(t)\right|^2$ as a function of $\chi_{RN}t$ with values of χ_1, χ_2, δ_1, and δ_2 given in arbitrary units. The values chosen are $\chi_1 = 1$, $\delta_1 = 1000$, $N = 500$, and $\{\chi_2 = 10, \delta_2 = -1000\}$ (Fig. 12.3) or $\{\chi_2 = 500, \delta_2 = -890\}$ (Fig. 12.4). For $\chi_2/\delta_1 = 0.01$, the exact [obtained from Eq. (12.29)] and "adiabatic" results are in good agreement, but for $\chi_2/\delta_1 = 0.5$, $\left|c_{01}^N(t)\right|^2$ is modulated at frequency δ_1, even though the two-level approximation remains valid. We shall see that this nonadiabatic behavior persists for the total Rydberg population when the two-level approximation is no longer valid. The oscillation frequency in Fig. 12.4 is much larger than the collective Rabi frequency owing to the large light shift associated with field 2.

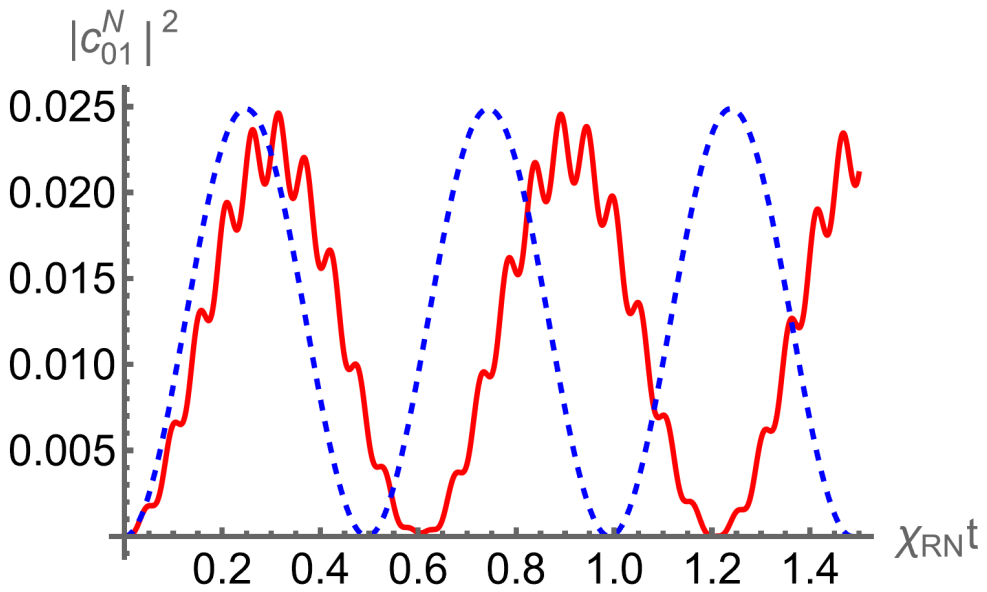

Figure 12.4: Population of the lowest state of the Rydberg ladder as a function of $\chi_{RN}t$ for $\chi_1 = 1$, $\chi_2 = 500$, $\delta_1 = 1000$, $\delta_2 = -890$, and $N = 500$. The solid red curve is the exact result and the dashed blue curve is the two-level result given by Eq. (12.35a).

12.4 Dressed Atom Basis

12.4.1 Constant Amplitude Dressed States

It turns out there can be some significant advantages if (semiclassical) dressed states are used [29]. In this subsection we consider constant amplitude fields, but it turns out that adiabatic dressed states, to be discussed in the following subsection, may be more useful. The equations of motion for the bare state amplitudes in the absence of field 2 are

$$\dot{a}_1 = -i\chi_1 a_2 \tag{12.36a}$$

$$\dot{a}_2 = -i\chi_1 a_1 - i\delta_1 a_2, \tag{12.36b}$$

which implies an effective Hamiltonian

$$\boldsymbol{H}_2 = \hbar \begin{pmatrix} 0 & \chi_1 \\ \chi_1 & \delta_1 \end{pmatrix}. \tag{12.37}$$

We diagonalize this Hamiltonian and obtain eigenvalues

$$E_{I,II} = \hbar\omega_{I,II} = \hbar\left[\frac{\delta_1}{2} \mp \frac{\Omega}{2}\right], \tag{12.38}$$

where

$$\Omega = \sqrt{\delta_1^2 + 4\chi_1^2}. \tag{12.39}$$

The corresponding eigenkets are

$$|I\rangle = \cos\theta\,|1\rangle + \sin\theta\,|2\rangle\,, \tag{12.40a}$$

$$|II\rangle = \cos\theta\,|2\rangle - \sin\theta\,|1\rangle\,, \tag{12.40b}$$

with

$$\cos\theta = \frac{\chi_1}{\sqrt{\chi_1^2 + \omega_I^2}}, \tag{12.41a}$$

$$\sin\theta = \frac{\omega_I}{\sqrt{\chi_1^2 + \omega_I^2}}. \tag{12.41b}$$

Note that for $\chi_1^2/\delta_1^2 \ll 1$,

$$\cos\theta \approx 1 - \frac{\chi_1^2}{2\delta_1^2}, \tag{12.42a}$$

$$\sin\theta \approx -\frac{\chi_1}{\delta_1}, \tag{12.42b}$$

$$\omega_I \approx -\frac{\chi_1^2}{\delta_1}. \tag{12.42c}$$

The bare and dressed state amplitudes are related by

$$a_I = \cos\theta a_1 + \sin\theta a_2, \tag{12.43a}$$

$$a_{II} = \cos\theta a_2 - \sin\theta a_1, \tag{12.43b}$$

$$a_1 = \cos\theta a_I - \sin\theta a_{II}, \tag{12.43c}$$

$$a_2 = \cos\theta a_{II} + \sin\theta a_I, \tag{12.43d}$$

and the initial condition for the dressed state amplitudes is

$$a_I(0) = \cos\theta; \quad a_{II}(0) = -\sin\theta. \tag{12.44}$$

It is now possible to introduce symmetric collective states as before. The ensemble wave function is given simply by

$$|\psi(t)\rangle = \prod_{j=1}^{N} \left(a_I\,|I\rangle_j + a_{II}\,|II\rangle_j\, e^{i\boldsymbol{k}_1\cdot\boldsymbol{R}_j - i\omega_1 t} + a_3\,|3\rangle_j\, e^{i\boldsymbol{k}_1\cdot\boldsymbol{R}_j - i\omega_1 t} e^{i\boldsymbol{k}_2\cdot\boldsymbol{R}_j - i\omega_2 t} \right), \tag{12.45}$$

where

$$|I\rangle_j = \cos\theta\,|1\rangle_j + \sin\theta\,|2\rangle_j\,, \tag{12.46a}$$

$$|II\rangle_j = \cos\theta\,|2\rangle_j - \sin\theta\,|1\rangle_j\,. \tag{12.46b}$$

When expanded, this gives a state vector that can be written as the sum of fully symmetric orthonormal dressed basis kets $|\widetilde{N;n,q}\rangle$ that have n excitations of state II and q excitations of level 3; that is

$$|\widetilde{N;n,q}\rangle = \frac{1}{\sqrt{C_n^N C_q^{N-n}}}\widetilde{\left|S_{nq}^N\right\rangle} \tag{12.47}$$

where the $\widetilde{\left|S_{nq}^N\right\rangle}$ are the fully symmetric, *unnormalized* states. In other words,

$$\begin{aligned}|\psi(t)\rangle &= \sum_{n,q} a_I^{N-n-q} a_{II}^n a_3^q \widetilde{\left|S_{nq}^N\right\rangle} \\ &= \sum_{n,q} c_{nq}^{Nd}(t)|\widetilde{N;n,q}\rangle,\end{aligned} \tag{12.48}$$

where n and q can vary from 0 to N with $n+q \le N$. It then follows immediately that

$$c_{nq}^{Nd} = \sqrt{C_n^N C_q^{N-n}}\, a_I^{N-n-q} a_{II}^n a_3^q. \tag{12.49}$$

Using Eqs. (12.43) and (12.15), one can show that the single atom dressed state amplitudes obey the evolution equations

$$\dot{a}_I = -i\omega_I a_I - i\chi_2 \sin\theta a_3, \tag{12.50a}$$

$$\dot{a}_{II} = -i\omega_{II} a_{II} - i\chi_2 \cos\theta a_3, \tag{12.50b}$$

$$\dot{a}_3 = -i\left(\delta_1+\delta_2\right) a_3 - i\chi_2 \cos\theta a_{II} - i\chi_2 \sin\theta a_I, \tag{12.50c}$$

from which it follows that the collective state amplitudes obey

$$\begin{aligned}\dot{c}_{nq}^{Nd} = &-i\left[(N-q)\,\omega_I + n\Omega + q\left(\delta_1+\delta_2\right)\right] c_{nq}^{Nd} - i\chi_2 \sin\theta\sqrt{(q+1)\,(N-n-q)}\, c_{n,q+1}^{Nd} \\ &- i\chi_2 \sin\theta\sqrt{q\,(N-n-q+1)}\, c_{n,q-1}^{Nd} - i\chi_2 \cos\theta\sqrt{n\,(q+1)}\, c_{n-1,q+1}^{Nd} \\ &- i\chi_2 \cos\theta\sqrt{q(n+1)}\, c_{n+1,q-1}^{Nd},\end{aligned} \tag{12.51}$$

where we have used the relation $\omega_{II} - \omega_I = \Omega$.

Redefining the zero of energy by setting

$$c_{nq}^{Nd}(t) = b_{nq}^{Nd}(t)e^{-iN\omega_I t}e^{-in\Omega t}, \tag{12.52}$$

we find, for a perfect blockade, that the needed equations are

$$\dot{b}_{n0}^{Nd} = -i\chi_2 \sin\theta\sqrt{(N-n)}b_{n1}^{Nd} - i\chi_2 e^{i\Omega t}\cos\theta\sqrt{n}b_{n-1,1}^{Nd}, \tag{12.53a}$$

$$\dot{b}_{n1}^{Nd} = -i\left(\delta_1+\delta_2-\omega_I\right)b_{n1}^{Nd} - i\chi_2\sin\theta\sqrt{N-n}b_{n0}^{Nd} - i\chi_2\cos\theta e^{-i\Omega t}\sqrt{n+1}b_{n+1,0}^{Nd}. \tag{12.53b}$$

The situation has changed dramatically from the bare basis (see Fig. 12.5, drawn for $\delta_1+\delta_2 = 0$). Having used a dressed basis, there is no longer any *direct* coupling up and down each of the ladders. Most of the coupling is between *adjacent* states of the two ladders having the *same* n and this coupling is enhanced by a factor of $\sqrt{N}$ for low lying states if $N \gg 1$. Note that the energy of state $|\widetilde{N;n,0}\rangle$ is lower than that of state $|\widetilde{N;n,1}\rangle$ by $-\hbar\omega_I$, *which is the ground state light shift associated with the first field* (recall that $-\omega_I \approx \chi_1^2/\delta_1 > 0$). In other words the dressed states automatically include this light shift. In addition there is coupling of order $\chi_2\sqrt{n}$ between states in different ladders differing in n by one. Since these states are separated in frequency by $\Omega \approx \delta_1 \gg \chi_2$, this coupling leads to contributions to state amplitudes of order $\chi_2\sqrt{n}/\Omega$.

If the χ_2 coupling between states differing in n by one is neglected, the problem reduces to a number of independent two state problems between different ladder states having the same n. In this limit, and in the limit that

$$|\sigma| = |\delta_1+\delta_2-\omega_I| \ll \chi_2|\sin\theta|\sqrt{(N-n)}, \tag{12.54}$$

the approximate solution of Eqs. (12.53) is

$$\left[b_{n0}^{Nd}(t)\right]^{(0)} = b_{n0}^{Nd}(0)\cos\left[\chi_2 t\sin\theta\sqrt{(N-n)}\right], \tag{12.55a}$$

$$\left[b_{n1}^{Nd}(t)\right]^{(0)} = -ib_{n0}^{Nd}(0)\sin\left[\chi_2 t\sin\theta\sqrt{(N-n)}\right], \tag{12.55b}$$

where

$$\begin{aligned} b_{nq}^{Nd}(0) &= \sqrt{C_n^N}a_I^{N-n}(0)a_{II}^n(0)\delta_{q,0} \\ &= \sqrt{C_n^N}\cos^{N-n}\theta\left[-\sin\theta\right]^n\delta_{q,0}. \end{aligned} \tag{12.56}$$

For $\theta \ll 1$ and $N \gg n$, $\left|b_{n0}^{Nd}(0)\right|^2$ approaches a Poisson distribution having average value $\langle n\rangle = N\chi_1^2/\delta_1^2 = n_2/4$. Good convergence is achieved if a maximum of $n_2/2$ steps in each ladder is

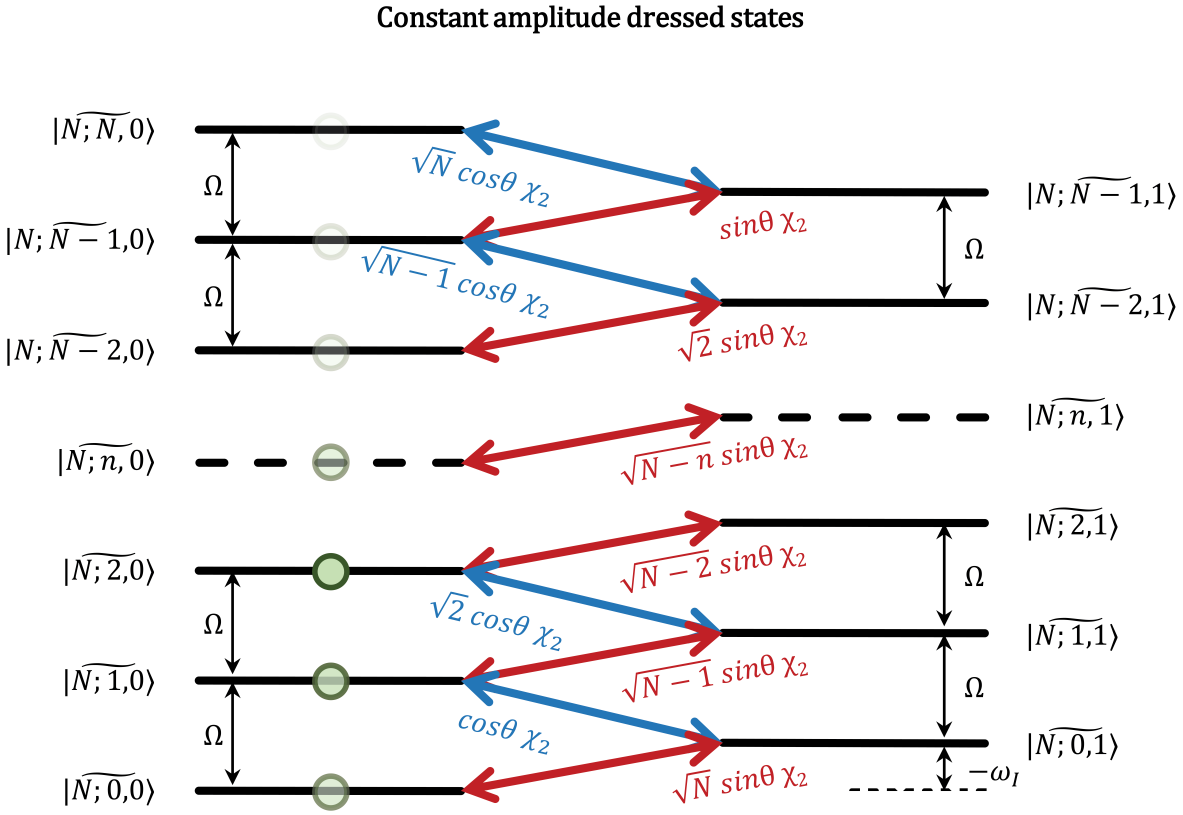

Figure 12.5: Fully-symmetric collective dressed states for constant amplitude fields when $\delta_1 + \delta_2 = 0$. In contrast to the bare state ladders, there is no longer any direct coupling up and down the ladders. However, initially there is now population in each of the states in the left ladder (represented by the shaded circles), with the relative populations determined from Eq. (12.56).

included. We have reduced the number of states from what was needed in the bare state basis by a factor of 2; moreover, we now have an approximate analytic solution.

We can improve upon this solution by using a truncated subspace for the amplitudes

$$\boldsymbol{b}_n^{Nd} = [b_{n0}^{Nd}, b_{n1}^{Nd}, \tilde{b}_{n+1,0}^{Nd}, \tilde{b}_{n+1,1}^{Nd}, \tilde{b}_{n-1,0}^{Nd}, \tilde{b}_{n-1,1}^{Nd}].$$

As is shown in the appendix, whenever the inequalities

$$\frac{\chi_1^2}{\delta_1^2} \ll 1; \quad \frac{\chi_2}{\delta_1} \ll 1; \quad N \gg n, \;\; \chi_{RN} \gg \left|\delta_1 + \delta_2 + \frac{\chi_1^2}{\delta_1}\right|, \tag{12.57}$$

hold, approximate solutions for the dressed state amplitudes are

$$b_{n0}^{Nd}(t) \approx b_{n0}^{Nd}(0) e^{-ist} \cos\left(\chi_{RN} t\right), \tag{12.58a}$$

$$b_{n1}^{Nd}(t) \approx i b_{n0}^{Nd}(0) e^{-ist} \sin\left(\chi_{RN} t\right), \tag{12.58b}$$

where

$$s = \frac{\chi_1^2}{2\delta_1} - \frac{\chi_2^2}{2\delta_1} + \frac{\delta_1 + \delta_2}{2} = \frac{\Delta}{2}. \tag{12.59}$$

To this order, the solution depends on n only through the initial conditions. A somewhat improved approximation can be obtained by using the exact solution for the truncated subspace given by Eq. (12.95) in the appendix. There are no collective light shifts, proportional to N, that enter the solution.

Some illustrative plots are given for $\mathrm{Im}\, b_{01}^{Nd}$ as a function of $\chi_{RN} t$ for $\delta_1 = -\delta_2$. In Fig. 12.6, $\chi_1 = \chi_2 = 1$, $\delta_1 = 100$, $N = 10,000$, and $n = 0$. For these parameters, $n_2 = 4$ and only the first 2 steps in each dressed state ladder are populated significantly. Moreover, $s = 0$, such that $\mathrm{Re}\, b_{01}^{Nd} \approx 0$. The solid red curve is the exact solution and the dashed blue curve, which virtually coincides with the exact solution, is the approximate solution given by Eq. (12.58b). Modifications of the transition amplitude introduced by light shifts can be seen in Fig. 12.7, in which $\chi_1 = 2$, $\chi_2 = 1$, $\delta_1 = 50$, $N = 100$, and $n = 0$. For these parameters, $s = 0.03$ and the light shifts lead to a modulation of the collective Rabi oscillations, but the exact and approximate solutions for both $\mathrm{Im}\, b_{01}^{Nd}$ and $\mathrm{Re}\, b_{01}^{Nd}$ (not shown) still are in excellent agreement. For larger values of χ_2/δ_1, the approximate expression given by Eq. (12.58b) begins to breakdown for two reasons. There are corrections *within* the truncated subspace of order χ_2/δ_1 and there is coupling between the truncated subspaces as well. This feature is illustrated in Fig. 12.8, in which $\chi_1 = 2$, $\chi_2 = 30$, $\delta_1 = 50$, $N = 100$, and $n = 0$. The dotted black curve is an improved approximation for $\mathrm{Im}\, b_{01}^{Nd}$ in the truncated subspace given by Eq. (12.95) of the appendix.

Having derived approximate expressions for the dressed state amplitudes, we can use these

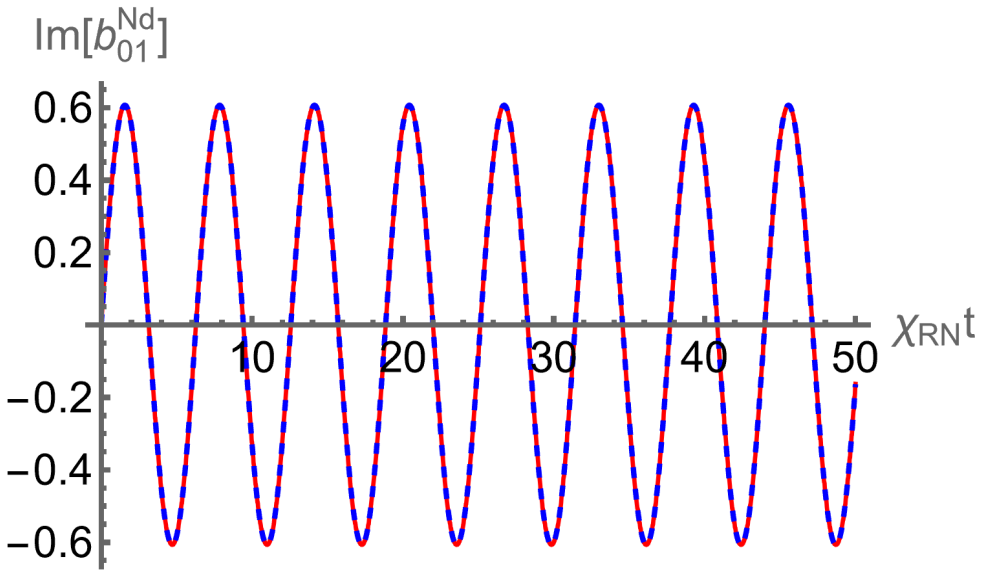

Figure 12.6: Imaginary part of the amplitude associated with the lowest level of the Rydberg ladder as a function of $\chi_{RN}t$ for $\chi_1 = \chi_2 = 1$, $\delta_1 = -\delta_2 = 100$, $N = 10,000$. The exact (solid red curve) and approximate solution given by Eq. (12.58b) (dashed blue curve) overlap.

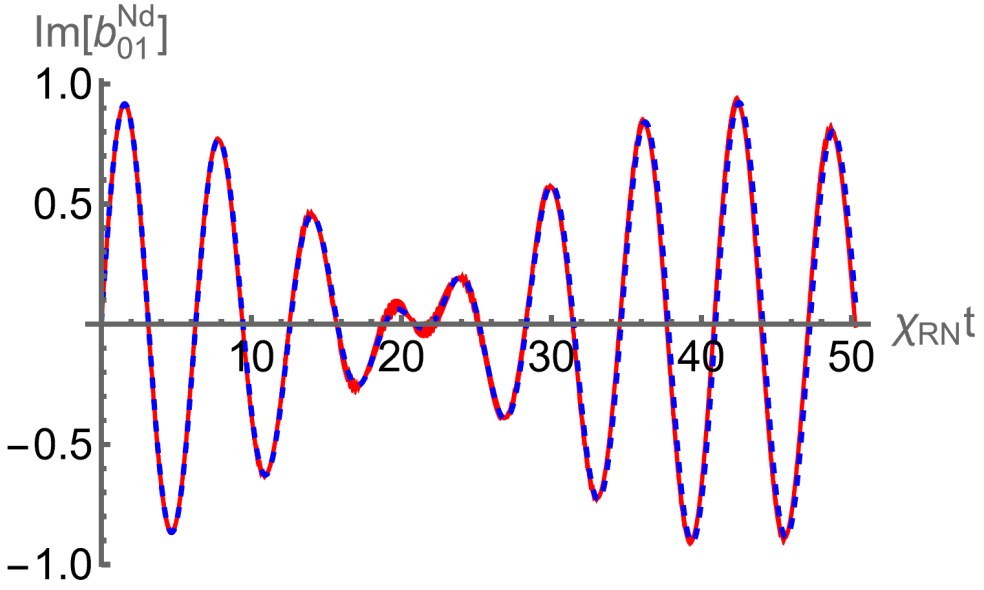

Figure 12.7: Imaginary part of the amplitude associated with the lowest level of the Rydberg ladder as a function of $\chi_{RN}t$ for $\chi_1 = 2$, $\chi_2 = 1$, $\delta_1 = -\delta_2 = 50$, $N = 100$. The exact (solid red curve) and approximate solution given by Eq. (12.58b) (dashed blue curve) begin to deviate from one another for large times.

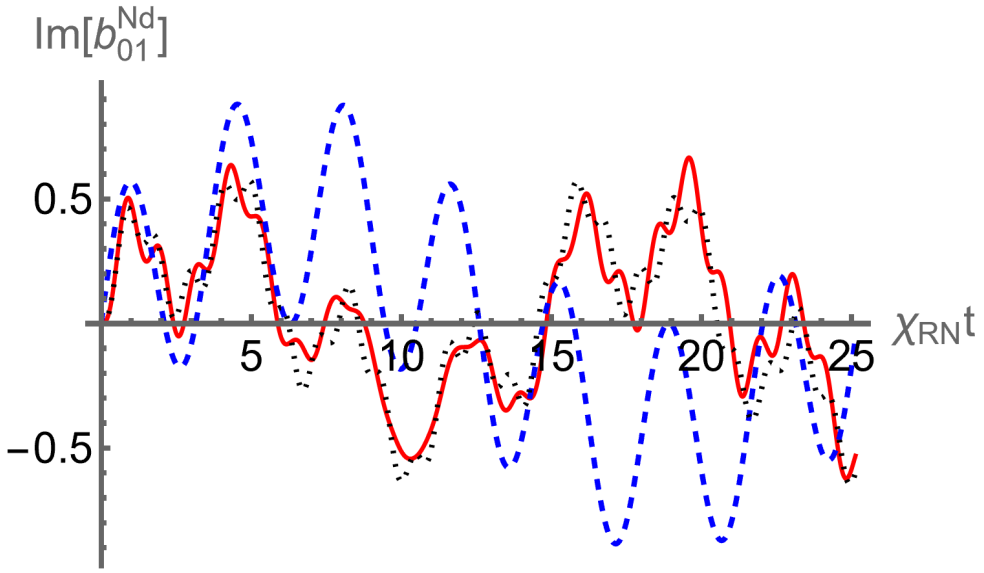

Figure 12.8: Imaginary part of the amplitude associated with the lowest level of the Rydberg ladder as a function of $\chi_{RN}t$ for $\chi_1 = 2$, $\chi_2 = 30$, $\delta_1 = -\delta_2 = 50$, $N = 100$. The exact (solid red curve) and approximate solution given by Eq. (12.58b) (dashed blue curve) no longer agree. The black dotted solution is an approximate solution in the truncated subspace described in the appendix.

results to obtain approximate expressions for the bare state amplitudes. From Eqs. (12.25), (12.43), and (12.49), it follows that the bare state amplitudes $c_{n0}^N(t)$ and $c_{n1}^N(t)$ can be expressed in terms of the dressed state solutions as

$$c_{n0}^N(t) = \sum_{\mu=0}^{N-n}\sum_{\nu=0}^{n}\sqrt{\frac{C_n^N}{C_{n+\mu-\nu}^N}}C_\mu^{N-n}C_\nu^n\,(-1)^\mu\,(\cos\theta)^{N-\mu-\nu}\,(\sin\theta)^{\mu+\nu}$$
$$\times\, e^{-i(n+\mu-\nu)\Omega t}e^{-iN\omega_I t}b_{n+\mu-\nu,0}^{Nd}(t), \tag{12.60a}$$
$$c_{n1}^N(t) = \sum_{\mu=0}^{N-n-1}\sum_{\nu=0}^{n}\sqrt{\frac{N-n}{N-n-\mu+\nu}}\sqrt{\frac{C_n^N}{C_{n+\mu-\nu}^N}}C_\mu^{N-1-n}C_\nu^n\,(-1)^\mu\,e^{-iN\omega_I t}$$
$$\times\,(\cos\theta)^{N-1-\mu-\nu}\,(\sin\theta)^{\mu+\nu}\,e^{-i(n+\mu-\nu)\Omega t}b_{n+\mu-\nu,1}^{Nd}(t). \tag{12.60b}$$

In the limit of large N, Eqs. (12.60), (12.58), and (12.56) can be combined to give the approximate

solutions

$$c_{n0}^{N}(t) \approx \sqrt{C_n^N}\left(1-e^{i\Omega t}\right)^n(-1)^n e^{-in\Omega t}\cos^n\theta\sin^n\theta e^{-iN\omega_I t} \times\left(\cos^2\theta+e^{-i\Omega t}\sin^2\theta\right)^{N-n}e^{-ist}\cos\left[\chi_2 t\sin\theta\sqrt{N}\right], \tag{12.61a}$$

$$c_{n1}^{N}(t) \approx -i\sqrt{C_n^N}\left(1-e^{i\Omega t}\right)^n(-1)^n e^{-in\Omega t}\cos^{n+1}\theta\sin^n\theta e^{-iN\omega_I t} \times\left(\cos^2\theta+e^{-i\Omega t}\sin^2\theta\right)^{N-1-n}e^{-ist}\sin\left[\chi_2 t\sin\theta\sqrt{N}\right]. \tag{12.61b}$$

If $\theta \ll 1$, we find

$$\left|c_{n0}^{N}(t)\right|^2 \approx C_n^N\left(\frac{2\chi_1^2}{\delta_1^2}\right)^n[1-\cos(\delta_1 t)]^n\exp\left[-2(N-n)\frac{\chi_1^2}{\delta_1^2}[1-\cos(\delta_1 t)]\right]\cos^2(\chi_{RN}t), \tag{12.62a}$$

$$\left|c_{n1}^{N}(t)\right|^2 \approx C_n^N\left(\frac{2\chi_1^2}{\delta_1^2}\right)^n[1-\cos(\delta_1 t)]^n\exp\left[-2(N-n-1)\frac{\chi_1^2}{\delta_1^2}[1-\cos(\delta_1 t)]\right]\sin^2(\chi_{RN}t). \tag{12.62b}$$

For $2N\chi_1^2/\delta_1^2 > 1$, the probabilities consist of a number of spikes under the envelope of the collective Rabi oscillations. For $n \ll 2N\chi_1^2/\delta_1^2$, the spikes are centered near $\delta_1 t = 2m\pi$, for integer m, but for $n \gg 2N\chi_1^2/\delta_1^2$, they are centered at $\delta_1 t = (2m+1)\pi$. This feature is seen in Fig. 12.9 where $\left|c_{n1}^N\right|^2$ is plotted as a function of $\chi_{RN}t$ for $\chi_1 = \chi_2 = 1$, $\delta_1 = -\delta_2 = 50$, $N = 10000$, and $n = 0, 16$.

In a typical experiment there is a read-out pulse following the excitation pulses applied at a time where all intermediate state populations have decayed. For large N, it is a fairly good approximation to assume that all the decay is confined to the fully symmetric states, provided the number of excited states $n_2 \ll N$ [112]. In that limit, the observed signal is proportional to the total Rydberg population P_R following the excitation pulse given by

$$P_R = \sum_{n=0}^{N-1}\left|c_{n1}^{N}(t)\right|^2 \approx \sin^2(\chi_{RN}t). \tag{12.63}$$

In some sense, this is a justification for the two-level approximation that is used to model this system. However, Eq. (12.63) is valid only when inequalities (12.57) hold. In the appendix, it is shown that an approximate solution giving first order corrections in χ_2/δ_1 is [113]

$$P_R \approx \sin^2(\chi_{RN}t) - \frac{\chi_{RN}}{\delta_1}\sin(\delta_1 t)\sin(2\chi_{RN}t), \tag{12.64}$$

assuming that $\delta_1 \gg \chi_{RN}$. Most of the modulation seen in Fig. 12.9 is now gone, but there remains

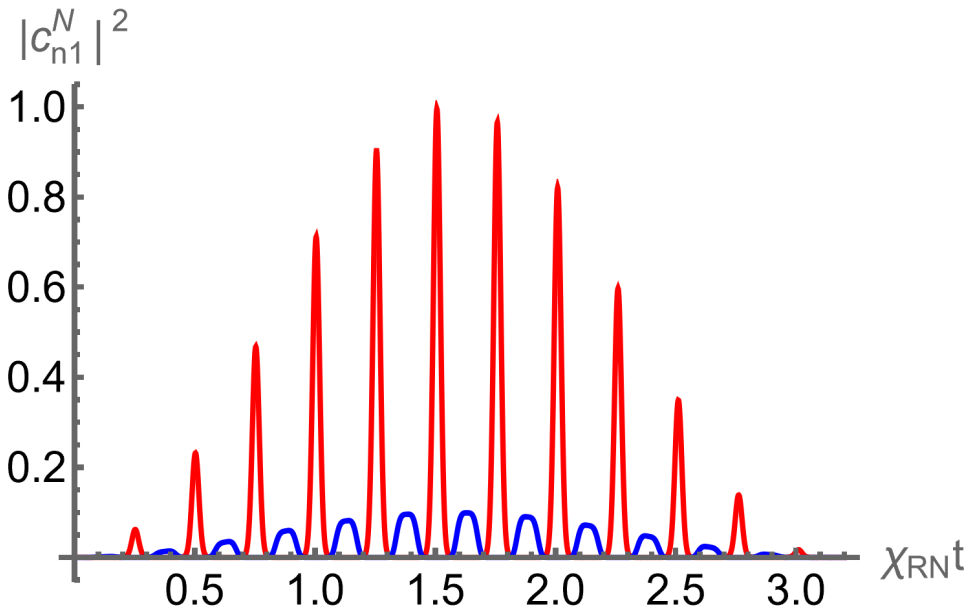

Figure 12.9: Graph of $\left|c^N_{n1}(t)\right|^2$ as a function of $\chi_{RN}t$ for $\chi_1 = \chi_2 = 1$, $\delta_1 = -\delta_2 = 50$, $N = 10000$, and $n = 0$ (large red spikes) and $n = 16$ (smaller blue peaks).

a small component of the signal which is modulated at frequency δ_1. This modulation can be seen in Fig. 12.10.

12.4.2 Adiabatic Dressed States

As long as $|\delta_1 T_p| \gg 1$ for the Gaussian pulse envelope of Eq. (12.5), we can use time-dependent adiabatic dressed states defined as in Eqs. (12.43), but with time-dependent $\theta(t)$. The evolution equations will be given by Eq. (12.51), if Ω, θ, and χ_2 are replaced by their time-dependent values, provided terms of order $\dot{\theta}(t) \approx |\delta_1 T_p| \ll 1$ can be neglected. The use of adiabatic dressed states changes things dramatically since the only adiabatic dressed state that is occupied at $t = -\infty$ is the $n = q = 0$ state (see Fig. 12.11). As time evolves the ensemble stays mainly in the lowest state of each ladder, with a contribution to the light shifts from the first excited state of each ladder. Thus, we get an excellent approximation to the exact result by considering only the two lowest states of each ladder (or even just the lowest states, with the second states adiabatically eliminated). Moreover following the pulse, all amplitudes except c^{Nd}_{00} and c^{Nd}_{01} go to zero. The adiabatic solution is generally valid for smooth pulses, provided

$$\Omega(t)T_p = \sqrt{\delta_1^2 + [\chi_1(t)]^2}T_p \gg 1; \tag{12.65}$$

that is, it is not restricted to values $[\chi_1(t)]^2/\delta_1^2 \ll 1$. Considering only the lowest two states [and

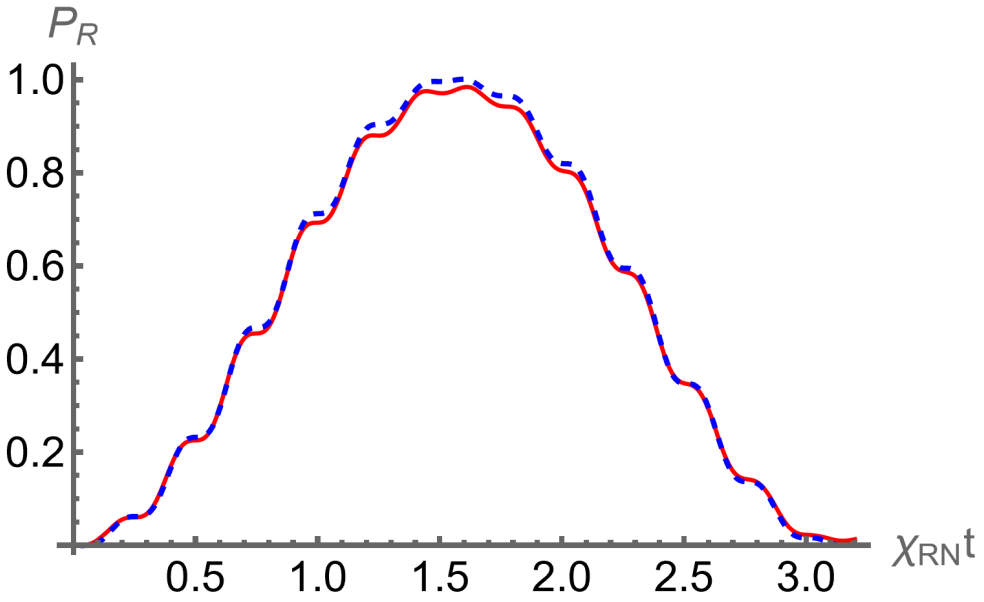

Figure 12.10: Graph of the total Rydberg population $P_R(t)$ as a function of $\chi_{RN}t$ for $\chi_1 = \chi_2 = 1$, $\delta_1 = -\delta_2 = 50$, and $N = 10000$. The exact (solid red curve) and approximate solution from Eq. (12.64) (dashed blue curve) are shown.

subtracting out an energy as in Eqs. (12.33)], we adiabatically eliminate the second state in the first ladder using

$$\tilde{c}_{10}^{Nd}(t) = -\frac{\chi_2(t)\cos\left[\theta(t)\right]\tilde{c}_{01}^{Nd}(t)}{\Omega(t)}, \tag{12.66}$$

leading to evolution equations for the lower state amplitudes [114]

$$d\tilde{c}_{00}^{Nd}/dt = -i\sqrt{N}\sin\left[\theta(t)\right]\chi_2(t)\tilde{c}_{01}^{Nd}, \tag{12.67a}$$

$$d\tilde{c}_{01}^{Nd}dt = -i\sqrt{N}\sin\left[\theta(t)\right]\chi_2(t)\tilde{c}_{00}^{Nd} - i\left[(\delta_1+\delta_2) - \omega_I(t) + \frac{\left[\chi_2(t)\cos\left[\theta(t)\right]\right]^2}{\Omega(t)}\right]\tilde{c}_{01}^{Nd}. \tag{12.67b}$$

Equations (12.67) lead to results that agree with the exact results when $|\delta_1 T_p| \gg 1$. This is true even when the inequalities (12.7) are violated. There is no modulation at frequency δ_1 in the adiabatic result. For the Gaussian pulse envelope of Eq. (12.5), in Fig. 12.12, we plot $\left|c_{01}^{N}(\infty)\right|^2 = \left|\tilde{c}_{01}^{Nd}(\infty)\right|^2$ as a function of $\chi_{RN}T/\sqrt{2}$ for $\chi_1 = 30$, $\chi_2 = 2$, $\delta_1 = -\delta_2 = 50$, $N = 100$, and compare it with the exact solution. The blue, dashed curve is the adiabatic solution and the red solid curve is the exact solution - as can be seen, they agree perfectly, even though $\chi_1/\delta_1 = 0.6$.

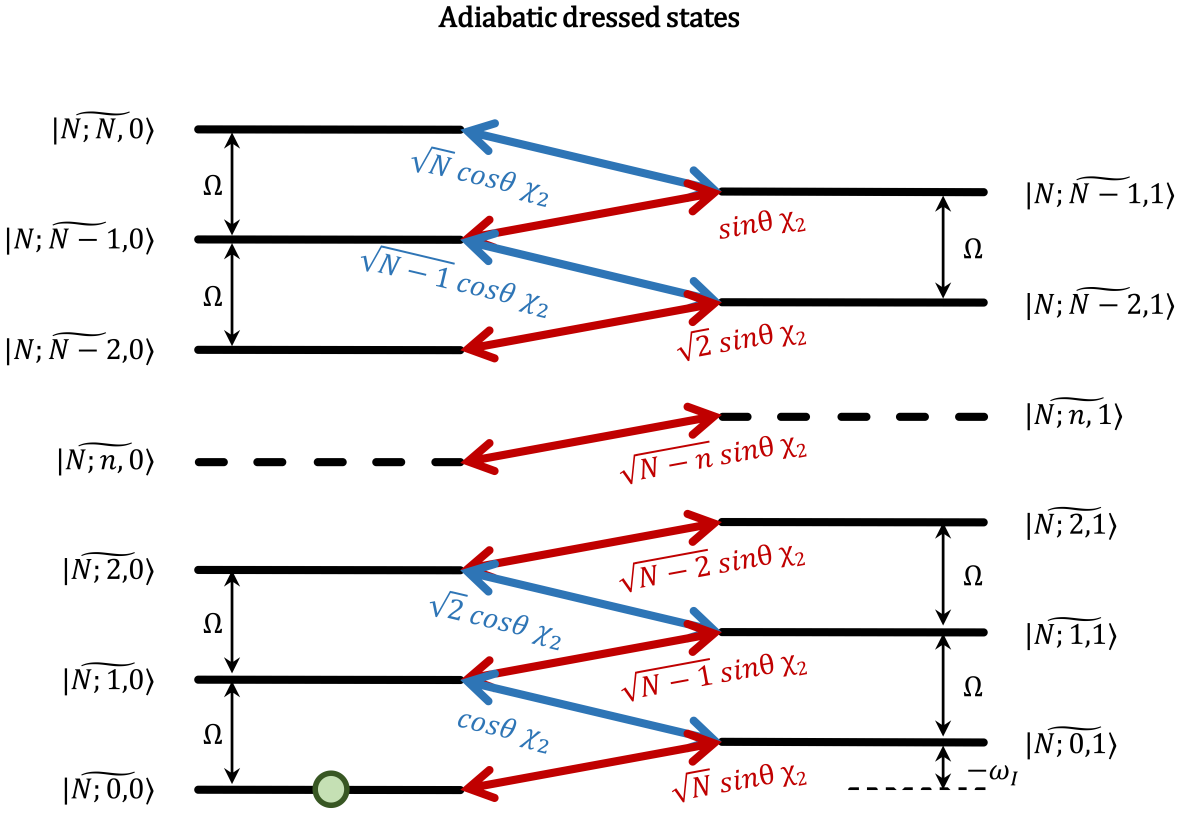

Figure 12.11: Fully-symmetric collective dressed state levels for adiabatic, time-dependent fields when $\delta_1 + \delta_2 = 0$. In contrast to the constant amplitude dressed ladders, the only state populated initially is the $|\widetilde{N;0,0}\rangle$ state and the only final states populated are $|\widetilde{N;0,0}\rangle$ and $|\widetilde{N;0,1}\rangle$. Although not indicated explicitly, χ_1, χ_2, Ω, and θ are functions of time.

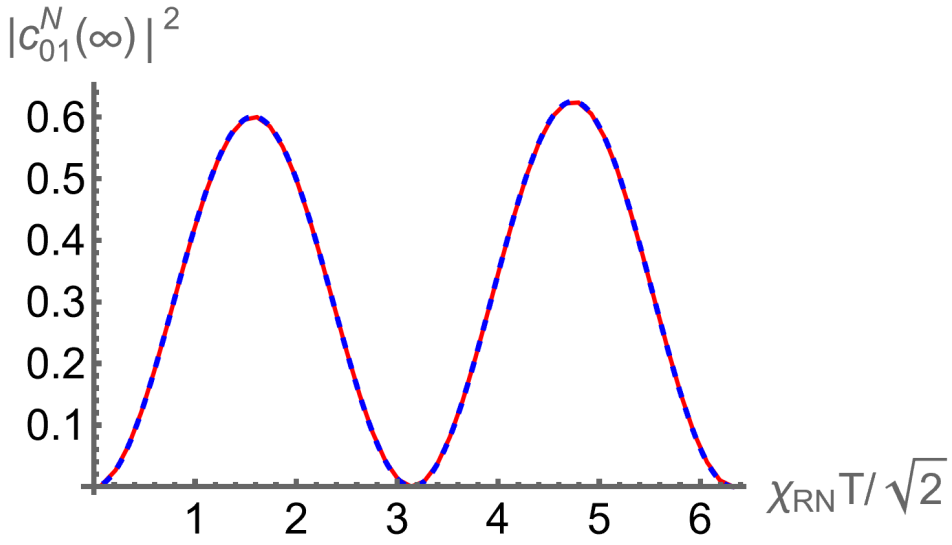

Figure 12.12: Graph of $\left|c_{01}^{N}(\infty)\right|^2$ as a function of $\chi_{RN}T/\sqrt{2}$ for $\chi_1 = 30$, $\chi_2 = 2$, $\delta_1 = -\delta_2 = 50$, and $N = 100$. The blue, dashed curve is the adiabatic solution and the red solid curve is the exact solution.

12.5 Effective Hamiltonian and the Holstein-Primakoff Transformation

The Hamiltonian that gives rise to the evolution Eqs. (12.26) is

$$\begin{aligned}
H = {} & \hbar \sum_{n,q} \left[n\delta_1 + q\left(\delta_1 + \delta_2\right) \right] |N;n,q\rangle \langle N;n,q| \\
& + \hbar\chi_1(t) \sum_{n=0}^{N-q+1} \sqrt{n\left(N-n-q+1\right)}\, |N;n,q\rangle \langle N;n-1,q| \\
& + \hbar\chi_1(t) \sum_{n=0}^{N-q} \sqrt{(n+1)\left(N-n-q\right)}\, |N;n,q\rangle \langle N;n+1,q| \\
& + \hbar\chi_2(t) \sum_{q=0}^{N-n} \sqrt{n\left(q+1\right)}\, |N;n,q\rangle \langle N;n-1,q+1| \\
& + \hbar\chi_2(t) \sum_{q=0}^{N-n} \sqrt{q\left(n+1\right)}\, |N;n,q\rangle \langle N;n+1,q-1|
\end{aligned} \tag{12.68}$$

and is exact. However in the limit that $N \gg n, q, 1$, it reduces to

$$\begin{aligned} H \approx & -\hbar \sum_{n,q} \left[n\delta_1 + q\left(\delta_1 + \delta_2\right) \right] |N; n, q\rangle \langle N; n, q| \\ & + \hbar\chi_1(t)\sqrt{N} \sum_{n} \left(\sqrt{n}\, |N; n, q\rangle \langle N, n-1, q| + \sqrt{(n+1)}\, |N; n, q\rangle \langle N; n+1, q| \right) \\ & + \hbar\chi_2(t) \sum_{q} \left(\begin{array}{c} \sqrt{n\left(q+1\right)}\, |N; n, q\rangle \langle N; n-1, q+1| \\ +\sqrt{q\left(n+1\right)}\, |N; n, q\rangle \langle N; n+1, q-1| \end{array} \right). \end{aligned} \tag{12.69}$$

This a Hamiltonian for coupled oscillators, in which one of the oscillators is driven by an incident field. That is, if the ladder operators for each oscillator are denoted by a and b, then

$$\begin{aligned} H \approx & \hbar \left[\delta_1 a^\dagger a + \left(\delta_1 + \delta_2\right) b^\dagger b \right] \\ & + \hbar\chi_1(t)\sqrt{N} \left(a + a^\dagger \right) \\ & + \hbar\chi_2(t) \left(a^\dagger b + b^\dagger a \right). \end{aligned} \tag{12.70}$$

Since these correspond to linear oscillators, there can be no nonlinear effects. To simulate the blockade we must truncate the b oscillator. That is we replace b by $\sigma_- = |1\rangle \langle 3|$, $b^\dagger$ by $\sigma_+ = |3\rangle \langle 1|$, and $b^\dagger b$ by $\sigma_+\sigma_- = |3\rangle \langle 3| = \sigma_{33}$, yielding

$$\begin{aligned} H \approx & \hbar \left[\delta_1 a^\dagger a + \left(\delta_1 + \delta_2\right) \sigma_{33} \right] \\ & + \hbar\chi_1(t)\sqrt{N} \left(a + a^\dagger \right) \\ & + \hbar\chi_2(t) \left(a^\dagger \sigma_- + \sigma_+ a \right), \end{aligned} \tag{12.71}$$

which corresponds to an oscillator driven by an off-resonant field that is coupled to a two-level atom. The excited state of the "two-level" atom is actually the collective Rydberg state.

The equation of motion for a is

$$\dot{a} = -i\delta_1 a - i\chi_1(t)\sqrt{N} - i\chi_2(t)\sigma_-. \tag{12.72}$$

The adiabatic solution of this equation is

$$a = -\frac{\chi_1(t)\sqrt{N} + \chi_2(t)\sigma_-}{\delta_1}. \tag{12.73}$$

Note that the adiabatic solution might fail when $\frac{[\chi_1(t)]^2 T}{\delta_1} > 1$.

The equations for the atomic operators are

$$\dot{\sigma}_{11} = i\chi_2(t)\left[\sigma_+ a - a^\dagger \sigma_-\right], \tag{12.74a}$$

$$\dot{\sigma}_{33} = -i\chi_2(t)\left[\sigma_+ a - a^\dagger \sigma_-\right], \tag{12.74b}$$

$$\dot{\sigma}_+ = i\left(\delta_1 + \delta_2\right)\sigma_+ - i\chi_2(t) a^\dagger \left[\sigma_{33} - \sigma_{11}\right], \tag{12.74c}$$

$$\dot{\sigma}_- = -i\left(\delta_1 + \delta_2\right)\sigma_- + i\chi_2(t)\left[\sigma_{33} - \sigma_{11}\right] a, \tag{12.74d}$$

where $\sigma_{11} = \sigma_-\sigma_+ = |1\rangle\langle 1|$. If we insert the solution (12.73) for a in these equations, we find

$$\dot{\sigma}_{11} = -i\frac{\chi_2(t)\chi_1(t)\sqrt{N}}{\delta_1}\left[\sigma_+ - \sigma_-\right], \tag{12.75a}$$

$$\dot{\sigma}_{33} = i\frac{\chi_2(t)\chi_1(t)\sqrt{N}}{\delta_1}\left[\sigma_+ - \sigma_-\right], \tag{12.75b}$$

$$\dot{\sigma}_+ = i\left(\delta_1 + \delta_2\right)\sigma_+ + i\frac{\chi_2(t)\chi_1(t)\sqrt{N}}{\delta_1}\left[\sigma_{33} - \sigma_{11}\right] - i\frac{\left[\chi_2(t)\right]^2}{\delta_1}\sigma_+, \tag{12.75c}$$

$$\dot{\sigma}_- = \left(\dot{\sigma}_+\right)^\dagger. \tag{12.75d}$$

These equations suggest that there is no level shift associated with the field χ_1, but this can be traced to the neglect of q in going from Eq. (12.68) to (12.69), under the assumption that $N \gg q$ (see below).

Suppose we want to find corrections to the excited state population resulting from multiple level 2 excitations. If we want to estimate corrections, we can look only at terms in the Hamiltonian related to the χ_1 field and drop the q terms in the Hamiltonian. In this limit

$$\begin{aligned} H = {} & \hbar\sum_n n\delta_1 |N;n\rangle\langle N;n| \\ & + \hbar\chi_1(t)\sum_{n=0}^{N-q+1}\sqrt{n\left(N-n+1\right)}\,|N;n\rangle\langle N;n-1| \\ & + \hbar\chi_1(t)\sum_{n=0}^{N-q}\sqrt{\left(n+1\right)\left(N-n\right)}\,|N;n\rangle\langle N;n+1|. \end{aligned} \tag{12.76}$$

We convert this to operators by replacing n by $a^\dagger a$ to arrive at

$$H \approx \hbar\delta_1 a^\dagger a + \hbar\chi_1(t)\sqrt{N}\left(\sqrt{\left(1-\frac{a^\dagger a}{N}\right)}a + a^\dagger\sqrt{\left(1-\frac{a^\dagger a}{N}\right)}\right), \tag{12.77}$$

where we have neglected terms of order $1/N$. This result has essentially the same form as the

Holstein-Primakoff (HP) transformation [109]. If we expand to lowest order, then

$$\begin{aligned} H \sim & \hbar\delta_1 a^\dagger a + \hbar\chi_1(t)\sqrt{N}\left(a + a^\dagger\right) \\ & - \hbar\chi_1(t)\frac{1}{2\sqrt{N}}\left(a^\dagger a a + a^\dagger a^\dagger a\right) \end{aligned} \tag{12.78}$$

Including the interaction with the second field

$$\begin{aligned} H \approx & \hbar\delta_1 a^\dagger a + \hbar\chi_1(t)\sqrt{N}\left(a + a^\dagger\right) \\ & - \hbar\chi_1(t)\frac{1}{2\sqrt{N}}\left(a^\dagger a a + a^\dagger a^\dagger a\right) \\ & + \hbar\chi_2(t)\left(a^\dagger\sigma_- + \sigma_+ a\right). \end{aligned} \tag{12.79}$$

The equation for $\dot{a}$ is

$$\dot{a} = -i\delta_1 a - i\chi_1(t)\sqrt{N} + i\chi_1(t)\frac{1}{2\sqrt{N}}\left(a^2 + 2a^\dagger a\right) - i\chi_2(t)\sigma_-. \tag{12.80}$$

One possibility is to put the adiabatic solution

$$a = -\frac{\chi_1(t)\sqrt{N} + \chi_2(t)\sigma_-}{\delta_1}. \tag{12.81}$$

in the third term and neglect the $\chi_2(t)\sigma_-$ term. Then

$$\dot{a} \approx -i\delta_1 a - i\chi_1(t)\sqrt{N}\left(1 - \frac{3}{2}\frac{\chi_1^2(t)}{\delta_1^2}\right) - i\chi_2(t)\sigma_-, \tag{12.82}$$

such that

$$a \approx -\frac{\chi_1(t)\sqrt{N}\left(1 - \frac{3}{2}\frac{\chi_1^2(t)}{\delta_1^2}\right) + \chi_2(t)\sigma_-}{\delta_1}. \tag{12.83}$$

As a consequence, the coupling is modified as

$$\sqrt{N}\frac{\chi_2(t)\chi_1(t)}{\delta_1} \to \sqrt{N}\frac{\chi_2(t)\chi_1(t)}{\delta_1}\left(1 - \frac{3}{2}\frac{\left[\chi_1(t)\right]^2}{\delta_1^2}\right), \tag{12.84}$$

consistent with the lowest order correction to the coupling in the adiabatic model given in Eq. (12.67).

The use of the HP approximation does not simplify the calculation. However, if the light shifts are negligible, it does provide a simple justification for the two-level model. The Hamiltonian of Eq. (12.71) can be viewed as the lowest order approximation to the HP transformation. Equation

(12.71) led to Eqs. (12.75). If the light shifts are neglected in Eqs. (12.75) and expectation values are taken, one arrives at density matrix equations consistent with the two-level approximation. In other words, the Heisenberg operator approach of the HP transformation allows one to arrive at expressions for the *total* Rydberg population without regard to the *individual* state populations of the ladder states.

12.5.0.1 How to include the light shift from the first field

Even with corrections, the Hamiltonian given by Eq. (12.79) does not contain the light shifts produced by field 1. The reason for this is clear. In the dressed basis, there are two ladders and the $q = 1$ ladder is shifted slightly from the $q = 0$ ladder. There is no analogous term in HP since we have assumed that $N \gg q$;, in effect, we treat $q = 0$ and $q = 1$ in the same manner. Thus to include the light shift in HP, we must somehow account for the q dependence. To do so we expand

$$\sqrt{n\left(N-n-q+1\right)} \approx \sqrt{nN} - \frac{q\sqrt{n}}{2\sqrt{N}} \tag{12.85}$$

As a consequence, the effective Hamiltonian given in Eq. (12.79) is replaced by

$$\begin{aligned} H \approx \hbar & \left[\delta_1 a^\dagger a + \left(\delta_1 + \delta_2 - \frac{\chi_1(t)\left(a + a^\dagger\right)}{2\sqrt{N}}\right) b^\dagger b\right] \\ & + \hbar\chi_1(t)\sqrt{N}\left(a + a^\dagger\right) \\ & + \hbar\chi_2(t)\left(a^\dagger b + b^\dagger a\right). \end{aligned} \tag{12.86}$$

If, in lowest approximation for large N, we replace $\left(a + a^\dagger\right)$ in the frequency term by

$$\left(a + a^\dagger\right) \approx -\frac{2\chi_1(t)\sqrt{N}}{\delta_1}, \tag{12.87}$$

then the effective Hamiltonian becomes

$$\begin{aligned} H \approx \hbar & \left[\delta_1 a^\dagger a + \left(\delta_1 + \delta_2 + \frac{\left[\chi_1(t)\right]^2}{\delta_1}\right) b^\dagger b\right] \\ & + \hbar\chi_1(t)\sqrt{N}\left(a + a^\dagger\right) \\ & + \hbar\chi_2(t)\left(a^\dagger b + b^\dagger a\right). \end{aligned} \tag{12.88}$$

We then proceed as before, so that the effective equations for the atomic operators are

$$\dot{\sigma}_{11} = -i\frac{\chi_2(t)\chi_1(t)}{\delta_1}\sqrt{N}\left[\sigma_+ - \sigma_-\right] \tag{12.89a}$$

$$\dot{\sigma}_{33} = i\chi_2(t)\left[\sigma_+ - \sigma_-\right] \tag{12.89b}$$

$$\dot{\sigma}_+ = i\left(\delta_1 + \delta_2 + \frac{\left[\chi_1(t)\right]^2}{\delta_1}\right)\sigma_+ + i\chi_2(t)\left[\sigma_{33} - \sigma_{11}\right] - i\frac{\left[\chi_2(t)\right]^2}{\delta_1}\sigma_+ \tag{12.89c}$$

$$\dot{\sigma}_- = \left(\dot{\sigma}_+\right)^\dagger. \tag{12.89d}$$

Now the light shifts from both fields are included. Moreover, if we also include the corrections to the coupling term given by Eq. (12.84), the HP and dressed state approaches are in excellent agreement in the limit that inequalities (12.7) hold.

12.6 Conclusions

We have presented a detailed theory of the Rydberg blockade, including contributions from multiple intermediate state excitations. It has been shown that a dressed state approach offers distinct advantages when multiple intermediate state excitations occur. In the case of fixed amplitude fields, the multiple intermediate excitations can result in comb-like modulated populations of *individual* states having one Rydberg excitation and $n \ll N$ intermediate state excitations. However, when summed over *all* such state populations, most of the modulation disappears and the system is described to a good approximation by an effective two-level model. In the case of adiabatic, pulsed fields, there is no such modulation and an effective two-level model (in the dressed basis), corrected for light shifts, can be used to model the system. The calculation has been restricted to fully symmetric (phased) states containing at most one Rydberg excitation. Spontaneous decay from the intermediate state will couple these states to states outside the symmetric subspace, but such effects are expected to provide only small corrections provided the number of excited states $n \ll N$ and $\left(\chi_1^2/\delta_1^2\right)\gamma_2 T \ll 1$. In other words, as was the case for the light shifts, there are no collective decay rates proportional to N that contribute to the signal [115]. In addition to solving this problem using conventional methods, we have shown that similar results could be obtained using a form of the Holstein-Primakoff transformation. Given the state of the art of current experiments involving atoms in lattices, it may be possible to test some of our predictions concerning the role of multiple intermediate excitations.

We would like to thank A. Kuzmich for helpful discussions. This research of PRB and HN is supported by the Air Force Office of Scientific Research and the National Science Foundation.

12.7 Appendix

We can improve upon the lowest order solution for the dressed state amplitudes by expanding the subspace for n excitations from two to six levels. That is, we look at a truncated subspace for dressed state amplitudes

$$\boldsymbol{b}_n^{Nd} = [b_{n0}^{Nd}, b_{n1}^{Nd}, \tilde{b}_{n+1,0}^{Nd}, \tilde{b}_{n+1,1}^{Nd}, \tilde{b}_{n-1,0}^{Nd}, \tilde{b}_{n-1,1}^{Nd}] \tag{12.90}$$

with

$$\tilde{b}_{n+1,0}^{Nd} = e^{-i\Omega t} b_{n+1,0}^{Nd}, \quad \tilde{b}_{n+1,1}^{Nd} = e^{-i\Omega t} b_{n+1,1}^{Nd}, \tag{12.91a}$$

$$\tilde{b}_{n-1,0}^{Nd} = e^{i\Omega t} b_{n-1,0}^{Nd}, \quad \tilde{b}_{n-1,1}^{Nd} = e^{i\Omega t} b_{n-1,1}^{Nd}. \tag{12.91b}$$

We truncate the space by considering *only* these amplitudes, which obey the matrix equation

$$i\hbar \dot{\boldsymbol{b}}_n^{Nd} = \boldsymbol{H}_n \boldsymbol{b}_n^{Nd}, \tag{12.92}$$

subject to the initial conditions $\boldsymbol{b}_n^{Nd}(0) = [b_{n0}^{Nd}(0),0,b_{n+1,0}^{Nd}(0), 0, b_{n-1,0}^{Nd}(0), 0]$ with

$$H_n = \hbar \begin{pmatrix} 0 & \chi(n,N) & 0 & 0 & 0 & \chi(n) \\ \chi(n,N) & \sigma & \chi(n+1) & 0 & 0 & 0 \\ 0 & \chi(n+1) & \Omega & \chi(n+1,N) & 0 & 0 \\ 0 & 0 & \chi(n+1,N) & \Omega+\sigma & 0 & 0 \\ 0 & 0 & 0 & 0 & -\Omega & \chi(n-1,N) \\ \chi(n) & 0 & 0 & 0 & \chi(n-1,N) & -\Omega+\sigma \end{pmatrix}, \tag{12.93}$$

where

$$\chi(n,N) = \chi_2 \sin\theta \sqrt{(N-n)},$$
$$\chi(n) = \sqrt{n}\chi_2 \cos\theta,$$

and

$$\sigma = \delta_1 + \delta_2 - \omega_I \tag{12.94}$$

The formal solution of Eq. (12.92) is

$$\boldsymbol{b}_n^{Nd}(t) = e^{-i\boldsymbol{H}_n t/\hbar} \boldsymbol{b}_n^{Nd}(0) \tag{12.95}$$

which can be evaluated numerically. In this truncated subspace the resulting solution is valid *only* for $b_{n0}^{Nd}(t)$ and $b_{n1}^{Nd}(t)$ and this solution provides an excellent approximation to the exact solution provided

$$\frac{\chi_2}{\delta_1} n \approx \frac{\Omega_1^2 \chi_2}{\delta_1^3} N \ll 1. \tag{12.96}$$

In fact, when this inequality holds, a first approximation can be obtained by considering only the $[b_{n0}^{Nd}, b_{n1}^{Nd}]$ subspace. For $N \gg n$, the analytic solution of Eq. (12.92) in this limited subspace is

$$\begin{aligned} b_{n0}^{Nd}(t) &= b_{n0}^{Nd}(0) e^{-i\sigma t/2} \cos\left(\frac{\sqrt{4\chi_{RN}^2 + \sigma^2}}{2} t\right) \\ &\quad + i b_{n0}^{Nd}(0) e^{-i\sigma t/2} \frac{\sigma}{\sqrt{4\chi_{RN}^2 + \sigma^2}} \sin\left(\frac{\sqrt{4\chi_{RN}^2 + \sigma^2}}{2} t\right), \end{aligned} \tag{12.97a}$$

$$b_{n1}^{Nd}(t) = i b_{n0}^{Nd}(0) e^{-i\sigma t/2} \frac{2\chi_{RN}}{\sqrt{4\chi_{RN}^2 + \sigma^2}} \sin\left(\frac{\sqrt{4\chi_{RN}^2 + \sigma^2}}{2} t\right). \tag{12.97b}$$

In this approximation, the total population P_R in the Rydberg ladder is equal to

$$P_R = \sum_{n=0}^{N-1} \left|b_{n1}^{Nd}(t)\right|^2 \approx \sum_{n=0}^{N} \left|b_{n1}^{Nd}(t)\right|^2 = \frac{4\chi_{RN}^2}{4\chi_{RN}^2 + \sigma^2} \sin\left(\frac{\sqrt{4\chi_{RN}^2 + \sigma^2}}{2} t\right) \tag{12.98}$$

and does not exhibit modulation at frequency δ_1.

In order to see if P_R can exhibit modulation at frequency δ_1, we must obtain corrections of order χ_2/δ_1. An approximate analytic solution to Eq. (12.92) can be obtained in the limit that

$$\frac{\chi_1^2}{\delta_1^2} \ll 1; \qquad |\sigma| \approx \left|\delta_1 + \delta_2 + \frac{\chi_1^2}{\delta_1^2}\right| \ll \chi_{RN}; \qquad N \gg n, \tag{12.99}$$

for which

$$\boldsymbol{H}_n \approx \hbar \begin{pmatrix} 0 & -\chi_{RN} & 0 & 0 & 0 & \sqrt{n}\chi_2 \\ -\chi_{RN} & \sigma & \sqrt{n+1}\chi_2 & 0 & 0 & 0 \\ 0 & \sqrt{n+1}\chi_2 & \delta_1 & -\chi_{RN} & 0 & 0 \\ 0 & 0 & -\chi_{RN} & \delta_1 + \sigma & 0 & 0 \\ 0 & 0 & 0 & 0 & -\delta_1 & -\chi_{RN} \\ \sqrt{n}\chi_2 & 0 & 0 & 0 & -\chi_{RN} & -\delta_1 + \sigma \end{pmatrix}. \tag{12.100}$$

To obtain the state amplitudes in this limit, we first use degenerate perturbation theory to diagonal-

ize the (nearly) degenerate $\left\{b_{n0}^{Nd}, b_{n1}^{Nd}\right\}$ sub-block. If $\chi_{RN} \gg |\sigma|$, the eigenvectors are then given approximately by

$$|\mu 0\rangle' \approx \frac{1}{\sqrt{2}}\left(|\mu 0\rangle + |\mu 1\rangle\right), \tag{12.101a}$$

$$|\mu 1\rangle' \approx \frac{1}{\sqrt{2}}\left(|\mu 0\rangle - |\mu 1\rangle\right), \tag{12.101b}$$

($\mu = n, n \pm 1$) and the transformed matrix by

$$\boldsymbol{H}_n'' \approx \hbar \begin{pmatrix} \frac{\sigma}{2} - \chi_{RN} & 0 & \sqrt{n+1}\frac{\chi_2}{2} & \sqrt{n+1}\frac{\chi_2}{2} & \sqrt{n}\frac{\chi_2}{2} & -\sqrt{n}\frac{\chi_2}{2} \\ 0 & \frac{\sigma}{2} + \chi_{RN} & -\sqrt{n+1}\frac{\chi_2}{2} & -\sqrt{n+1}\frac{\chi_2}{2} & \sqrt{n}\frac{\chi_2}{2} & -\sqrt{n}\frac{\chi_2}{2} \\ \sqrt{n+1}\frac{\chi_2}{2} & -\sqrt{n+1}\frac{\chi_2}{2} & \frac{\sigma}{2} + \delta_1 - \chi_{RN} & 0 & 0 & 0 \\ \sqrt{n+1}\frac{\chi_2}{2} & -\sqrt{n+1}\frac{\chi_2}{2} & 0 & \frac{\sigma}{2} + \delta_1 + \chi_{RN} & 0 & 0 \\ \sqrt{n}\frac{\chi_2}{2} & \sqrt{n}\frac{\chi_2}{2} & 0 & 0 & \frac{\sigma}{2} - \delta_1 - \chi_{RN} & 0 \\ -\sqrt{n}\frac{\chi_2}{2} & -\sqrt{n}\frac{\chi_2}{2} & 0 & 0 & 0 & \frac{\sigma}{2} - \delta_1 + \chi_{RN} \end{pmatrix} \tag{12.102}$$

We now use non-degenerate perturbation theory, assuming that $\delta_1 \gg \chi_{RN}$, to obtain the eigenenergies,

$$E_1'' \approx \hbar\left(-\chi_{RN} + s\right); \quad E_2'' \approx \hbar\left(\chi_{RN} + s\right), \tag{12.103a}$$

$$E_{3n}'' \approx \hbar\left(s + \delta_1 - \chi_{RN} + \frac{(n+2)\,\chi_2^2}{\delta_1}\right), \tag{12.103b}$$

$$E_{4n}'' \approx \hbar\left(s + \delta_1 + \chi_{RN} + \frac{(n+2)\,\chi_2^2}{\delta_1}\right), \tag{12.103c}$$

$$E_{5n}'' \approx \hbar\left(s - \delta_1 - \chi_{RN} - \frac{(n-1)\,\chi_2^2}{\delta_1}\right), \tag{12.103d}$$

$$E_{6n}'' \approx \hbar\left(s - \delta_1 + \chi_{RN} - \frac{(n-1)\,\chi_2^2}{\delta_1}\right), \tag{12.103e}$$

where

$$s = \frac{\chi_1^2}{2\delta_1} - \frac{\chi_2^2}{2\delta_1} + \frac{\delta_1 + \delta_2}{2}. \tag{12.104}$$

The eigenkets associated with these eigenenergies are given approximately by [113]

$$|n0\rangle^{''} \approx |n0\rangle' \approx \frac{1}{\sqrt{2}}\left(|n0\rangle + |n1\rangle\right), \tag{12.105a}$$

$$|n1\rangle'' \approx |n1\rangle' \approx \frac{1}{\sqrt{2}}\left(|n0\rangle - |n1\rangle\right), \tag{12.105b}$$

$$\begin{aligned}|n+1,0\rangle'' &\approx |n+1,0\rangle' + \sqrt{n+1}\frac{\chi_2}{2\delta_1}\left(|n0\rangle' - |n1\rangle'\right)\\ &= \frac{1}{\sqrt{2}}\left(|n+1,0\rangle + |n+1,1\rangle\right) + \sqrt{n+1}\frac{\chi_2}{\sqrt{2}\delta_1}|n1\rangle,\end{aligned} \tag{12.105c}$$

$$\begin{aligned}|n+1,1\rangle'' &\approx |n+1,1\rangle' + \sqrt{n+1}\frac{\chi_2}{2\delta_1}\left(|n0\rangle' - |n1\rangle'\right)\\ &= \frac{1}{\sqrt{2}}\left(|n+1,0\rangle - |n+1,1\rangle\right) + \sqrt{n+1}\frac{\chi_2}{\sqrt{2}\delta_1}|n1\rangle,\end{aligned} \tag{12.105d}$$

$$\begin{aligned}|n-1,0\rangle'' &\approx |n-1,0\rangle' - \sqrt{n}\frac{\chi_2}{2\delta_1}\left(|n0\rangle' + |n1\rangle'\right)\\ &= \frac{1}{\sqrt{2}}\left(|n-1,0\rangle + |n-1,1\rangle\right) - \sqrt{n}\frac{\chi_2}{\sqrt{2}\delta_1}|n0\rangle,\end{aligned} \tag{12.105e}$$

$$\begin{aligned}|n-1,1\rangle'' &\approx |n-1,1\rangle' + \sqrt{n}\frac{\chi_2}{2\delta_1}\left(|n0\rangle' + |n1\rangle'\right)\\ &= \frac{1}{\sqrt{2}}\left(|n-1,0\rangle - |n-1,1\rangle\right) + \sqrt{n}\frac{\chi_2}{\sqrt{2}\delta_1}|n0\rangle\end{aligned} \tag{12.105f}$$

The state vector $|\psi(t)\rangle$ in this subspace is expanded as

$$\begin{aligned}|\psi(t)\rangle = &\left[b_{n0}^{Nd}(0)\right]^{''} e^{i\chi_{RN}t}e^{-ist}|n0\rangle'' + \left[b_{n1}^{Nd}(0)\right]'' e^{-i\chi_{RN}t}e^{-ist}|n1\rangle''\\ &+ \left[b_{n+1,0}^{Nd}(0)\right]'' e^{-i\delta_1 t}|n+1,0\rangle'' + \left[b_{n+1,1}^{Nd}(0)\right]'' e^{-i\delta_1 t}|n+1,1\rangle''\\ &+ \left[b_{n-1,0}^{Nd}(0)\right]'' e^{i\delta_1 t}|n-1,0\rangle'' + \left[b_{n-1,1}^{Nd}(0)\right]'' e^{i\delta_1 t}|n-1,1\rangle''\end{aligned} \tag{12.106}$$

Using the fact that

$$\left[b_{n0}^{Nd}(0)\right]'' \approx \frac{1}{\sqrt{2}}b_{n0}^{Nd}(0) - \sqrt{n+1}\frac{\chi_2}{\sqrt{2}\delta_1}b_{n+1,0}^{Nd}(0), \tag{12.107a}$$

$$\left[b_{nn}^{Nd}(0)\right]'' \approx \frac{1}{\sqrt{2}}b_{n0}^{Nd}(0) + \sqrt{n+1}\frac{\chi_2}{\sqrt{2}\delta_1}b_{n+1,0}^{Nd}(0), \tag{12.107b}$$

$$\left[b_{n+1,0}^{Nd}(0)\right]'' \approx \frac{1}{\sqrt{2}}b_{n+1,0}^{Nd}(0); \quad \left[b_{n+1,1}^{Nd}(0)\right]'' \approx \frac{1}{\sqrt{2}}b_{n+1,0}^{Nd}(0), \tag{12.107c}$$

$$\left[b_{n-1,0}^{Nd}(0)\right]'' \approx \frac{1}{\sqrt{2}}b_{n-1,0}^{Nd}(0); \quad \left[b_{n-1,1}^{Nd}(0)\right]'' \approx \frac{1}{\sqrt{2}}b_{n-1,0}^{Nd}(0), \tag{12.107d}$$

we find the state amplitudes

$$b_{n0}^{Nd}(t) \approx b_{n0}^{Nd}(0)e^{-ist}\cos\left(\chi_{RN}t\right) - ib_{n+1,0}^{Nd}(0)e^{-ist}\frac{\chi_2}{\delta_1}\sqrt{n+1}\sin\left(\chi_{RN}t\right),$$
$$- ib_{n-1,0}^{Nd}(0)\frac{\chi_2}{\delta_1}\sqrt{n}e^{i\delta_1 t}e^{-ist}\sin\left(\chi_{RN}t\right), \tag{12.108a}$$
$$b_{n1}^{Nd}(t) \approx ib_{n0}^{Nd}(0)e^{-ist}\sin\left(\chi_{RN}t\right)$$
$$+ b_{n+1,0}^{Nd}(0)\frac{\chi_2}{\delta_1}\sqrt{n+1}\left(e^{-i\delta_1 t}-1\right)e^{-ist}\cos\left(\chi_{RN}t\right). \tag{12.108b}$$

In writing these equations, we have neglected contributions from the light shifts of field 2 in the correction terms of order χ_2/δ_1. It then follows that the total Rydberg population,

$$P_R \approx \sum_{n=0}^{N}\left|b_{n1}^{Nd}(t)\right|^2 \approx \sin^2\left(\chi_{RN}t\right)$$
$$- \frac{\chi_2}{\delta_1}\sin\left(\delta_1 t\right)\sin\left(2\chi_{RN}t\right)\sum_{n=0}^{N}\sqrt{n+1}b_{n0}^{Nd}(0)b_{n+1,0}^{Nd}(0), \tag{12.109}$$

exhibits modulation at frequency δ_1, with a modulation depth of order χ_2/δ_1. For $\left(\chi_1/\delta_1\right)^2 \ll 1$ and $N \gg 1$,

$$\sum_{n=0}^{N}\sqrt{n+1}b_{n0}^{Nd}(0)b_{n+1,0}^{Nd}(0) \approx 2\frac{\chi_1}{\delta_1}\sqrt{N}. \tag{12.110}$$

CHAPTER 13

Trapped Alkali-metal Rydberg Qubit

Quantum technologies offer transformative advances in storage, processing, and communication of information compared to established classical approaches. The recipe for combining distant quantum processors into a single quantum network involves three key ingredients: qubits, quantum logic for entanglement generation and correction, and interaction interfaces [116, 117]. Neutral atomic ensembles are a strong candidate to serve as a basis for scalable quantum networks [39, 80, 118, 119]. Collective qubits based on atomic hyperfine ground states can be converted, on-demand, into single photons [120], making them well-suited for scalable quantum network-type protocols over telecom-wavelength optical fibers [41, 121]. Notably, collective atomic qubit states between ground and Rydberg states can be deterministically created and coherently manipulated in the regime of the excitation blockade [122, 123, 21, 12, 14, 40, 5, 124, 125], allowing for dramatically faster remote entanglement generation compared with probabilistic approaches [10, 11].

In order to use the Rydberg blockade in quantum information processing, the (optical) ground-Rydberg atomic coherence must be preserved. Ideally, this is achieved if the atoms are confined in a potential $U(\mathbf{r})$ that is identical for the ground and the Rydberg levels. However, in a regular far-off-resonance optical dipole trap, e.g., based on a 1064 nm laser for Rubidium atoms, the spatially inhomogeneous energy shifts $U(\mathbf{r})$ are entirely different for the ground and Rydberg states. For (trapped) ground-level atoms, the dynamic polarizability in a (red-detuned) light field is positive, whereas Rydberg electrons are nearly free, and their polarizability is approximately equal to that of a free electron, which is negative. This means that atoms in Rydberg states are anti-trapped since they are pushed out of the laser field intensity maxima. This problem leads to the necessity of shutting off the trap fields for the duration of quantum operations. The repeated process of turning the trap fields on and off heats the atoms and dramatically shortens their lifetime to μs, limiting its utility [126, 127].

In a state-insensitive (or "magic-wavelength") trap proposal of Refs. [26, 27], the frequency of an optical lattice is tuned to the blue side of an atomic resonance from the Rydberg level to an intermediate level, creating positive polarizability of the Rydberg level. For example, if the (1012 nm) lattice field is detuned by $\simeq (52/n)^3$ GHz from the $|nS_{1/2}\rangle \leftrightarrow |6P_{3/2}\rangle$ transition in atomic

Rb, the depth of the trapping potentials for the ground- and Rydberg-level atoms are approximately equal. This method has been demonstrated by our group [40, 48, 128] and by Goldschmidt *et al.* [28]. More recently, trapped single-atom Rydberg qubits have been demonstrated in alkaline-earth atoms [129].

Here we report observations of dynamics of a Rydberg qubit encoded in an ensemble of $\sim 10^3$ atoms that are confined in a state-insensitive optical lattice trap. We observe coherent driving and Ramsey interference measurements of light shifts induced on either the lower or the upper qubit state, on timescales of order ~ 10 μs. The dynamics of the trapped qubit and the light shifts are well-described by an effective two-level model with possible dephasing factors included, i.e. laser phase noise, atom number fluctuation, and so on. The experimental setup is shown in Fig. 13.1(a). ^{87}Rb atoms are collected in a magneto-optical trap (MOT) and are subsequently loaded into a far-off resonance (YAG, 1064nm) cross-dipole trap. The longitudinal extent of the atomic cloud is ~ 10 μm along the excitation field direction. Next, the atoms are transferred from the cross-dipole trap to a state-insensitive optical lattice. The lattice is formed by a horizontally-polarized and retro-reflected laser field, which is detuned from the $|6P_{3/2}\rangle \leftrightarrow |75S_{1/2}\rangle$ transition by $\Delta_m/2\pi \simeq 367$ MHz - the so-called "magic" value of the detuning for which the potential depths for the ground and the Rydberg atomic states are equal. After the transfer, the lattice depth is adiabatically lowered.

The atoms are driven by laser fields E_1 (780 nm, σ^-) and E_2 (480 nm, σ^+) from the ground state $|g\rangle = |5S_{1/2}, F = 2, m_F = -2\rangle$ to the Rydberg state $|r\rangle = |75S_{1/2}, m_J = -1/2\rangle$ with a detuning of $\Delta/2\pi = 480$ MHz from the intermediate state $|p\rangle = |5P_{3/2}, F = 3, m_F = -3\rangle$, with respective Rabi frequencies Ω_1 and Ω_2, Fig. 13.1(b). In the Rydberg excitation blockade regime, ideally, the atoms will undergo an oscillation between two collective (Dicke) atomic states, $|0\rangle = \prod_{i=1}^{N} |g_i\rangle$ and $|1\rangle = \frac{1}{\sqrt{N}} \sum_{i=1}^{N} e^{i(\mathbf{k_1}+\mathbf{k_2})\cdot\mathbf{r_i} - i(\omega_1+\omega_2)t} |g_1 \ldots r_i \ldots g_N\rangle$, where N is the total number of atoms participating in the many-body blockade. After a controllable delay, T_s, following the excitation pulse, a readout pulse E_r (with Rabi frequency Ω_r) that is resonant with the $|r\rangle$ to $|p\rangle$ transition frequency is applied and leads to phase-matched emission having frequency ω_e (see the Supplementary Material for experimental details).

We model our system as an effective two-level system with a closed-transition between the states $|0\rangle$ and $|1\rangle$. The collective Rabi frequency of this two-state model is $\Omega_N = \sqrt{N}\Omega$, where $\Omega = \frac{\Omega_1\Omega_2}{2\Delta}$ is the effective two-photon, single-atom Rabi frequency. With the two-photon detuning δ set equal to zero, the population of the many-body Rydberg state $|1\rangle$ is $\rho_{11} = \frac{1}{2}(1 - e^{-\frac{\gamma_1}{2}t} \cos\sqrt{N}\Omega\, T_p)$, where T_p is the pulse duration of a constant amplitude pulse whose pulse area is equal to that of the actual pulse. We have incorporated dephasing from relaxation processes such as that produced by laser frequency noise into our model by assuming that the coherence ρ_{01} decays at rate γ_1, which agrees well with the measured laser linewidth in our system. The intensity of the retrieved signal is proportional to this population.

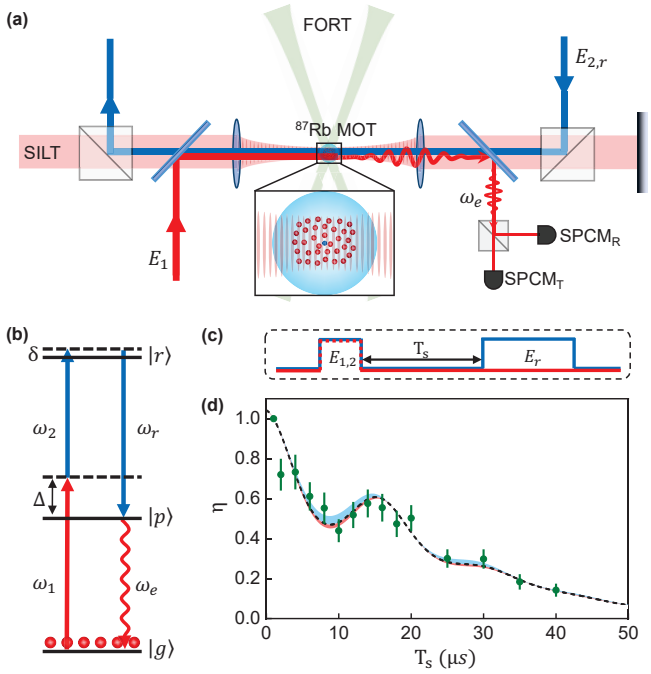

Figure 13.1: (a) Experimental setup: an ultracold ^{87}Rb atomic ensemble is prepared in a one-dimensional state-insensitive lattice trap (SILT) formed by a 1012 nm retro-reflected beam using atoms that have been transferred from a crossed far-off-resonance dipole trap (FORT) formed by focused yttrium aluminum-garnet (YAG) laser beams. Excitation fields E_1 (780 nm) and E_2 (480 nm) drive atoms from $|g\rangle$ to $|p\rangle$ and from $|p\rangle$ to $|r\rangle$, respectively. A retrieval pulse E_r leads to phase-matched emission that is coupled into a pair of single-mode fibers and subsequently measured by single-photon counting modules SPCM$_\mathrm{T}$ and SPCM$_\mathrm{R}$. (b) Single atom energy levels for ^{87}Rb: $|g\rangle = |5S_{1/2}, F = 2, m_F = -2\rangle$, $|p\rangle = |5P_{3/2}, F = 3, m_F = -3\rangle$, and $|r\rangle = |nS_{1/2}, m_J = -1/2\rangle$. (c) Timing sequence for the ground-Rydberg spin-wave coherence measurement. (d) Normalized signal η as a function of storage time T_s for quantum number $n = 75$. The storage efficiency is normalized to that at 1 μs. Blue and red bands represent temperatures 40 % lower and higher than the best-fit value, respectively.

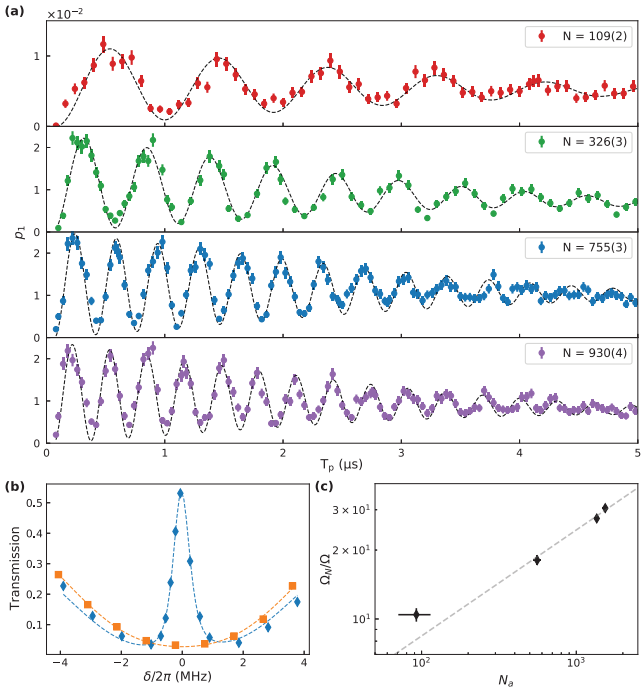

Figure 13.2: (a) Collective Rabi oscillation as function of the pulse duration T_p for different numbers of atoms. Red: $N = 109(2)$; green: $N = 326(3)$; blue: $N = 755(3)$; purple: $N = 930(4)$. Here, $\Omega_1/2\pi = 9.2$ MHz, $\Omega_2/2\pi = 10.8$ MHz, $\Omega_r/2\pi = 11.5$ MHz. The dashed lines are theoretical results using an effective two-state model. The error bars represent one standard deviation ($\sqrt{M}$) for M photoelectric counting events. (b) probe transmission (orange square) and EIT (blue diamond) measurement for $N = 755(9)$, consistent with an OD = 3.5. (c) The enhancement of the collective Rabi frequency Ω_N/Ω as a function of number of atoms N_a determined by the absorption measurement. The data are fit with a function $\Omega_N = \Omega N_a^k$ with the best-fit value $k = 0.463(5)$. The error bars represent the standard errors of the respective fits.

To describe combined effects of spin-wave dephasing and loss of the Rydberg state component, we include an overall exponential damping of the retrieved signal $\sim e^{-\alpha t}$. We account for fluctuations in atomic number by weighting the retrieved signal with the probability distribution $f(k, N)$ to have k atoms in the interaction, volume when the average number in the volume is N. On averaging over k for the Poisson distribution $f(k) = \frac{N^k e^{-N}}{k!}$, we find that the oscillation amplitude is damped by a factor $\exp(-t^2/\tau_1^2)$, where $\tau_1 = 2\sqrt{2}/\Omega$, and that the photoelectric detection probability per trial p_1 for the retrieved signal is given by

$$p_1 \simeq \frac{1}{2}\xi e^{-\alpha T_p}(1 - e^{-\frac{\gamma_1}{2}T_p} e^{-T_p^2/\tau_1^2} \cos\sqrt{N}\Omega\, T_p), \tag{13.1}$$

where ξ is the overall retrieval and detection efficiency. Intensity fluctuations of the driving fields would also damp the oscillation visibility, but these effects are negligible in our experiment.

The normalized storage efficiency η [48] is plotted as a function of storage period T_s for a trap depth of $\simeq 40$ μK in Fig. 13.1(c), showing that the coherence lifetime for the ground-Rydberg coherence can be extended up to $\simeq 20$ μs, which is an order of magnitude improvement over that achieve with atomic ensembles in free space [12, 14, 21, 76, 15]. The longer lifetime allows us to vary the excitation pulse duration to tens of μs, instead of varying the excitation field strength as we did previously [14]. As a result, the light shifts caused by the excitation laser fields can be kept constant over the extent of the measurement. The methods we employ to control laser phase noise and intensity fluctuations, to reduce electric field shifts, to minimize atom number variation or loss, and to suppress the effects of atomic thermal motion are outlined.

The population of the upper qubit state is measured by mapping it into a phase-matched retrieved field. The associated photoelectric detection probability per trial p_1 are recorded as a function of the excitation pulse duration time T_p, while the storage period $T_s = 1$ μs is kept constant. In Fig. 13.2, the resulting collective Rabi oscillations are shown for a lattice trap depth of 60 μK for varying atomic density, controlled by altering the YAG power. As expected, the oscillation frequency increases with the atomic density, but all the signals vanish within 5 μs, due to the limitation of $\tau_1 \approx 4.3$ μs. The dashed curves are theory fits based on Eq. 13.1. As the YAG power is raised up from 6 W to 35 W, the fitted value for the number of atoms N increases from $\simeq 10^2$ to $\simeq 10^3$. The fit value for the global dephasing factor $\gamma_1/2\pi \simeq 40$ kHz is consistent with the laser linewidth estimated from the excitation spectra. The best fit for α for all four sets of data is $\alpha/2\pi \approx 0.008$ MHz, which agrees with the coherence time of 20 μs shown in Fig. 13.1(c).

For an independent determination of the atom number and single-atom Rabi frequency, we measure the atomic density using absorption of a transmitted probe field, both with and without a control-EIT (electromagnetic-induced transparency) field. For example, the measured optical depth (OD) of $\simeq 3.5$ for a YAG power of 20 W that can be extracted from the transmission curves shown in Fig. 13.2(b) corresponds to an atomic density having peak value of $2.9 \times 10^{11}\text{cm}^{-3}$. In Fig. 13.2(c) we plot the normalized collective Rabi frequency Ω_N/Ω as a function of the number of atoms N_a in the interaction volume. We confirm the collective Rabi frequency Ω_N is enhanced by a factor $\sqrt{N}$ with respect to the single-atom value, by fitting the function $\Omega_N = \Omega N_a^k$ and finding a best-fit value $k = 0.463(5)$. The discrepancy for low atom numbers results from a relatively large error of OD fit value when the absorption is small.

We confirm that the Rydberg blockade is fully operational in our system by measuring the second-order autocorrelation function $g^{(2)}(0) < 0.2$ within the time interval of Rabi oscillations [Fig. 13.3] and demonstrate the multi-particle entanglement [130, 131, 132] of the $W-$state $|1\rangle$ within the ensemble. To investigate the main contributions to the damping of the Rabi oscillations, we vary the Rabi frequency and the atom number in a shallower trap depth of 40 μK to minimize the effects of atomic thermal motion and collisions. In Fig. 13.3 (a), the signal exhibits 9 oscillation

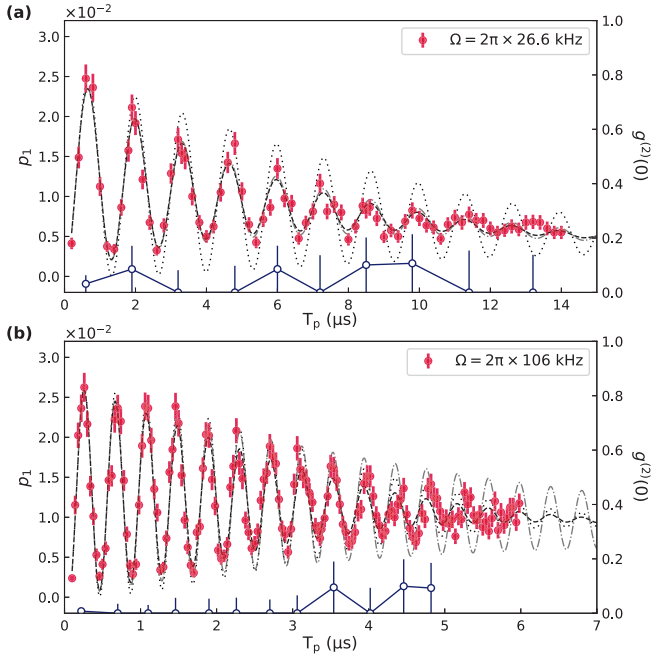

Figure 13.3: Collective Rabi oscillation as function of the pulse duration for different Rabi frequency, (a) $\Omega_1/2\pi = 4.7$ MHz, $\Omega_2/2\pi = 5.4$ MHz, $N = 797(7)$. (b) $\Omega_1/2\pi = 9.2$ MHz, $\Omega_2/2\pi = 10.8$ MHz, $N = 553(2)$. The dashed line shows best fit from theory with dephasing and atom number fluctuations. The dotted line shows the simulation without dephasing, and the dash-dotted line shows the simulation without atom number fluctuations. The blue hollow circles represent the second-order intensity correlation function at zero delay $g^{(2)}(0)$, which is below 0.2 within the Rabi oscillations, suggesting a well-established Rydberg blockade.

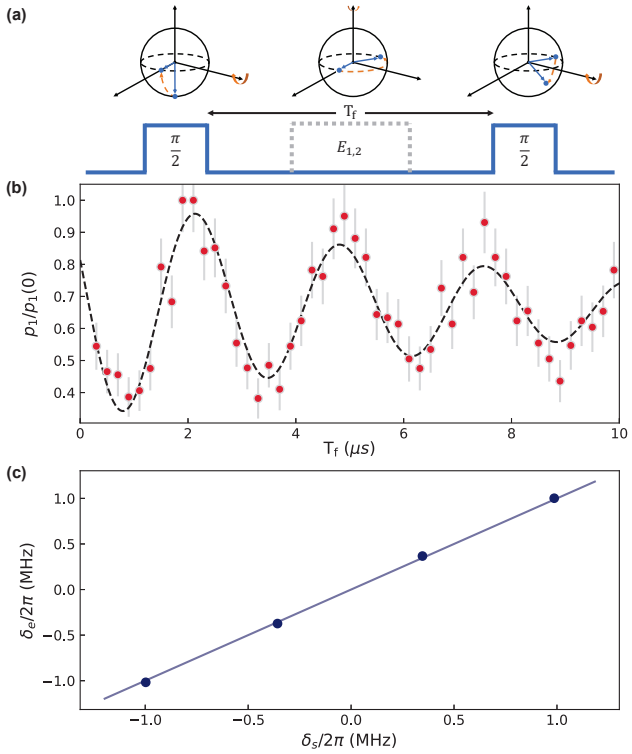

Figure 13.4: Ramsey interferometry of the trapped qubit. (a) Schematic and timing sequence. (b) Evolution of the $|1\rangle$ state versus free evolution time T_f between the two $\pi/2$ pulses of detuning $\delta_s/2\pi$ = -0.3 MHz and pulse width 0.45 μs. Dashed line represents the sinusoidal fit with an exponential decay. The error bars represent one standard deviation ($\sqrt{M}$) for M photoelectric counting events. (c) The detuning extracted from the sinusoidal fit versus detuning set to ω_1. The line represents the fitted result of $\delta_e = k\delta_s + b$ with k = 1.022(6) and b = 0.000(6) MHz. The error bar of each point is within the size of the marker.

cycles within 12 μs are shown for a smaller Rabi frequency Ω. Approximately four times higher Rabi frequency, but fewer atoms in the blockade volume are used for data in Fig. 13.3(b). In this limit, 13 oscillation cycles are damped within $\simeq$ 6 μs. These results indicate that for in the case of Fig. 13.3 (a), the dephasing is due mainly to the dephasing parameter γ_1 term. If this parameter is set equal to zero [resulting in the dotted line in Fig. 13.3 (a)], the oscillations damp more slowly than the data, while the atom number fluctuations has little impact on the visibility damping [resulting in the dash-dotted line in Fig. 13.3 (a)]. In the case of Fig. 13.3 (b), the damping of the oscillations can be ascribed chiefly to the Poisson distribution of number of atoms, N_e, that limits the visible number of the oscillation periods. If atom number fluctuations are neglected [resulting in the dash-dotted line in Fig. 13.3 (b)], the oscillations persist for a time longer than the experimental observation period. However, the oscillations damping is similar to the data when we eliminate the dephasing γ_1 [resulting in the dotted line in Fig. 13.3 (b)]. These results indicate that a combination of a narrower (e.g., 1 kHz) laser linewidth and a sub-Poisson atom-number

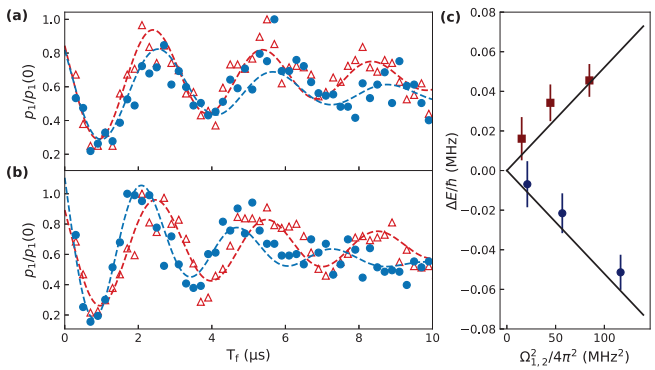

Figure 13.5: Ramsey interferometry with dressing field light shift. (a) Ramsey interferometry with (blue circles) and without (red triangles) dressing field of $\Omega_1/2\pi = 3.9$ MHz. (b) Ramsey interferometry with (blue circles) and without (red triangles) dressing field of $\Omega_2/2\pi = 10.8$ MHz. The detuning of the $\pi/2$ pulses is set to $\delta_s/2\pi$ = -0.3 MHz. (c) Light shift ΔE versus dressing field Rabi frequency Ω_1 and Ω_2. Red squares represent varying the Ω_1 field and blue circles represent varying the Ω_2 field. Black lines represent the theoretical curve of $\Delta E = \hbar(\Omega_1^2 - \Omega_2^2)/(4\Delta)$.

distribution [133, 134] may be able to prolong the lifetime of the collective Rabi oscillation to tens of micro-seconds. Notably, with a large intermediate state detuning and a shallow lattice trap depth, spontaneous decay from the Rydberg level and the influence of blackbody radiation can be neglected in our system.

To further investigate the nature of the collective state, we perform Ramsey interferometry. First, we apply two off-resonance $\pi/2$ pulses separated by a variable free evolution time T_f, followed by a phase-matched retrieval of the $|1\rangle$ state population. Using this protocol, we obtain the oscillation of the retrieved signal as a function of T_f shown in Figure 13.4 (a). In order to explore different Ramsey scenarios, we change the two photon detuning by varying the detuning δ_s of the ω_1 field. We extract the measured detuning δ_e from the oscillation period in the Ramsey interferometry by the fitting equation $p_1/p_1(0) = \frac{1}{2}(1 + \exp(-\gamma T_f)\cos(\delta_e T_f + \phi))$. The decay time constant $1/\gamma$ for the Ramsey interferometry in Figure 13.4 (a) is 6.89 ± 1.3 μs. The phase offset $\phi/2\pi = 0.14$ is due to the finite (0.45 μs) duration of $\pi/2$ pulses. We fit our results using $\delta_e = k\delta_s + b$, with $k = 1.022(6)$ and $b = 2\pi \times 0.000(6)$ MHz [Figure 13.4 (b)].

To determine whether or not there are any collective light shifts, we add a dressing field E_1 or E_2 during the T_f period. With the presence of the dressing field, the oscillation frequency of the Ramsey interferometry will be changed from δ_e to $\delta_e + \Delta E/\hbar$, where ΔE is the light shift produced by the two excitation fields. It is expected that $\Delta E = \hbar(\Omega_1^2 - \Omega_2^2)/(4\Delta)$, with no enhancement from collective effects. We measure the dependence of ΔE on $\Omega_{1,2}$ by changing the power of the dressing field and observing the change in frequency of the Ramsey interferometry signal. We observe either an increase or a decrease in oscillation frequency as we increase Ω_1 and

Ω_2 respectively, as shown in Figure 13.5 (a) and (b). Figs. 13.5 (c) shows the light shift induced by different Ω_1 and Ω_2 as well as theory curves, confirming that there is no *relative* collective light shift between the two levels.

In summary, we have demonstrated long-lived Rabi oscillations and measured light shifts for a collective Rydberg qubit held in an optical lattice that is state-insensitive for the ground and Rydberg levels. Whereas the coupling producing the Rabi oscillations is enhanced by a factor of $\sqrt{N}$, there is no corresponding enhancement for the light shifts. These results provide new evidence that collective Rydberg qubits can be used to create high-fidelity photon-photon gates [5], deterministic single photons [120], and multiple qubits [135] for scalable quantum networking.

13.1 I. THEORETICAL METHODS

13.1.1 A. Theoretical model for an effective two-level system

We adopt a simplified theoretical description in which the blockade is fully operational. Each atom is modeled as a three-level atom with lower state $|g\rangle$ (ground state), intermediate state $|p\rangle$, and upper state $|r\rangle$ (Rydberg level). There are two fields present

$$\mathbf{E}_1(\mathbf{R},t) = \frac{1}{2}E_1 f(t)\boldsymbol{\epsilon}_1 e^{i\mathbf{k}_1\cdot\mathbf{R}-i\omega_1 t} + \text{c.c.}; \tag{13.2a}$$

$$\mathbf{E}_2(\mathbf{R},t) = \frac{1}{2}E_2 f(t)\boldsymbol{\epsilon}_2 e^{i\mathbf{k}_2\cdot\mathbf{R}-i\omega_2 t} + \text{c.c.} \tag{13.2b}$$

Field $\mathbf{E}_1(\mathbf{R},t)$ $[\mathbf{E}_2(\mathbf{R},t)]$ has propagation vector $\mathbf{k}_1$ $[\mathbf{k}_2]$, frequency $\omega_1 = k_1 c$ $[\omega_2 = k_2 c]$, and polarization $\boldsymbol{\epsilon}_1$ $[\boldsymbol{\epsilon}_2]$. We define detunings

$$\Delta_1 = \omega_1 - \omega_{pg}; \quad \Delta_2 = \omega_2 - \omega_{rp}, \tag{13.3}$$

where ω_{pg} is the intermediate state to ground state frequency and ω_{rp} is the Rydberg state to intermediate state frequency. It is assumed that $|\Delta_1| \gg |\Delta_1 + \Delta_2|$. The function $f(t)$ is a smooth function having temporal with T satisfying $|\Delta_1|\,T \gg 1$, where T is some effective pulse width. Decay is neglected. Field $\mathbf{E}_1(\mathbf{R},t)$ drives the $|g\rangle \leftrightarrow |p\rangle$ transition and field $\mathbf{E}_2(\mathbf{R},t)$ drives the $|p\rangle \leftrightarrow |r\rangle$ transition with associated (assumed real) Rabi frequencies $\Omega_1 = 2\chi_1$ and $\Omega_2 = 2\chi_2$, respectively.

We first neglect any Rydberg-Rydberg interactions and assume that the field amplitudes are

constant over the sample. Then the ensemble wave function is given simply by the factorized state

$$|\psi(t)\rangle = \prod_{j=1}^{N} \Big(\; a_g(t)\,|g\rangle_j + a_p(t)\,|p\rangle_j \, e^{i\mathbf{k_1}\cdot\mathbf{R}_j - i\omega_1 t} + a_r(t)\,|r\rangle_j \, e^{i\mathbf{k_1}\cdot\mathbf{R}_j - i\omega_1 t} e^{i\mathbf{k_2}\cdot\mathbf{R}_j - i\omega_2 t} \; \Big), \quad (13.4)$$

where N is the number of atoms, $\mathbf{R_j}$ is the position of atom j and the $a_n(t)$ are the state amplitudes for a single atom that obey the equations of motion

$$\dot{a}_g = -i\chi_1 f(t) a_p, \quad (13.5a)$$

$$\dot{a}_p = -i\chi_1 f(t) a_g - i\chi_2 f(t) a_r + i\Delta_1 a_p, \quad (13.5b)$$

$$\dot{a}_r = -i\chi_2 f(t) a_p + i\left(\Delta_1 + \Delta_2\right) a_r. \quad (13.5c)$$

When expanded, the state vector $|\psi(t)\rangle$ can be written as a sum of fully symmetric orthonormal phased basis kets $|N; n, q\rangle$ that have n excitations of level $|p\rangle$ and q excitations of level $|r\rangle$; that is

$$|N; n, q\rangle = \frac{1}{\sqrt{C_n^N C_q^{N-n}}} \left|S_{nq}^N\right\rangle, \quad (13.6)$$

where the $\left|S_{nq}^N\right\rangle$ are fully symmetric, *unnormalized* phased states and C_n^N is a binomial coefficient. In other words,

$$|\psi(t)\rangle = \sum_{n,q} a_g^{N-n-q} a_p^n a_r^q \left|S_{nq}^N\right\rangle = \sum_{n,q} c_{nq}^N(t)\,|N; n, q\rangle\,, \quad (13.7)$$

where n and q can vary from 0 to N with $n+q \leq N$. It then follows immediately that the collective state amplitudes $c_{nq}^N(t)$ are related to the individual atom state amplitudes via

$$c_{nq}^N = \sqrt{C_n^N C_q^{N-n}}\, a_g^{N-n-q} a_p^n a_r^q, \quad (13.8)$$

When used with Eqs. (12.15), this leads to the evolution equations

$$\begin{aligned} \dot{c}_{nq}^N = \quad & -i\chi_1 f(t)\sqrt{n\left(N-n-q+1\right)} c_{n-1,q}^N - i\chi_1 f(t)\sqrt{(n+1)\left(N-n-q\right)} c_{n+1,q}^N \\ & -i\chi_2 f(t)\sqrt{n\left(q+1\right)} c_{n-1,q+1}^N - i\chi_2 f(t)\sqrt{q(n+1)} c_{n+1,q-1}^N \\ & +i\left[n\Delta_1 + q\left(\Delta_1+\Delta_2\right)\right] c_{nq}^N \end{aligned} \quad (13.9)$$

subject to the initial condition $c_{nq}^N(-\infty) = \delta_{n,0}\delta_{q,0}$, where $\delta_{n,m}$ is a Kronecker delta. We introduce the blockade by assuming that $c_{nq}^N = 0$ for $q > 1$.

Equation (12.26) can be solved numerically. For our experimental conditions, however, the

inequalities

$$\frac{N\chi_1^2}{\Delta_1^2} \ll 1; \quad \frac{\sqrt{N}\chi_1\chi_2}{\Delta_1^2} \ll 1 \tag{13.10}$$

hold. This means that there is at most one (collective) intermediate state excitation. Moreover these conditions are sufficient for adiabatically eliminating intermediate states. The truncated equations with $n \leq 1$ and $q \leq 1$ are

$$\begin{aligned}
\dot{c}_{00}^N &= -i\chi_1 f(t)\sqrt{N}c_{10}^N, && \text{(13.11a)}\\
\dot{c}_{10}^N &= i\Delta_1 c_{10}^N - i\chi_1 f(t)\sqrt{N}c_{00}^N - i\chi_2 f(t)c_{01}^N, && \text{(13.11b)}\\
\dot{c}_{01}^N &= i\left(\Delta_1+\Delta_2\right)c_{01}^N - i\chi_2 f(t)c_{10}^N - i\chi_1 f(t)\sqrt{N-1}c_{11}^N, && \text{(13.11c)}\\
\dot{c}_{11}^N &= i\left(2\Delta_1+\Delta_2\right)c_{11}^N - i\chi_1 f(t)\sqrt{N-1}c_{01}^N && \text{(13.11d)}
\end{aligned}$$

Adiabatically eliminating c_{10}^N and c_{11}^N, we find

$$\begin{aligned}
c_{10}^N &\approx \frac{\chi_1 f(t)\sqrt{N}c_{00}^N + \chi_2 f(t)c_{01}^N}{\Delta_1}, && \text{(13.12a)}\\
c_{11}^N &\approx \frac{\chi_1 f(t)\sqrt{N-1}}{\Delta_1}c_{01}^N, && \text{(13.12b)}
\end{aligned}$$

which, when substituted into the original equations, yield

$$\begin{aligned}
\dot{c}_{00}^N &= -\frac{iN\chi_1^2 f^2(t)}{\Delta_1}c_{00}^N - \frac{i\sqrt{N}\chi_1\chi_2 f^2(t)}{\Delta_1}c_{01}^N, && \text{(13.13a)}\\
\dot{c}_{01}^N &= i\left(\Delta_1+\Delta_2\right)c_{01}^N - \frac{i\chi_2^2 f^2(t)}{\Delta_1}c_{01}^N\\
&\quad - \frac{i\left(N-1\right)\chi_1^2 f^2(t)}{\Delta_1}c_{01}^N - \frac{i\sqrt{N}\chi_1\chi_2 f^2(t)}{\Delta_1}c_{00}^N. && \text{(13.13b)}
\end{aligned}$$

If we let

$$\begin{aligned}
c_{00}^N &= \tilde{c}_{00}^N \exp\left[-\frac{iN\chi_1^2}{\Delta_1}\int_{-\infty}^{t} f^2(t')dt'\right]\\
c_{01}^N &= \tilde{c}_{01}^N \exp\left[-\frac{iN\chi_1^2}{\Delta_1}\int_{-\infty}^{t} f^2(t')dt'\right]
\end{aligned}$$

then

$$d\tilde{c}_{00}^{N}/dt = -\frac{i\sqrt{N}\chi_1\chi_2 f^2(t)}{\Delta_1}\tilde{c}_{01}^{N}, \tag{13.14a}$$

$$d\tilde{c}_{01}^{N}/dt = -\frac{i\sqrt{N}\chi_1\chi_2 f^2(t)}{\Delta_1}\tilde{c}_{00}^{N} + i\left(\Delta_1+\Delta_2\right)\tilde{c}_{01}^{N} - \frac{i\left(\chi_2^2-\chi_1^2\right)f^2(t)}{\Delta_1}\tilde{c}_{01}^{N}, \tag{13.14b}$$

which are the effective two-level equations. Although there is a collective light shift for *each* of these amplitudes, there is no *relative* collective light shift between the two levels.

The phase matched signal varies as

$$\sum_{j,j'=1}^{N}\left\langle \sigma_{21}^{(j)}\sigma_{12}^{(j')}\right\rangle,$$

where $\sigma_{21}^{(j)}\left[\sigma_{12}^{(j)}\right]$ is a raising [lowering] operator for atom j.The blockade creates a final state after the two-photon excitation of

$$|\psi(t)\rangle = c_{00}^{N}(t)\,|N;0,0\rangle + c_{01}^{N}(t)\,|N;0,1\rangle\,. \tag{13.15}$$

In calculating

$$\sum_{j,j'}\left\langle \sigma_{21}^{(j)}\sigma_{12}^{(j')}\right\rangle.$$

following the readout pulse, only matrix elements between $\langle N;0,1|$ and $|N;0,1\rangle$ are nonvanishing; that is, the signal varies as $\left|c_{01}^{N}(T^{+})\right|^2$, where T^{+} is the time following the two-photon excitation pulse.

We relabel state amplitude $\tilde{c}_{00}^{N}$ as c_0 and $\tilde{c}_{01}^{N}$ as c_1, set $\Delta_1=\Delta$, define

$$\Omega = \frac{\Omega_1\Omega_2}{2\Delta} = \frac{2\chi_1\chi_2}{\Delta}, \tag{13.16a}$$

$$\Omega_N = \sqrt{N}\Omega, \tag{13.16b}$$

$$\delta = \Delta_1+\Delta_2+\frac{\left(\Omega_1^2-\Omega_2^2\right)f^2(t)}{4\Delta_1} \tag{13.16c}$$

and replace the pulsed fields with constant amplitude fields having pulse duration T_p (such an assumption does not affect the overall nature of the solutions). Moreover, to account for relaxation processes such as those produced by laser frequency noise, we go over to density matrix equations and introduce a dephasing rate γ_1 for the off-diagonal matrix elements, leading to optical Bloch

equations of the form:

$$\dot{\rho}_{00} = -\frac{i}{2}\left(\Omega_N \rho_{01} - \Omega_N^* \rho_{10}\right), \tag{13.17a}$$

$$\dot{\rho}_{11} = \frac{i}{2}\left(\Omega_N \rho_{01} - \Omega_N^* \rho_{10}\right), \tag{13.17b}$$

$$\dot{\rho}_{01} = -\left(\gamma_1 - i\delta\right)\rho_{01} - \frac{i\Omega_N^*}{2}\left(\rho_{00} - \rho_{11}\right), \tag{13.17c}$$

$$\dot{\rho}_{10} = -\left(\gamma_1 + i\delta\right)\rho_{10} + \frac{i\Omega_N}{2}\left(\rho_{00} - \rho_{11}\right), \tag{13.17d}$$

where we have generalized the equations to allow for complex Ω_N.

By solving the above equations in the conditions of $\delta = 0$ and $\gamma_1 \ll \sqrt{N}\,|\Omega|$, we obtain the population of the many-body Rydberg state $|1\rangle$ as

$$\rho_{11} = \frac{1}{2}(1 - e^{-\frac{\gamma_1}{2}T_p}\cos\sqrt{N}\,|\Omega|\ T_p). \tag{13.18}$$

It has been shown that when laser linewidth is modelled as white frequency noise (Markovian approximation), it provides a contribution to the decay of the relevant atomic coherence [136, 137]. Our numerical simulations along the lines of Ref. [138] confirm that the impact of the white laser frequency noise on the Rabi oscillations is equivalent to using a decay rate γ_1 for the atomic coherence. A time-dependent Rabi frequency $\Omega(t) = \Omega_0 \exp[i\,\phi(t)]$ is used in the optical Bloch equations 13.17, with $\phi(t)$ being the time trace of the phase noise gener ated from the spectral noise density $S_\phi(f)$ [139]. For white noise, the spectral density $S_\phi(f) = h_0/f^2$, where the coefficient h_0 can be related to the laser linewidth with a Lorentzian shape by $\gamma_1 = 2\pi^2 h0$ [140, 141]. With the laser locking servo bump suppressed in our system, the use of a Lorentzian laser frequency profile with linewidth γ_1 is a reasonable approximation. After obtaining the time series of the phase $\phi(t)$, we numerically simulate the time-dependent optical Bloch equations using the Runge-Kutta method. In Fig. 13.6(a), we show one thousand individual samples (gray lines) and their average (red line) for a white frequency noise spectrum with $h_0 = 0.08$ MHz, assuming no other damping process, and observe a slow damping of the oscillation. Comparison of this result with the solution to the master equations [Eq. 13.17] without phase noise but with a dephasing $\gamma_1 = 2\pi \times 0.04$ MHz, as well as the analytical solution in Eq. 13.18, indicates that all three Rabi oscillation traces agree well with each other, as shown in Fig. 13.6(b).

13.1.2 B. Brief review on the theory of magic-wavelength trap

We briefly review the theory of the magic-wavelength lattice trap along the lines of our prior study [48]. Assuming all the atoms are confined in the state-insensitive lattice trap and neglecting

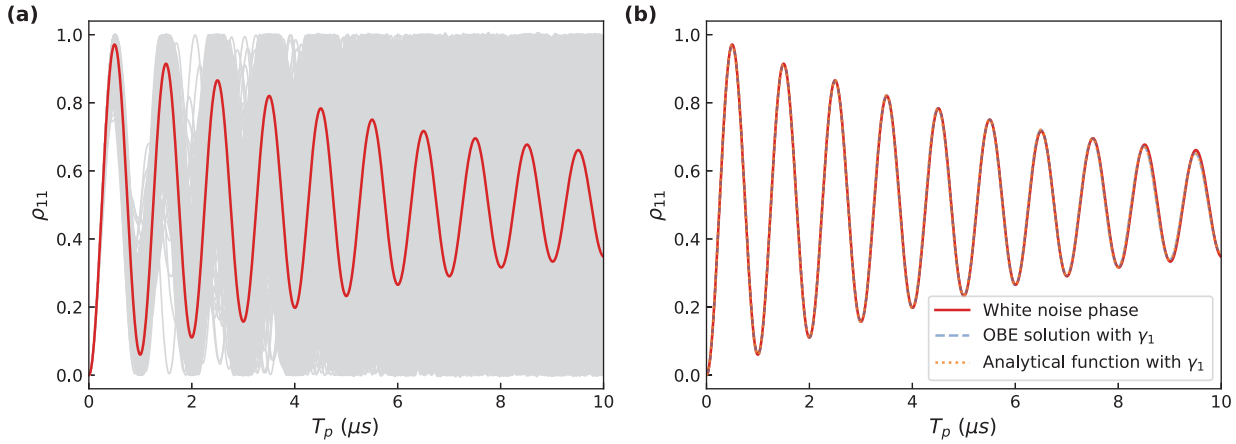

Figure 13.6: Influence of laser phase noise. (a) Numerical simulations for Rabi oscillation in the presence of white frequency noise. The gray lines are individual realizations for 1000 numerical samples with random processes on $\phi(t)$ generation. The red line is the average of the 1000 samples. (b) Comparison of the simulations with different mechanisms. The red solid line is from the solution to the optical Bloch equations only with the white noise phase, same as in (a). The blue dashed line is from the solution to the master equations [Eq. 13.17] only with a dephasing rate γ_1. The orange dotted line is from the analytical function in Eq. 13.18 with a dephasing rate γ_1. Atom number N = 100, the single-atom Rabi frequency $\Omega/2\pi = 0.1$ MHz, $h_0 = 0.08$ MHz, the dephasing rate $\gamma_1/2\pi = 0.04$ MHz.

Rydberg-Rydberg interactions, we find that the phase-matched retrieval signal at time T_s normalized to that at $T_s = 1\ \mu$s, can be written as

$$\eta(T_s) = G(T_s)/G(T_s = 1\mu s); \tag{13.19}$$

with

$$G(T_s) = \left| \int_{-\infty}^{\infty} dX \int_0^{\infty} \rho d\rho f(\rho, X) \mathcal{N}(\rho, X) C(\rho, X, T_s) \right|^2 \times e^{-T_s/\tau_{eff}}, \tag{13.20}$$

The transverse and longitudinal effects combine to produce an atomic density profile $\mathcal{N}(\rho, X)$ given by

$$\mathcal{N}(\rho, X) = \exp\left[\frac{U_0}{2k_B T}\mathcal{I}(\rho, X)\right] \exp\left[-\frac{X^2}{L^2}\right]. \tag{13.21}$$

The distribution $f(\rho, X)$ appearing in Eq. (13.20) is equal to the product of the spatially dependent envelopes of the excitation and retrieval electric field amplitudes, namely

$$f(\rho, X) = \left(\frac{w_{E_1,0}}{w_{E_1}(X)}\right) \exp\left[-\frac{\rho^2}{w_{E_1}^2(X)}\right] \times \left\{\left(\frac{w_{E_2,0}}{w_{E_2}(X)}\right) \exp\left[-\frac{\rho^2}{w_{E_2}^2(X)}\right]\right\}^2, \tag{13.22}$$

where $w_{i,0}$ are the transverse waists of the beams at the foci, $w_i(X) = w_{i,0}\sqrt{1+\left(\frac{X}{X_{ri}}\right)^2}$, and X_{ri} is the Rayleigh length for beam i. In our experiment, $w_{E_1,0} = 6$ μm, $w_{E_{2/r},0} = 15$ μm.

The factor $C(X,\rho,T_s)$ is the product of a non-lattice contribution, $e^{-i\omega_d(\rho,X)T_s}$, and a lattice contribution corresponding to motional dephasing, given by

$$C(X,\rho,T_s) = \sum_{q,q',q''}^{q_{\max}} e^{-i\omega_d(\rho,X)T_s}\rho_{1q'',1q'}(0) \times M_{1q';3q}\left[-k\mathbf{u}_x\right] M_{3q;1q''}\left[k\mathbf{u}_x\right] e^{i\left(\omega_{q'}^{(1)}-\omega_q^{(3)}\right)T_s}. \quad (13.23)$$

where the frequencies $\omega_{q'}^{(1)}$ and $\omega_q^{(3)}$ are obtained as eigenvalues of the potentials

$$U_1^{(l)}(X) = -U_0\cos^2\left(k_L X\right); \quad (13.24a)$$

$$U_3^{(l)}(X) = -\frac{U_0}{\alpha_g}\cos^2\left(k_L X\right) \times \left[\frac{D_n^2}{6\hbar\Delta} - |\alpha_f|\,\theta_n\right], \quad (13.24b)$$

respectively.

We include three dissipative mechanisms that affect the ground-Rydberg coherence lifetime. The effective population decay lifetime is given by

$$\frac{1}{\tau_{eff}} = \frac{1}{\tau_{6p,n}} + \frac{1}{\tau_n^{(0)}} + \frac{1}{\tau_n^{(bb)}}, \quad (13.25)$$

where $\tau_{6p,n}$, $\tau_n^{(0)}$, and $\tau_n^{(bb)}$ are the contributions from the lattice-induced population decay of the $6p_{3/2}$ level, Rydberg level decay at zero temperature, and blackbody induced transitions, respectively. Explicitly

$$\tau_{6p,n} = \frac{h\Delta_{m,n}}{U_0}\tau_{6p,0}; \quad (13.26a)$$

$$\tau_n^{(0)} = \tau^{(0)}(n^*)^{2.94}; \quad (13.26b)$$

$$\tau_n^{(bb)} = \frac{3\hbar(n^*)^2}{4\alpha_{FS}^3 k_B T}, \quad (13.26c)$$

where $\tau_{6p,0} = 125$ ns, $\tau^{(0)} = 1.43$ ns, $T = 293$ K, and $n^* = n - 3.13$ is the effective electronic quantum number, α_{FS} is the fine structure constant. At low n, the lifetime is limited mainly by spontaneous decay and blackbody transitions. With $n \gtrsim 40$, the dephasing produced by the non-lattice potential begins to reduce the lifetime, an effect that saturates for $n \gtrsim 60$. For still higher values of n, the lattice induced population of the $6p_{3/2}$ begins to play an important role in limiting the coherence lifetime. The reason for this is that the magic detuning $\Delta_{m,n}$ decreases with increasing n. In our system, the principal quantum number is $n = 75$, and the lattice trap depth is

$40-60$ μK, hence the blackbody radiation time constant is $\tau_{75}^{(bb)} = 267$ μs, the Rydberg level decay constant at zero temperature is $\tau_{75}^{(0)} = 411$ μs, but the lattice-induced population decay constant is $\tau_{6p,75} \approx 54 - 36$ μs, which mainly limits the ground-Rydberg coherence lifetime in our system.

13.2 II. EXPERIMENTAL SETUP

13.2.1 A. Timing sequence and source efficiency

In our experiment, to realize a small and dense atomic ensemble, we initially prepare the atoms in a magneto optical trap (MOT), transfer into a far-off-resonance crossed dipole trap (FORT), and finally load into a state-insensitive lattice trap (SILT), as shown in Fig. 13.7(a). The transfer efficiency is about 70%.

After every atom loading process, we first apply an optical pumping (OP, 795 nm, F=2 to F'=2, $\sigma-$) and a repumper optical pumping (RP OP, 780 nm, F=1 to F'=2, π) to prepare all the atoms to $|G\rangle$, and then run 10 excitation and retrieval experimental trials as a loop, as shown in Fig. 13.7(b). For each loading period, we discard the first 100 loops to make sure that all atoms are in the ground state with the correct magnetic sublevel, and then we repeat the loop for 50 times to get efficient photon generation rate. The excitation and retrieval pulses have approximately rectangular shapes with rising and falling edges of $\lesssim$50 ns extent. The emitted light is gated by an acousto-optic modulator (AOM) (not shown in Fig. 1(a)), then split by a beam splitter and directed into two single-mode optical fibers (SMFs), coupled to the single-photon counting modules (SPCMs).

Therefore, the photoelectric detection probability per trial p_1 (in Figs. 2 and 3 in the main text) is obtained by photon counts per atom loading (Fig. 13.9 as an example) divided by 500 trials. To suppress the measurement uncertainty, for each point in Figs. 2 and 3, we repeat the atom loading sequence for 16 times, which is 8000 trials and then get the total photon counts to calculate the photoelectric detection probability per trial p_1.

The photon transmission and detection efficiency η_{td} is given by $\eta_{td} = \eta_c\eta_o\eta_f\eta_d = 0.16$, where $\eta_c = 0.95, \eta_o = 0.55, \eta_f = 0.55, \eta_d = 0.55$ are the vacuum cell transmission, optics transmission (including an AOM gate), fiber coupling, and single-photon detection efficiencies, respectively.

For the storage and retrieval protocol, we follow the procedures in Ref. [14] to measure the storage and retrieval efficiency. We first obtain the storage efficiency η_s through the measurement of the transmitted fraction of Ω_1 with and without Ω_2. To protect the SPCM but have a measurable absorption, we use a much weaker 780 pulse but a smaller intermediate state detuning of 40 MHz, and obtain $\eta_s = 0.028(3)$. Afterwards, we apply the retrieval field Ω_r at $T_s = 1$ μs, and obtain $\eta_s\eta_r = 0.0066(3)$, resulting in $\eta_r = 0.23(3)$, which is similar to the value reported in Ref. [14]. The conditions here are the same as those in Fig. 3 of the main text. The retrieval efficiency will

vary with different atomic density or positions [120]. We notice that the definition of the retrieval efficiency in our system is the photon generation probability in Ref. [120], which is a product of the writing, storage and retrieval efficiencies and is estimated to be 0.40(4) in their system.

The main limiting factor for the source efficiency in our system is the retrieval process, which can be optimized by increasing the optical depth [120]. In addition, the optical transmission and detection efficiency can be improved with better mirrors, gated AOM and single-photon detectors. In principle, we may achieve one order of magnitude improvement for the photon generation efficiency.

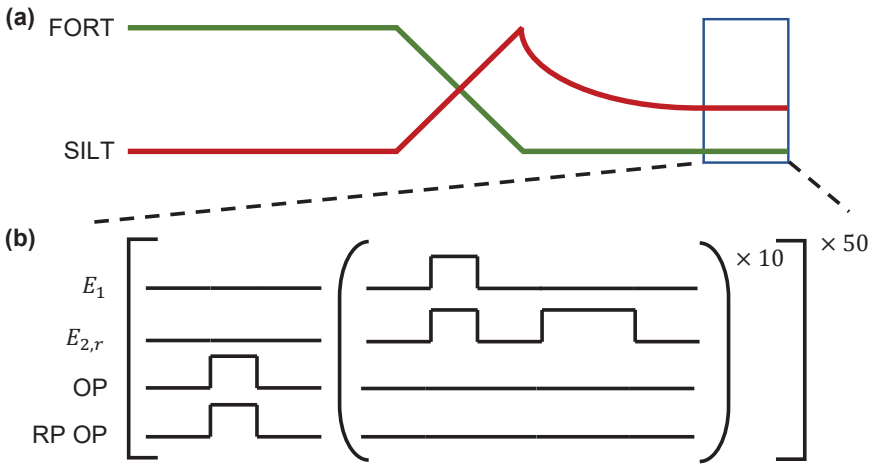

Figure 13.7: (a) Timing sequence of atomic cloud forming process. (b) Timing sequence of Rydberg excitation, retrieval, and optical pumping process.

13.2.2 B. Calibration for sample size and atom number

We first determine the longitudinal size of our atomic ensemble by measurement of the interaction-induced dephasing dynamics [142, 143, 144], and obtain $L_z = 2\sigma_z \approx 10$ μm for a Gaussian distribution of $\lambda(z) = a_z \exp -|z|^2/\sigma_z^2$. The excitation beams are focused onto the atoms with beam waists $w_{E_1,0} = 6$ μm and $w_{E_2,0} = 15$ μm. From the fluorescence image, we confirm that the excitation beam size is much smaller than that of the atomic ensemble in the trap, so that the transverse dimension is determined by the excitation Gaussian beam of E_1 field with a waist $w_{E_1,0} = 6$ μm. The minimum blockade radius in our system is estimated to be $R_b = (C_6/\hbar\Omega)^{1/6} = 16.3$ μm by using $C_6/(2\pi) \approx -\hbar \cdot 1,948$ GHz·μm^6 for $n = 75$ [34], therefore entirely covering the excited ensemble, as one should expect in order to observe the many-body Rabi oscillations and the single-photon generation. The effectiveness of Rydberg-level interactions in creating a blockade is also demonstrated by measuring the second-order intensity correlation function at zero

delay, $g^{(2)}(0)$, as a function of pulse duration for many-body Rabi oscillation. $g^{(2)}(0)$ is calculated using $g^{(2)}(0) = P_{\rm TR}P_{\rm G}/(P_{\rm T}P_{\rm R})$, where $P_{\rm T}$ and $P_{\rm R}$ represent the photon counts in each SPCM, $P_{\rm TR}$ is the coincidence counts between the two SPCMs, and $P_{\rm G}$ records the total trial gates. We achieve $g^{(2)} < 0.2$ within the time interval of Rabi oscillations in Fig. 3 in the main text.

Afterwards, for an independent determination of the atom number, we measure the optical depth (OD) by absorption of a transmitted probe field, both with and without a control-EIT field. As an example, in Fig. 2(b) in the main text, the measured OD is $\simeq 3.5$ for YAG power 20 W. The atomic density can be determined from the optical depth by using the relationship OD $= \sigma \int_{-\infty}^{\infty} \lambda(z)dz$, where $\sigma = 2.9 \times 10^{-13}\text{m}^{-2}$ is the absorption cross section. This results in the value of peak atom density $a_z = 2.9 \times 10^{11}\text{cm}^{-3}$. We can also calibrate the relationship between the effective single-atom Rabi frequencies of $\Omega_{1,2}$ and their intensities through the two-level absorption and three-level EIT measurement.

Hence, the number of atoms in the blockade volume is given by $N_a = \iiint_V n(x, y, z)dV$, where V is the excitation volume of the ensemble. Therefore, we confirm the collective Rabi frequency Ω_N is enhanced by a factor $\sqrt{N}$ with respect to the single-atom result, by fitting the function $\Omega_N = \Omega N_a^k$ with the best-fit value $k = 0.463(5)$. The discrepancy for low atom numbers results from a relatively large error of OD fit value when the absorption is small.

13.2.3 C. System stabilization and performance

To achieve a long-lived Rydberg qubit, we implement a variety of techniques to stabilize our system of cold Rydberg atomic ensembles:

Narrowing laser linewidth. The two lasers (780 nm and 960 nm external-cavity diode lasers from MOGLabs) are frequency stabilized by a standard Pound–Drever–Hall (PDH) technique to an ultra-low expansion (ULE) high finesse cavity of finesse $F \simeq 2 \times 10^3$ and free-spectral-range $\text{FSR} \simeq 1.5$ GHz. The PDH locking suppresses frequency noise of the lasers, resulting in a narrow linewidth of $\approx 20 - 40$ kHz. However, high frequency noise cannot be suppressed using the PDH locking due to the finite feedback bandwidth, which could result in servo bump several MHz away from the locking position. We use the high finesse cavity as a spectral filter for servo bumps and then phase lock our excitation lasers to the cavity transmitted light by a fast servo (Vescent D2-135). The linewidth of the beat signal after phase-locking is within 1 kHz. The 480 nm laser is frequency doubled from the 960 nm laser by a Toptica SHG.

With laser linewidth narrowed to tens of kHz, we measure the excitation spectrum with weak driving powers, as shown in Fig. 13.8, for different pulse duration times. As can be seen, for longer pulse duration, the bandwidth of the excitation spectrum decreases accordingly. The data are fit with the function of $f(\delta) = a/(\delta^2 + \sigma^2)|\text{sinc}(\delta\, T_p)|^2 + z$, where the sinc function results from the

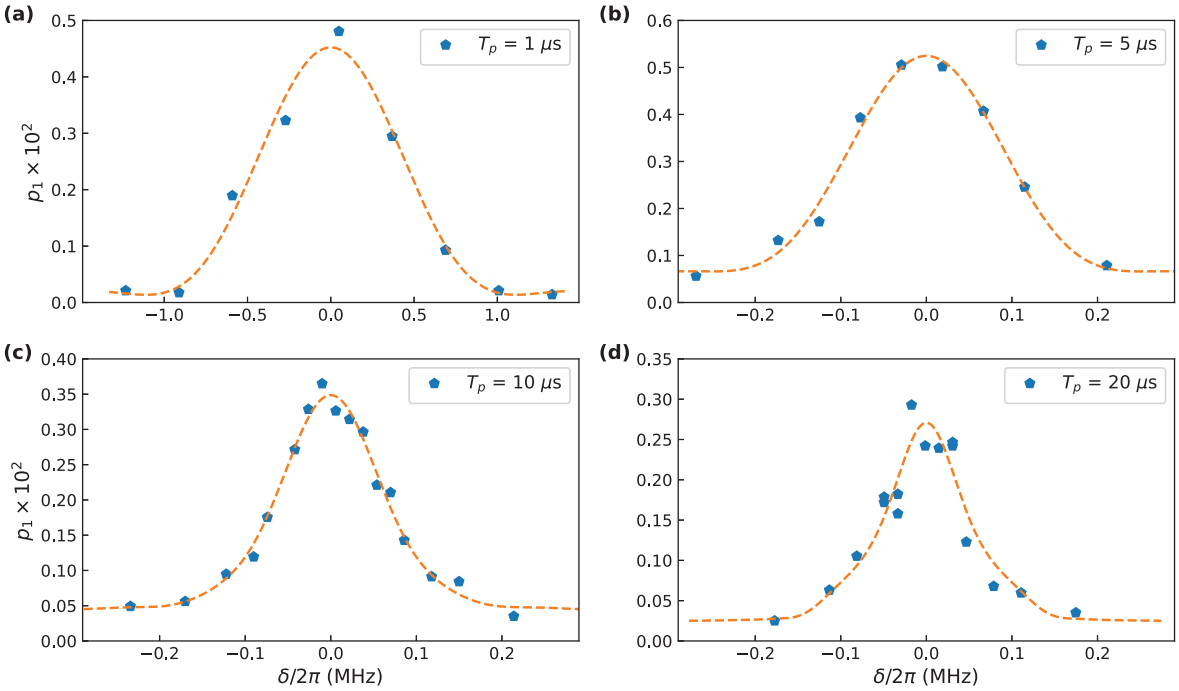

Figure 13.8: The excitation spectra for different pulse durations. (a)-(d): 1 μs, 5 μs, 10 μs, 20 μs, respectively. The dashed lines are the fitting curves with the function of $f(\delta) = a/(\delta^2 + \sigma^2)|\mathrm{sinc}(\delta\, T_p)|^2 + z$. The best-fit value for all the excitation spectra is $\sigma/2\pi = 40(4)$ kHz.

Fourier transformation of the rectangular pulse shape of the excitation light, and the uncertainty σ represents the laser linewidth. In our system, the best-fit value for all the excitation spectra is $\sigma/2\pi = 40(4)$ kHz, which reflects the HWHM of the effective overall laser line shape, as well as the dephasing γ_1.

Stabilizing laser intensity. Each excitation beam intensity is stabilized to $\sim 0.14\%$ by a photodiode and an AOM, which is also used for controlling the pulse duration of the Rabi oscillation excitation. We use a sample-and-hold method to pause the intensity feedback during the Rydberg pulses to avoid introducing additional intensity noise due to the limited bandwidth of our locking module New Focus LB-1005. Therefore, in our system, after intensity stabilization, the fluctuation percentage is $\beta \approx 0.2\%$. Allowing for intensity fluctuations $I \sim I_0 \exp(-(I - I_0)^2/(\beta I_0)^2)$, the visibility damping of the Rabi oscillations will have an additional decay factor $\exp(-t^2/\tau_2^2)$, where $\tau_2 = \sqrt{2}/(\beta\sqrt{N}\Omega) \gg \tau_1$ (the Gaussian decay time constant from atom number fluctuation), so the time constant for the Gaussian decay in Eq. 1 of the main text is $1/\tau^2 = 1/\tau_1^2 + 1/\tau_2^2 \approx 1/\tau_1^2$.

Reducing electric field fluctuation. We observe slow drifts in the resonant frequency of the $|6 = 5P_{3/2}\rangle \leftrightarrow |75S_{1/2}\rangle$ transition on the scale of several MHz, which is probably due to fluctuation in electric field induced by Rb ion build-up on the cell wall. By placing eight 1 W ultraviolet LEDs of wavelength 365 nm on the glass cell, we are able to stabilize the Rydberg resonance fre-

quency within tens of kilohertz. The most stable configuration is reached by applying the UV light at the end of the experimental sequence; it is turned on for 800 ms after the Rydberg excitation period and turned off before the MOT preparation.

Suppressing atomic thermal motion. We utilize a magic-wavelength optical lattice to trap the excited Rydberg atoms and adiabatically lower the trap depth to eliminate the atomic thermal motion dephasing. Without switching on and off the optical trap, the heating effect from the trap blinking can also be reduced.

In Fig.2 of the main text, to achieve higher atom number, we use a deeper lattice trap of $60\ \mu$K, while in Fig. 3 of the main text, we adopt a lower trap depth of $40\ \mu$K to minimize atomic thermal motion and collisions, so that we would expect longer coherence time of the collective qubit, which will be mainly limited by the laser linewidth or the atom number distribution.

Minimizing atom number variation or loss. To have the consistent atom number in each atom loading, we stabilize the MOT laser power, as well as the YAG and lattice power to $< 1\%$ fluctuation. Furthermore, we minimize the variation of atom numbers between different measurement trials by discarding the first 100 loops to make sure that all atoms are in the ground state with the correct magnetic sublevel, and then we repeat the loop for 50 times to have more flat collection counts, which means the atom number remains similar for different loops in this condition. The photon counts follow a Poisson distribution and do not fluctuate with time, as shown in Fig. 13.9. We measured the generated photon counts for 200 atom loading sequences. The moving average of every 5 atom loading remains around the overall average of 15.6, and the distribution agrees well with the Poissonian one with rate of 15.6 and a corresponding uncertainty of 3.9.

With limited excitation loops, we can also reduce an atom loss mechanism produced by the excitation lasers and optical pumping. By measuring the absorption of 780 nm probe light, coupled to the ground $|G\rangle$ state to the intermediate $|P\rangle$ state, after our Rydberg excitation sequence to calibrate the ground state population, we observe both the optical depth (OD) and the fluorescence image drops to 80% for 10 μs of Rydberg excitation. We expect the number of atoms in our system to decay with a time constant of 40 μs.

After all these stabilization efforts, the possible dephasing sources for a collective qubit in an atomic ensemble that remain are:

- Atomic thermal motion: the spin-wave coherence time is about 20 μs in our system [Fig. 1(c) in the main text], including contributions from the lattice-induced population decay of the $6p_{3/2}$ level, Rydberg level decay at zero temperature, and blackbody induced transitions.

- Poisson distribution on atom numbers: $\tau_1 = 2\sqrt{2}/\Omega$, which depends on the single-atom Rabi frequency.

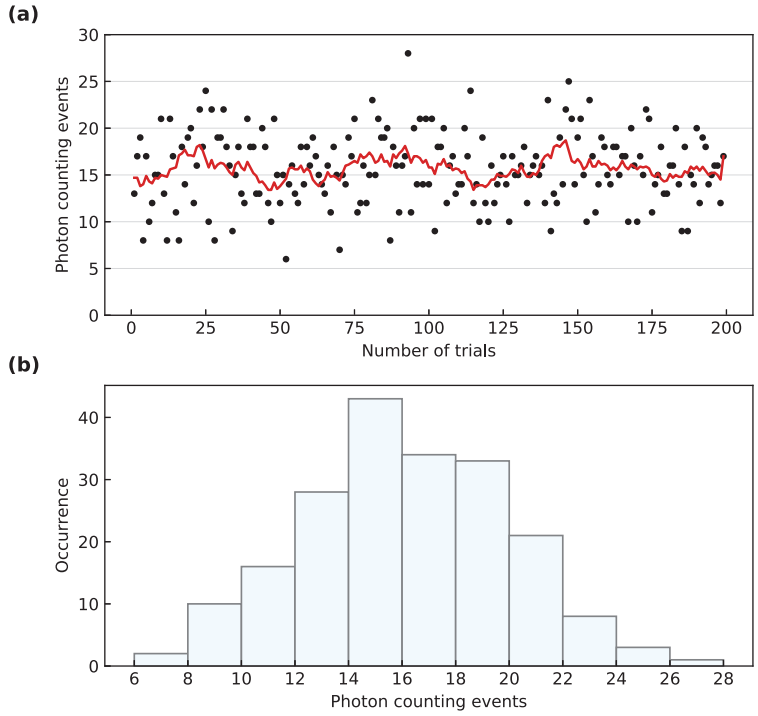

Figure 13.9: The photon counts per atom loading (3.5 s) are measured for 200 atom loading sequences, which shows the Poisson distribution. The lattice trap depth is 60 μK, and the pulse duration is 900 ns.

- Laser phase noise: $1/(\gamma_1/2) \approx 8$ μs, which is limited by the laser linewidth.
- Laser intensity fluctuation: $\tau_2 = \sqrt{2}/(\beta\sqrt{N}\Omega) \ll \tau_1$, where the fluctuation percentage $\beta \approx 0.2\%$ after intensity stabilization.

13.2.4 D. Witness for the many-body entanglement

We follow the M-separability witness for the many-particle entanglement in Ref [130] and give some details for the derivation of a lower bound of P_2 given P_1. Since we are concerned with at most a single excitation in the Rydberg blockade, it is sufficient to work with pure states of the form

$$|\Psi\rangle = |\phi_1\rangle \otimes ... \otimes |\phi_M\rangle = \otimes_{i=1}^{M}(a_i|0\rangle + b_i|1\rangle), \tag{13.27}$$

where $a_i^2 + b_i^2 = 1$. We can get the one-photon and two-photon probability to be

$$P_1 = |\langle 1|\Psi\rangle|^2 = \frac{|A|^2}{M}\left|\sum_i \frac{b_i}{a_i}\right|^2 \tag{13.28}$$

$$P_2 = |\langle 2|\Psi\rangle|^2 = \frac{2|A|^2}{M^2}\left|\sum_{i<j} \frac{b_i b_j}{a_i a_j}\right|^2 \tag{13.29}$$

with $A = \prod_{i=1}^{M} a_i$, and $|2\rangle = \sum_{i<j} |G \ldots R_i \ldots R_j \ldots G\rangle$ is the doubly excited state.

To find the lowest bound of P_2 given any P_1, we use the Lagrange multiplier method, which is suitable for constrained minimization problems. In our case, we consider

$$\mathcal{L} = P_2 + \lambda(P_1 - C). \tag{13.30}$$

For $M = 2$ and a given P_1, if we set $a_1 = 1, b_1 = 0, a_2 = \sqrt{1-2P_1}, b_2 = \sqrt{2P_1}$, we can get $P_2 = 0$ for any P_1. We can also infer a upper boundary for P_1 that is $P_1 = 0.5$, as depicted in Fig. 13.10. For the case $M = 3$, we performed a Monte-Carlo simulation on a_i and b_i to explore all possible $\langle 1|\Psi\rangle$ and $\langle 2|\Psi\rangle$ combinations. The simulation result is shown in Fig. 13.10 where the gray dots represent the Monte Carlo results for $M = 3$, and the orange line describes the contour for the simulation result. Notice that the orange line gets ragged for low P_2 value due to the limited number of points.

Using the $g^{(2)}(0)$ data in Fig. 3 in the main text, we extract one photon and two photon collection rates, p_1 and p_2 respectively. p_1 and p_2 are transformed into $\langle 1|\Psi\rangle$ and $\langle 2|\Psi\rangle$ by $\langle 1|\Psi\rangle = P_1 = p_1/\eta_{\text{tot}}$ and $\langle 2|\Psi\rangle = P_2 = p_2/\eta_{\text{tot}}^2$, where $\eta_{\text{tot}} = \eta_r \eta_{td} = 0.0368(48)$ with the retrieval efficiency $\eta_r = 0.23(3)$ and the photon transmission and detection efficiency $\eta_{td} = 0.16$, as mentioned before. The red triangles and purple circles represent data points in Fig. 3(a) and (b), respectively. The two points of Rabi angle $\sqrt{N}\Omega t = \pi$ fall into the range of $M = 1$ but not $M = 2$, therefore, we can conclude that we have at most 1 excitation blockade site and the entanglement depth is at least $K = N/M \geq 800$. The rest of the points are at least falling in the range of $M = 3$, but due to the decrease of the storage efficiency for the long pulse duration, it is difficult to confirm the subgroup number M. All the data shows the non-separable properties of our Rydberg atomic ensemble. We may use this method to perform a deterministic single photon generation with even lower Rydberg states and weak laser excitations, or to realize some multi-particle entanglement applications.

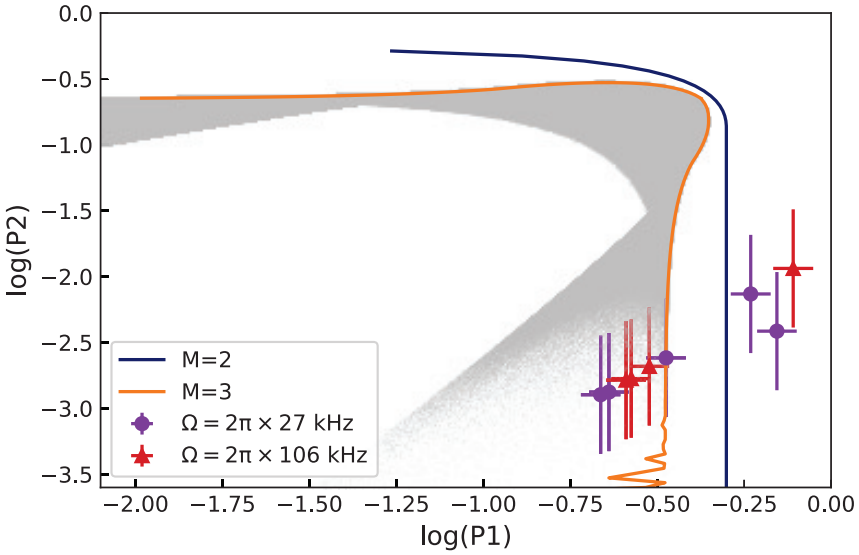

Figure 13.10: Many-body entanglement. The data are the peaks of Rabi oscillations in Fig. 3 in main text. The blue lines is M = 2 and the orange line is M = 3. The gray dots are Monte Carlo simulations for M = 3. The red triangles and purple circles are the peaks of $\sqrt{N}\Omega t = m\pi$. The first peaks of the many-body Rabi oscillations in Fig. 3(a) and (b) of the main text lie in the right side of the $M = 1$, indicating the entanglement depth in our system is at least K = N/M ≥ 800. The error bars include the one standard deviation of photon counts and one standard error of total photon source efficiency.

APPENDIX A

List of Programs:

The online repository for the below programs can be accessed via

Google Drive:

https://drive.google.com/drive/folders/1EPKIrka23wtUX1jVoAxqhDTz4DcZGfEs?usp=sharing

GitHub:

https://github.com/HNNguyen92/Thesis

Email:

HuyNNguyen92@gmail.com

1. Lightshift calculator: Calculate level shifts for the D_2 line with a 1064 nm trapping field.
2. Hologram generation : Calculate phase holograms utilizing the Gerchberg Saxton algorithm.
3. ECDL mode selection : Model the frequency mode selection process as a function of cavity lengths and filter angle.
4. PDH error signal : Model the PDH error signal for different mixing phase and cavity parameters.
5. Radiation pattern from Rydberg Array: Calculate the radiative patterns utilizing a two-photon scheme and an array of atoms.
6. Many Body Rabi Oscillations : Calculate the dynamics associated with many body Rabi oscillations utilizing a collective basis.

BIBLIOGRAPHY

[1] Andreas Neuzner, Matthias Körber, Stephan Dürr, Gerhard Rempe, and Stephan Ritter. Breakdown of atomic hyperfine coupling in a deep optical-dipole trap. *Physical Review A*, 92(5), November 2015.

[2] Bindiya Arora and B. K. Sahoo. State-insensitive trapping of rb atoms: Linearly versus circularly polarized light. *Physical Review A*, 86(3), September 2012.

[3] Daniel J. Thompson and Robert E. Scholten. Narrow linewidth tunable external cavity diode laser using wide bandwidth filter. *Review of Scientific Instruments*, 83(2):023107, February 2012.

[4] Thomas F. Gallagher. *Rydberg atoms*. Cambridge Univ. Press, 1994.

[5] M. Saffman, T. G. Walker, and K. Mølmer. Quantum information with rydberg atoms. *Reviews of Modern Physics*, 82(3):2313–2363, August 2010.

[6] M. D. Lukin, M. Fleischhauer, R. Cote, L. M. Duan, D. Jaksch, J. I. Cirac, and P. Zoller. Dipole blockade and quantum information processing in mesoscopic atomic ensembles. *Physical Review Letters*, 87(3), June 2001.

[7] M. Saffman and T. G. Walker. Creating single-atom and single-photon sources from entangled atomic ensembles. *Physical Review A*, 66(6), December 2002.

[8] P. Kómár, T. Topcu, E. M. Kessler, A. Derevianko, V. Vuletic, J. Ye, and M. D. Lukin. Quantum network of atom clocks: A possible implementation with neutral atoms. *Physical Review Letters*, 117(6), August 2016.

[9] Bo Zhao, Markus Müller, Klemens Hammerer, and Peter Zoller. Efficient quantum repeater based on deterministic rydberg gates. *Physical Review A*, 81(5), May 2010.

[10] E. Brion, F. Carlier, V. M. Akulin, and K. Mølmer. Quantum repeater with rydberg-blocked atomic ensembles in fiber-coupled cavities. *Physical Review A*, 85(4), April 2012.

[11] Yang Han, Bing He, Khabat Heshami, Cheng-Zu Li, and Christoph Simon. Quantum repeaters based on rydberg-blockade-coupled atomic ensembles. *Physical Review A*, 81(5), May 2010.

[12] Y. O. Dudin and A. Kuzmich. Strongly interacting rydberg excitations of a cold atomic gas. *Science*, 336(6083):887–889, May 2012.

[13] D. Maxwell, D. J. Szwer, D. Paredes-Barato, H. Busche, J. D. Pritchard, A. Gauguet, K. J. Weatherill, M. P. A. Jones, and C. S. Adams. Storage and control of optical photons using rydberg polaritons. *Physical Review Letters*, 110(10), March 2013.

[14] Y. O. Dudin, L. Li, F. Bariani, and A. Kuzmich. Observation of coherent many-body rabi oscillations. *Nature Physics*, 8(11):790–794, September 2012.

[15] L. Li, Y. O. Dudin, and A. Kuzmich. Entanglement between light and an optical atomic excitation. *Nature*, 498(7455):466–469, June 2013.

[16] Thibault Peyronel, Ofer Firstenberg, Qi-Yu Liang, Sebastian Hofferberth, Alexey V. Gorshkov, Thomas Pohl, Mikhail D. Lukin, and Vladan Vuletic. Quantum nonlinear optics with single photons enabled by strongly interacting atoms. *Nature*, 488(7409):57–60, July 2012.

[17] Ofer Firstenberg, Thibault Peyronel, Qi-Yu Liang, Alexey V. Gorshkov, Mikhail D. Lukin, and Vladan Vuletic. Attractive photons in a quantum nonlinear medium. *Nature*, 502(7469):71–75, September 2013.

[18] Simon Baur, Daniel Tiarks, Gerhard Rempe, and Stephan Dürr. Single-photon switch based on rydberg blockade. *Physical Review Letters*, 112(7), February 2014.

[19] Daniel Tiarks, Simon Baur, Katharina Schneider, Stephan Dürr, and Gerhard Rempe. Single-photon transistor using a förster resonance. *Physical Review Letters*, 113(5), July 2014.

[20] H. Gorniaczyk, C. Tresp, J. Schmidt, H. Fedder, and S. Hofferberth. Single-photon transistor mediated by interstate rydberg interactions. *Physical Review Letters*, 113(5), July 2014.

[21] Matthew Ebert, Alexander Gill, Michael Gibbons, Xianli Zhang, Mark Saffman, and Thad G. Walker. Atomic fock state preparation using rydberg blockade. *Physical Review Letters*, 112(4), January 2014.

[22] D. Barredo, S. Ravets, H. Labuhn, L. Béguin, A. Vernier, F. Nogrette, T. Lahaye, and A. Browaeys. Demonstration of a strong rydberg blockade in three-atom systems with anisotropic interactions. *Physical Review Letters*, 112(18), May 2014.

[23] Y.-Y. Jau, A. M. Hankin, T. Keating, I. H. Deutsch, and G. W. Biedermann. Entangling atomic spins with a rydberg-dressed spin-flip blockade. *Nature Physics*, 12(1):71–74, October 2015.

[24] Johannes Zeiher, Rick van Bijnen, Peter Schauß, Sebastian Hild, Jae yoon Choi, Thomas Pohl, Immanuel Bloch, and Christian Gross. Many-body interferometry of a rydberg-dressed spin lattice. *Nature Physics*, 12(12):1095–1099, August 2016.

[25] Hannes Bernien, Sylvain Schwartz, Alexander Keesling, Harry Levine, Ahmed Omran, Hannes Pichler, Soonwon Choi, Alexander S. Zibrov, Manuel Endres, Markus Greiner, Vladan Vuletic, and Mikhail D. Lukin. Probing many-body dynamics on a 51-atom quantum simulator. *Nature*, 551(7682):579–584, November 2017.

[26] M. S. Safronova, Carl J. Williams, and Charles W. Clark. Optimizing the fast rydberg quantum gate. *Physical Review A*, 67(4), April 2003.

[27] M. Saffman and T. G. Walker. Analysis of a quantum logic device based on dipole-dipole interactions of optizzcally trapped rydberg atoms. *Physical Review A*, 72(2), August 2005.

[28] E. A. Goldschmidt, D. G. Norris, S. B. Koller, R. Wyllie, R. C. Brown, J. V. Porto, U. I. Safronova, and M. S. Safronova. Magic wavelengths for the 5s-18s transition in rubidium. *Physical Review A*, 91(3), March 2015.

[29] P. R. Berman and Vladimir Malinovsky. *Principles of laser spectroscopy and quantum optics*. Princeton University Press, 2011.

[30] R. H. Leonard and C. A. Sackett. Effect of trap anharmonicity on a free-oscillation atom interferometer. *Physical Review A*, 86(4), October 2012.

[31] R. Zhao, Y. O. Dudin, S. D. Jenkins, C. J. Campbell, D. N. Matsukevich, T. A. B. Kennedy, and A. Kuzmich. Long-lived quantum memory. *Nature Physics*, 5(2):100–104, December 2008.

[32] S D Jenkins, T Zhang, and T A B Kennedy. Motional dephasing of atomic clock spin waves in an optical lattice. *Journal of Physics B: Atomic, Molecular and Optical Physics*, 45(12):124005, jun 2012.

[33] Turker Topcu and Andrei Derevianko. Intensity landscape and the possibility of magic trapping of alkali-metal rydberg atoms in infrared optical lattices. *Physical Review A*, 88(4), October 2013.

[34] N. Šibalić, J.D. Pritchard, C.S. Adams, and K.J. Weatherill. ARC: An open-source library for calculating properties of alkali rydberg atoms. *Computer Physics Communications*, 220:319–331, November 2017.

[35] Anatole Abragam. *The Principles of Nuclear Magnetism*. Oxford Univ. Press, 2006.

[36] J. C. Bergquist, Wayne M. Itano, and D. J. Wineland. Recoilless optical absorption and doppler sidebands of a single trapped ion. *Physical Review A*, 36(1):428–430, July 1987.

[37] R. H. Dicke. The effect of collisions upon the doppler width of spectral lines. *Physical Review*, 89(2):472–473, January 1953.

[38] L.-M. Duan, M. D. Lukin, J. I. Cirac, and P. Zoller. Long-distance quantum communication with atomic ensembles and linear optics. *Nature*, 414(6862):413–418, November 2001.

[39] D. N. Matsukevich and A. Kuzmich. Quantum state transfer between matter and light. *Science*, 306(5696):663–666, October 2004.

[40] Lin Li and A Kuzmich. Quantum memory with strong and controllable rydberg-level interactions. *Nature Communications*, 7(1), November 2016.

[41] A. G. Radnaev, Y. O. Dudin, R. Zhao, H. H. Jen, S. D. Jenkins, A. Kuzmich, and T. A. B. Kennedy. A quantum memory with telecom-wavelength conversion. *Nature Physics*, 6(11):894–899, September 2010.

[42] Y. O. Dudin, R. Zhao, T. A. B. Kennedy, and A. Kuzmich. Light storage in a magnetically dressed optical lattice. *Physical Review A*, 81(4), April 2010.

[43] Y. O. Dudin, L. Li, and A. Kuzmich. Light storage on the time scale of a minute. *Physical Review A*, 87(3), March 2013.

[44] Stig Stenholm. Dynamics of trapped particle cooling in the lamb–dicke limit. *Journal of the Optical Society of America B*, 2(11):1743, November 1985.

[45] Mariusz Gajda, Piotr Krekora, and Jan Mostowski. Light scattering by an ultracold trapped atom. *Physical Review A*, 54(1):928–942, July 1996.

[46] M. Martinez-Dorantes, W. Alt, J. Gallego, S. Ghosh, L. Ratschbacher, and D. Meschede. State-dependent fluorescence of neutral atoms in optical potentials. *Physical Review A*, 97(2), February 2018.

[47] G. Raithel, W. D. Phillips, and S. L. Rolston. Collapse and revivals of wave packets in optical lattices. *Physical Review Letters*, 81(17):3615–3618, October 1998.

[48] J. Lampen, H. Nguyen, L. Li, P. R. Berman, and A. Kuzmich. Long-lived coherence between ground and rydberg levels in a magic-wavelength lattice. *Physical Review A*, 98(3), September 2018.

[49] Stephen M. Barnett and Paul M. Radmore. *Methods in theoretical quantum optics*. Clarendon Press, 2005.

[50] Thomas R. Carver. Mathieu's functions and electrons in a periodic lattice. *American Journal of Physics*, 39(10):1225–1230, October 1971.

[51] J. L. Cohen and P. R. Berman. Transit-time effects in coherent transient spectroscopy. *Physical Review A*, 54(6):5262–5274, December 1996.

[52] S. Zhang, F. Robicheaux, and M. Saffman. Magic-wavelength optical traps for rydberg atoms. *Physical Review A*, 84(4), October 2011.

[53] Turker Topcu and Andrei Derevianko. Intensity landscape and the possibility of magic trapping of alkali-metal rydberg atoms in infrared optical lattices. *Physical Review A*, 88(4), October 2013.

[54] Atreju Tauschinsky, Richard Newell, H. B. van Linden van den Heuvell, and R. J. C. Spreeuw. Measurement of rb87 rydberg-state hyperfine splitting in a room-temperature vapor cell. *Physical Review A*, 87(4), April 2013.

[55] Julian Naber, Atreju Tauschinsky, Ben van Linden van den Heuvell, and Robert Spreeuw. Electromagnetically induced transparency with rydberg atoms across the breit-rabi regime. *SciPost Physics*, 2(2), April 2017.

[56] H. Saßmannshausen, F. Merkt, and J. Deiglmayr. High-resolution spectroscopy of rydberg states in an ultracold cesium gas. *Physical Review A*, 87(3), March 2013.

[57] P. R. Berman, H. Nguyen, and A. Kuzmich. Theory of coherent optical transients with quantized atomic motion. *Physical Review A*, 99(1), January 2019.

[58] Alan Corney. *Atomic and laser spectroscopy*. Clarendon Press, 2010.

[59] Wenhui Li, I. Mourachko, M. W. Noel, and T. F. Gallagher. Millimeter-wave spectroscopy of cold rb rydberg atoms in a magneto-optical trap: Quantum defects of the ns,np, and nd series. *Physical Review A*, 67(5), May 2003.

[60] Dieter Meschede. Centimeter-wave spectroscopy of highly excited rubidium atoms. *Journal of the Optical Society of America B*, 4(3):413, March 1987.

[61] D. A. Steck.

[62] B. Dubetsky and P. R. Berman. $\lambda/4$, $\lambda/8$, and higher order atom gratings via raman transitions, 2002.

[63] Albert Einstein. Zur Quantentheorie der Strahlung. *Physikalische Zeitschrift*, 18:121–128, January 1917.

[64] Z. Y. Ou, L. J. Wang, and L. Mandel. Photon amplification by parametric downconversion. *Journal of the Optical Society of America B*, 7(2):211, February 1990.

[65] A. Lamas-Linares, J. C. Howell, and D. Bouwmeester. Stimulated emission of polarization-entangled photons. *Nature*, 412(6850):887–890, August 2001.

[66] A. Lamas-Linares, Christoph Simon, John C. Howell, and Dik Bouwmeester. Experimental quantum cloning of single photons. *Science*, 296(5568):712–714, April 2002.

[67] F. W. Sun, B. H. Liu, Y. X. Gong, Y. F. Huang, Z. Y. Ou, and G. C. Guo. Stimulated emission as a result of multiphoton interference. *Physical Review Letters*, 99(4), July 2007.

[68] Shuai Dong, Xin Yao, Wei Zhang, Sijing Chen, Weijun Zhang, Lixing You, Zhen Wang, and Yidong Huang. True single-photon stimulated four-wave mixing. *ACS Photonics*, 4(4):746–753, March 2017.

[69] Zhe-Yu Jeff Ou. *Multi-photon quantum interference*. Springer, 2010.

[70] R. H. Dicke. Coherence in spontaneous radiation processes. *Physical Review*, 93(1):99–110, January 1954.

[71] P. R. Berman and A. Kuzmich. Coincidence counts and stimulated emission resulting from weak pulsed-field–atom interactions. *Physical Review A*, 101(3), March 2020.

[72] R. HANBURY BROWN and R. Q. TWISS. Correlation between photons in two coherent beams of light. *Nature*, 177(4497):27–29, January 1956.

[73] Melissa Cray, Mei-Li Shih, and Peter W. Milonni. Stimulated emission, absorption, and interference. *American Journal of Physics*, 50(11):1016–1021, November 1982.

[74] E. Urban, T. A. Johnson, T. Henage, L. Isenhower, D. D. Yavuz, T. G. Walker, and M. Saffman. Observation of rydberg blockade between two atoms. *Nature Physics*, 5(2):110–114, January 2009.

[75] Alpha Gaëtan, Yevhen Miroshnychenko, Tatjana Wilk, Amodsen Chotia, Matthieu Viteau, Daniel Comparat, Pierre Pillet, Antoine Browaeys, and Philippe Grangier. Observation of collective excitation of two individual atoms in the rydberg blockade regime. *Nature Physics*, 5(2):115–118, January 2009.

[76] Johannes Zeiher, Peter Schauß, Sebastian Hild, Tommaso Macrì, Immanuel Bloch, and Christian Gross. Microscopic characterization of scalable coherent rydberg superatoms. *Physical Review X*, 5(3), August 2015.

[77] P. A. Franken, A. E. Hill, C. W. Peters, and G. Weinreich. Generation of optical harmonics. *Phys. Rev. Lett.*, 7:118–119, Aug 1961.

[78] P. D. Maker, R. W. Terhune, M. Nisenoff, and C. M. Savage. Effects of dispersion and focusing on the production of optical harmonics. *Phys. Rev. Lett.*, 8:21–22, Jan 1962.

[79] N. A. Kurnit, I. D. Abella, and S. R. Hartmann. Observation of a photon echo. *Phys. Rev. Lett.*, 13:567–568, Nov 1964.

[80] T. Chanelière, D. N. Matsukevich, S. D. Jenkins, S.-Y. Lan, T. A. B. Kennedy, and A. Kuzmich. Storage and retrieval of single photons transmitted between remote quantum memories. *Nature*, 438(7069):833–836, 2005.

[81] P. R. Berman and J.-L. Le Gouët. Phase-matched emission from an optically thin medium following one-photon pulse excitation: Energy considerations. *Physical Review A*, 83(3), March 2011.

[82] U. Eichmann, J. C. Bergquist, J. J. Bollinger, J. M. Gilligan, W. M. Itano, D. J. Wineland, and M. G. Raizen. Young's interference experiment with light scattered from two atoms. *Phys. Rev. Lett.*, 70:2359–2362, Apr 1993.

[83] S. Wolf, J. Wechs, J. von Zanthier, and F. Schmidt-Kaler. Visibility of Young's interference fringes: Scattered light from small ion crystals. *Phys. Rev. Lett.*, 116:183002, May 2016.

[84] P. Obšil, A. Lešundák, T. Pham, G. Araneda, M. Čížek, O. Číp, R. Filip, and L. Slodička. Multipath interference from large trapped ion chains. *New J. Phys.*, 21(9):093039, 2019.

[85] C. Weitenberg, P. Schauß, T. Fukuhara, M. Cheneau, M. Endres, I. Bloch, and S. Kuhr. Coherent light scattering from a two-dimensional mott insulator. *Phys. Rev. Lett.*, 106:215301, May 2011.

[86] G. Birkl, M. Gatzke, I. H. Deutsch, S. L. Rolston, and W. D. Phillips. Bragg scattering from atoms in optical lattices. *Phys. Rev. Lett.*, 75:2823–2826, Oct 1995.

[87] S. Slama, C. von Cube, A. Ludewig, M. Kohler, C. Zimmermann, and Ph. W. Courteille. Dimensional crossover in Bragg scattering from an optical lattice. *Phys. Rev. A*, 72:031402, Sep 2005.

[88] B. B. Blinov, D. L. Moehring, L.-M. Duan, and C. Monroe. Observation of entanglement between a single trapped atom and a single photon. *Nature*, 428(6979):153–157, 2004.

[89] J. Volz, M. Weber, D. Schlenk, W. Rosenfeld, J. Vrana, K. Saucke, C. Kurtsiefer, and H. Weinfurter. Observation of entanglement of a single photon with a trapped atom. *Phys. Rev. Lett.*, 96:030404, Jan 2006.

[90] D. N. Matsukevich, T. Chanelière, S. D. Jenkins, S.-Y. Lan, T. A. B. Kennedy, and A. Kuzmich. Entanglement of remote atomic qubits. *Phys. Rev. Lett.*, 96:030405, Jan 2006.

[91] D. L. Moehring, P. Maunz, S. Olmschenk, K. C. Younge, D. N. Matsukevich, L.-M. Duan, and C. Monroe. Entanglement of single-atom quantum bits at a distance. *Nature*, 449(7158):68–71, 2007.

[92] J. Hofmann, M. Krug, N. Ortegel, L. Gérard, M. Weber, W. Rosenfeld, and H. Weinfurter. Heralded entanglement between widely separated atoms. *Science*, 337(6090):72–75, 2012.

[93] T. Xia, M. Lichtman, K. Maller, A. W. Carr, M. J. Piotrowicz, L. Isenhower, and M. Saffman. Randomized benchmarking of single-qubit gates in a 2d array of neutral-atom qubits. *Phys. Rev. Lett.*, 114:100503, Mar 2015.

[94] Y. Wang, A. Kumar, T.-Y. Wu, and D. S. Weiss. Single-qubit gates based on targeted phase shifts in a 3d neutral atom array. *Science*, 352(6293):1562–1565, 2016.

[95] H. Levine, A. Keesling, G. Semeghini, A. Omran, T. T. Wang, S. Ebadi, H. Bernien, M. Greiner, V. Vuletic, H. Pichler, and M. D. Lukin. Parallel implementation of high-fidelity multiqubit gates with neutral atoms. *Phys. Rev. Lett.*, 123:170503, Oct 2019.

[96] T. M. Graham, M. Kwon, B. Grinkemeyer, Z. Marra, X. Jiang, M. T. Lichtman, Y. Sun, M. Ebert, and M. Saffman. Rydberg-mediated entanglement in a two-dimensional neutral atom qubit array. *Phys. Rev. Lett.*, 123:230501, Dec 2019.

[97] C. Monroe, R. Raussendorf, A. Ruthven, K. R. Brown, P. Maunz, L.-M. Duan, and J. Kim. Large-scale modular quantum-computer architecture with atomic memory and photonic interconnects. *Phys. Rev.*, 89:022317, 2014.

[98] B. R. Mollow. Power spectrum of light scattered by two-level systems. *Phys. Rev.*, 188:1969–1975, Dec 1969.

[99] W. M. Itano, J. C. Bergquist, J. J. Bollinger, D. J. Wineland, U. Eichmann, and M. G. Raizen. Complementarity and Young's interference fringes from two atoms. *Phys. Rev. A*, 57:4176–4187, Jun 1998.

[100] N. Schlosser, G. Reymond, and P. Grangier. Collisional blockade in microscopic optical dipole traps. *Phys. Rev. Lett.*, 89:023005, Jun 2002.

[101] C. Tuchendler, A. M. Lance, A. Browaeys, Y. R. P. Sortais, and P. Grangier. Energy distribution and cooling of a single atom in an optical tweezer. *Phys. Rev. A*, 78:033425, Sep 2008.

[102] Y. R. P. Sortais, H. Marion, C. Tuchendler, A. M. Lance, M. Lamare, P. Fournet, C. Armellin, R. Mercier, G. Messin, A. Browaeys, and P. Grangier. Diffraction-limited optics for single-atom manipulation. *Phys. Rev. A*, 75:013406, Jan 2007.

[103] Alberto Rojo (private communication).

[104] See, for example, E. Urban, T. A. Johnson, T., Henage, L. Isenhower, D.D. Yavuz, T. G. Walker, and M. Saffman, Nature Phys **5**, 110–114 (2009); A. Gaëtan, Y. Miroshnychenko, T Wilk, A. Chotia, M. Viteau, D. Comparat, P. Pillet, A. Browaeys, and P. Grangier, Nature Phys. **5**, 115–118 (2009).

[105] See, for example, D. Tong, S. M. Farooqi, J. Stanojevic, S. Krishnan, Y. P. Zhang, R. Côté, E. E. Eyler, and P. L. Gould, Phys. Rev. Lett. **93**, 063001 (2004); K. Singer, M. Reetz-Lamour, T. Amthor, L. G. Marcassa, and M. Weidemüller, Phys. Rev. Lett. **93**, 163001 (2004); T. Cubel Liebisch, A. Reinhard, P. R. Berman, and G. Raithel, Phys. Rev. Lett. **95**, 253002 (2005); R. Heidemann, U. Raitzsch, V. Bendkowsky, B. Butscher, R. Löw, L. Santos, and T. Pfau, Phys. Rev. Lett. **99**, 163601 (2007); Y. O. Dudin, L. Li, F. Bariani, and A. Kuzmich, Nat. Phys. **8**, 790 (2012); J. Zeiher, P. Schauß, S. Hild, T. Macrì, I. Bloch, and C. Gross, Phys. Rev. X **5**, 031015 (2015); C. Qiao, C. Tan, J. Siegl, F. Hu, Z. Niu, Y. Jiang, M. Weidemüller, and B. Zhu, Phys. Rev. A **103**, (2021).

[106] Nathan Shammah, Shahnawaz Ahmed, Neill Lambert, Simone De Liberato, and Franco Nori. Open quantum systems with local and collective incoherent processes: Efficient numerical simulations using permutational invariance. *Physical Review A*, 98(6), December 2018.

[107] For reviews of this subject, see D. Comparat and P. Pillet, J. Opt. Soc. Am. B **27**, A208 (2010); A. Browaeys and T. Lahaye, Nature Phys.

[108] Some authors have examined how decay of the intermediate state modifies the Rydberg dynamics, but using approaches very different than the one that we use. See C. Ates, T. Pohl, T. Pattard, and J. M. Rost, Phys. Rev. A **76**, 013413 (2007) ; R. V. Skannrup, T. v Weerden, Y. vd Werf, T. Johri1, E. J. D. Vredenbregt and S. J. J. M. F. Kokkelmans, J. Phys. B: At. Mol. Opt. Phys. **53,** 084008 (2020), and references therein.

[109] T. Holstein and H. Primakoff. Field dependence of the intrinsic domain magnetization of a ferromagnet. *Physical Review*, 58(12):1098–1113, December 1940.

[110] The decay rate is essentially that associated with the Rabi oscillations of a single atom.

[111] Even though $N \gg 1$ and $N \gg n_2$ it would be a mistake to replace $\sqrt{N-1}$ by $\sqrt{N}$ in Eq. (12.31b). If we did so, we would miss the light shift associated with field 1. A similar feature arises in our discussion of the Holstein-Primakoff transformation.

[112] It can be shown that the branching ratio for decay from level $(n,0)$ to $(n-1,0)$ is $(N-n+1)/N$ and for decay from level $(n,1)$ to $(n-1,1)$ is $(N-n)/N$. Therefore, if $N \gg 1$ and if the number of intermediate state excitations is much less than N, most of the decay is confined to the fully symmetric states.

[113] For the Hamiltonian given by Eq. (12.102) non-degenerate perturbation theory can be used to obtain the 3rd through 6th eigenkets, but not the first and second when χ_2 is comparable with χ_{RN} (see P. Berman, Introductory Quantum Mechanics (Springer, Cham, Switzerland, 2018), Sec. 14..2). Thus, in estimating the state amplitudes we miss a term of order χ_2/δ_1 that displaces the state amplitudes but is not modulated at frequency δ_1. This explains the discrepancy between the approximate and exact solutions seen in Fig. 12.10. Note, however, that Eqs. (12.108) conserve probability to order χ_2/δ_1. If $\chi_2/\delta_1 \ll 1$, we found that a somewhat better approximation is obtained if the $\sin^2(\chi_{RN}t)$ term in Eq. (12.109) is replaced by $\sin^2(\chi_{RN}t)\left(1-\frac{N\chi_2\chi_1^2}{6\delta_1^3}\right)$.

[114] Jaksch et al [D. Jaksch, J. I. Cirac, P. Zoller, S. L. Rolston, R. Côté, and M. D. Lukin, Phys. Rev. Lett. **85**, 2208 (2000)] point out the advantage of using adiabatic states in the two-atom, two state model.

[115] We have run some simulations including decay that confirm that the Rabi oscillations are not damped at a rate proportional to N, even when there are many intermediate state excitations; however, decay *can* wash out some of the modulation of the total Rydberg population.

[116] Christoph Simon. Towards a global quantum network. *Nature Photonics*, 11(11):678–680, October 2017.

[117] Stephanie Wehner, David Elkouss, and Ronald Hanson. Quantum internet: A vision for the road ahead. *Science*, 362(6412), October 2018.

[118] James K. Thompson, Jonathan Simon, Huanqian Loh, and Vladan Vuletic. A high-brightness source of narrowband, identical-photon pairs. *Science*, 313(5783):74–77, July 2006.

[119] Yu-Ao Chen, Shuai Chen, Zhen-Sheng Yuan, Bo Zhao, Chih-Sung Chuu, Jörg Schmiedmayer, and Jian-Wei Pan. Memory-built-in quantum teleportation with photonic and atomic qubits. *Nature Physics*, 4(2):103–107, January 2008.

[120] D. P. Ornelas-Huerta, A. N. Craddock, E. A. Goldschmidt, A. J. Hachtel, Y. Wang, P. Bienias, A. V. Gorshkov, S. L. Rolston, and J. V. Porto. On-demand indistinguishable single photons from an efficient and pure source based on a rydberg ensemble. *Optica*, 7(7):813–819, Jul 2020.

[121] Y. O. Dudin, A. G. Radnaev, R. Zhao, J. Z. Blumoff, T. A. B. Kennedy, and A. Kuzmich. Entanglement of light-shift compensated atomic spin waves with telecom light. *Physical Review Letters*, 105(26), December 2010.

[122] Wenchao Xu, Aditya V. Venkatramani, Sergio H. Cantú, Tamara Šumarac, Valentin Klüsener, Mikhail D. Lukin, and Vladan Vuletic. Fast preparation and detection of a rydberg qubit using atomic ensembles. *Physical Review Letters*, 127(5), July 2021.

[123] Nicholas L. R. Spong, Yuechun Jiao, Oliver D. W. Hughes, Kevin J. Weatherill, Igor Lesanovsky, and Charles S. Adams. Collectively encoded rydberg qubit. *Physical Review Letters*, 127(6), August 2021.

[124] Harry Levine, Alexander Keesling, Ahmed Omran, Hannes Bernien, Sylvain Schwartz, Alexander S. Zibrov, Manuel Endres, Markus Greiner, Vladan Vuletic, and Mikhail D. Lukin. High-fidelity control and entanglement of rydberg-atom qubits. *Physical Review Letters*, 121(12), September 2018.

[125] Ivaylo S. Madjarov, Jacob P. Covey, Adam L. Shaw, Joonhee Choi, Anant Kale, Alexandre Cooper, Hannes Pichler, Vladimir Schkolnik, Jason R. Williams, and Manuel Endres. High-fidelity entanglement and detection of alkaline-earth rydberg atoms. *Nature Physics*, 16(8):857–861, May 2020.

[126] Henning Labuhn, Daniel Barredo, Sylvain Ravets, Sylvain de Léséleuc, Tommaso Macrì, Thierry Lahaye, and Antoine Browaeys. Tunable two-dimensional arrays of single rydberg atoms for realizing quantum ising models. *Nature*, 534(7609):667–670, June 2016.

[127] Johannes Zeiher, Peter Schauß, Sebastian Hild, Tommaso Macrì, Immanuel Bloch, and Christian Gross. Microscopic characterization of scalable coherent rydberg superatoms. *Physical Review X*, 5(3), August 2015.

[128] H. Nguyen, J. Lampen, P. R. Berman, and A. Kuzmich. Differential nuclear-spin-dependent light shifts and state mixing of rydberg atoms. *Physical Review A*, 100(3), September 2019.

[129] J. T. Wilson, S. Saskin, Y. Meng, S. Ma, R. Dilip, A. P. Burgers, and J. D. Thompson. Trapping alkaline earth rydberg atoms optical tweezer arrays. *Physical Review Letters*, 128(3), January 2022.

[130] Florian Fröwis, Peter C. Strassmann, Alexey Tiranov, Corentin Gut, Jonathan Lavoie, Nicolas Brunner, Félix Bussières, Mikael Afzelius, and Nicolas Gisin. Experimental certification of millions of genuinely entangled atoms in a solid. *Nature Communications*, 8(1), October 2017.

[131] Robert McConnell, Hao Zhang, Jiazhong Hu, Senka Ćuk, and Vladan Vuletic. Entanglement with negative wigner function of almost 3, 000 atoms heralded by one photon. *Nature*, 519(7544):439–442, March 2015.

[132] Florian Haas, Jürgen Volz, Roger Gehr, Jakob Reichel, and Jérôme Estève. Entangled states of more than 40 atoms in an optical fiber cavity. *Science*, 344(6180):180–183, April 2014.

[133] Yibo Wang, Sayali Shevate, Tobias Martin Wintermantel, Manuel Morgado, Graham Lochead, and Shannon Whitlock. Preparation of hundreds of microscopic atomic ensembles in optical tweezer arrays. *npj Quantum Information*, 6(1), June 2020.

[134] S. Whitlock, C. F. Ockeloen, and R. J. C. Spreeuw. Sub-poissonian atom-number fluctuations by three-body loss in mesoscopic ensembles. *Physical Review Letters*, 104(12), March 2010.

[135] Mohammadsadegh Khazali and Klaus Mølmer. Fast multiqubit gates by adiabatic evolution in interacting excited-state manifolds of rydberg atoms and superconducting circuits. *Physical Review X*, 10(2), June 2020.

[136] G. S. Agarwal. Exact solution for the influence of laser temporal fluctuations on resonance fluorescence. *Physical Review Letters*, 37(21):1383–1386, November 1976.

[137] G. S. Agarwal. Quantum statistical theory of optical-resonance phenomena in fluctuating laser fields. *Physical Review A*, 18(4):1490–1506, October 1978.

[138] Sylvain de Léséleuc, Daniel Barredo, Vincent Lienhard, Antoine Browaeys, and Thierry Lahaye. Analysis of imperfections in the coherent optical excitation of single atoms to rydberg states. *Physical Review A*, 97(5), May 2018.

[139] P. Cladé, Ph.D. thesis, Université Paris 6, 2004.

[140] X. Jiang, M. Friesen, J. Scott, and M. Saffman, "The effect of laser noise on Rabi oscillation fidelity", *Bulletin of the American Physical Society* (2021).

[141] G. M. Stéphan, T. T. Tam, S. Blin, P. Besnard, and M. Têtu. Laser line shape and spectral density of frequency noise. *Physical Review A*, 71(4), April 2005.

[142] Y. Mei, Y. Li, H. Nguyen, P. R. Berman, and A. Kuzmich, "Dynamics of interaction-induced dephasing for collective Rydberg excitations", in preparation (2021).

[143] Y. O. Dudin, F. Bariani, and A. Kuzmich. Emergence of spatial spin-wave correlations in a cold atomic gas. *Physical Review Letters*, 109(13), September 2012.

[144] F. Bariani, Y. O. Dudin, T. A. B. Kennedy, and A. Kuzmich. Dephasing of multiparticle rydberg excitations for fast entanglement generation. *Physical Review Letters*, 108(3), January 2012.